All-Optical 3R Regeneration for Agile All-Photonic Networks

by

Christopher Joshua Shiro Ito

A thesis submitted to the

Department of Electrical and Computer Engineering

in conformity with the requirements for the degree of

Doctor of Philosophy

Queen's University

Kingston, Ontario, Canada

August 2007

Library and Archives Canada

Published Heritage Branch

395 Wellington Street
Ottawa ON K1A 0N4
Canada

Bibliothèque et Archives Canada

Direction du Patrimoine de l'édition

395, rue Wellington
Ottawa ON K1A 0N4
Canada

Your file Votre référence
ISBN: 978-0-494-37215-9
Our file Notre référence
ISBN: 978-0-494-37215-9

Abstract

Transmission impairments degrade the quality of optical signals, ultimately limiting the achievable transmission distance. Optical 3R regenerators provide an effective means of coping with transmission impairments by restoring the quality of optical signals through reamplification, reshaping, and retiming (3Rs), thereby enabling reliable transmission over long distances. Beyond the 3Rs, however, regenerators must also be able to operate within the practical constraints of the network. The specific network of interest in this thesis is referred to as an *agile all-photonic network* (AAPN).

In AAPNs, traffic consists of optical packets that are routed through the core of the network without undergoing optical-to-electrical conversion for signal processing (e.g., 3R regeneration). As a result, 3R regeneration must be performed all-optically, otherwise known as *all-optical 3R regeneration* (AO-3R). Although a variety of AO-3R techniques have been demonstrated, none have been specifically designed to operate within the practical constraints of AAPNs.

In this thesis, a 10 Gb/s all-optical 3R regeneration (AO-3R) technique is proposed, specifically designed to operate within the practical constraints of AAPNs. The technique performs AO-3R in a novel 2-stage design. In the first stage, all-optical retiming is achieved using a self-pulsating distributed feedback laser (SP-DFBL) for all-optical

clock recovery and cross-phase modulation (XPM) in highly nonlinear fiber (HNLF) with offset spectral slicing for the retiming. In the second stage, all-optical reshaping (and reamplification) is achieved using self-phase modulation (SPM) in HNLF with offset spectral slicing.

Experimental assessment of the AO-3R system performance yields excellent results. In particular, AO-3R is shown to improve the performance of input signals degraded by transmission impairments, such as amplified spontaneous emission (ASE) noise, while providing low sensitivity to input signal properties, such as the state-of-polarization. Furthermore, AO-3R is shown to successfully achieve its ultimate goal for AAPNs — the regeneration of optical packets.

Acknowledgments

I have been most blessed to be surrounded by wonderfully inspiring people throughout life and especially during my Ph.D. program. I would like to acknowledge and thank the following people.

My supervisor, Dr. John Cartledge. An absolutely superb mentor, he has always been supportive and encouraging in my research. He taught me to be analytical, and perhaps more importantly, to conduct myself as a professional; skills and craft that will carry me well beyond the ivied walls of Queen's.

Dr. Cartledge has also been instrumental in providing financial support during my program. Sources of funding I would like to thank are the Natural Sciences and Engineering Research Council (NSERC); eMPOWR Canada; and the Association of Universities and Colleges of Canada (AUCC).

I salute the members of the Lightwave Systems Research Laboratory for providing more scholarship than any textbook ever could. In particular, Iannick Monfils and David Krause are not only good friends, and colleagues in the program, but have been great teachers, and have been part of many fruitful discussions. This strong support network has kept me motivated (and sane) along the way.

I have also been fortunate to have the loving support of my family. I would like to thank the newest members of my family, my father- and mother-in-law, Wayne and Betty Baxter. Your constant encouragement, through cards and conversations, has picked me up when I've needed it the most. I would also like to thank my step-parents, Ana Ito and Dr. Richard McCutcheon, for their support throughout the years and for becoming such an important part of my life. Most of all, I would like to thank my parents, Toshio Ito and Dr. Amy McCutcheon. You have always encouraged me to follow my dreams. Because of your love and support, I believe I can reach them. Thank you for always believing in me.

Last, but certainly not least, I would like to thank my wife, Jennie. I don't think I could have done this without you. I can't even begin to tell you how much I appreciate all you've done to help me through this challenging time. While the last few years have been a time of new findings, both academic and personal, you have truly been my greatest discovery.

Contents

List of Tables

List of Figures

Chapter 1

Introduction

1.1 Agile All-Photonic Networks (AAPNs)

Optical networks have enabled the transmission of vast amounts of information, seemingly instantly, across the world. As the demand for "instant" access to information increases, particularly high bandwidth information, optical networks will be forced to adapt to meet the needs of the end-user. To address this need, a Canadian research network was formed to develop the next generation of optical networks. The name coined for such optical networks are *Agile All-Photonic Networks* or AAPNs, for short. The aim of the agile all-photonic networks (AAPNs) research network is to develop an all-photonic network core that stretches as close as possible to the end-user [1]. To achieve this aim, research has been focused on the development of two key areas: network architectures and enabling technologies.

For the network architecture, an overlaid star network has been proposed [2]. In this topology, each "star" consists of a core (switching) node connected to every edge

node in the network. The edge nodes provide the network with *agility* by dynamically allocating resources (e.g., bandwidth) to traffic flows as the demand varies. To achieve optimal use of available bandwidth, edge nodes parse information into small bandwidth bins of time and wavelength. To the physical network layer, the traffic appears bursty, consisting of optical packets of information. The optical packets are routed between edge nodes through an *all-photonic* network core.

The aim of an all-photonic network core is to transmit optical packets between edge nodes without any optical-to-electrical-to-optical (OEO) conversions, for example, in optical switching and optical regeneration. Since a considerable portion of network cost is associated with OEO conversions [3], it is highly desirable to eliminate such conversions within the core of the network. In addition to cost, OEO conversions limit the potential for ultra-high speed transmission since the electronics, not the optics, are limiting. To eliminate OEO conversions, while still ensuring reliable transmission, the development of enabling technologies is essential for the success of AAPNs.

1.2 Optical Regeneration in AAPNs

Optical regeneration is one of the key enabling technologies for AAPNs. As optical signals travel through the network, they become degraded by transmission impairments and amplified spontaneous emission (ASE) noise from optical amplification. Optical regenerators provide an effective means of ensuring reliable transmission by restoring signal quality. The level of restoration depends on the network requirements: 1R regenerators reamplify; 2R regenerators reamplify and reshape; 3R regenerators reamplify, reshape, and retime (e.g., Fig. 1.1). For AAPNs, a combination of 1R, 2R,

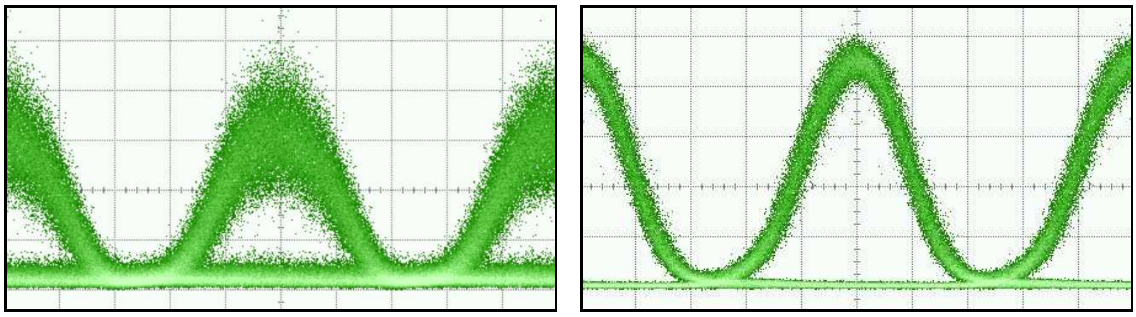

Figure 1.1: Example of a 10 Gb/s optical signal degraded by ASE noise (a) before and (b) after 3R regeneration (20 ps/div).

and 3R regenerators will be required. 3R regenerators, in particular, will be required to enable reliable transmission over long distances. The focus of this thesis is on the design of a 3R regenerator that is suitable for AAPNs.

To determine suitability, it is important to identify the requirements for 3R regenerators within the context of AAPNs. Since 3R regeneration is performed in the all-photonic network core, the regeneration should be achieved without OEO conversion. This means that the optical signal remains as an optical signal during the regeneration. Also, to reduce the complexity of resource management, the regenerated signal should have the same carrier wavelength as the input signal. In other words, the input signal should not be wavelength converted. Similarly, for consistent retransmission, the regenerated signal should have the same modulation format and pulse width (i.e., duty cycle) as the input signal. In AAPNs, optical signals are return-to-zero (RZ) intensity modulated at a bit rate of 10 Gb/s. For this modulation format and bit rate, practical pulse widths are 33 to 66 ps (i.e., 33 to 66% duty cycle).

The nature of the traffic also has implications on the requirements for 3R regeneration in AAPNs. In particular, dynamic routing of optical packets introduces

variability in transmission impairments (degradation) and input signal properties. The regenerator should therefore be able to restore the quality of signals with varying degrees of degradation. For example, input signals may vary in the extent of degradation caused by ASE noise, group velocity dispersion (GVD), and polarization mode dispersion (PMD). The regenerator should also be able to cope with variable input signal properties. Specifically, regenerator performance should exhibit low sensitivity to the input signal state-of-polarization (SOP), average input power, and input wavelength. For practical implementation, it is particularly important that the regenerator performance not be dependent on the input signal SOP.

The final requirement for 3R regeneration is also related to the nature of the traffic in AAPNs, specifically, optical packets. In AAPNs, the packet length is 10 μs and the inter-packet guard length is 1 μs. For 10 Gb/s signals, in terms of bit lengths, the packet length is 100 kbits and the inter-packet guard length is equivalent in duration to 10 kbits. To achieve optimal throughput, regeneration should be achieved within as few bits of the start of the packet as possible. In general, for 2R, regeneration can be achieved upon packet arrival (e.g., bit 1), while for 3R, regeneration can only be achieved once a clock signal has been recovered (e.g., bit 20). Therefore, for AAPNs, it is critical that the clock signal be recovered within the first few bits of the packet.

1.3 Thesis Contributions

In AAPNs, the fundamental requirement for regeneration is that the 3Rs (reamplification, reshaping, and retiming) be performed without OEO conversions. When the 3Rs are performed without OEO conversions, the regeneration is commonly referred

to as all-optical 3R regeneration (AO-3R). Although a variety of AO-3R techniques have been proposed (Sect. 2.2), none have been specifically designed to meet the requirements of AAPNs. To address this need, the thesis provides the following original contributions:

1. A novel technique for 10 Gb/s all-optical 3R regeneration (AO-3R), specifically designed to meet the requirements of AAPNs (Ch. 2) [4].

2. Demonstration that AO-3R can be made polarization insensitive without any additional complexity or control of the clock signal polarization (Ch. 3) [4], [5].

3. Demonstration that AO-3R can be achieved for 10 Gb/s signals with practical input and output pulse widths (Ch. 4) [4].

4. Evaluation of AO-3R system performance within the context of (Ch. 5):

   (a) Transmission impairments [4].

   (b) Input signal properties [4], [6].

   (c) Optical packets [4].

Chapter 2

Regenerator Design

2.1 Introduction

The first step in the design of a 3R regenerator is to identify its requirements within the context of the network. In Sect. 1.2, the requirements for 3R regeneration were identified within the context of agile all-photonic networks (AAPNs). One of the requirements is that 3R regeneration be performed all-optically. In the literature, a variety of techniques have been proposed for all-optical 3R regeneration (AO-3R). In Sect. 2.2, the techniques are reviewed with a focus on suitability for AAPNs. Based on the review, it is concluded that a technique for AO-3R does not currently exist that meets the complete requirements of AAPNs. To address this need, a new technique for AO-3R is proposed, specifically designed to meet the requirements of AAPNs. The design approach and principle of regeneration are described in Sect. 2.3. In Sect. 2.4, implementation of the regenerator design is presented. The implementation presented in this section is used in the experimental assessment of regenerator performance.

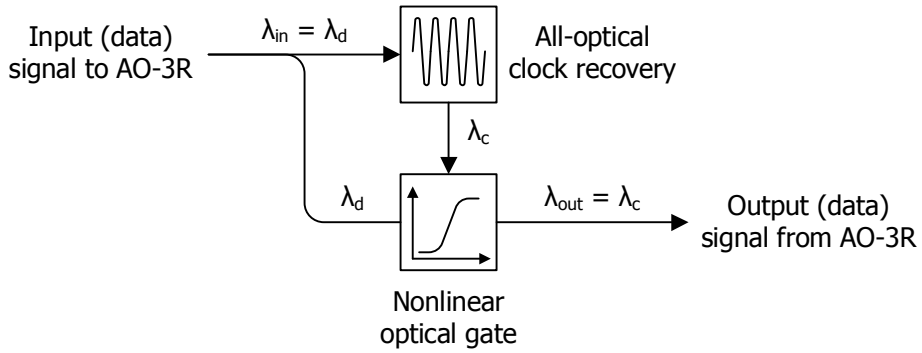

Figure 2.1: Generic scheme for all-optical 3R regeneration (AO-3R).

2.2 Literature Review: All-Optical 3R Regeneration

All-optical 3R regeneration (AO-3R) is generally achieved using the scheme shown in Fig. 2.1. In this scheme, the input (data) signal ($\lambda_{in} = \lambda_d$) is coupled into two paths. In the top path, an optical clock signal is recovered (λ_c). In the bottom path, the clock and data signals are coupled into a nonlinear optical gate, where the data (pump) signal intensity is used to optically gate the clock (probe) signal: high intensity (1-bits) opens the gate; low intensity (0-bits) closes the gate. Through optical gating, intensity modulation on the data signal is translated to the clock signal. Since the data signal either opens or closes the gate, variations in its intensity (noise) are not passed to the clock signal. In other words, optical gating reshapes the input signal. Furthermore, provided the clock signal has lower jitter than the input (data) signal, optical gating also retimes the input signal. The gated clock signal therefore serves as a 3R regenerated version of the input signal ($\lambda_{out} = \lambda_c$).

Several techniques for all-optical clock recovery and nonlinear optical gating have been proposed. In the next section, techniques for all-optical clock recovery are reviewed with a focus on suitability for all-optical 3R regeneration (AO-3R) in AAPNs.

2.2.1 All-Optical Clock Recovery

Clock recovery is the process of extracting the clock frequency f_c from an input signal with the intent of generating an electrical or optical clock signal with a period of $1/f_c$. For AO-3R, since gating is performed optically, clock recovery should generate an optical clock signal. In today's optical networks, clock recovery is performed electrically. In this approach, clock recovery requires optical-to-electrical (OE) conversion of the input optical signal. An electrical clock signal is then recovered from the electrical input signal, for example, using a phase locked loop (PLL) [7]. To generate an optical clock signal, electrical-to-optical (EO) conversion must be performed on the recovered electrical clock signal. Since optical-to-electrical-to-optical (OEO) conversion is required to generate an optical clock signal, recovering an optical clock signal electrically can be a rather costly process. Furthermore, the time required to recover the optical clock signal, known as the locking time, is on the order of microseconds [8], which is not acceptable within the context of AAPNs.

As described in Sect. 1.2, traffic in AAPNs will be bursty in nature. Specifically, traffic will consist of 10 μs optical packets (100 kbits) with 1 μs inter-packet guard times. To achieve optimal throughput, regeneration should be achievable within as few input signal bits as possible. This requires fast clock recovery with a locking time and release time that is on the order of nanoseconds (e.g., 20 bits). In addition, since

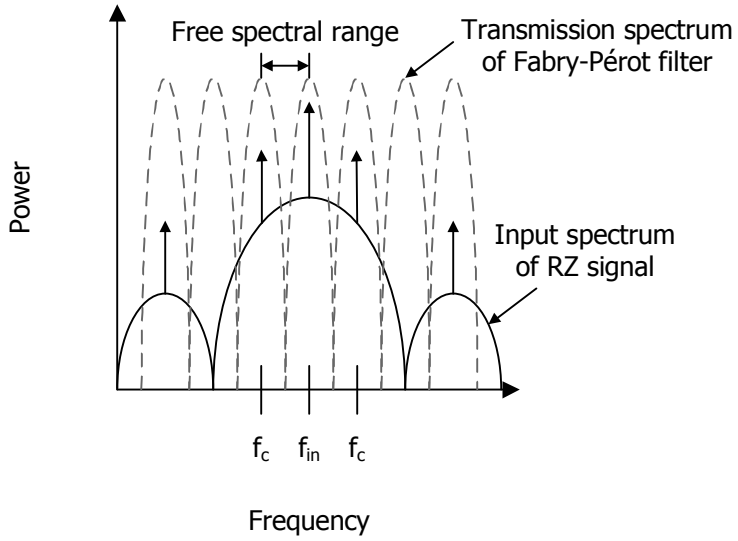

Figure 2.2: Clock recovery: Transmission spectrum of a Fabry-Pérot filter.

traffic will be dynamically routed through the network, input signal properties may vary from packet-to-packet. Therefore, clock recovery should also provide low sensitivity to input signal properties, such as average input power, state-of-polarization (SOP), and wavelength.

Techniques that recover an optical clock signal without OEO conversion have demonstrated the potential for meeting the requirements of AAPNs. Such techniques are commonly referred to as *all-optical clock recovery*. Although a variety of all-optical clock recovery techniques have been demonstrated [9–20], only two meet the requirement of having locking times on the order of nanoseconds: Fabry-Pérot filters (FPFs) [14, 16, 18] and self-pulsating distributed feedback lasers (SP-DFBLs) [21].

Fabry-Pérot Filters (FPFs)

Fabry-Pérot filters (FPFs) achieve all-optical clock recovery by optically filtering the clock harmonics of an input return-to-zero (RZ) signal. An illustration of a FPF

transmission spectrum is shown in Fig. 2.2. When the clock frequency component f_c of an input signal coincides with one of the peaks in the transmission spectrum, the clock frequency resonates in the FPF cavity [9]. Provided the free spectral range (FSR) is equal to the clock frequency of the input signal (e.g., 10 GHz), clock harmonics also resonate in the cavity. As a result, FPFs generate an optical clock signal oscillating at the clock frequency of the input signal.

Using stabilization of the clock signal amplitude as a measure of locking and release times, FPFs have demonstrated locking times as short as 0.2 ns (2 bits) and release times as short as 1.6 ns (16 bits) [18]. Although FPFs provide fast locking and release times, the clock signal amplitude often exhibits pattern effects [14]. In other words, the clock signal amplitude varies depending on the input bit sequence. The amplitude variation is caused by the exponential decay of the resonant signal, which occurs in the absence of an input signal (i.e., 0-bits) [22]. In particular, the finesse determines the rate of decay of the resonant frequency. In general, the lower the finesse, the shorter the decay time. Since FPFs with high finesse have longer decay times, they also exhibit less pattern effects. The tradeoff, however, is that FPFs with high finesse have longer locking and release times [14] and increased sensitivity to variations in clock frequency [22]. FPFs with low finesse shorten locking and release times [18], however, they often suffer from intense pattern effects [18]. To compensate, amplitude equalization using an ultrafast nonlinear interferometer (UNI) has been proposed [14]. While effective, the requirement of amplitude equalization increases the complexity of this approach to clock recovery.

Furthermore, FPFs are sensitive to the input signal wavelength. To satisfy the resonant condition, the input signal wavelength must coincide with one of the transmission peaks. While the center frequency of the transmission peaks can be tuned by temperature, the tuning range is often limited. In addition, FPFs are also sensitive to the input signal SOP. For example, varying the input signal SOP has been shown to cause the clock signal amplitude to vary by 6 dB [23]. Therefore, because of pattern effects and sensitivity to the input signal wavelength and SOP, FPFs are not the most ideal solution for all-optical clock recovery in AAPNs.

Self-Pulsating Distributed Feedback Lasers (SP-DFBLs)

SP-DFBLs may be the most ideal solution currently available for all-optical clock recovery in AAPNs. Before describing the properties of SP-DFBLs, the laser structure and principle of operation are described. In terms of structure, the laser consists of three-sections in an InGaAsP/InP ridge waveguide [24]. The first and third sections are DFB laser sections. The first section is operated above transparency, providing the lasing signal. The third section is operated close to transparency. This section provides a dispersive (Bragg) reflector, which reflects the lasing signal back into the first section of the laser. The second section is a phase tuning section. This section is also operated close to transparency and is used to spectrally correlate the lasing wavelength with the negative slope of the dispersive reflector. An illustration of the lasing wavelength relative to the reflectivity spectrum of the dispersive reflector is shown in Fig. 2.3 [25].

While all-optical clock recovery in a SP-DFBL can be achieved by different mechanisms [25–28], dispersive self-Q-switching (DSQS) is particularly well-suited for 10 Gb/s

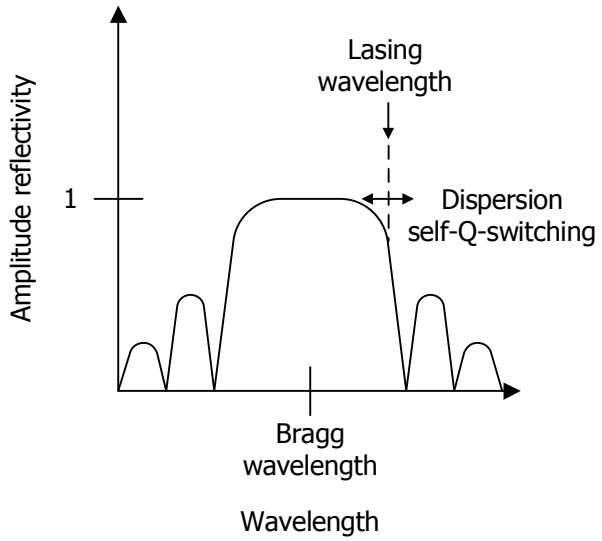

Figure 2.3: Clock recovery: Reflectivity spectrum of a SP-DFBL.

signals [25]. Using Fig. 2.3, DSQS can be explained as follows. In its initial state, the lasing wavelength coincides with the negative slope of the dispersive reflector. This causes the signal power to be reflected back into the lasing section. As a result, signal power increases due to an increase in stimulated emission (i.e., rising edge of clock pulse), which in turn, decreases the carrier density in the lasing section. The decrease in carrier density causes the refractive index to decrease, which chirps the lasing wavelength to a higher wavelength. In the reflectivity spectrum (Fig. 2.3), the lasing wavelength shifts towards a region of low reflectivity. This causes a decrease in signal power reflected back into the lasing section. As a result, signal power decreases due to a decrease in stimulated emission (i.e., falling edge of clock pulse), which in turn, increases the carrier density in the lasing section. The increase in carrier density causes the refractive index to increase, which chirps the lasing wavelength to a lower wavelength. In the reflectivity spectrum (Fig. 2.3), the lasing wavelength shifts

towards a region of high reflectivity. The process continually repeats inside the laser, thereby generating a self-pulsation (SP) signal.

All-optical clock recovery is achieved through synchronization of the SP frequency f_{sp} to the clock frequency f_c of the input signal (i.e., $f_{sp} = f_c$). Synchronization is achieved through intensity modulation of the input signal, which modulates the carrier density of the lasing section at a frequency f_c. This causes the lasing (SP) wavelength to chirp at a rate equal to f_c. As a result, the SP signal oscillates at f_c, thereby producing a synchronized optical clock signal.

SP-DFBLs provide many properties that make them well-suited for all-optical clock recovery in AAPNs. For example, like FPFs, SP-DFBLs have fast locking times. Using stabilization of the clock signal amplitude as a measure of locking time, SP-DFBLs have demonstrated locking times as short as 1 ns (10 bits) [21]. Fortunately, unlike FPFs, SP-DFBLs do not exhibit pattern effects. For example, in [12], an input $2^{31}-1$ pseudorandom bit sequence (PRBS) did not cause pattern effects in the recovered clock signal. This indicates that SP-DFBLs are capable of remaining synchronized to the clock frequency of an input signal for at least 30 consecutive 0-bits.

In addition, SP-DFBLs are capable of synchronizing (locking) over a wide range of input clock frequencies. In [15], the SP frequency f_{sp} was shown to lock over a 250 MHz range of input clock frequencies f_c (i.e., $f_{sp} = f_c \pm 125$ MHz). Providing a wide locking range is important since it increases the robustness of clock recovery to variations in input clock frequency. The robustness is further enhanced by the ability to tune f_{sp} over a frequency range of 5 to 22 GHz [12].

Furthermore, SP-DFBLs exhibit low sensitivity to input signal properties, such as average input power [15], SOP [11], and wavelength [11]. SP-DFBLs are also capable

of providing a recovered clock signal with low timing jitter (e.g., < 2 ps [12]). The ability to provide a recovered clock signal with lower timing jitter than the input signal is essential for achieving the retiming aspect of AO-3R.

Since the properties of SP-DFBLs are well-suited for AAPNs, the AO-3R technique proposed in this thesis uses a SP-DFBL[1] for all-optical clock recovery. In the next section, techniques for nonlinear optical gating are reviewed. Like all-optical clock recovery, the focus of the review is on the suitability of optical gating techniques for AO-3R in AAPNs.

2.2.2 Nonlinear Optical Gating

Cross-Absorption Modulation (XAM)

One technique achieves optical gating using cross-absorption modulation (XAM) in an electroabsorption modulator (EAM) [29–31]. XAM refers to the process in which a pump signal modulates the absorption of a probe signal. An EAM is a semiconductor waveguide that serves as the absorbing medium. The principle of optical gating based on XAM in an EAM is described as follows.

As the input pump signal power increases, pump signal photons are absorbed by the waveguide. In the process, carriers are generated in the active region. As carriers accumulate, they drift and diffuse through the active region. This causes a field screening effect, which reduces the ability of the waveguide to absorb input photons [32]. In other words, the absorption becomes saturated. An input probe signal therefore experiences low absorption allowing it to pass through the waveguide (i.e., open gate).

[1] Specifications for the SP-DFBL are described in Sect. 3.2.

As the input pump signal power decreases, carriers are swept out of the active region, allowing the waveguide to regain its ability to absorb input photons. An input probe signal therefore experiences high absorption preventing it from passing through the waveguide (i.e., closed gate).

When the input pump signal is intensity modulated (i.e., data signal), the gate is opened during high intensity (1-bits) and closed during low intensity (0-bits). When the probe signal is a pulse train (i.e., clock signal), clock pulses are passed through the gate for 1-bits and not passed through the gate for 0-bits. Therefore, through optical gating, intensity modulation on the data signal is translated to the clock signal, which serves as the 3R regenerated data signal.

XAM in an EAM provides the advantage of being able to achieve optical gating in a compact device that is potentially integrateable with semiconductor devices (e.g., lasers). The disadvantage, however, is that EAMs are not generally designed for optical-to-optical (OO) applications, such as XAM. In particular, EAMs are not typically capable of handling the high input signal power required to saturate the absorption (e.g., 19 dBm) [31]. Furthermore, because the absorption is sensitive to the input signal SOP [31] and wavelength [33], [34], optical gates based on XAM in an EAM may not be a well-suited technique for AO-3R in AAPNs.

Cross-Gain/Phase Modulation (XGM/XPM)

Another technique achieves optical gating using the combined effects of cross-gain modulation (XGM) and cross-phase modulation (XPM) in a semiconductor optical amplifier (SOA) [35–42]. XGM/XPM refers to the process in which a pump signal modulates the gain/phase of a probe signal. An SOA is a semiconductor waveguide

that serves as the gain/phase medium. The principle of optical gating based on XGM/XPM in an SOA is described as follows.

As the input pump signal power increases, the pump signal achieves gain through stimulated emission. In the process, carriers are depleted in the active region. As carriers become depleted, two effects occur. First, the available gain is reduced. In other words, the gain becomes saturated. Second, the refractive index increases. When these effects occur, an input probe signal experiences low gain and a decrease in phase. As a result, low probe signal power passes through the waveguide (i.e., closed gate). As the input pump signal power decreases, carriers are replenished in the active region. This has the effect of increasing the available gain and decreasing the refractive index. When this occurs, an input probe signal experiences high gain and an increase in phase. As a result, high probe signal power passes through the waveguide (i.e., open gate).

When the input pump signal is intensity modulated (i.e., data signal), the gate is closed during high intensity (1-bits) and opened during low intensity (0-bits). When the probe signal is a pulse train (i.e., clock signal), clock pulses are passed through the gate for 0-bits and not passed through the gate for 1-bits. Therefore, through optical gating, intensity modulation on the data signal is inverted and translated to the clock signal, which serves as the regenerated data signal.

Like XAM in an EAM, XGM/XPM in a SOA provides the advantage of being able to achieve optical gating in a compact device (i.e., micrometer length) that is potentially integrateable with semiconductor devices (e.g., lasers). However, unlike EAMs, SOAs have the disadvantage of having relatively long carrier recovery times (e.g., 20-200 ps) [43]. As a result, XGM causes the regenerated signal to suffer from pattern effects,

which manifest as waveform distortion and degradation to the extinction ratio (ER) [44–46]. Also, since SOAs inherently produce amplified spontaneous emission (ASE) noise, the regenerated signal also suffers from degradation to the signal-to-noise ratio (SNR) [47].

In addition, XPM causes the regenerated signal to experience time varying changes in phase. Since the change in phase is induced by a high power signal, the regenerated signal often suffers from considerable frequency chirp [44], [46]. This has important implications for transmission since XPM induced frequency chirp accelerates pulse broadening induced by group velocity dispersion (GVD) [48].

Although detrimental for transmission, XPM can be used to improve the performance of the optical gate. In particular, an interferometric configuration uses XPM to its advantage. Because of the improvement in performance, a variety of interferometric configurations have been proposed, including integrated SOA-Mach-Zehnder interferometer (SOA-MZI) [35,36,40,42,49], SOA-MZI super-structure [38], [23], and SOA-delayed interferometer (SOA-DI) [39], [41]. Although the implementations are different, the basic principle of optical gating is the same. For simplicity, the principle of optical gating for an interferometric configuration is described using a SOA-DI.

To aid in the description, consider the illustration of a SOA-DI shown in Fig. 2.4. The illustration is based on an implementation presented in [39]. At the input, the data (pump) and clock (probe) signals are coupled into a SOA. As described above, intensity modulation on the data signal is translated to the clock signal (i.e., modulated probe signal) through XGM in the SOA. The modulated probe signal is split into the two branches of a delayed interferometer (DI). In the top branch, the probe signal is delayed by one bit period. In the bottom branch, the probe signal is phase-shifted. The

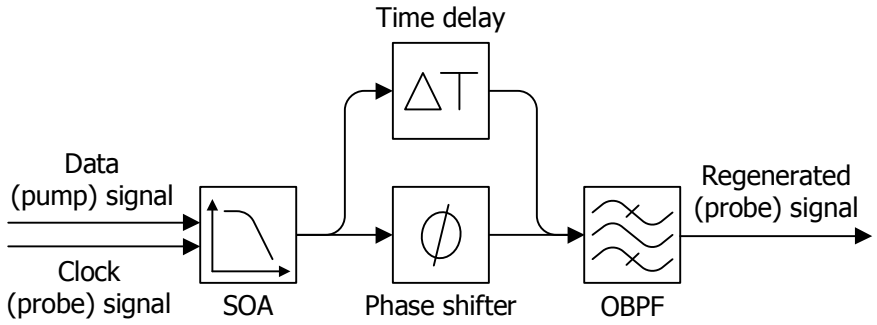

Figure 2.4: Optical gating: XGM/XGM in a SOA-DI configuration.

delay is used to compensate for the carrier recovery time by defining a transmission window for probe pulses. The phase shift is used to compensate for XPM by providing a relative phase difference of 0 or π between the interfering probe signals. When the relative phase difference is 0, probe signals interfere constructively, thereby allowing transmission of the probe pulse (i.e., open gate). When the relative phase difference is π, probe signals interfere destructively, thereby not allowing transmission of the probe pulse (i.e., closed gate). The probe signal is filtered using an optical bandpass filter (OBPF) and serves as the 3R regenerated signal.

The performance of XGM/XPM in a SOA is improved using interferometric configurations, such as SOA-DIs. In particular, interferometric configurations reduce pattern effects. For example, in [39], 40 Gb/s error free operation was demonstrated using a SOA-DI for an input $2^{31} - 1$ PRBS. Also, through constructive and destructive interference, interferometric configurations provide an increase in the ER [44], [50].

In addition, since the interference condition only requires an XPM induced phase change of π, XPM induced frequency chirp is decreased [44], [46]. Furthermore, the input signal power only needs to be high enough to induce a phase change of π. This allows the input signal power to be reduced, which reduces XGM. As a

result, wavelength dependent gain is reduced, thereby providing optical gating with low sensitivity to the input signal wavelength. With the use of polarization insensitive SOAs [51], it may be possible to achieve optical gating with low sensitivity to the input signal SOP.

While lower sensitivity to the input signal SOP and wavelength can be achieved, interferometric configurations often suffer from increased sensitivity to the input signal power. The increase in sensitivity occurs since the XPM induced phase is proportional to the input signal power. Therefore, variation in input signal power causes variation in XPM induced phase changes, which imbalances the constructive-destructive interference condition. As a result, performance of the optical gate is degraded. Therefore, because of its high sensitivity to input signal power and added ASE noise, optical gates based on XGM/XPM in a SOA-interferometer may not be the most well-suited technique for AO-3R in AAPNs.

Four-Wave Mixing (FWM)

An alternate technique achieves optical gating using four-wave mixing (FWM) in a highly nonlinear fiber (HNLF) [52–54]. FWM is a nonlinear effect that arises from the third-order nonlinear susceptibility $\chi^{(3)}$ in optical fibers [55]. Through $\chi^{(3)}$, FWM transfers power from a high intensity pump signal f_{pu} to a probe signal f_{pr}, while simultaneously generating a new (idler) signal $f_i = 2f_{pu} - f_{pr}$. Although FWM can be achieved in a SOA, added ASE noise and low FWM efficiency degrade performance [56–58]. FWM in optical fibers avoids the degradation caused by ASE noise. In addition, the use of special optical fibers, known as highly nonlinear fibers (HNLFs) for their enhanced nonlinearity, increase FWM efficiency. The principle of optical

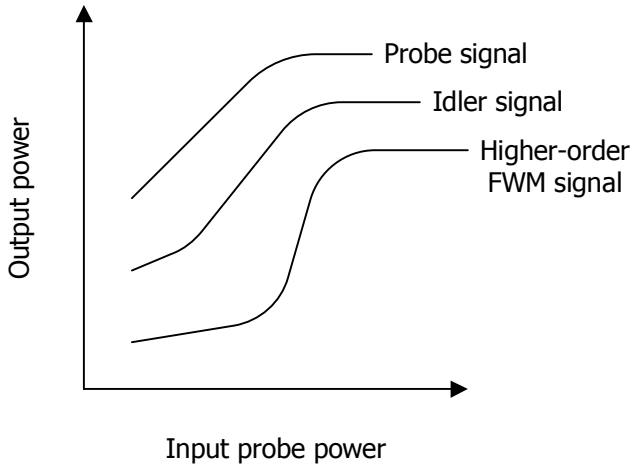

Figure 2.5: Optical gating: FWM power transfer characteristics.

gating based on FWM in a HNLF is described as follows.

To aid in the description, consider an illustration of the FWM power transfer characteristic (PTC) shown in Fig. 2.5. The PTC is a measure of output power versus input probe power. In Fig. 2.5, PTCs are shown for the probe, idler, and higher-order four-wave mixing (HO-FWM) signals. The HO-FWM signals are generated through a FWM process between the pump, probe and idler signals [59, 60]. An illustration of the FWM signal spectrum is shown in Fig. 2.6.

In FWM based optical gating, the probe signal controls the gating. For example, as the probe signal power increases, the probe signal achieves gain through a transfer of power from the pump signal (i.e., optical parametric amplification (OPA)). In the process, an idler signal is simultaneously generated. The idler signal also achieves gain through a transfer of power from the pump signal. As the idler signal power increases, HO-FWM signals are generated through a transfer of power from the pump, probe, and idler signals. Through pump depletion [61], the gain saturates. As a result,

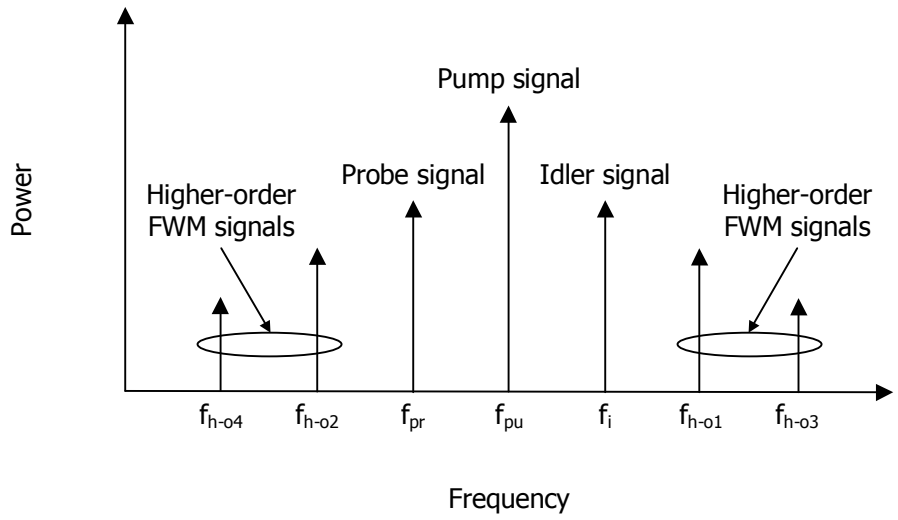

Figure 2.6: Optical gating: FWM signal spectrum.

FWM signal power is high at the output of the fiber (i.e., open gate). As the probe signal power decreases, the gain is no longer saturated and the probe signal achieves constant gain. When the probe signal power is sufficiently low, the idler signal power becomes lower than the probe signal since the probe signal serves as the seed for idler generation. Similarly, HO-FWM signals have even lower power since the idler serves as the seed for HO-FWM generation. Therefore, when the probe signal power is sufficiently low, FWM signal power is low at the output of the fiber (i.e., closed gate). In particular, for low probe signal power, from highest to lowest FWM signal power, the order is as follows: probe, idler, HO-FWM signals.

When the input probe signal is intensity modulated (i.e., data signal) and the pump signal is a pulse train (i.e., clock signal), the gate is opened during high data signal intensity (1-bits) and closed during low data signal intensity (0-bits). Therefore, in a sense, the pump (clock) signal performs a logical AND operation on the probe (data) signal. Since the pump is a clock signal, through optical gating, the FWM

signals (i.e., probe, idler, and HO-FWM) achieve 3R regeneration. However, since the power transfer characteristics differ (Fig. 2.5), FWM signals differ in their regenerative performance.

For the data (probe) signal, it has the unique property of achieving 3R regeneration without wavelength conversion [54]. However, because the data signal is amplified for low signal power (0-bits), low noise power is also amplified, degrading the SNR [60]. Since the data signal serves as the seed for generation of the idler signal, low noise power in the data signal is suppressed in the idler signal, which improves the SNR. Using the same argument, low noise power in the data signal is even more suppressed in HO-FWM signals, thereby further improving the SNR [60]. In general, HO-FWM signals suppress low data signal power, which also improves the ER [60], [52]. The tradeoff, however, is that HO-FWM signals, and FWM signals in general, often experience considerable pulse compression [62–64], which may not be acceptable in practical systems.

Furthermore, FWM efficiency is highly sensitive to the input signal SOP [55]. FWM efficiency, which determines the extent of power transfer between FWM signals, is also sensitive to the input signal wavelengths and power. To explain the source of the sensitivity, consider the expression for FWM efficiency η, given by [65]

$$\eta = \frac{\alpha^2}{\alpha^2 + \Delta k^2} \left\{ 1 + \frac{4 \exp(-\alpha L) \sin^2(\Delta k L/2)}{[1 - \exp(-\alpha L)]^2} \right\} \tag{2.1}$$

where Δk is the phase matching term, and α and L are the fiber attenuation coefficient and length, respectively. The FWM efficiency η is maximum when the phase matching term $\Delta k = 0$, where [66]

$$\Delta k = \Delta k_L + \Delta k_{NL} \tag{2.2}$$

Δk_L is the linear phase matching term and Δk_{NL} is the nonlinear phase matching term.

In terms of wavelength sensitivity, the dependence of FWM efficiency $\eta(\Delta k)$ on input (pump and probe) signal wavelengths is observed in Δk_L, where [65]

$$\begin{aligned} \Delta k_L &= 2\beta(f_{pu}) - \beta(f_{pr}) - \beta(f_i) \\ &= -\frac{2\pi c \lambda_0^3}{\lambda_{pu}^3 \lambda_{pr}^3}(\lambda_{pu} - \lambda_{pr})^2(\lambda_{pu} - \lambda_0)S \end{aligned} \tag{2.3}$$

β is the propagation constant, and S and λ_0 are the dispersion slope and zero dispersion wavelength, respectively. Although FWM efficiency is sensitive to the pump (clock) and probe (data) signal wavelengths, the sensitivity has been reduced by using a dispersion-flattened HNLF (i.e., low dispersion slope S) [67].

In terms of signal power sensitivity, the dependence of FWM efficiency $\eta(\Delta k)$ on input (pump and probe) signal power P is observed in Δk_{NL}, where [66]

$$\Delta k_{NL} = \gamma(2P_{pr} - P_{pu} - P_i) \tag{2.4}$$

γ is the fiber nonlinear coefficient. The sensitivity to input signal power arises from self-phase modulation (SPM) and cross-phase modulation (XPM) effects induced by the high power pump (clock) signal [68]. Considering the high sensitivity of FWM to the input signal SOP, wavelength, and power, optical gates based on FWM in a HNLF may also not be the most well-suited technique for AO-3R in AAPNs.

Cross-Phase Modulation (XPM)

XPM is another nonlinear effect that can be used in optical fibers to achieve optical gating [69–74]. Like FWM, XPM is a $\chi^{(3)}$ process that has a femtosecond response time [55]. Because of its ultra-fast response time, there has been considerable interest

in optical gating techniques based on XPM in HNLFs. This has produced a variety of techniques, including Kerr shutters [69], [70], nonlinear optical loop mirrors (NOLMs) [71], [72], and offset spectral slicing [73], [74]. Although effective, to varying degrees, the performance is often dependent on the input signal state-of-polarization (SOP). In particular, Kerr shutters require an input signal with a fixed SOP. While achievable in a controlled environment, such as a laboratory, in a practical system the input signal SOP is generally unknown and varies randomly over time. Although NOLMs also require an input signal with a fixed SOP, techniques have been proposed that eliminate the requirement [75], [76]. However, NOLMs are often highly sensitive to environment influences, such as temperature fluctuations and mechanical vibrations, that cause the SOP to vary randomly in the loop structure.

With additional complexity, the technique based on XPM (in a HNLF) and offset spectral slicing can also achieve independence from the input signal SOP [77]. In other words, the technique can be made *polarization insensitive*. In addition, because the technique does not rely on a loop structure, it does not suffer from the same pitfalls as NOLMs. The technique based on XPM and offset spectral slicing therefore provides a promising approach to optical gating.

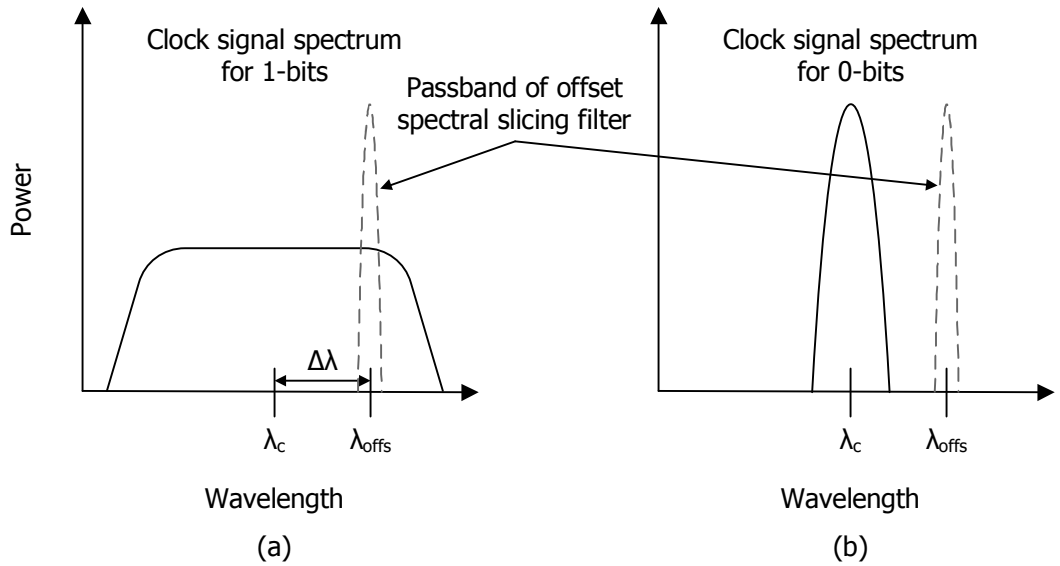

Figure 2.7: Optical gating: Clock signal spectrum for (a) 1-bits and (b) 0-bits when XPM is induced by data signal.

The principle of optical gating is described as follows. An input data signal is used to induce XPM onto a clock signal in a HNLF. Through, XPM the clock signal experiences spectral broadening, where the extent of spectral broadening is proportional to the intensity of the data signal. To aid the explanation, consider an illustration of the XPM clock signal spectrum when the data signal intensity is (a) high (1-bits) and (b) low (0-bits) (Fig 2.7). When the data signal intensity is high (1-bits), the clock signal experiences wide spectral broadening (Fig 2.7a). As a result, the clock signal spectrum broadens into the passband of a filter offset $\Delta\lambda$ from the input clock signal wavelength λ_c. The filter slices the spectrum, allowing transmission of the clock pulse through the filter (i.e., open gate). Conversely, when the data signal intensity is low (0-bits), the clock signal does not experience wide spectral broadening (Fig 2.7b). As a result, the clock signal spectrum does not broaden into the passband of the offset filter. The filter, therefore, does not slice the spectrum, preventing transmission of the

clock pulse through the filter (i.e., closed gate). Therefore, through offset spectral slicing, intensity modulation on the data signal is translated to the clock signal, which serves as the 3R regenerated data signal.

In terms of performance, XPM and offset spectral slicing has been shown to achieve low sensitivity to the input signal wavelength [74]. In [74], low wavelength sensitivity was achieved using a HNLF with a short length to reduce walk-off effects (see Sect. 3.3.1). Although XPM and offset spectral slicing can achieve low sensitivity to the input signal wavelength and SOP, the technique suffers from high sensitivity to the input signal power and pulse shape. The sensitivity arises from the XPM induced phase[2] $\phi_{XPM}(t)$

$$\phi_{XPM}(t) = 2\gamma L_{eff}|E_{pu}(t)|^2 \tag{2.5}$$

where L_{eff} is the fiber effective length (see Sect. 3.3.1). $E_{pu}(t)$ is the optical field of the pump signal. In this case, the pump is the input data signal (i.e., $E_d(t) = E_{pu}(t)$). Since the data signal power $P_d(t) = |E_d(t)|^2$, Eq. 2.5 can be expressed as

$$\phi_{XPM}(t) = 2\gamma L_{eff} P_d(t) \tag{2.6}$$

The extent of XPM induced spectral broadening is governed by the instantaneous change in carrier frequency of the clock signal Δf_c, where

$$\begin{aligned} \Delta f_c &= -\frac{1}{2\pi}\frac{\delta\phi_{XPM}(t)}{\delta t} \\ &= -\frac{1}{2\pi}\frac{\delta}{\delta t}\left[2\gamma L_{eff} P_d(t)\right] \\ &= -\frac{\gamma L_{eff}}{\pi}\frac{\delta P_d(t)}{\delta t} \end{aligned} \tag{2.7}$$

[2]In Eq. 2.5, the clock and data signals are assumed to be copolarized

Therefore, since $\Delta f_c \propto \delta P_d(t)/\delta t$, the extent of clock signal spectral broadening is dependent on the input data signal power and pulse shape (i.e., $P_d(t)$).

In AAPNs, packet routing from multiple transmission sources may lead to variability in the input signal power and pulse shape (i.e., $P_d(t)$). It is therefore highly desirable that the optical gate not be dependent on $P_d(t)$. In the next section, a technique is proposed that retains the low sensitivity to the input signal SOP and wavelength, while also providing low sensitivity to $P_d(t)$. The technique and the approach used in its design are described next.

2.3 Design Approach

In the previous section, SP-DFBLs were identified as being the most well-suited all-optical clock recovery technique for AAPNs. For optical gating, the technique based on XPM and offset spectral slicing is also promising since it provides the lowest sensitivity to input (data) signal properties, such as the input signal SOP and wavelength. The tradeoff, however, is that the technique is highly sensitive to the input signal power and pulse shape (i.e., $P_d(t)$). Also, with the exception of OPA, like the other optical gating techniques, XPM and offset spectral slicing translate intensity modulation on the data signal to the clock signal, providing the regenerated signal. As a result, the input signal is wavelength converted to the clock signal wavelength. Therefore, to retain the input signal wavelength in the regenerated signal, a wavelength conversion stage is required. A modified scheme for AO-3R that retains the input signal wavelength in the regenerated signal is shown in Fig. 2.8.

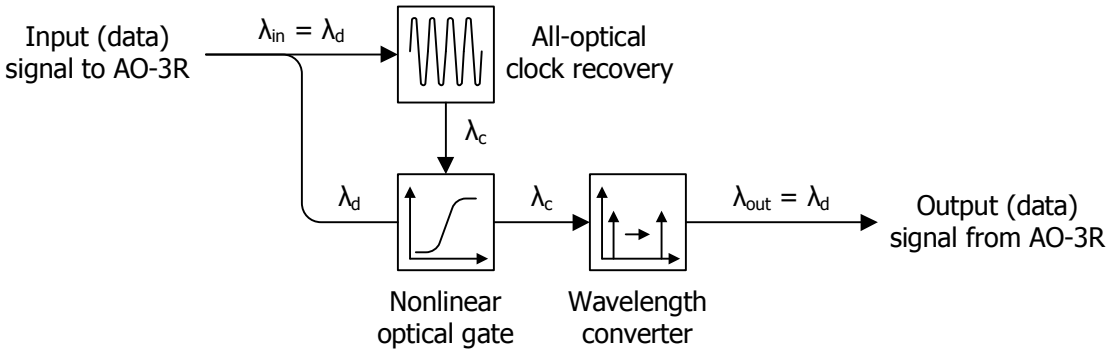

Figure 2.8: Modified scheme for all-optical 3R regeneration (AO-3R).

In the modified scheme, after optical gating a wavelength conversion stage converts the clock signal wavelength λ_c back to the input (data) signal wavelength λ_d. Before describing the proposed implementation for wavelength conversion, the optical gating technique based on XPM and offset spectral slicing is revisited. In the previous section, the technique was shown to be sensitive to $P_d(t)$. By making a simple modification, the technique can be made insensitive to $P_d(t)$. The modification is to reverse the roles of the data and clock signals — instead of using the data signal to induce XPM onto the clock signal, use the clock signal to induce XPM onto the data signal. This means that the pump signal is now the clock signal (i.e., $E_{pu} = E_c$). With this modification, substituting $E_{pu} = E_c$ into Eq. 2.5 reveals

$$\begin{aligned} \phi_{XPM}(t) &= 2\gamma L_{eff}|E_c(t)|^2 \\ &= 2\gamma L_{eff}P_c(t) \end{aligned} \tag{2.8}$$

Since the clock signal is the pump signal for XPM, the data signal experiences XPM induced spectral broadening. The extent of spectral broadening is governed by the instantaneous change in carrier frequency of the data signal Δf_d. Therefore, replacing

Δf_c with Δf_d in Eq. 2.7 and substituting Eq. 2.8 for $\phi_{XPM}(t)$ provides

$$\Delta f_d = -\frac{\gamma L_{eff}}{\pi}\frac{\delta P_c(t)}{\delta t} \tag{2.9}$$

Therefore, since $\Delta f_d \propto \delta P_c(t)/\delta t$, the extent of the data signal spectral broadening is independent of the input (data) signal power and pulse shape (i.e., $P_d(t)$).

While improving performance with respect to the input signal power and pulse shape, the modified technique also provides the opportunity to reduce the complexity required to achieve low sensitivity to the input signal SOP. In particular, additional complexity (and/or control/stability of the clock signal SOP) is often required to achieve low sensitivity to the input signal SOP (i.e., polarization independence). In the modified technique, polarization independence can be achieved without any additional complexity.

The ability to achieve polarization independence without any additional complexity was first demonstrated in application to all-optical demultiplexing [78]. In [78], a 10 GHz optical clock signal was used to demultiplex a 160 Gb/s input signal through XPM and offset spectral slicing. It was shown that the demultiplexing can be made polarization insensitive by proper selection of the slicing filter offset wavelength λ_{offs}. That is, a wavelength exists in the XPM broadened data signal spectrum that has the same spectral power regardless of the input signal SOP. In other words, the wavelength is polarization insensitive. By centering the offset spectral slicing filter at the polarization insensitive wavelength λ_{pi} (i.e., $\lambda_{offs} = \lambda_{pi}$), polarization independent all-optical demultiplexing was achieved. Although the application is different, the principle behind the demultiplexing is the same as the modified technique for optical gating — XPM induced by a clock signal onto a data signal followed by offset spectral slicing.

Therefore, in this thesis it is proposed that the technique for achieving polarization independence without any additional complexity can be extended to optical gating for all-optical 3R regeneration (AO-3R).

An additional advantage of the modified XPM technique is that difference between the input (data) signal wavelength λ_d and the offset sliced signal wavelength λ_{offs} is merely the filter offset $\Delta\lambda_{XPM}$ (i.e., $\lambda_{offs} = \lambda_d + \Delta\lambda_{XPM}$), where $\Delta\lambda_{XPM} \approx 1$ nm. Therefore, after spectral slicing, to retain the input (data) signal wavelength, the sliced signal only needs to be reconverted by $\Delta\lambda_{XPM}$. By reducing the difference in wavelength, a significant advantage is achieved. In general, optical gating involves conversion of the input (data) signal wavelength λ_d to the clock signal wavelength λ_c (Fig. 2.1). To reconvert the wavelength back to the input (data) signal wavelength, an additional (intermediate) signal is required at λ_d. Since wavelength conversion typically involves a nonlinear interaction between the clock signal and the intermediate signal [79], [65], additional complexity is required to satisfy polarization sensitivity requirements [67], [80]. In the modified XPM technique, since the input (data) signal wavelength is only converted by $\Delta\lambda_{XPM}$, the wavelength can be reconverted using a similar technique — SPM and offset spectral slicing, where the SPM slicing filter offset $\Delta\lambda_{SPM} = -\Delta\lambda_{XPM}$. Therefore, no additional intermediate signal is required for wavelength conversion, and since SPM is inherently polarization insensitive, no additional complexity is required to achieve polarization independent wavelength conversion.

One tradeoff, however, with the modified XPM technique is that optical gating, in the conventional sense, is no longer achieved since pulses are transmitted through the gate regardless of their intensity (i.e., 1- or 0-bits). In a sense, the gate is always open. To illustrate, consider the diagram of the XPM data signal spectrum when the

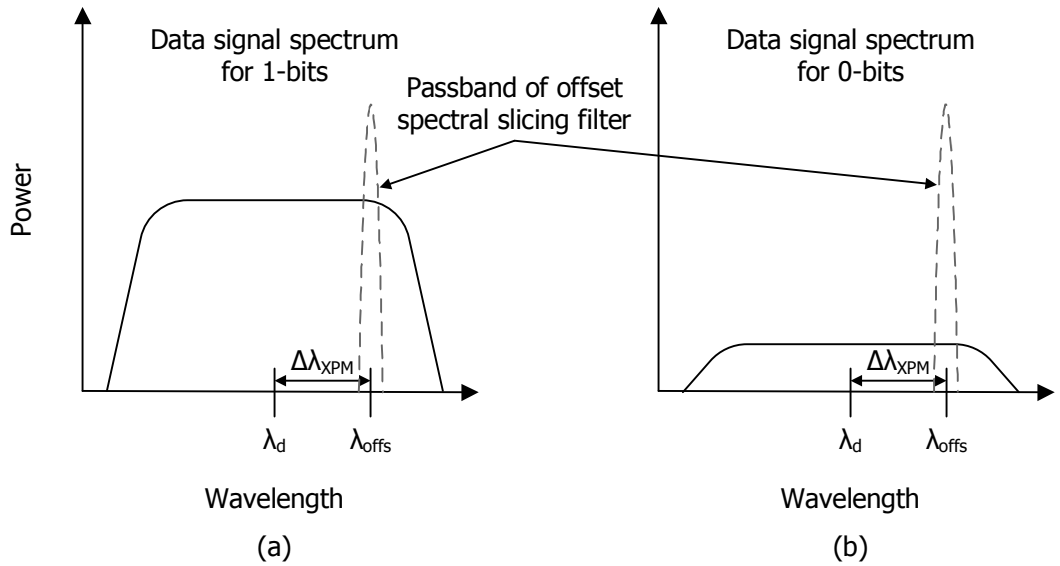

Figure 2.9: Modified optical gating: Data signal spectrum for (a) 1-bits and (b) 0-bits when XPM is induced by clock signal.

data signal intensity is (a) high (1-bits) and (b) low (0-bits) (Fig 2.9). Since the clock signal induces the XPM, the data signal experiences the same spectral broadening for 1- and 0-bits. Therefore, the data signal spectrum for 1- and 0- bits both broaden into the passband of a filter offset $\Delta\lambda_{XPM}$ from the input data signal wavelength λ_d. Since the filter slices the spectrum of 1- and 0-bits, data pulses pass through the filter regardless of their intensity.

Since there is no discrimination between 1- and 0-bits, one might ask the question: What is achieved by optical "gating"? The answer is *retiming*. That is, provided the (recovered) clock signal has lower timing jitter than the input (data) signal, the modified XPM technique provides retiming of the data signal. To explain, it is convenient to consider to effect of XPM and offset spectral slicing in the time domain.

As a comparison, consider the case where the data signal induces phase modulation onto itself (i.e., SPM). In Fig. 2.10, the data signal is shown (a) before and (b) after

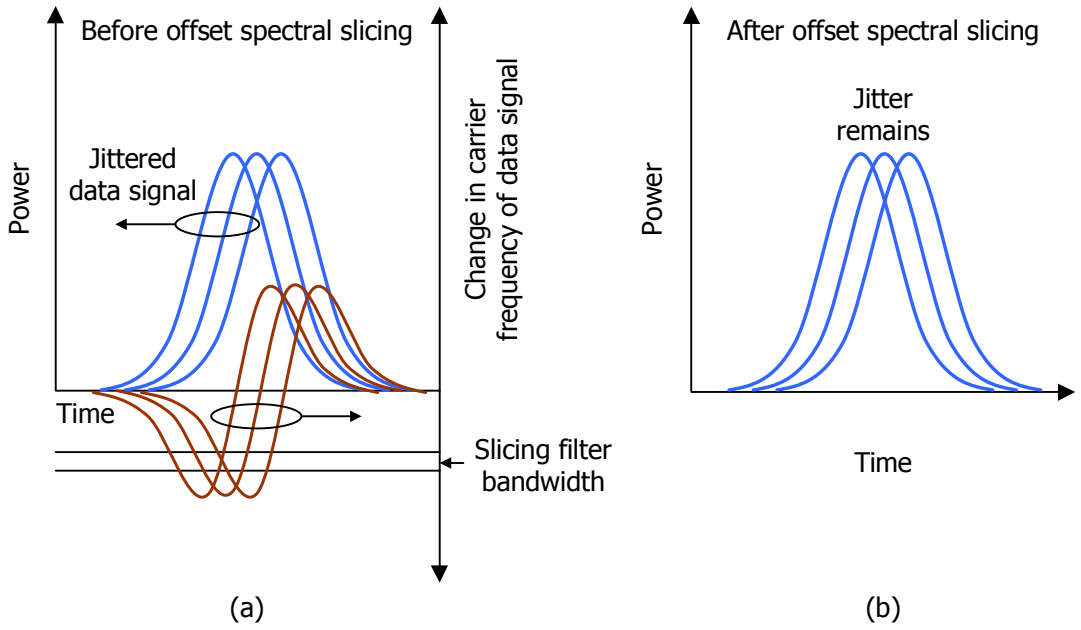

Figure 2.10: Data signal induced frequency chirp (a) before and (b) after slicing.

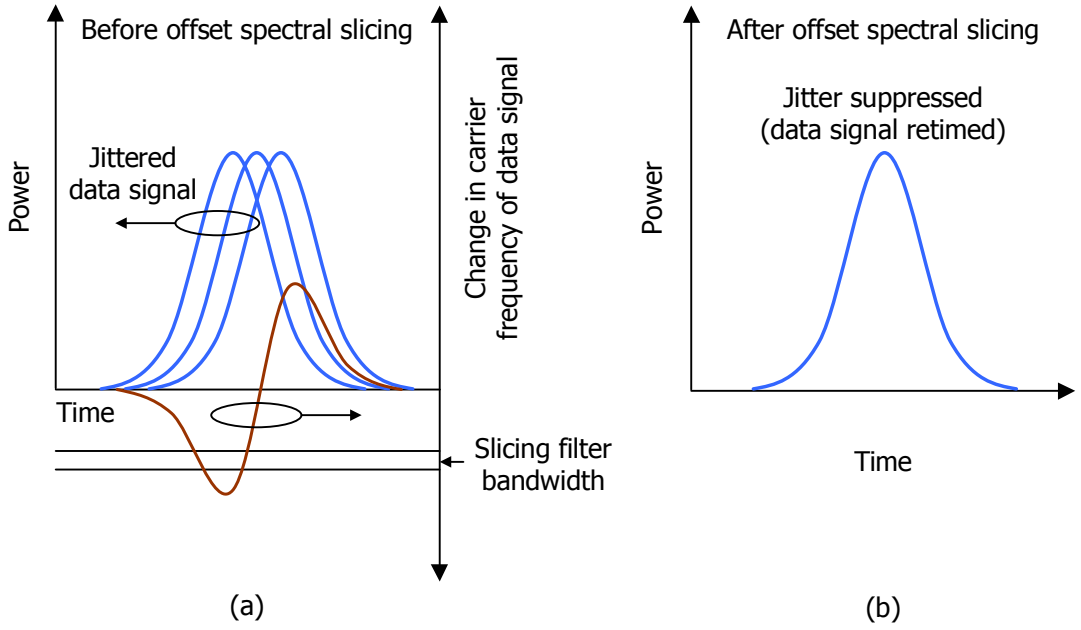

Figure 2.11: Clock signal induced frequency chirp (a) before and (b) after slicing.

spectral slicing. When the data signal induces phase modulation onto itself, timing jitter in the data signal translates to timing jitter in the induced frequency chirp. This means that the frequency chirp becomes shifted in time relative to the position of the data pulse. This causes the carrier frequency of the data pulses to enter the passband of the offset slicing filter at different instances in time (Fig. 2.10a). As a result, after spectral slicing, timing jitter in the data signal is translated to the sliced signal (Fig. 2.10b).

In contrast, consider the case where the clock signal induces phase modulation onto the data signal (i.e., modified XPM technique). In Fig. 2.11, the data signal is shown (a) before and (b) after spectral slicing. When the clock signal induces phase modulation onto the data signal, timing jitter in the data signal does not get translated to timing jitter in the induced frequency chirp. This means that the frequency chirp does not get shifted in time relative to the position of the data pulse. This causes the carrier frequency of the data pulses to enter the passband of the offset slicing filter at the same instance in time (Fig. 2.10a). As a result, after spectral slicing, timing jitter in the data signal is suppressed in the sliced signal (Fig. 2.10b). In other words, the input signal is retimed.

Although the modified XPM technique achieves retiming, as previously described, it does not provide conventional optical gating functions, such as reshaping. In addition, because of offset spectral slicing, wavelength reconversion is required to maintain the input signal wavelength in the regenerated signal. A second stage is therefore required that provides both reshaping and wavelength reconversion functions. A technique based on SPM (in a HNLF) and offset spectral slicing satisfies both requirements.

The technique based on SPM and offset spectral slicing was first proposed by Mamyshev [81].The SPM technique is based on the same principle as the XPM technique described in the previous section — spectral broadening and offset spectral slicing. The only difference is that in the SPM technique, spectral broadening of the data signal is induced by the data signal itself (i.e., SPM). In other words, the intensity of the data signal determines the extent of spectral broadening. To illustrate, recall from the previous section that the extent of spectral broadening is governed by the induced frequency chirp Δf_d. For SPM, the induced frequency chirp $\Delta f_d \propto \delta\phi_{SPM}(t)/\delta t$, where the SPM induced phase $\phi_{SPM}(t)$ is given by

$$\phi_{SPM}(t) = \gamma L_{eff} P_d \tag{2.10}$$

Since $\phi_{SPM}(t) \propto P_d$, the SPM frequency induced chirp $\Delta f_d \propto \delta P_d(t)/\delta t$, where $P_d(t)$ is the power (intensity) of the data signal.

With offset spectral slicing, the SPM technique achieves the reshaping function. More specifically, offset spectral slicing reduces amplitude variations (noise) in the input data signal. To aid in the explanation, consider the diagrams of 1-bits with amplitude noise (a) before and (b) after spectral slicing in the time (Fig. 2.12) and frequency domains (Fig. 2.13). Before spectral slicing, in the time domain 1-bits show amplitude variations (noise) (Fig. 2.12a). In the frequency domain, amplitude variations translate to variations in the extent of spectral broadening (Fig. 2.13a). Since the amplitude variations are broadened over a wide frequency range, spectral variations are reduced over the narrow sliced frequency range (i.e., filter bandwidth). After spectral slicing, the sliced signal spectrum therefore shows reduced variations in spectral power (Fig. 2.13b). As a result, in the time domain 1-bits show reduced

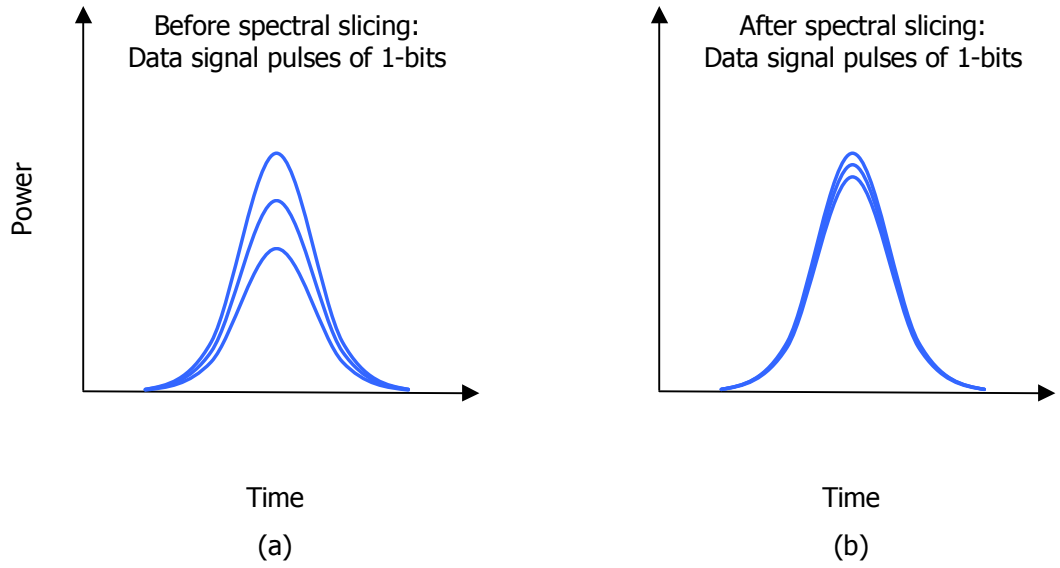

Figure 2.12: 1-bits: Data signal pulses (a) before and (b) after spectral slicing.

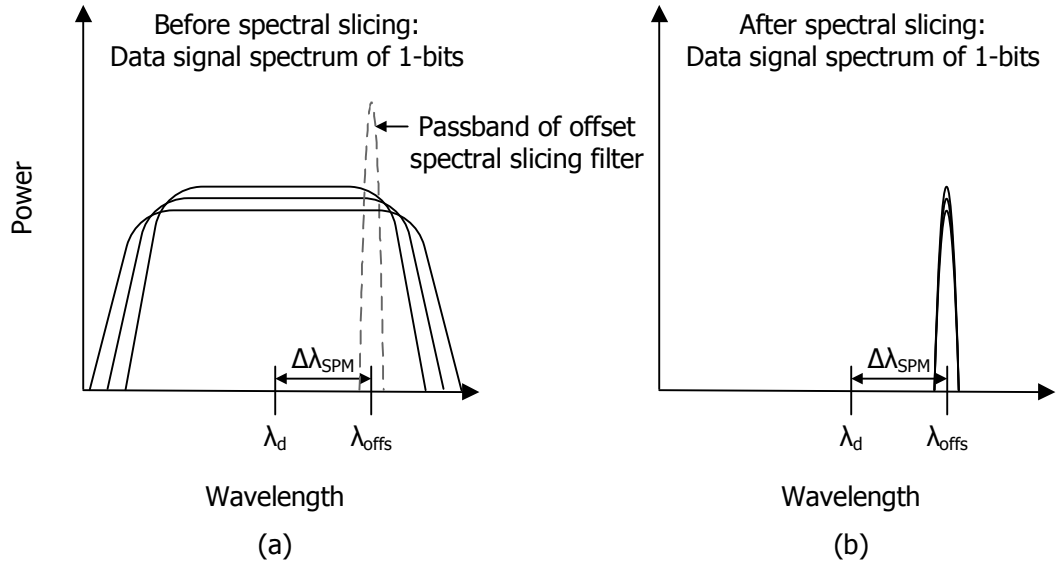

Figure 2.13: 1-bits: Data signal spectrum (a) before and (b) after spectral slicing.

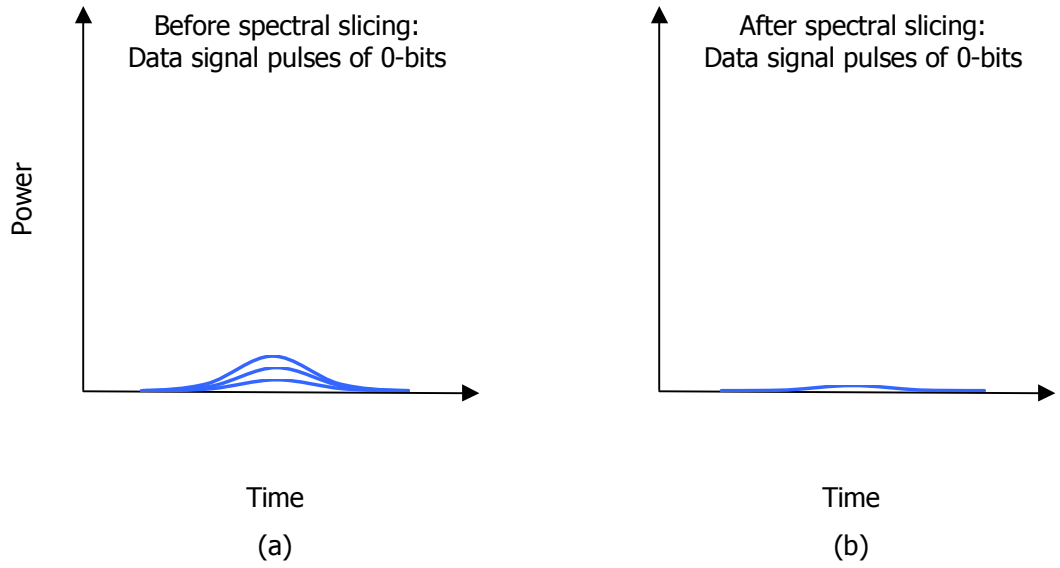

Figure 2.14: 0-bits: Data signal pulses (a) before and (b) after spectral slicing.

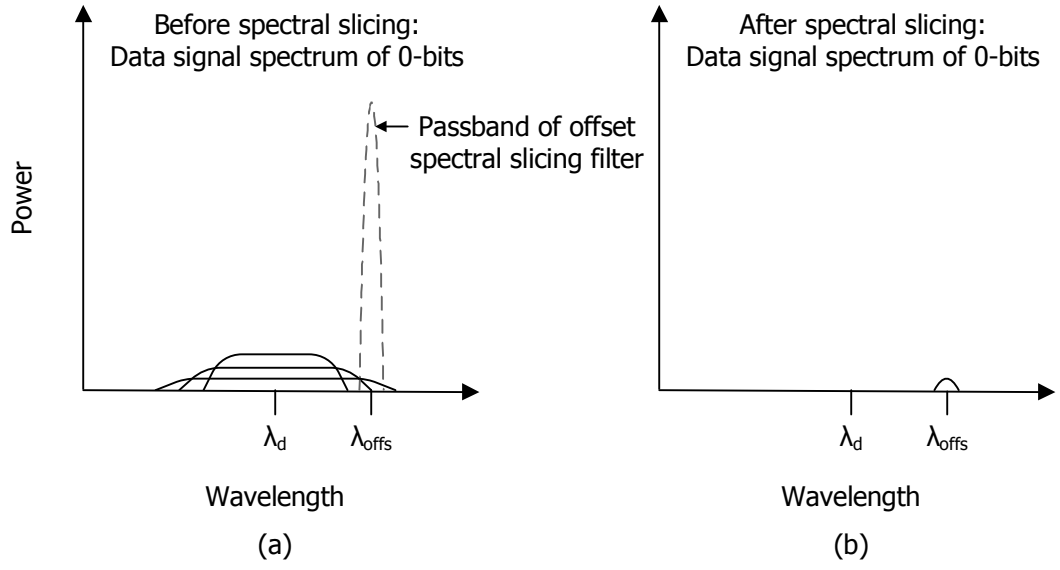

Figure 2.15: 0-bits: Data signal spectrum (a) before and (b) after spectral slicing.

amplitude variations (noise) (Fig. 2.12b).

A similar result is achieved for 0-bits with amplitude noise (Figs. 2.14 and 2.15). In addition to suppressing amplitude variations (noise), signal power in the 0-bits is also reduced since some 0-bits have insufficient power to broaden the signal spectrum into the passband of the offset spectral slicing filter (Figs. 2.15a and 2.15b). As a result, after spectral slicing, amplitude variations (noise) and signal power are reduced in the 0-bits (Figs. 2.14a and 2.14b).

Wavelength reconversion is also achieved by offset spectral slicing. To illustrate, consider the data signal spectrum for the XPM (Fig. 2.16) and SPM techniques (Fig. 2.17). Using the XPM technique for retiming, offset spectral slicing converts the input (data) signal wavelength $\lambda_{in} = \lambda_d$ to an intermediate signal wavelength $\lambda_d^{'} = \lambda_d + \Delta\lambda_{XPM}$, where $\Delta\lambda_{XPM}$ is the XPM slicing filter offset (Fig. 2.16). The intermediate signal serves as the input signal for the SPM technique. Using the SPM technique for reshaping, offset spectral slicing converts the intermediate signal wavelength $\lambda_d^{'}$ to the output signal wavelength λ_{out}. When the SPM slicing filter offset $\Delta\lambda_{SPM} = -\Delta\lambda_{XPM}$

$$\begin{aligned} \lambda_{out} &= \lambda_d^{'} + \Delta\lambda_{SPM} \\ &= \lambda_d^{'} - \Delta\lambda_{XPM} \\ &= \lambda_d^{'} - (\lambda_d^{'} - \lambda_d) \\ &= \lambda_d \\ &= \lambda_{in} \end{aligned} \tag{2.11}$$

Therefore, provided $\Delta\lambda_{SPM} = -\Delta\lambda_{XPM}$, the input signal wavelength $\lambda_{in} = \lambda_d$ is retained in the (regenerated) output signal $\lambda_{out} = \lambda_d$.

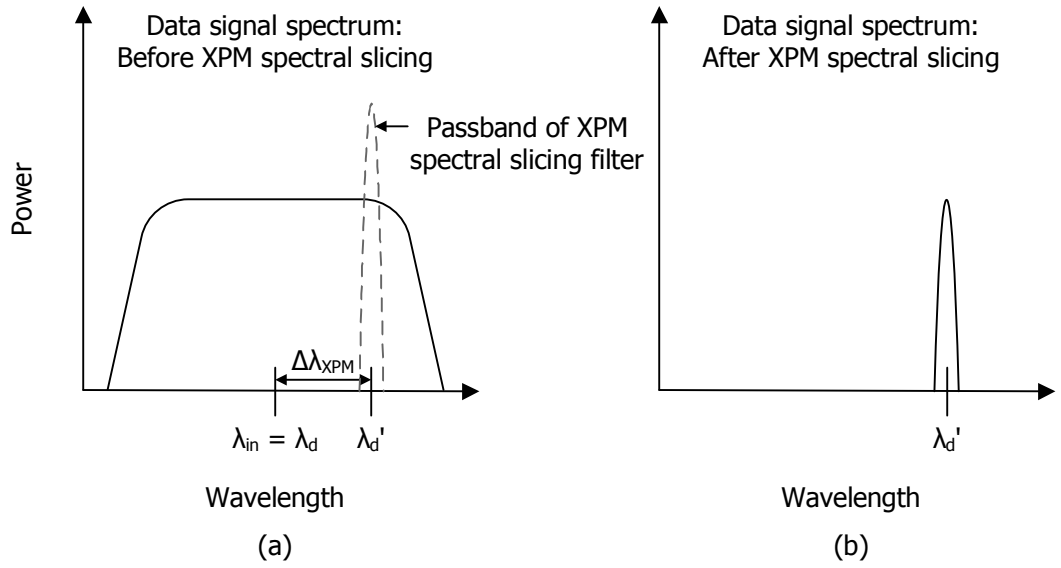

Figure 2.16: XPM: Data signal spectrum (a) before and (b) after spectral slicing.

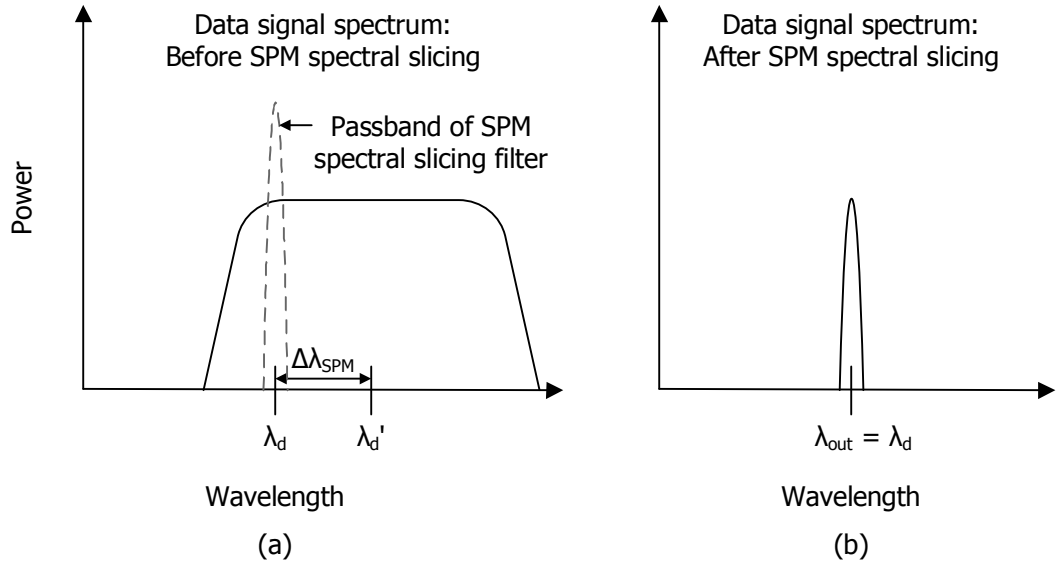

Figure 2.17: SPM: Data signal spectrum (a) before and (b) after spectral slicing.

The SPM technique therefore satisfies the requirements of reshaping and wavelength reconversion. Furthermore, because SPM is polarization and wavelength independent, the technique is also insensitive to the input signal's SOP and wavelength. However, because SPM spectral broadening is governed by the intensity (power) of the data signal, the SPM technique is sensitive to the input (data) signal power and pulse shape (i.e., $P_d(t)$). The sensitivity to $P_d(t)$ is reduced by performing the retiming (XPM) before the reshaping (SPM). Since the XPM technique slices a narrow region of the input (data) signal spectrum, variations in input (data) signal power are reduced in the sliced signal. In addition, the shape of the slicing filter passband reshapes the sliced signal pulses. Therefore, after XPM spectral slicing, variations in input (data) signal pulse shape are eliminated in the sliced signal. In other words, the XPM technique provides the SPM technique with the same pulse shape. This is particularly important since it has been shown that the SPM technique can be significantly affected by the input pulse shape [82].

The SPM technique is also well-suited for reshaping since the sliced (output) signal pulse shape and pulse width are determined by the shape and bandwidth of the SPM slicing filter (see Sect. 4.3.1). Therefore, with proper design of the SPM slicing filter, the input signal pulse shape and pulse width can be retained in the regenerated output signal (see Sect. 4.3.3).

In summary, the proposed technique achieves all-optical 3R regeneration (AO-3R) in two stages: retiming (XPM) and reshaping (SPM) (Fig. 2.18). In the first stage, an optical clock signal is recovered using a self-pulsating distributed feedback laser (SP-DFBL). The clock signal λ_c retimes the input (data) signal $\lambda_{in} = \lambda_d$ through XPM in a HNLF and offset spectral slicing. This produces an intermediate (retimed) signal

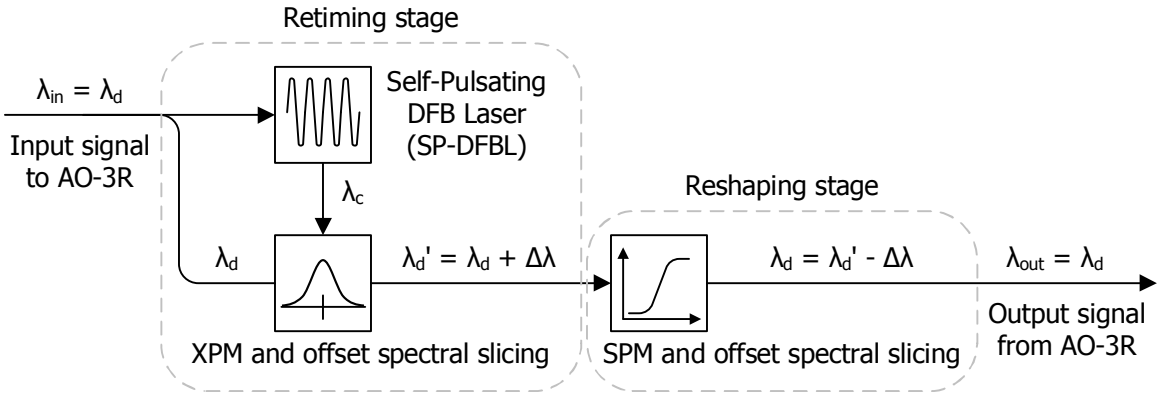

Figure 2.18: Proposed technique for all-optical 3R regeneration (AO-3R).

$\lambda_d^{'}$, which serves as the input signal to the second stage. In the second stage, the intermediate signal $\lambda_d^{'}$ is reshaped, reamplified, and wavelength reconverted to λ_d using SPM in a HNLF and offset spectral slicing. This produces the 3R regenerated output signal $\lambda_{out} = \lambda_d$.

As an example, signals at different stages of AO-3R are shown in Figs. 2.19 and 2.20. An input signal with considerable timing jitter and amplitude noise is shown in Fig. 2.19a. After the retiming stage, the timing jitter is reduced, but the amplitude noise remains (Fig. 2.19b). To reduce the amplitude noise, the retimed signal serves as the input signal to the reshaping stage (Fig. 2.20a). After the reshaping stage, the amplitude noise is also reduced. Therefore, after both stages the timing jitter and amplitude noise on the input signal are both reduced (Fig. 2.20b).

In this section, the design of a proposed all-optical 3R regenerator (AO-3R) was presented. To assess the performance, practical implementation of the design is required. In the next section, implementation of the design is described.

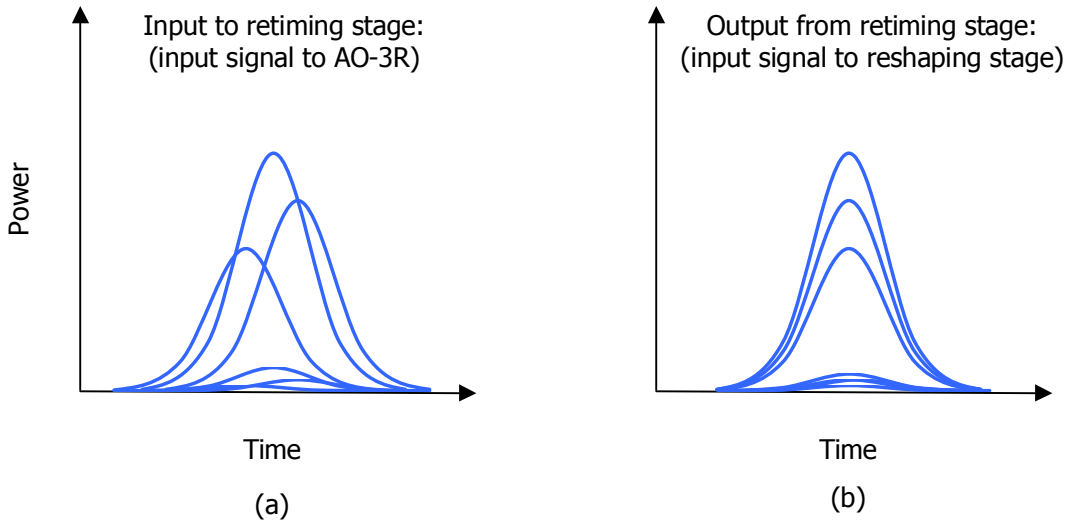

Figure 2.19: Retiming stage: (a) input and (b) output signals.

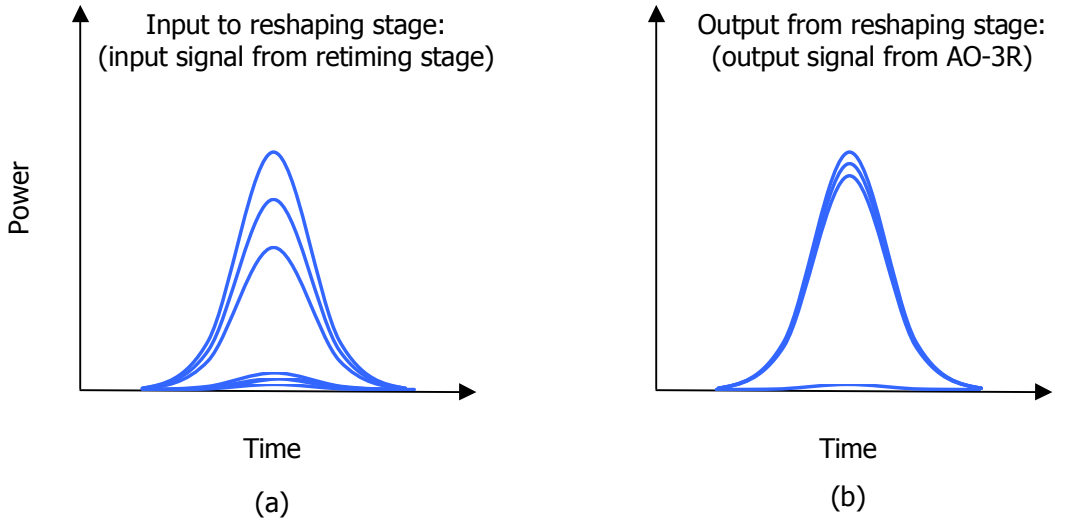

Figure 2.20: Reshaping stage: (a) input and (b) output signals.

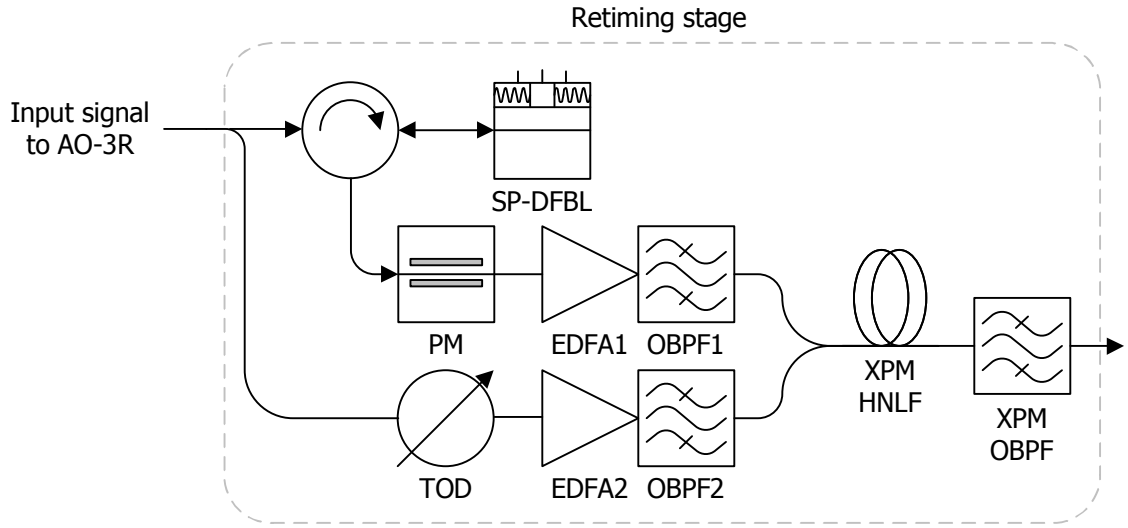

Figure 2.21: Implementation of the retiming stage.

2.4 Implementation

2.4.1 Retiming Stage

Implementation of the retiming stage is shown in Fig. 2.21. The input data signal is split into two paths. In the top path, the data signal is coupled into a self-pulsating distributed feedback laser (SP-DFBL). The SP-DFBL recovers an optical clock signal, which is coupled through a circulator to a phase modulator (PM). The PM increases the stimulated Brillouin scattering (SBS) threshold of the clock signal [83]. The clock signal is amplified in an erbium-doped fiber amplifier (EDFA1) and filtered using an optical bandpass filter (OBPF1). The filter suppresses out-of-band ASE noise. After filtering, the clock signal is coupled into a highly nonlinear fiber (XPM HNLF).

In the bottom path, a tunable optical delay (TOD) aligns the data and clock signal pulses in the HNLF. Before the data signal is coupled into the HNLF, it is amplified in

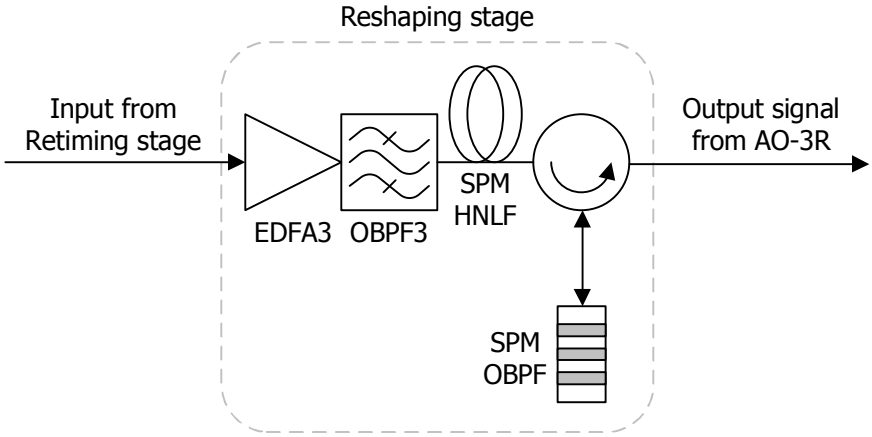

Figure 2.22: Implementation of the reshaping stage.

EDFA2 and filtered using OBPF2. Like OBPF1, OBPF2 suppresses out-of-band ASE noise. Once coupled into the HNLF, the clock (pump) signal induces XPM onto the data (probe) signal. At the output of the HNLF, the broadened data signal spectrum is sliced using an OBPF (XPM OBPF). The sliced (retimed) data signal serves as the input signal to the reshaping stage.

2.4.2 Reshaping Stage

Implementation of the reshaping stage is shown in Fig. 2.22. At the input, the retimed data signal is amplified in EDFA3. The amplified signal is filtered using OBPF3 to suppress out-of-band ASE noise. After filtering, the amplified signal is coupled into a HNLF (SPM HNLF). Once coupled into the HNLF, the amplified signal experiences SPM. At the output of the HNLF, the broadened data signal spectrum is sliced using a custom-designed optical filter (SPM OBPF). The sliced (reshaped) signal is coupled through a circulator and output from the regenerator, providing the 3R signal.

2.4.3 Regenerator

As described in Sect. 2.3, AO-3R is achieved by retiming in the first stage, then reshaping (and reamplifying) in the second stage. A diagram of the two stages together, providing the complete implementation of AO-3R, is shown in Fig. 2.23.

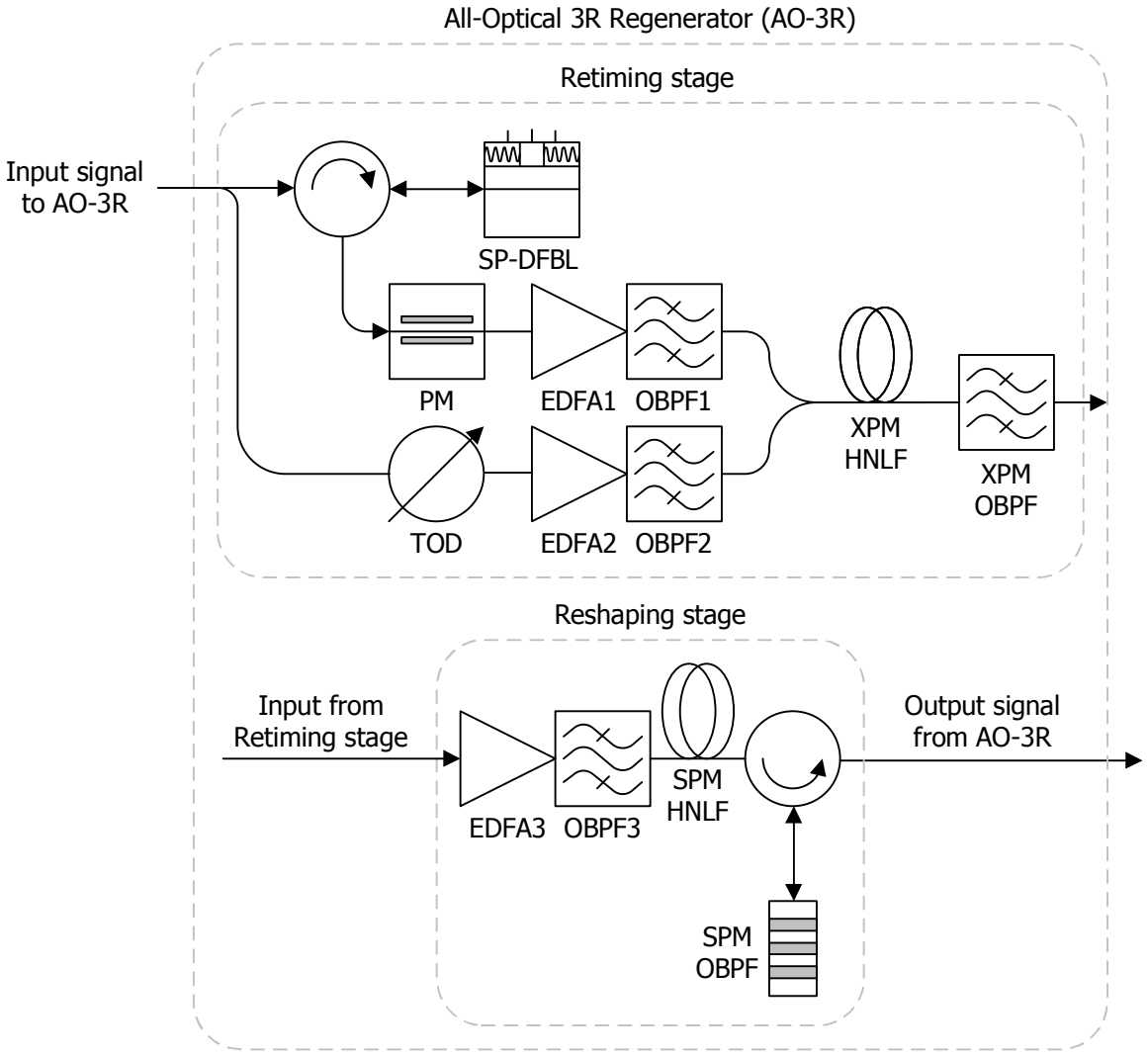

Figure 2.23: Implementation of the all-optical 3R regenerator (AO-3R).

2.5 Conclusions

In this chapter, techniques for all-optical 3R regeneration (AO-3R) were reviewed with a focus on suitability for agile all-photonic networks (AAPNs). Two main components of AO-3R were identified: all-optical clock recovery and nonlinear optical gating. For all-optical clock recovery, self-pulsating distributed feedback lasers (SP-DFBLs) were found to be well-suited for AAPNs. For nonlinear optical gating, a technique based on XPM in a HNLF with offset spectral slicing was found to be the most well-suited for AAPNs. However, because of its sensitivity to input signal properties, the XPM technique requires modification.

A modified technique based on XPM/SPM in a HNLF with offset spectral slicing has been proposed that is specifically designed to meet the requirements of AO-3R in AAPNs. For example, the regenerator achieves 3R regeneration all-optically. In addition, the regenerator provides low sensitivity to input signal properties, such as the input signal SOP, wavelength, power, and pulse shape. Also, the desired input signal properties, such as input signal wavelength and pulse width, are retained in the regenerated signal. Finally, the use of fast clock recovery enables the regenerator to achieve its ultimate goal for AAPNs — regeneration of optical packets.

Chapter 3

Retiming Stage

3.1 Introduction

All-optical retiming is typically achieved through a nonlinear interaction between an optical data signal and a recovered optical clock signal. For example, nonlinear effects in optical fibers, such as cross-phase modulation (XPM) [74] and four-wave mixing (FWM) [53], provide an effective means of achieving all-optical retiming. The tradeoff, however, is the inherent sensitivity of the nonlinear effects to the state-of-polarization (SOP) of the input signal. Since the input signal SOP is generally unknown, the polarization sensitivity of the nonlinear effects presents a considerable challenge to all-optical retiming. To address this challenge, several techniques for achieving polarization independence have been suggested, including depolarization [80], polarization diversity [67], fiber twisting for circularly polarizing fiber [84], and the use of fiber birefringence [85]. While effective, the techniques often require careful control of the clock signal polarization and/or additional complexity.

In Sect. 2.3, a technique was introduced that achieves polarization insensitive all-optical demultiplexing without additional control or complexity [78]. Since the basic principle of the demultiplexing technique is the same as the proposed retiming technique — XPM in a highly nonlinear fiber (HNLF) with offset spectral slicing — it is proposed that polarization insensitive all-optical retiming can also be achieved without any additional control or complexity.

In this chapter, the design guidelines and operating conditions required to achieve polarization insensitive all-optical retiming are described. For the operating conditions, experimental results on the properties of the retiming stage are reported. The design guidelines, operating conditions, and experimental results are presented in two sections: XPM spectral broadening (Sect. 3.3) and offset spectral slicing (Sect. 3.4). First, the implementation used for all-optical clock recovery is revisited (Sect. 3.2).

3.2 All-Optical Clock Recovery

As described in Sect. 2.2.1, for all-optical 3R regeneration (AO-3R) in agile all-photonic networks (AAPNs), the most suitable technique for all-optical clock recovery is dispersive self-Q-switching (DSQS) in a self-pulsating distributed feedback laser (SP-DFBL). The principle of all-optical clock recovery in a SP-DFBL was described in Sect. 2.2.1. In this section, specifications for the SP-DFBL used for all-optical clock recovery in the retiming stage are presented.

The SP-DFBL is from the Heinrich-Hertz-Institut (HHI). The laser structure consists of three sections in an InGaAsP/InP ridge waveguide [24]: first and third sections

are each 250 μm in length; second section is 300 μm in length. The device is temperature controlled (e.g., 20°C) with DC bias currents applied to the three laser sections: first section is biased above transparency (e.g., 90 mA); second and third sections are biased near transparency (e.g., 10 mA). Under these operating conditions, the self-pulsation (SP) frequency f_{sp} is within the required locking range of the input clock frequency $f_c = 9.95328$ GHz (i.e., $f_{sp} = 9.95328$ GHz $\pm$ 125 MHz).

To recover an optical clock signal, the SP frequency must lock onto the clock frequency of the input signal. This requires an input signal with a strong spectral component at its clock frequency. Input signals modulated using a return-to-zero (RZ) format meet the requirement. As an example of locking, the RF spectrum for the SP frequency before and after an (RZ) input signal is coupled into the SP-DFBL is shown in Fig. 3.1. Before input signal coupling, the SP frequency exhibits considerable phase noise (timing jitter). However, after input signal coupling, the SP frequency suppresses its phase noise as it locks onto the clock frequency of the input signal. As a result, the SP-DFBL produces a (recovered) optical clock signal. Since the SP frequency only locks onto the clock frequency of the input signal, timing jitter in the input signal is suppressed in the recovered clock signal.

As an example of timing jitter suppression, consider the eye diagrams shown in Fig. 3.2. The eye diagrams and timing jitter (rms) are measured using a digital communication analyzer (DCA) (electrical bandwidth = 55 GHz) with a precision timebase (intrinsic jitter = 200 fs). As seen in Fig. 3.2, timing jitter in the input signal (5.4 ps) is well suppressed in the recovered clock signal (2.1 ps). The recovered clock signal has a carrier wavelength $\lambda_c = 1538.63$ nm and full-width at half-maximum (FWHM) pulse width $T_{FWHM,c} = 36$ ps.

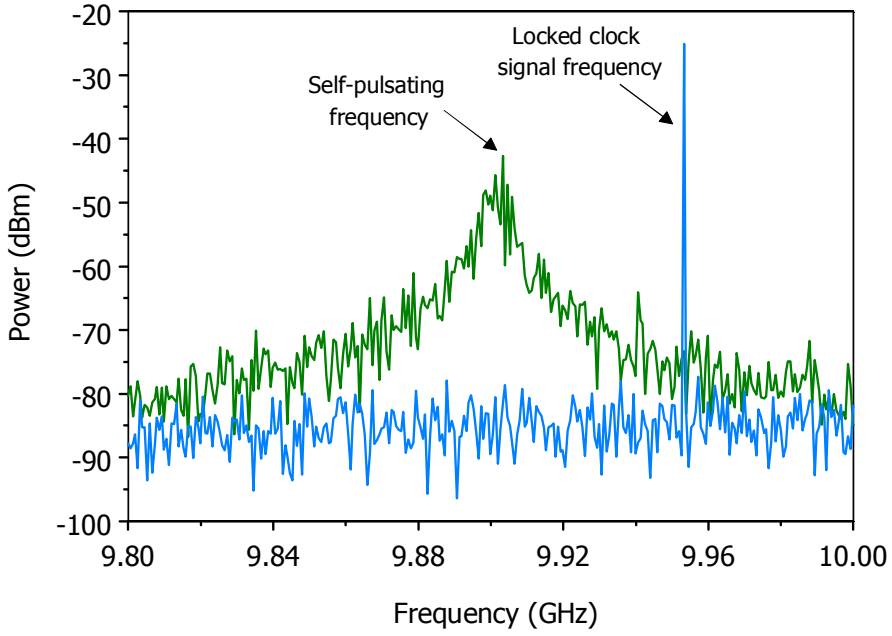

Figure 3.1: Clock recovery: RF spectrum of self-pulsating and locked clock signal.

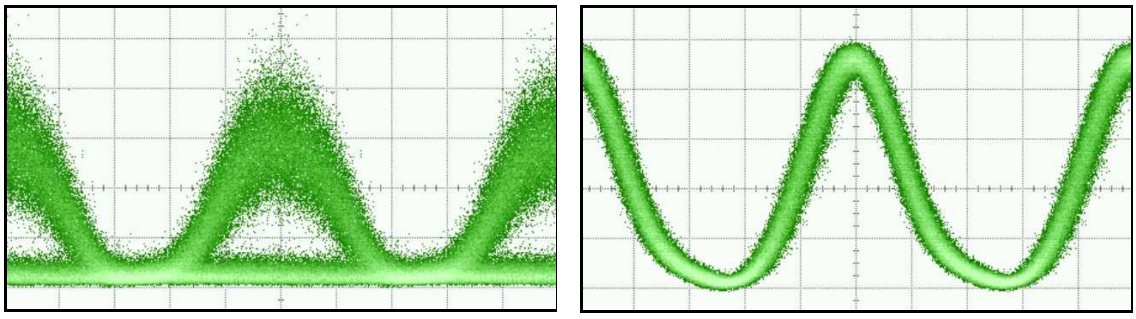

Figure 3.2: Clock recovery: Eye diagrams of (a) input signal and (b) output recovered clock signal (20 ps/div).

3.3 XPM Spectral Broadening

3.3.1 Design Guidelines

As proposed in Sect. 2.3, all-optical retiming is achieved using XPM in HNLF and offset spectral slicing. For XPM in HNLF, proper design of the clock signal and fiber operating conditions achieve optimal spectral broadening of the data signal. Optimal spectral broadening is achieved when the data signal spectrum broadens widely, allowing an offset filter to slice a region of the broadened spectrum. Wide spectral spectral broadening is achieved by increasing the maximum XPM induced phase $\phi_{XPM,max}$

$$\phi_{XPM,max} = 2b\gamma P_{0,c} L_{eff} \tag{3.1}$$

where $1/3 \leq b \leq 1$ is the polarization factor, γ is the fiber nonlinear coefficient, L_{eff} is the fiber effective length, and $P_{0,c}$ is the peak power of the clock signal. Therefore, to achieve wide spectral broadening, fiber (γ, L_{eff}) and clock signal ($P_{0,c}$) parameters should be designed to increase $\phi_{XPM,max}$.

Optimal spectral broadening is also achieved when the XPM efficiency is maximum. This occurs when the maximum XPM spectral energy coincides with the sliced spectral region. To maximize XPM efficiency, the relative time delay between the clock and data signal $\Delta\tau_{cd}$ should be designed to shift the XPM spectral energy to the sliced spectral region.

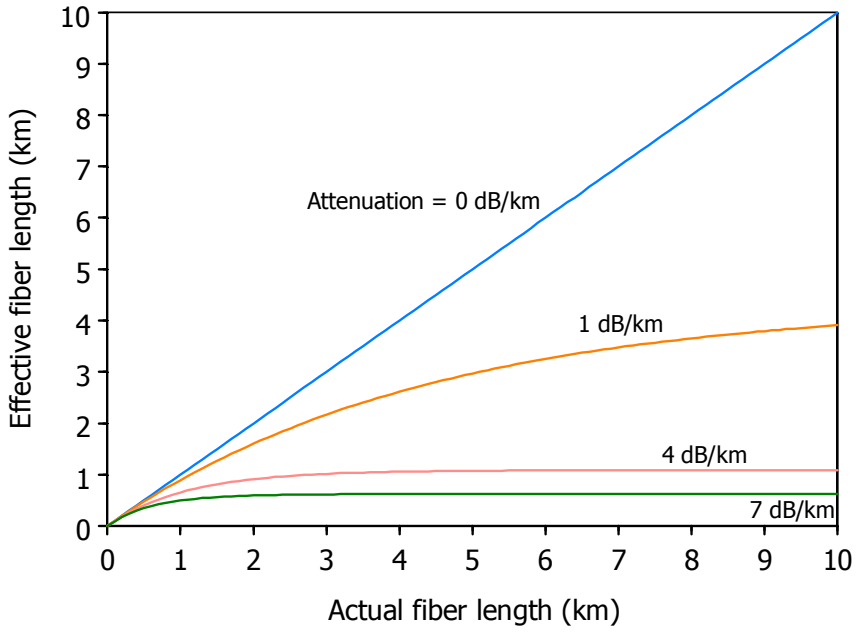

Figure 3.3: Dependence of effective fiber length on actual fiber length and attenuation.

Fiber Parameters

To increase $\phi_{XPM,max}$, a fiber should be selected that has a high nonlinear parameter γ and high effective length L_{eff} (Eq. 3.1). Special fibers, known as highly nonlinear fibers (HNLFs), have a high value for γ [86–89]. The tradeoff, however, is that HNLFs typically have a higher attenuation coefficient α than standard single-mode fibers (SMFs) [86], [87]. To achieve a high effective length L_{eff}, it is important to select a HNLF that has high nonlinearity (γ) and low attenuation (α).

To understand the implications of fiber attenuation on effective length, it is important to distinguish between fiber length and effective length. The fiber length L refers to the physical length of the fiber. Whereas the effective length L_{eff} refers to an equivalent length in which the fiber can be considered lossless (i.e., $\alpha = 0$).

The effective length is defined as [55]

$$L_{eff} = \frac{1 - \exp(-\alpha L)}{\alpha} \tag{3.2}$$

To illustrate the implications of fiber attenuation α on the effective length L_{eff}, Eq. 3.2 is used to plot L_{eff} versus L for different values of α (Fig. 3.3). For a given L, the results show that L_{eff} varies greatly with α. The maximum $L_{eff} = L$ is achieved when $\alpha = 0$ dB/km (i.e., lossless fiber). As α increases, the difference between L_{eff} and L increases exponentially. In fact, α limits the maximum achievable L_{eff}. That is, the effective length is bounded by $L_{eff} < 1/\alpha$ (Eq. 3.2). Therefore, depending on the fiber attenuation, to obtain a high effective length it is not necessarily advantageous to select the longest available fiber length. Instead, to obtain a high effective length, it is more important to select a HNLF with low attenuation and short length, than high attenuation and long length. The use of a short fiber length is particularly important for achieving wide spectral broadening since it minimizes walk-off between the clock and data signals.

Walk-off refers to the temporal separation of clock and data pulses, with different carrier frequencies, during propagation. Because of a group velocity mismatch between the signals, the temporal separation increases during propagation. In other words, the pulses "walk-off" from each other. Since XPM relies on the temporal overlap of clock and data pulses, walk-off can significantly affect XPM spectral broadening [55]. The walk-off length provides a measure of propagation distance in which pulses no longer overlap in time. Therefore, to increase $\phi_{XPM,max}$, the fiber length L should be selected such that it is much shorter than the walk-off length L_W (i.e., $L \ll L_W$), defined as

$$L_W = \frac{T_{0,d}}{|d|} \tag{3.3}$$

where $T_{0,d}$ is the data pulse half-width at 1/e of the peak power. d is the group velocity mismatch parameter defined as

$$d = \frac{v_{g,c} - v_{g,d}}{v_{g,c} v_{g,d}} \tag{3.4}$$

where $v_{g,c}$ and $v_{g,d}$ are the clock and data signal group velocities, respectively. The group velocity for each signal $v_{g,k}$ ($k = \{c, d\}$) is defined as

$$v_{g,k} = \frac{L}{\Delta\tau_{g,k}} \tag{3.5}$$

$$\approx (\Delta\lambda_k |D_k|)^{-1} \tag{3.6}$$

where $\Delta\tau_{g,k}$ is the group delay, $\Delta\lambda_k$ is the spectral width, and D_k is the fiber dispersion parameter. To reduce walk-off, the HNLF should be designed to have a large walk-off length. The walk-off length is increased by decreasing the group velocity mismatch between the clock and data signals (Eq. 3.4). This is can be achieved by selecting a HNLF with a low dispersion slope $S = \Delta D/\Delta\lambda$. When S is low, the clock and data signals experience similar dispersion (i.e., $D_c \approx D_d$). The signals therefore also experience similar group delays (i.e., $\Delta\tau_{g,c} \approx \Delta\tau_{g,d}$) or, equivalently, similar group velocities (i.e, $v_{g,c} \approx v_{g,d}$). As $v_{g,c} \to v_{g,d}$, the group velocity mismatch parameter $d \to 0$ (Eq. 3.4) and the walk-off length $L_W \to \infty$ (Eq. 3.3).

The walk-off length can also be increased by selecting a HNLF with high dispersion. Intuitively, higher dispersion increases pulse overlap since pulse broadening increases with dispersion. The tradeoff is that pulse broadening decreases the peak power of signals. In particular, pulse broadening of the clock signal decreases its peak power $P_{0,c}$. Since the maximum XPM phase $\phi_{XPM,max} \propto P_{0,c}$ (Eq. 3.1), higher dispersion is counterproductive for increasing $\phi_{XPM,max}$. Therefore, to increase $\phi_{XPM,max}$ the

HNLF should be designed to have low dispersion (i.e., $D \approx 0$) at the clock signal wavelength λ_c. In addition, the dispersion should also be normal (i.e., $D < 0$) at λ_c in order to prevent degradation of the signal from modulation instability (MI) [90].

Signal Parameters

To increase $\phi_{XPM,max}$, the clock signal should be operated at a high peak power $P_{0,c}$ (Eq. 3.1). One means of increasing the peak power is to compress the clock signal pulse width $T_{0,c}$. However, to achieve pulse compression, additional complexity is required. As an alternative, the peak power can also be increased by optical amplification. However, the power is ultimately limited by stimulated Brillouin scattering (SBS) [55]. When the average power exceeds the SBS threshold, backscattered (Stokes) power increases rapidly. Although SBS causes the forward propagating power to decrease, the main limitation of SBS is the degradation it can cause to the signal-to-noise ratio (SNR) of the clock signal [91]. In particular, SBS can degrade the SNR of the clock signal through an increase in relative intensity noise (RIN) caused by beating of the forward propagating clock signal and the Rayleigh scattered Stokes signal [92].

To increase the clock signal power without degrading the SNR, the SBS threshold should be increased. An effective means of increasing the SBS threshold is to modulate the optical phase of the clock signal [93]. By modulating the optical phase, spectral power is distributed over a wider frequency range. Therefore, although the average signal power is the same, the powers of the peak spectral components are reduced. This allows the signal power to be further increased before the SBS threshold is exceeded. Using this approach, a 19 dB increase in the SBS threshold of a continuous wave (CW) signal (6 to 25 dBm) has been demonstrated [83].

The use of phase modulation is particularly effective for enabling an increase in clock signal power because the clock signal phase does not affect the XPM. This is because XPM is induced by the intensity of the clock signal, not its phase. Therefore, the phase of the clock signal, whether induced by external phase modulation or self-phase modulation (SPM), does not affect spectral broadening of the data signal.

Since the retiming is achieved by XPM, SPM of the data signal should be minimal. To reduce SPM, the data signal power input to the HNLF should not be too high. However, since spectral slicing reduces the signal power, to reduce the impact of added amplified spontaneous emission (ASE) noise from reamplification, the power input to the HNLF should not be too low. Therefore, a balance between high (SPM) and low (ASE) input power to the HNLF should be achieved. It is recommended that the input power be increased as high as possible before the onset of SPM. A general guideline is that the maximum SPM phase $\phi_{SPM,max} < 0.1$ rad [48], where

$$\phi_{SPM,max} = \gamma P_{0,d} L_{eff} \tag{3.7}$$

and $P_{0,d}$ is the peak power of the data signal. For $\phi_{SPM,max} < 0.1$ rad,

$$P_{0,d} < \frac{0.1}{\gamma L_{eff}} \tag{3.8}$$

While the data signal power to coupled into the HNLF is important in terms of SPM, the data signal power coupled into the SP-DFBL is important for the recovered clock signal jitter. Specifically, the data signal power coupled into the SP-DFBL should be selected to provide the minimum clock signal jitter (Sect. 5.3.2). Although the clock signal jitter is insensitive to the data signal wavelength λ_d [15], λ_d should be selected sufficiently far from λ_c to prevent cross-talk between the broadened spectra, but sufficiently close to λ_c to prevent walk-off between the clock and data signals.

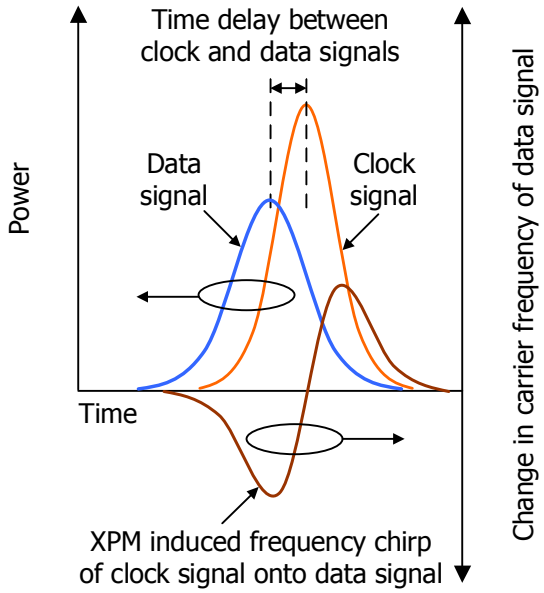

Figure 3.4: Effect of time delay on XPM induced frequency chirp.

Time Delay

The optimal time delay between the clock and data signals maximizes the XPM efficiency. Consider the illustration of time delay and XPM induced frequency chirp shown in Fig. 3.4. The time delay refers to the relative delay between the peak of the clock and data pulses. Depending on the time delay, XPM induced frequency chirp on the data signal is shifted relative to its pulse position. In other words, the delay controls the temporal position of the chirp. When the delay is such that the peak chirp (change in frequency) coincides with the peak of the data pulse, the maximum spectral power occurs at the maximum chirp. In terms of maximum XPM efficiency, this is the optimal delay since spectrally slicing the XPM data signal spectrum near the maximum chirp maximizes the sliced signal power (i.e., conversion of phase modulation to intensity modulation).

To determine the optimal time delay, consider the XPM induced frequency chirp on the data signal Δf_d for Gaussian shaped pulses

$$\begin{aligned}
\Delta f_d &= -\frac{1}{2\pi}\frac{\delta\phi_{XPM}}{\delta t} \\
&= -\frac{1}{2\pi}\frac{\delta}{\delta t}\left[2b\gamma P_c(t)L_{eff}\right] \\
&= -\frac{b\gamma L_{eff}}{\pi}\frac{\delta}{\delta t}\left[P_c(t)\right] \\
&= -\frac{b\gamma L_{eff}}{\pi}\frac{\delta}{\delta t}\left[P_{0,c}\exp\left\{-\left(\frac{t}{T_{0,c}}\right)^2\right\}\right] \\
&= \frac{2b\gamma P_{0,c}L_{eff}}{\pi {T_{0,c}}^2}t\exp\left\{-\left(\frac{t}{T_{0,c}}\right)^2\right\} \qquad (3.9)
\end{aligned}$$

The optimal time delay $\Delta\tau_{cd,opt}$ is found by solving $\delta\Delta f_d/\delta t = 0$ for $t = \Delta\tau_{cd,opt}$. From Eq. 3.9, $\delta\Delta f_d/\delta t = 0$ is

$$\begin{aligned}
0 &= \frac{\delta}{t}\left[\frac{2b\gamma P_{0,c}L_{eff}}{\pi {T_{0,c}}^2}t\exp\left\{-\left(\frac{t}{T_{0,c}}\right)^2\right\}\right] \\
&= 1 - 2\left(\frac{t}{T_{0,c}}\right)^2 \qquad (3.10)
\end{aligned}$$

Solving for $t = \Delta\tau_{cd,opt}$, the optimal time delay is therefore

$$\Delta\tau_{cd,opt} = \pm\frac{T_{0,c}}{\sqrt{2}} \qquad (3.11)$$

where $\pm$ indicates peak chirp for the minimum and maximum change in frequency.

Based on the design guidelines, operating conditions required to achieve optimal spectral broadening are obtained. In particular, operating conditions for the fiber, clock and data signals, and relative time delay between signals are defined.

3.3.2 Operating Conditions

For completeness, operating conditions for the SP-DFBL are also provided. The applied currents are: lasing section I_{las} = 88.23 mA, phase section I_{pha} = 11.16 mA, reflector section I_{ref} = 9.86 mA. The temperature controller is set to T = 19.96°C. Under these operating conditions, the self-pulsation (SP) frequency f_{sp} = 9.9033 GHz. For an input data signal frequency f_d = 9.95328 GHz, the SP frequency is within the locking range of $f_{sp} = f_d \pm 125$ MHz (i.e., $|f_{sp} - f_d| = 49.98$ MHz < 125 MHz) [15].

Fiber Parameters

A HNLF is selected that has both high nonlinearity γ = 10.5 $W^{-1}km^{-1}$ and low loss α = 0.76 dB/km. At the zero dispersion wavelength λ_0 = 1566 nm the selected fiber has low dispersion slope S_0 = 0.016 ps/nm^2-km. The fiber length L = 4 km is chosen as a compromise between a long length for increasing $\phi_{XPM,max}$ (i.e., $\phi_{XPM,max} \propto L_{eff}(L)$) and a short length for reducing walk-off effects (i.e., $L \ll L_W$). For L = 4 km, the effective length L_{eff} = 2.88 km.

Signal Parameters

The SP-DFBL recovers an optical clock signal with a carrier wavelength λ_c = 1538.63 nm and pulse width $T_{FWHM,c}$ = 36 ps. At λ_c, the fiber dispersion D = -0.44 ps/nm-km. After clock recovery, a $LiNbO_3$ phase modulator is used to increase the SBS threshold of the clock signal. The modulator is driven with a 1 GHz RF sinusoidal signal (V_π = 9 V) [83]. After phase modulation, the clock signal is amplified to a peak power $P_{0,c}$ = 150 mW and coupled into the HNLF.

The data signal is also amplified and coupled into the HNLF. The peak power $P_{0,d}$ is determined using Eq. 3.8. For the fiber operating conditions, SPM spectral broadening is minimal for $P_{0,d} < 0.1/\gamma L_{eff} = 3.3$ mW. For clock recovery, the data signal power coupled into the SP-DFBL is set to obtain minimum clock signal jitter. An average input power of -1.5 dBm provides the minimum clock signal jitter of 1.8 ps (rms). The jitter is obtained for an input data pulse width $T_{FWHM,d} = 47$ ps and wavelength $\lambda_d = 1544.55$ nm. At λ_d, the fiber dispersion D = -0.34 ps/nm-km. For the fiber and signal operating conditions, both cross-talk and walk-off effects are negligible.

Time Delay

The optimal time delay between the clock and data signals $\Delta\tau_{cd,opt}$ is determined using Eq. 3.11. To align the peak chirp (i.e., minimum change in frequency or maximum change in wavelength) of the clock signal with peak of the data signal pulse, the data signal should be delayed by $\Delta\tau_{cd,opt}$. Using a tunable optical delay (TOD), the data signal is delayed by $\Delta\tau_{cd,opt} = T_{0,c}/\sqrt{2}$ (Eq. 3.11). Since the recovered clock signal has a pulse width $T_{0,c} = 21.6$ ps ($T_{0,c} = T_{FWHM,c}/2\sqrt{\ln(2)}$), the optimal time delay $\Delta\tau_{cd,opt} = 15.3$ ps.

3.3.3 Experimental Results

To verify the optimal time delay $\Delta\tau_{cd,opt}$ experimentally, the time delay is first set to provide an XPM broadened data signal spectrum that is symmetric about its input wavelength. For this time delay, the peak of clock and data pulses are aligned in time

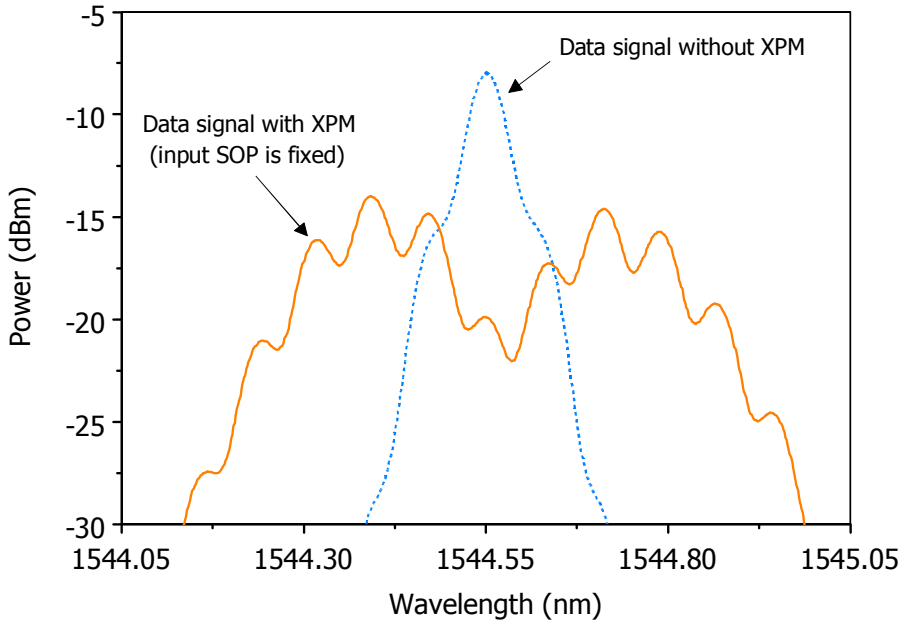

Figure 3.5: XPM broadened data signal spectrum: Time delay $\Delta\tau_{cd} = 0$ ps, input SOP is fixed (RBW = 0.06 nm).

(i.e., $\Delta\tau_{cd} = 0$ ps). For $\Delta\tau_{cd} = 0$ ps, the XPM broadened data signal spectrum at the output of the HNLF is shown in Fig. 3.5. The spectrum is not perfectly symmetric because of the slight group velocity mismatch between clock and data signals. However, the spectrum is nearly symmetric, exhibiting the characteristic spectral peaks of an XPM broadened signal spectrum with near zero dispersion [55].

In Fig. 3.5, the spectral broadening is achieved for a fixed input signal SOP. The clock signal SOP is also fixed since the SP-DFBL always provides the same SOP. The relative SOPs of the clock and data signals affect the spectral broadening because XPM is a polarization sensitive nonlinear effect, where the XPM phase ϕ_{XPM}(t) is

$$\phi_{XPM}(t) = 2b\gamma P_c(t) L_{eff} \tag{3.12}$$

b is the polarization factor, which depends on the relative SOPs of the clock and data

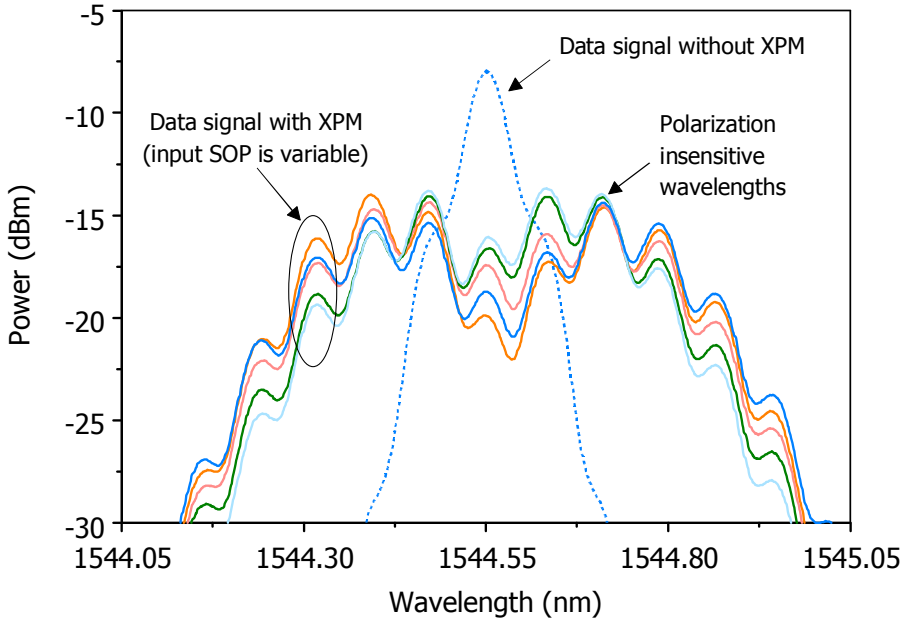

Figure 3.6: XPM broadened data signal spectrum: Time delay $\Delta\tau_{cd} = 0$ ps, input SOP is variable (RBW = 0.06 nm).

signals (i.e., $1/3 \leq b \leq 1$). When the SOPs are orthogonal (e.g., linear horizontal and linear vertical), the XPM phase is minimum (i.e., $b = 1/3$). When the SOPs are co-polarized (e.g., both linear horizontal), the XPM phase is maximum (i.e., $b = 1$). Other combinations of SOPs (e.g., linear horizontal and elliptical) have intermediate XPM phase (i.e., $1/3 < b < 1$). As a result of the polarization sensitivity, the XPM broadened spectrum for variable input SOPs are qualitatively different. Because of the spectral differences, there may be implications in terms of the quality of spectrally sliced (retimed) signals subject to variable input SOPs.

The XPM broadened data signal spectrum for variable input signal SOPs is shown in Fig. 3.6. The input signal SOP is randomly varied using a polarization controller with continuously rotating $\lambda/2$ and $\lambda/4$ waveplates at the input of the regenerator.

Sensitivity to the input signal SOP is seen in the varying amounts of spectral broadening. In particular, for different input signal SOPs the spectral peaks show large variations in amplitude (e.g., > 3 dB). However, because the relative phase of the frequency components is independent of polarization, spectral peaks occur at the same frequency (wavelength) regardless of the input signal SOP.

An interesting observation is made from Fig. 3.5 — regardless of the input signal SOP the spectral power is very similar at $\lambda = 1544.71$ nm. In other words, XPM is polarization insensitive at this wavelength. This is a remarkable property of XPM because it provides a polarization insensitive wavelength for spectral slicing [78].

Being a relatively recent discovery [78], an explanation for the polarization insensitive wavelength has yet to be provided. To provide an intuitive explanation, consider the characteristics of XPM chirp for a Gaussian shaped pulse shown in Fig. 3.7. Two observations can be made about the chirp. First, the magnitude of the chirp depends on the polarization factor b (Eq. 3.9). Second, the chirp is nonlinear. The nonlinearity of the chirp implies that the carrier has the same instantaneous frequency at two instances in time. The spectral power at the instantaneous frequency can be viewed as the interference (vector sum) of two waves having the same frequency, but different phase. When the frequencies are in-phase the vector sum is maximum, which produces amplitude peaks in the XPM spectrum (Fig. 3.5). Because the phase is independent of polarization, spectral amplitude peaks occur at the same frequency regardless of the input signal SOP (Fig. 3.6). For a specific frequency, it is speculated that an interference condition exists in which the vector sum produces the same spectral amplitude for any input signal SOP. This frequency is the *polarization insensitive frequency* (wavelength).

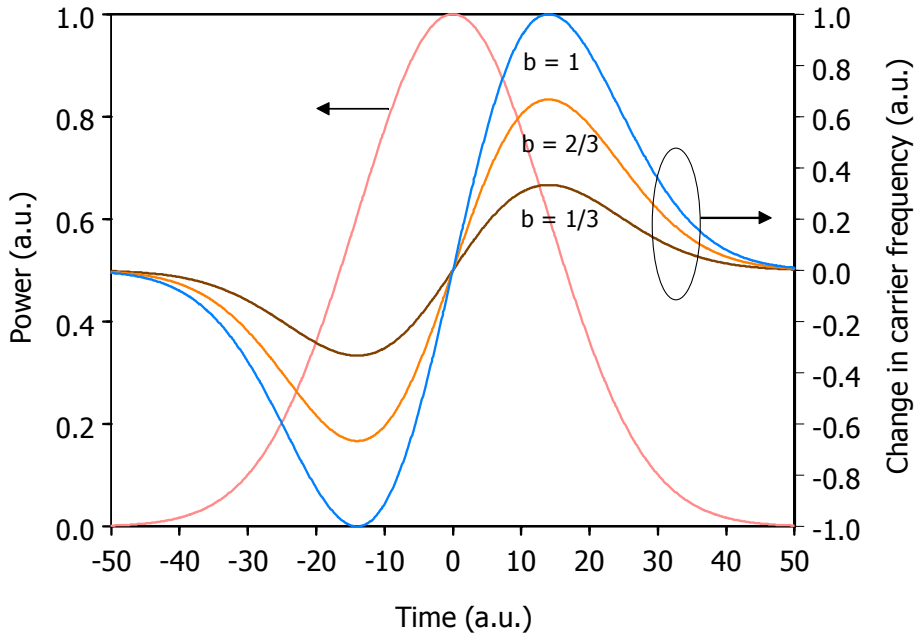

Figure 3.7: Example of XPM induced frequency chirp for a Gaussian shaped pulse.

Before proceeding with the polarization insensitive wavelength, the effect of the time delay is studied for a fixed input signal SOP. The XPM broadened data signal spectrum for variable time delay $\Delta\tau_{cd}$ is shown in Fig. 3.8. The time delay has the effect of frequency-shifting the XPM spectral energy. This occurs because the XPM chirp is time-shifted relative to the temporal position of the data pulses. When the maximum chirp coincides with the peaks of the data pulses, the XPM spectral energy is shifted towards higher frequencies (lower wavelengths) (e.g., $\Delta\tau_{cd}$ = -15 ps). Likewise, when the minimum chirp coincides with peak of the data pulses, the XPM spectral energy is shifted towards lower frequencies (higher wavelengths) (e.g., $\Delta\tau_{cd}$ = 15 ps).

With the time delay fixed at $\Delta\tau_{cd}$ = 15 ps, the XPM broadened data signal spectrum for variable input signal SOP is shown in Fig. 3.9. Two observations can be made from this figure. First, the polarization insensitive wavelength (λ = 1544.71 nm) is

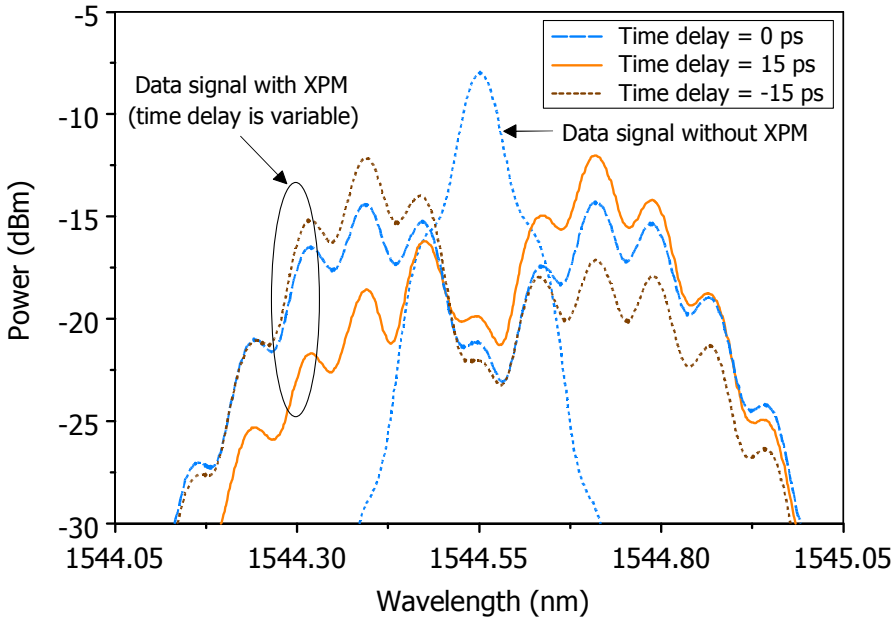

Figure 3.8: XPM broadened data signal spectrum: Time delay $\Delta\tau_{cd}$ is variable, input SOP is fixed (RBW = 0.06 nm).

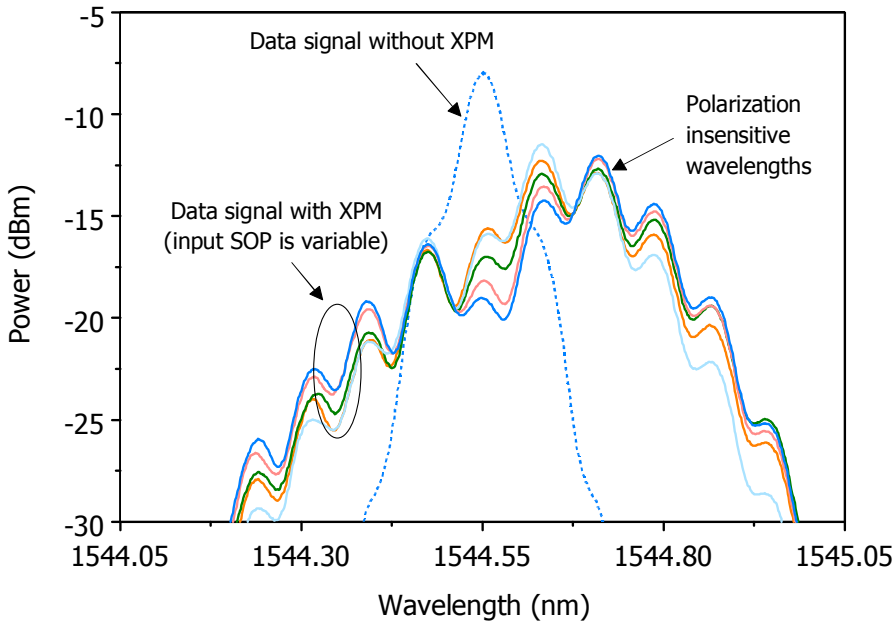

Figure 3.9: XPM broadened data signal spectrum: Time delay $\Delta\tau_{cd}$ = 15 ps, input SOP is variable (RBW = 0.06 nm).

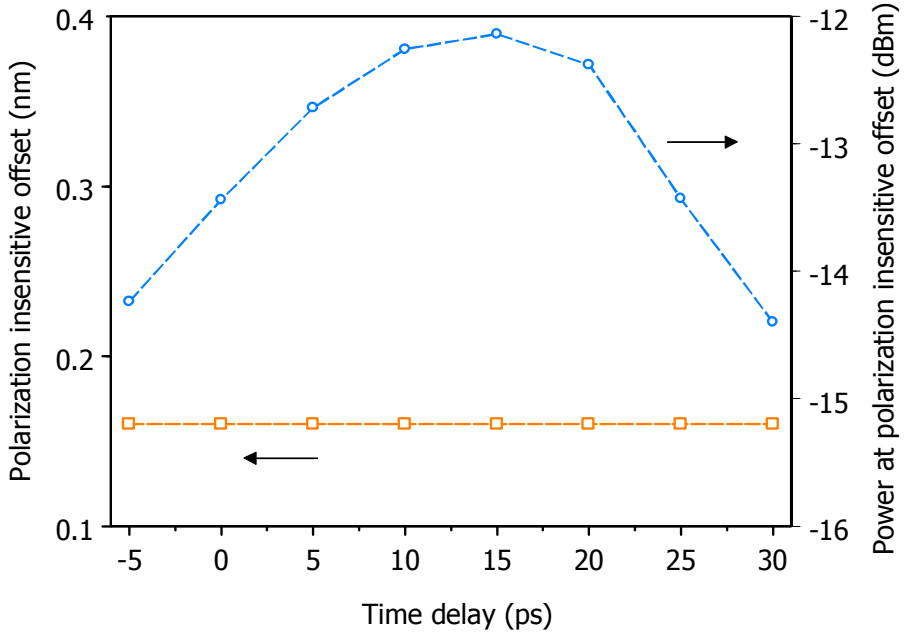

Figure 3.10: Dependence of polarization insensitive offset/power on time delay.

the same for $\Delta\tau_{cd} = 0$ ps (Fig. 3.6) and $\Delta\tau_{cd} = 15$ ps (Fig. 3.9). Second, compared to $\Delta\tau_{cd} = 0$ ps (Fig. 3.6), the power at the polarization insensitive wavelength is increased for $\Delta\tau_{cd} = 15$ ps. This means that by setting the appropriate time delay the XPM efficiency can be increased when the spectrum is sliced at the polarization insensitive wavelength.

Results for the effect of time delay $\Delta\tau_{cd}$ on the polarization insensitive offset (wavelength) and corresponding power are shown in Fig. 3.10. The results confirm that the polarization insensitive wavelength is independent of $\Delta\tau_{cd}$. Also, the maximum power (i.e., maximum XPM efficiency) occurs for $\Delta\tau_{cd} = 15$ ps. This result is in good agreement with the predicted optimal delay $\Delta\tau_{cd,opt} = T_{0,c}/\sqrt{2} = 15.3$ ps (Eq. 3.11).

3.4 Offset Spectral Slicing

3.4.1 Design Guidelines

After XPM spectral broadening, the data signal spectrum is sliced at an offset wavelength, providing the retimed signal. In the previous section, the XPM broadened data signal spectrum was shown to have a polarization insensitive wavelength. The polarization insensitive wavelength serves as a natural center wavelength for the spectral slicing filter. In this section, an equation is fit to experimental results, providing an expression for the polarization insensitive filter offset.

To derive the expression, consider the experimental results for time delay $\Delta\tau_{cd} =$ 15 ps (Figs. 3.9 and 3.10). When $\Delta\tau_{cd} = 15$ ps, the XPM spectral power is maximum at the polarization insensitive wavelength (Fig. 3.9). The power at the polarization insensitive wavelength is also maximum when the peak XPM chirp coincides with the peaks of the data pulses (Fig. 3.10). This implies that the polarization insensitive wavelength corresponds to the peak XPM chirp (wavelength).

Consider the XPM chirp for the data signal Δf_d

$$\Delta f_d = -\frac{1}{2\pi}\frac{\delta\phi_{XPM}}{\delta t} \tag{3.13}$$

Including the time delay $\Delta\tau_{cd}$, the XPM phase ϕ_{XPM}(t) is

$$\phi_{XPM}(t) = 2b\gamma P_c(t - \Delta\tau_{cd})L_{eff} \tag{3.14}$$

where the clock signal power $P_c(t - \Delta\tau_{cd})$ is

$$P_c(t - \Delta\tau_{cd}) = P_{0,c}\exp\left\{-\left(\frac{t - \Delta\tau_{cd}}{T_{0,c}}\right)^2\right\} \tag{3.15}$$

Substituting Eqs. 3.14 and 3.15 into Eq. 3.13 provides

$$\begin{aligned} \Delta f_d &= -\frac{1}{2\pi}\frac{\delta \phi_{XPM}}{\delta t} \\ &= -\frac{1}{2\pi}\frac{\delta}{\delta t}\left[2b\gamma P_c(t-\Delta\tau_{cd})L_{eff}\right] \\ &= \frac{2b\gamma P_{0,c}L_{eff}}{\pi {T_{0,c}}^2}(t-\Delta\tau_{cd})\exp\left\{-\left(\frac{t-\Delta\tau_{cd}}{T_{0,c}}\right)^2\right\} \end{aligned} \tag{3.16}$$

Solving $\delta\Delta f/\delta t = 0$ for t provides

$$t = \Delta\tau_{cd} \pm \frac{T_{0,c}}{\sqrt{2}} \tag{3.17}$$

where $\pm$ indicates positive and negative frequency maxima. For the positive frequency, substituting Eq. 3.17 into Eq. 3.16 reveals the peak XPM chirp frequency Δf_{pk}

$$\Delta f_{pk} = \sqrt{\frac{2}{e}}\frac{b\gamma P_{0,c}L_{eff}}{\pi T_{0,c}} \tag{3.18}$$

In terms of wavelength, the peak XPM chirp wavelength $\Delta\lambda_{pk}$ is

$$\Delta\lambda_{pk} = \sqrt{\frac{2}{e}}\frac{b\gamma P_{0,c}L_{eff}\lambda^2}{\pi c T_{0,c}} \tag{3.19}$$

Eq. 3.19 provides an expression for the polarization insensitive offset $\Delta\lambda_{pi}$, where $\Delta\lambda_{pi} = \Delta\lambda_{pk}$. The value for the polarization constant b is found by fitting Eq. 3.19 to experimental results. The experimental and predicted (fitted) results are shown in Fig. 3.11. Results for the predicted polarization insensitive offset (Eq. 3.19) show good agreement with experimental results for $b = 1/3$. Substituting $b = 1/3$ into Eq. 3.19 provides an expression for the polarization insensitive offset $\Delta\lambda_{pi}$

$$\begin{aligned} \Delta\lambda_{pi} &= \sqrt{\frac{2}{e}}\frac{\gamma P_{0,c}L_{eff}\lambda^2}{3\pi c T_{0,c}} \\ &= \frac{a_{pi}\gamma P_{0,c}L_{eff}\lambda^2}{\pi c T_{0,c}} \end{aligned} \tag{3.20}$$

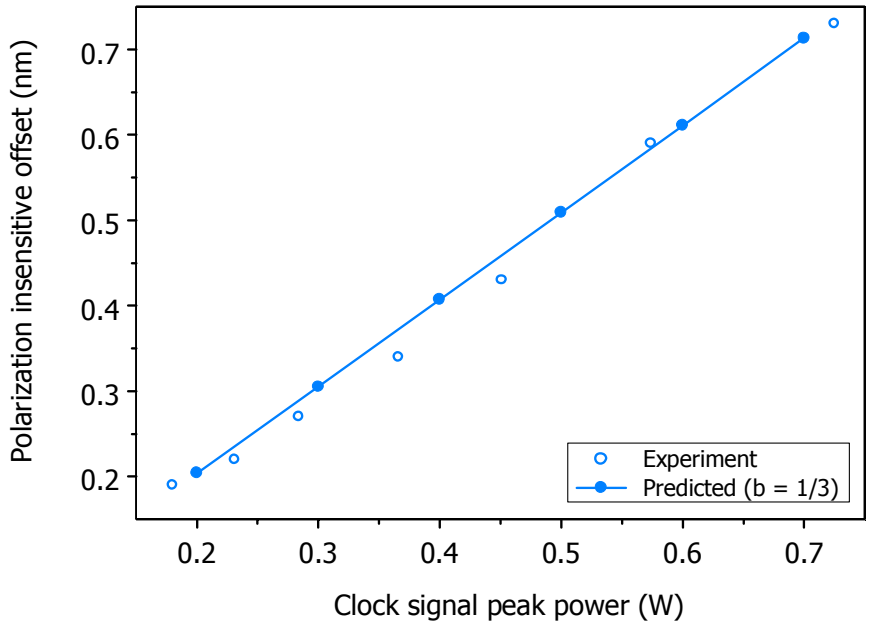

Figure 3.11: Dependence of polarization insensitive offset on clock signal peak power.

where $a_{pi} \approx 0.3$. From this expression, it can be observed that $\Delta\lambda_{pi}$ is independent of the time delay $\Delta\tau_{cd}$. The expression is therefore consistent with the experimental results shown in Fig. 3.10. Using Eq. 3.20, the polarization insensitive offset can be predicted for the clock signal and fiber operating conditions. The polarization insensitive offset can then be used as the slicing filter offset to provide a polarization insensitive sliced (retimed) signal.

3.4.2 Operating Conditions

The optical filter used for the spectral slicing has a Gaussian shaped passband and a bandwidth of 0.25 nm. For the clock signal and fiber operating conditions, the polarization insensitive offset $\Delta\lambda_{pi} = 0.16$ nm (Eq. 3.20). The slicing filter offset $\Delta\lambda_{XPM}$ is set to the polarization insensitive offset $\Delta\lambda_{pi}$ (i.e., $\Delta\lambda_{XPM} = 0.16$ nm). For

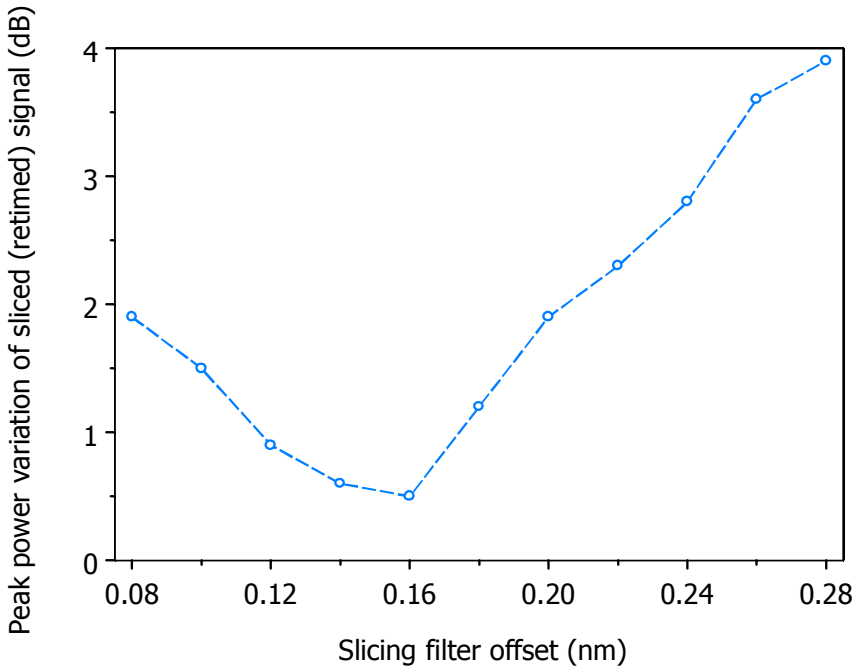

Figure 3.12: Dependence of peak power variation in sliced signal on slicing filter offset.

an input (data) signal wavelength $\lambda_d = 1544.55$ nm, the polarization insensitive sliced signal wavelength $\lambda_d^{'} = \lambda_d + \Delta\lambda_{XPM} = 1544.71$ nm. The time delay $\Delta\tau_{cd}$ is set to the optimal time delay $\Delta\tau_{cd,opt}$ (i.e., $\Delta\tau_{cd} = 15$ ps).

3.4.3 Experimental Results

The polarization sensitivity of the sliced (retimed) signal is determined by varying (scrambling) the input signal SOP and measuring its peak power variation on a DCA. The results for peak power variation versus slicing filter offset $\Delta\lambda_{XPM}$ are shown in Fig. 3.12. The minimum peak power variation (0.5 dB) is obtained at the polarization insensitive offset $\Delta\lambda_{XPM} = \Delta\lambda_{pi} = 0.16$ nm. As the offset deviates from the polarization insensitive offset, peak power variations in the sliced signal increase. In particular,

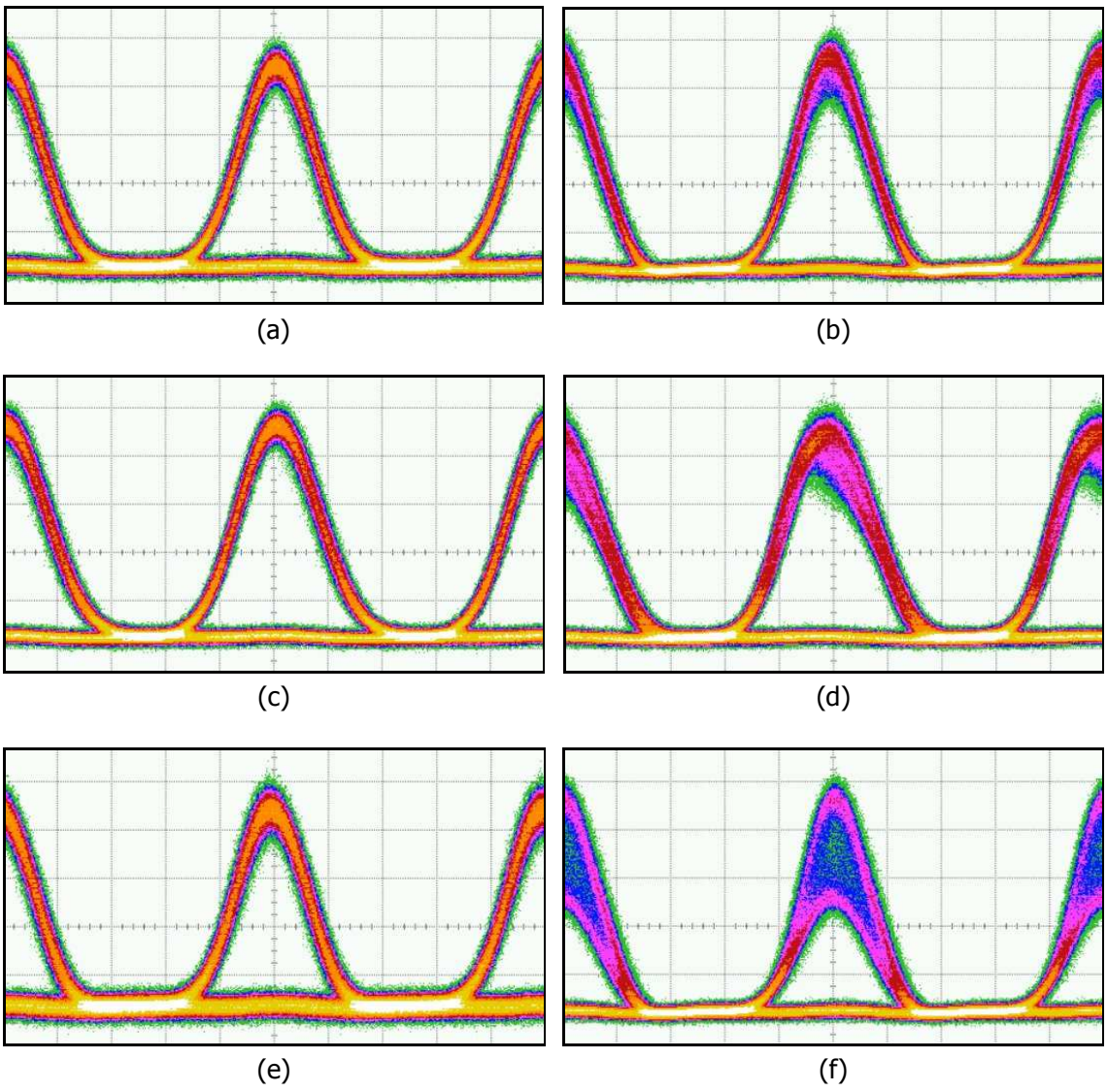

Figure 3.13: Eye diagrams of sliced (retimed) signal for different slicing filter offsets with polarization scrambling (PS) off and on: 0.16 nm with PS (a) off and (b) on; 0.11 nm with PS (c) off and (d) on; 0.21 nm with PS (e) off and (f) on (20 ps/div).

peak power variations increase rapidly when $\Delta\lambda_{XPM} > \Delta\lambda_{pi}$. This occurs because of an increase in spectral power variations between the XPM spectrum for different input signal SOPs (Fig. 3.9). When the XPM spectrum is sliced, spectral power variations in the filter passband translate to amplitude variations in the sliced (retimed) signal.

Eye diagrams of the sliced (retimed) signal for different slicing filter offsets with the input signal SOP scrambling off and on are shown in Fig. 3.13. The eye diagrams show three cases for the slicing filter offset $\Delta\lambda_{XPM}$. When $\Delta\lambda_{XPM} = \Delta\lambda_{pi}$ (Fig. 3.13a-b) there is little difference between eye diagrams with input polarization scrambling off (Fig. 3.13a) and on (Fig. 3.13b). This is the optimal filter offset since it provides a sliced signal with the lowest sensitivity to the input signal SOP.

When $\Delta\lambda_{XPM} \neq \Delta\lambda_{pi}$, the sensitivity to input signal SOP increases. For example, when $\Delta\lambda_{XPM} < \Delta\lambda_{pi}$ (Fig. 3.13c-d), compared to the eye diagram with input polarization scrambling off (Fig. 3.13c), the eye diagram with input polarization scrambling on shows an increase in amplitude variations (Fig. 3.13d). Similar behaviour is observed when $\Delta\lambda_{XPM} > \Delta\lambda_{pi}$ (Fig. 3.13e-f). However, in this case, the eye diagram with input polarization scrambling on shows an even greater increase in amplitude variations (Fig. 3.13f). As previously described, the increase in amplitude variations is caused by an increase in spectral power variations between input signal SOPs over the filter passband.

Having obtained the optimal slicing filter offset, the issue of the optimal time delay $\Delta\tau_{cd,opt}$ is revisited. In addition to maximizing the XPM efficiency, the optimal delay also provides a well-balanced retimed signal with minimal transfer of phase noise to amplitude noise. To aid in the explanation, consider the illustration of time delay and slicing of a jittered data signal shown in Fig. 3.14. In Fig. 3.14a, the clock and data

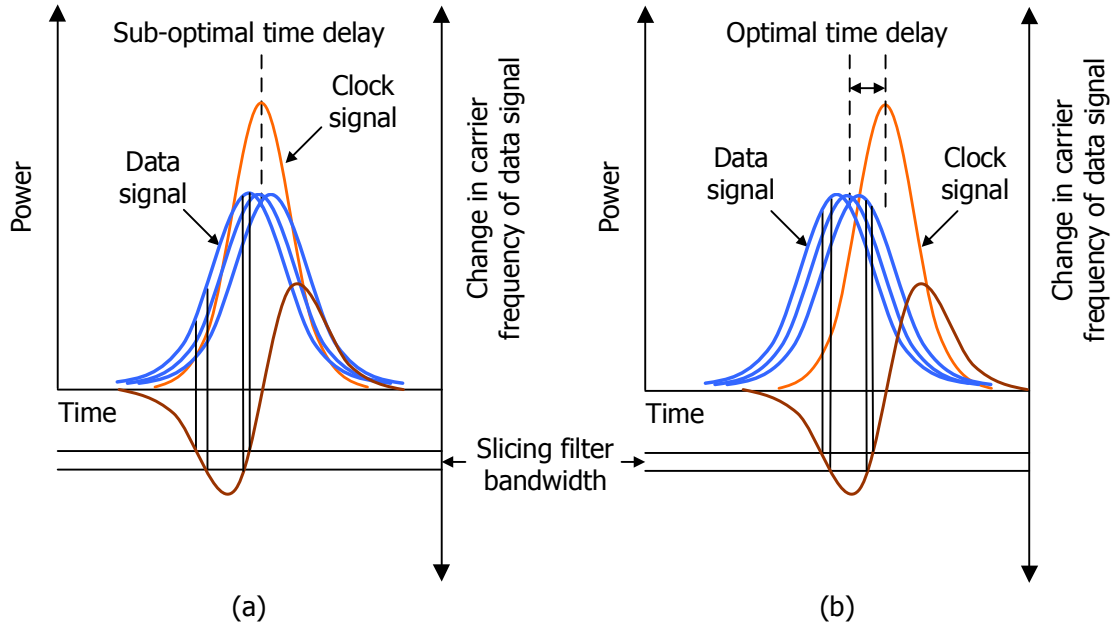

Figure 3.14: Effect of time delay on the slicing of a jittered data signal.

signals are aligned in time (i.e., $\Delta\tau_{cd} = 0$ ps). This means that the peak XPM chirp and signal slicing occur at the edge of the data pulse. Slicing the edge of the data pulse has implications on the properties of the retimed signal. First, since the data signal is not sliced at its peak, the XPM efficiency is not maximized. As a result, the retimed signal power is also not maximized. Second, the sliced regions of the pulse are asymmetric in terms of integrated pulse power. The asymmetry leads to an imbalance of jitter on the rising and falling edges of the retimed signal. Third, phase noise on the edge of the data pulse gets translated to amplitude noise in the retimed signal. Because slicing the edge of the data pulse has negative implications on the properties of the retimed signal, the time delay illustrated in Fig. 3.14a is sub-optimal.

The optimal time delay is illustrated in Fig. 3.14b. In this figure, peak XPM chirp and signal slicing occur at the center (peak) of the data pulse (e.g., $\Delta\tau_{cd} = 15$ ps).

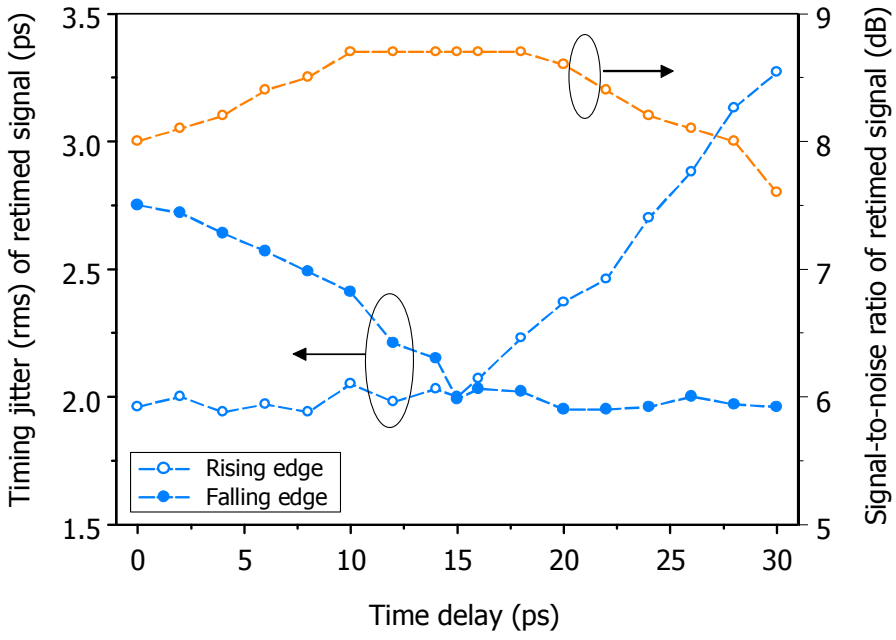

Figure 3.15: Dependence of timing jitter and SNR on time delay.

Slicing the peak of the data pulse also has implications on the properties of the retimed signal. First, since the data signal is sliced at its peak, the XPM efficiency is maximized. As a result, the retimed signal power is also maximized. Second, the sliced regions of the pulse are more symmetric in terms of integrated pulse power. The symmetry leads to well-balanced jitter on the rising and falling edges of the retimed signal. Third, the transfer of phase noise to amplitude noise is minimal in the retimed signal.

The transfer of phase noise to amplitude noise is measured in terms of degradation to the retimed signal SNR. The dependence of the retimed signal SNR and timing jitter on the time delay is shown in Fig. 3.15. For the measurement, the input signal SNR = 8.1 dB and jitter = 2.7 ps (rms). The clock signal jitter = 2.0 ps. The SNR and timing jitter are measured on a DCA (electrical bandwidth = 55 GHz). For the

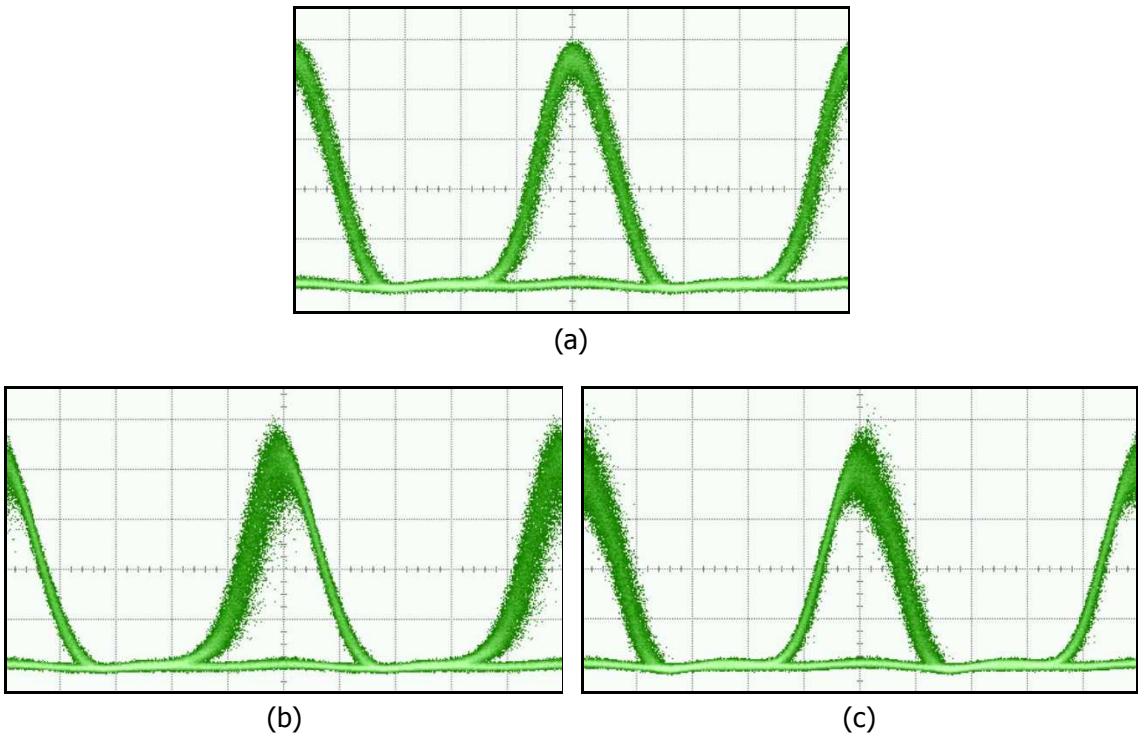

Figure 3.16: Eye diagrams of sliced (retimed) signal for different time delays $\Delta\tau_{cd}$: (a) $\Delta\tau_{cd} = 15$ ps, (b) $\Delta\tau_{cd} = 30$ ps, (c) $\Delta\tau_{cd} = 0$ ps (20 ps/div).

measurement of timing jitter, a precision timebase is used with an intrinsic jitter = 200 fs. The results shown in Fig. 3.15 confirm the intuitive description on the effects of time delay on the properties of the retimed signal. For example, at the optimal time delay (i.e., $\Delta\tau_{cd} = 15$ ps), the SNR = 8.7 dB and the jitter = 2.0 ps is well-balanced on the rising and falling edges. The slight SNR improvement comes from filtering of out-of-band ASE noise. At sub-optimal time delays, the retimed signal SNR is degraded by the transfer of phase noise to amplitude noise. Whereas the retimed signal jitter is imbalanced by the asymmetry of the sliced regions.

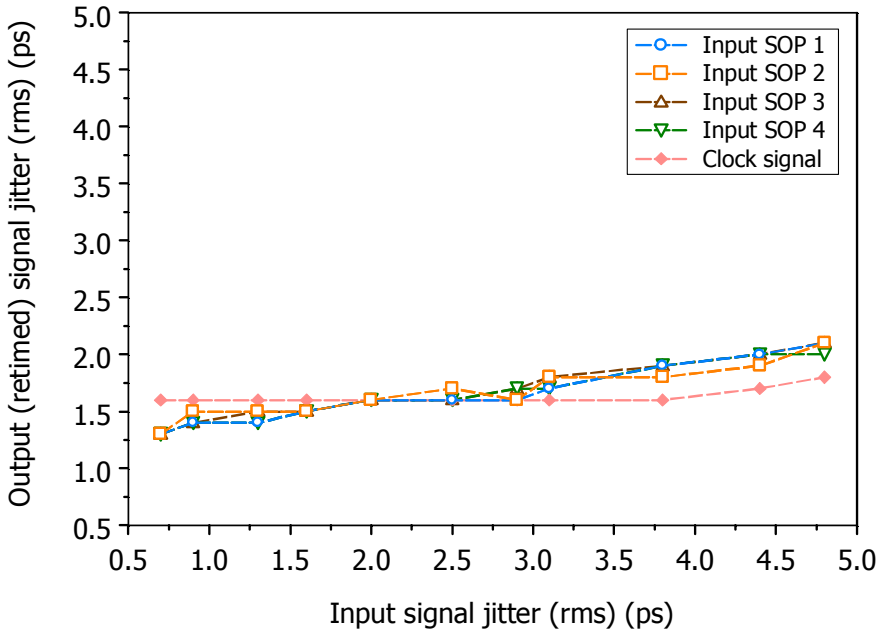

Figure 3.17: Jitter transfer characteristic: Output versus input signal jitter.

The effect of time delay can be observed in the retimed signal eye diagrams shown in Fig. 3.16. The eye diagrams are consistent with the results shown in Fig. 3.15. For the optimal delay (e.g., $\Delta\tau_{cd} = 15$ ps), the retimed signal eye diagram shows minimum amplitude noise (maximum SNR) and well-balanced timing jitter in the rising and falling edges (Fig. 3.16a). In contrast, for sub-optimal delays (e.g., $\Delta\tau_{cd} = 0$ and -15 ps), the retimed signal eye diagrams have increased amplitude noise (decreased SNR) and an imbalance of timing jitter in the rising and falling edges (Fig. 3.16b-c).

Output versus input jitter is measured for the optimal delay ($\Delta\tau_{cd,opt} = 15$ ps) and slicing filter offset ($\Delta\lambda_{XPM} = 0.16$ nm), providing the jitter transfer characteristic (JTC). The JTC is measured for different input signal SOPs. A representative sample of four input SOPs are shown in Fig. 3.17. Two observations can be made form the JTC. First, the jitter of the retimed signal closely follows the jitter of the recovered

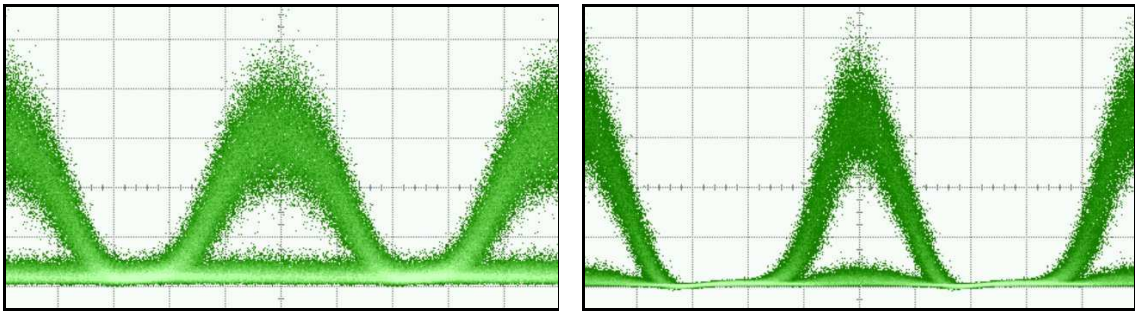

Figure 3.18: Eye diagrams of (a) input signal and (b) retimed signal (20 ps/div).

clock signal. Since the clock signal jitter is generally lower than the input signal, the retimed signal also has lower jitter than the input signal. Second, the retimed signal shows low sensitivity to the input signal SOP. Over four input signal SOPs, the retimed signal jitter varies by only $\pm$ 0.1 ps. The retiming stage therefore provides jitter suppression with low sensitivity to the input signal SOP.

As an example of retiming, the eye diagram for a jittered input signal and corresponding retimed signal are shown in Fig. 3.18. The input signal shows both phase noise (jitter) and amplitude noise (Fig. 3.18a). The retimed signal shows reduced jitter, but similar amplitude noise (Fig. 3.18b). Specifically, the jitter of the input signal is reduced from 4.5 to 2.1 ps. The amplitude noise is not reduced in the retiming stage because the XPM is induced by the clock signal, not the data signal. This means that the XPM is the same for each data bit. Since the XPM is independent of the data signal intensity (i.e., amplitude), there is no discrimination between variations in the input signal amplitude (i.e., noise). Amplitude noise in the input signal is therefore translated to the retimed signal. The retimed signal serves as the input signal to the reshaping stage, where the amplitude noise of the signal is reduced.

3.5 Conclusions

The technique proposed for polarization insensitive all-optical demultiplexing [78] is successfully extended to all-optical retiming [5]. Based on XPM in HNLF with offset spectral slicing, the technique achieves polarization insensitive all-optical retiming without additional control or complexity. This is achieved through a remarkable property of XPM that provides a wavelength in the broadened signal spectrum with nearly the same spectral power regardless of the input signal SOP. By simply offsetting the spectral slicing filter at the wavelength, polarization insensitive all-optical retiming is achieved. An expression is derived to predict the polarization insensitive offset (wavelength) based on clock (pump) signal and fiber parameters. The expression shows good agreement with experimental results for a fitted (polarization) factor $b = 1/3$.

While proper selection of the filter offset achieves polarization independence, proper selection of the time delay achieves the desired properties for the retimed signal. The time delay shifts the XPM frequency chirp in time relative to the position of the data pulses. The time delay is optimal when the peak XPM frequency chirp coincides with the peak of the data pulses. For this time delay, the XPM efficiency is maximal since the maximum spectral power coincides with the polarization insensitive wavelength. Slicing the spectrum at the polarization insensitive wavelength therefore provides maximum power in the sliced (retimed) signal. Because the peak of the data pulses are sliced, the sliced (retimed) signal also exhibits well-balanced timing jitter and minimal increase in amplitude noise. An expression derived for the optimal time delay shows good agreement with experimental results.

Chapter 4

Reshaping Stage

4.1 Introduction

All-optical reshaping has been proposed using self-phase modulation (SPM) in a highly nonlinear fiber (HNLF) with offset spectral slicing [81]. Since SPM is a polarization insensitive nonlinear effect, the technique is insensitive to the state-of-polarization (SOP) of the input signal. Also, since SPM has a femtosecond response time, the technique is readily scalable to ultra-high bit rates (e.g., 160 Gb/s). Because of its ability to achieve polarization independence and ultra-high bit rate operation, the all-optical reshaping technique originally proposed in [81] has generated considerable research activity over the past years [82, 94–98]. In particular, all-optical reshaping (i.e., 2R regeneration) has been demonstrated for 40 [96], 80 [94], and 160 Gb/s signals [99]. Although the technique has been successfully demonstrated for all-optical reshaping, it has only been achieved using very narrow input pulses (e.g., 6.25 ps) [96]. In practical systems, 10 Gb/s signals do not typically have such narrow pulse widths.

In general, 10 Gb/s RZ signals have pulse widths between 33 and 66 ps. For practical implementation, it is important to achieve all-optical reshaping for 10 Gb/s signals with typical pulse widths.

In this chapter, the design guidelines and operating conditions required to achieve all-optical reshaping for 10 Gb/s signals with typical pulse widths are described. For the designed operating conditions, experimental results on the properties of the reshaping stage are reported. Similar to the retiming stage, the design guidelines, operating conditions, and experimental results for the reshaping stage are presented in two sections: SPM spectral broadening (Sect. 4.2) and offset spectral slicing (Sect. 4.3).

4.2 SPM Spectral Broadening

4.2.1 Design Guidelines

For all-optical reshaping based on SPM in HNLF with offset spectral slicing, the SPM signal spectrum should be designed to broaden flatly. This allows an offset filter to slice a flat region of the SPM broadened signal spectrum, thereby reshaping the sliced signal spectrum by the shape of the filter passband. The design guidelines for achieving flat spectral broadening were originally proposed in application to supercontinuum (SC) generation [100]. In [100], two equation were fit to numerical simulations of SPM spectral broadening, providing guidelines for achieving flat spectral broadening (i.e., spectral amplitude fluctuations < 1 dB) with maximum spectral width:

$$\xi \approx \frac{a_\xi}{N} \tag{4.1}$$

$$M \approx a_M N \tag{4.2}$$

where ξ is the normalized propagation length and M is the corresponding spectral broadening (magnification) factor. a_ξ and a_M are coefficients that depend on the input pulse shape. Eqs. 4.1 and 4.2 are valid for $10 \leq N \leq 150$ [100], where N is the soliton order, defined as

$$N = \sqrt{\frac{L_D}{L_{NL}}} \tag{4.3}$$

The dispersion length $L_D = {T_{0,in}}^2/|\beta_2|$ and the nonlinear length $L_{NL} = 1/\gamma P_{0,in}$, where $T_{0,in}$ is the input pulse half-width at 1/e of the peak power, β_2 is the second-order dispersion parameter, γ is the fiber nonlinear parameter, and $P_{0,in}$ is the input signal peak power.

By definition, the normalized propagation length $\xi = L_{eff}/L_D$ (Eq. 4.1), where L_{eff} is the effective fiber length. The magnification factor $M = \Delta\lambda_{out}/\Delta\lambda_{in}$ (Eq. 4.2), where $\Delta\lambda_{in}$ and $\Delta\lambda_{out}$ are the signal spectral widths at the input and output of the fiber, respectively. Recently, Eqs. 4.1 and 4.2 were used to define operating conditions for SPM spectral broadening in application to 40 Gb/s all-optical reshaping [96]. Among the operating conditions, the FWHM input pulse width $T_{FWHM,in} = 6.25$ ps ($T_{0,in} = T_{FWHM,in}/2\sqrt{\ln(2)}$).

To understand the implications of input pulse width $T_{0,in}$ on the required operating conditions for SPM spectral broadening, consider Eqs. 4.1 and 4.2 in terms of signal and fiber parameters. From Eq. 4.1, the effective fiber length L_{eff} required to achieve flat spectral broadening is

$$\begin{aligned} L_{eff} &\approx \frac{a_\xi L_D}{N} \\ &= a_\xi \sqrt{L_D L_{NL}} \\ &= \frac{a_\xi T_{0,in}}{\sqrt{\gamma P_{0,in}|\beta_2|}} \end{aligned} \tag{4.4}$$

From Eq. 4.2, the corresponding SPM spectral width $\Delta\lambda_{out}$ is

$$\begin{aligned} \Delta\lambda_{out} &\approx a_M \Delta\lambda_{in} N \\ &= a_M \Delta\lambda_{in} \sqrt{\frac{L_D}{L_{NL}}} \\ &= a_M \Delta\lambda_{in} T_{0,in} \sqrt{\frac{\gamma P_{0,in}}{|\beta_2|}} \end{aligned} \tag{4.5}$$

With respect to the input pulse width $T_{0,in}$, the required effective fiber length $L_{eff} \propto T_{0,in}$ (Eq. 4.4) and the corresponding SPM spectral width $\Delta\lambda_{out} \propto T_{0,in}$ (Eq. 4.5).

For the same duty cycle, 10 Gb/s pulse widths are 4 times larger than 40 Gb/s pulse widths. Therefore, to achieve 10 Gb/s all-optical reshaping, 40 Gb/s operating conditions for the effective fiber length L_{eff} should be increased by a factor of 4 ($L_{eff} \propto T_{0,in}$). For example, typical 40 Gb/s operating conditions include: fiber length $L = 2.5$ km and fiber attenuation coefficient $\alpha = 0.6$ dB/km ($\alpha = 0.14$ km^{-1}) [96]. Using Eq. 3.2, the effective fiber length $L_{eff} = 2.1$ km. Therefore, 10 Gb/s operating conditions require $L_{eff} = 4 \times 2.1$ km $= 8.4$ km.

To determine the fiber length required to provide $L_{eff} = 8.4$ km, consider Eq. 3.2 solved for fiber length L

$$L = -\frac{\ln(1 - \alpha L_{eff})}{\alpha} \tag{4.6}$$

Since $L \propto \ln(1 - \alpha L_{eff})$, for any fiber length, the effective fiber length is bounded by $L_{eff} < 1/\alpha$. For fiber attenuation coefficient $\alpha = 0.6$ dB/km ($\alpha = 0.14$ km^{-1}), the maximum effective fiber length $L_{eff} < 7.14$ km. Therefore, the required effective fiber length $L_{eff} = 8.4$ km can not be achieved. An alternative is to maintain the 40 Gb/s operating conditions for $L_{eff} = 2.1$ km and to redesign the operating conditions of other fiber and/or signal parameters.

Operating conditions for the input signal peak power $P_{0,in}$ can be redesigned to maintain $L_{eff} = 2.1$ km. Since $L_{eff} \propto T_{0,in}/\sqrt{P_{0,in}}$ (Eq. 4.4), to maintain L_{eff} for 10 Gb/s input signals, 40 Gb/s operating conditions for $P_{0,in}$ should be increased by a factor of 16. For example, typical 40 Gb/s operating conditions are: $P_{0,in} = 1.9$ W [96]. Therefore, 10 Gb/s input signals require $P_{0,in} = 16 \times 1.9$ W $= 30.4$ W. Aside from the cost associated with the increase in power consumption, input signal peak power of this magnitude stimulates undesirable fiber nonlinear effects, such as stimulated Brillouin scattering (SBS) and stimulated Raman scattering (SRS), is potentially damaging to expensive devices, and even worse, poses a considerable safety risk. It is therefore highly desirable to maintain (or lower) the requirements for the input signal peak power $P_{0,in} = 1.9$ W.

Operating conditions for the fiber nonlinear parameter γ can be redesigned to maintain $L_{eff} = 2.1$ km and $P_{0,in} = 1.9$ W. Since $L_{eff} \propto T_{0,in}/\sqrt{P_{0,in}\gamma}$ (Eq. 4.4), to maintain L_{eff} and $P_{0,in}$ for 10 Gb/s input signals, 40 Gb/s operating conditions for γ should be increased by a factor of 16. For example, typical 40 Gb/s operating conditions are: $\gamma = 8.4$ W^{-1}km^{-1} [96]. Therefore, 10 Gb/s input signals require $\gamma = 16 \times 8.4$ W^{-1}km^{-1} $= 134.4$ W^{-1}km^{-1}. To achieve an increase in γ, consider the defining parameters

$$\gamma = \frac{2\pi n_2}{\lambda A_{eff}} \tag{4.7}$$

where λ is the input signal wavelength, n_2 is the fiber nonlinear refractive index coefficient, and A_{eff} is the fiber effective core area. In general, the input signal wavelength is within the range of $1530 < \lambda < 1565$ nm. Therefore, λ does not have a significant impact on γ. This leaves the properties of the fiber: n_2 and A_{eff}.

One means of increasing γ is to use novel fiber materials that increase the nonlinear refractive index coefficient n_2. For example, the use of soft glasses, such as chalcogenide (e.g., As_2Se_3) and bismuth-oxide (e.g., Bi_2O_3), have been shown to provide high nonlinear parameters (e.g., γ = 1,100 $W^{-1}km^{-1}$ [88]). The tradeoff, however, is that soft glasses typically have high attenuation coefficients (e.g., α = 800 dB/km [88]). Although the nonlinearity is high in soft glasses, since the attenuation is also high, the required effective length may not be maintainable. Because of the impact of attenuation on the effective length, it is convenient to define a figure of merit FOM = γL_{eff}. Therefore, instead of of increasing γ by a factor of 16, γ should be increased to maintain the FOM. For example, typical 40 Gb/s operating conditions include: γ = 8.4 $W^{-1}km^{-1}$ and L_{eff} = 2.1 km [96], providing FOM = 17.64 W^{-1}.

Consider the use of Bi_2O_3 fiber (γ = 1,100 $W^{-1}km^{-1}$, α = 800 dB/km [88]) for maintaining FOM = 17.64 W^{-1}. To maintain FOM = 17.64 W^{-1}, the required effective length L_{eff} = FOM/γ = 16 m. However, since the maximum effective length is bounded by $L_{eff} < 1/\alpha$ = 5.4 m, the FOM can not be maintained for 10 Gb/s input signals using Bi_2O_3 fiber.

An alternate means of increasing γ is to increase the optical field confinement by decreasing the effective core area of the fiber A_{eff}. The effective area of the fiber can be decreased by increasing the difference in refractive index between the core and cladding Δn. A novel approach uses fibers composed of an array of tiny air holes. Such fibers are commonly known as as photonic crystal fiber (PCF) or holey fiber (HF). To date, the highest γ has been reported for HF: γ = 56.2 $W^{-1}km^{-1}$ [89]. For this fiber, the corresponding α = 12 dB/km. To maintain FOM = 17.64 W^{-1}, the required effective length L_{eff} = FOM/γ = 314 m. The maximum effective length is bounded

by $L_{eff} < 1/\alpha = 362$ m. Since the required effective length is less than the maximum effective length, the FOM can be maintained for 10 Gb/s input signals using HF.

Although the FOM can be maintained using HF, such fibers are limited in commercial availability. At the present time, Si-based highly nonlinear fiber (HNLF) is more readily available. It is therefore suggested that a Si-based HNLF be used to maintain γ= 8.4 $W^{-1}km^{-1}$ and that other operating conditions of the fiber be redesigned.

Operating conditions for the second-order dispersion parameter β_2 can be redesigned to maintain L_{eff} = 2.1 km, $P_{0,in}$ = 1.9 W, and γ= 8.4 $W^{-1}km^{-1}$. Since $L_{eff} \propto T_{0,in}/\sqrt{P_{0,in}\gamma|\beta_2|}$ (Eq. 4.4), to maintain L_{eff}, $P_{0,in}$, and γ for 10 Gb/s input signals, 40 Gb/s operating conditions for $|\beta_2|$ should be increased by a factor of 16. In practice, β_2 is more commonly referred to by the fiber dispersion parameter D, where

$$D = -\frac{2\pi c}{\lambda^2}\beta_2 \tag{4.8}$$

Since $|D| \propto |\beta_2|$, equivalently, 40 Gb/s operating conditions for $|D|$ should be increased by a factor of 16. For example, typical 40 Gb/s operating conditions are: D = -0.7 ps/nm-km [96]. Therefore, 10 Gb/s input signals require $D = 16 \times$ -0.7 ps/nm-km = -11.2 ps/nm-km.

Selecting the appropriate dispersion parameter is the simplest way to maintain the 40 Gb/s operating conditions for 10 Gb/s signals with practical input pulse widths. For example, unlike the nonlinear parameter, the fiber dispersion parameter can be engineered without increasing the attenuation [101]. As a result, the effective length and FOM are maintained. Furthermore, by engineering the fiber dispersion parameter, the operating conditions of only one parameter require redesign.

4.2.2 Operating Conditions

Using the operating conditions for 40 Gb/s signals as a guideline [96], operating conditions are defined for 10 Gb/s signals with practical input pulse widths. Since the input pulse width $T_{0,in}$ increases by a factor of 4, the fiber dispersion parameter D for 40 Gb/s signals is increased by a factor of 16 for 10 Gb/s signals ($T_{0,in} \propto \sqrt{|D|}$). Therefore, since D = -0.7 ps/nm-km for 40 Gb/s signals [96], for 10 Gb/s signals the dispersion parameter is designed to be $D = 16 \times$ -0.7 ps/nm-km = -11.2 ps/nm-km.

Although the dispersion parameter has been specified, highly nonlinear fiber (HNLF) with exactly the same dispersion parameter as specified may not be commercially available. The approach is to select a HNLF with a dispersion parameter that is similar to the designed value. The HNLF selected for the reshaping stage has a dispersion parameter D = -8.3 ps/nm-km.

The difference between the designed (D = -11.2 ps/nm-km) and actual (D = -8.3 ps/nm-km) dispersion parameters has implications on the required input signal peak power. To illustrate, it is convenient to translate D to β_2 (Eq. 4.8): designed $\beta_2 = 14.3$ ps^2/km, actual $\beta_2 = 10.6$ ps^2/km. From Eq. 4.4, the required input signal peak power $P_{0,in}$ is

$$P_{0,in} \approx \frac{(a_\xi T_{0,in})^2}{\gamma {L_{eff}}^2 |\beta_2|} \tag{4.9}$$

$$= \left(\frac{a_\xi}{L_{eff}}\right)^2 \frac{L_D}{\gamma} \tag{4.10}$$

Since the actual $\beta_2 = 10.6$ ps^2/km is less than the designed $\beta_2 = 14.3$ ps^2/km and $P_{0,in} \propto 1/|\beta_2|$ (Eq. 4.9), for the actual HNLF selected, the input signal peak power $P_{0,in}$ should therefore be increased. Since it is highly desirable to avoid having to increase $P_{0,in}$, operating conditions are redefined to reduce peak power requirements.

One means of reducing input signal peak power $P_{0,in}$ requirements is to increase the $\gamma {L_{eff}}^2$ product ($P_{0,in} \propto 1/\gamma {L_{eff}}^2$) (Eq. 4.9). However, as described in Sect. 3.3.1, the effective fiber length L_{eff} is bounded by the fiber attenuation coefficient α ($L_{eff} < 1/\alpha$). Therefore, to increase the $\gamma {L_{eff}}^2$ product, a HNLF should be selected with high nonlinearity (γ) and low loss (α).

The HNLF selected for the reshaping stage has the following properties at $\lambda =$ 1550 nm: $D =$ -8.3 ps/nm-km, $\gamma =$ 10.5 $W^{-1}km^{-1}$, $\alpha =$ 0.77 dB/km, $L =$ 3 km. For these properties, the HNLF provides an effective fiber length $L_{eff} =$ 2.33 km with a high $\gamma {L_{eff}}^2$ product: $\gamma {L_{eff}}^2 =$ 56.84 km/W.

Another means of reducing input signal peak power $P_{0,in}$ requirements is to decrease the input signal pulse width $T_{0,in}$ ($P_{0,in} \propto (a_\xi T_{0,in})^2$) (Eq. 4.9). The input signal pulse shape (a_ξ) and pulse width $T_{0,in}$ are determined by the retiming stage. Specifically, the pulse shape and pulse width of input signals to the reshaping stage are determined by the passband shape and bandwidth, respectively, of the spectral slicing filter in the retiming stage. The spectral slicing filter provides the reshaping stage with an input signal that has Gaussian shaped pulses and pulse width $T_{FWHM,in} =$ 30 ps, which translates to $a_\xi \approx$ 2.1 [100] and $T_{0,in} =$ 18 ps ($T_{0,in} = T_{FWHM,in}/2\sqrt{\ln(2)}$), respectively.

For the fiber and signal operating conditions selected for the reshaping stage, to achieve SPM spectral broadening with maximum spectral width and low amplitude ripple, the required input signal peak power $P_{0,in} \approx$ 2.36 W (Eq. 4.9). The corresponding spectral broadening factor $M \approx$ 30 (Eq. 4.5). Therefore, after SPM spectral broadening, an input signal with spectral width $\Delta\lambda_{in} =$ 0.12 nm has an output signal spectral width $\Delta\lambda_{out} = M\Delta\lambda_{in} \approx$ 3.6 nm. An experimental measurement of SPM spectral

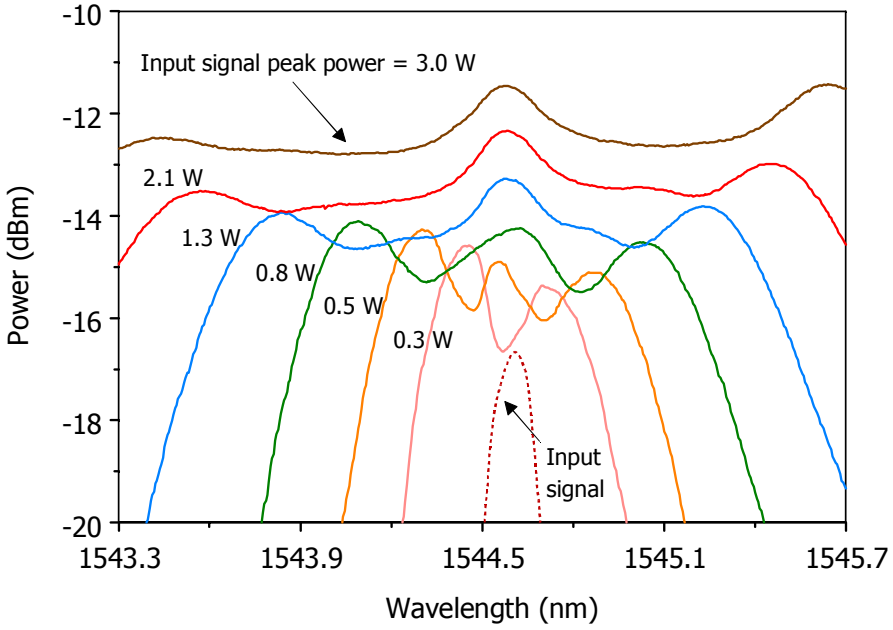

Figure 4.1: Dependence of SPM spectral broadening on input peak power.

broadening using the fiber and signal operating conditions selected for the reshaping stage ($\lambda_{in} = 1544.6$ nm) shows good agreement with predicted results (Fig. 4.1).

In Fig. 4.1, the SPM spectrum exhibits low amplitude ripple (i.e., < 1 dB) for $P_{0,in} < 2.36$ W. In particular, a flat spectral region can be obtained for spectral slicing provided that $P_{0,in} > 1.3$ W. Therefore, the input signal peak power requirements can be reduced while maintaining flat spectral broadening. The tradeoff is that the SPM spectral width is reduced. However, since only a narrow region of the SPM spectrum is sliced (e.g., 0.09 nm), the tradeoff is acceptable for all-optical reshaping. Although the input signal peak power can be reduced, the optimal power depends on the slicing filter offset. In the next section, experimental results are reported for a slicing filter offset $\Delta\lambda_{SPM} = 0.8$ nm.

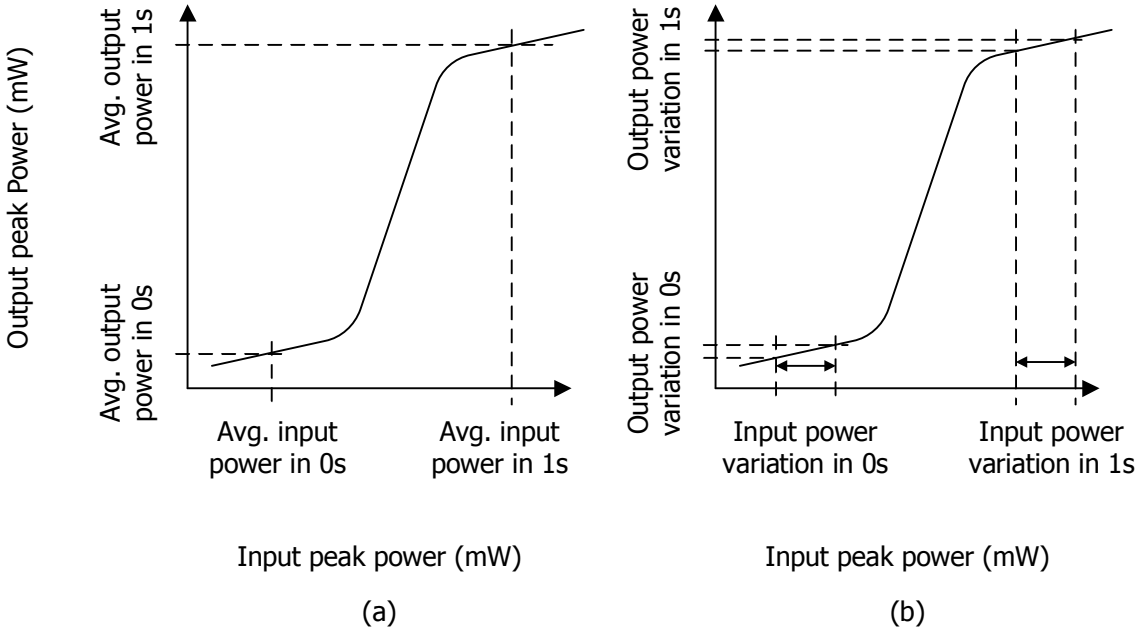

Figure 4.2: Power transfer characteristics: Improvements in (a) ER and (b) SNR.

4.2.3 Experimental Results

The performance of the reshaping stage is measured in terms of the power transfer characteristic (PTC) and output signal extinction ratio (ER) and signal-to-noise ratio (SNR)[1]. The PTC is a measure of the power transfer from input to the output signal in the reshaping stage, which provides information on improvements that can be obtained in terms of the output signal ER and SNR. As an example, a typical PTC is illustrated in Fig. 4.2.

10 Gb/s experimental results on the performance of the reshaping stage are presented. With respect to the fiber dispersion, performance using the fiber designed for

[1]The PTC (input and output signal peak powers), ER, and SNR are measured using a digital communication analyzer (DCA) (electrical bandwidth = 55 GHz).

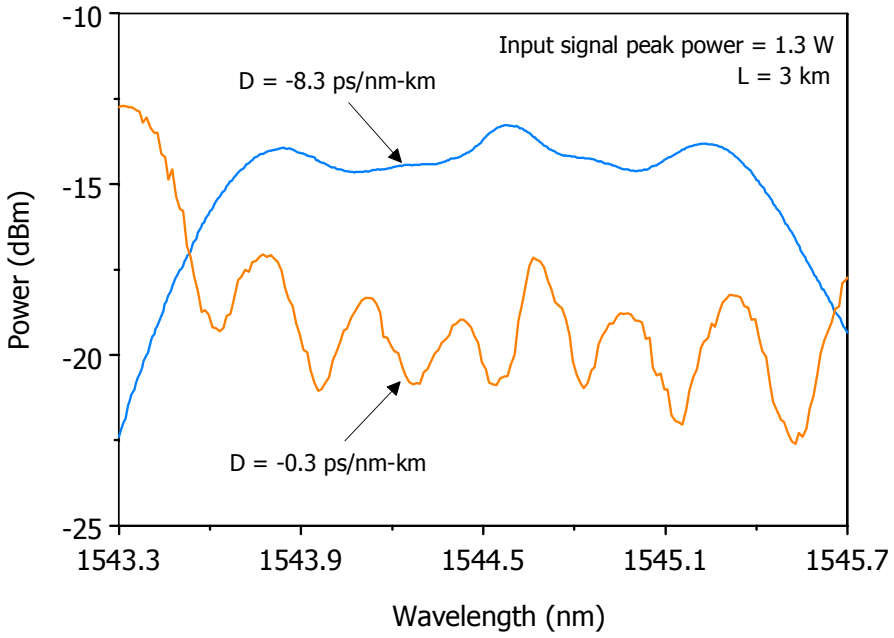

Figure 4.3: Dependence of SPM spectral characteristics on fiber dispersion.

10 Gb/s input pulse widths[2] (47 ps) is compared with a fiber designed for 40 Gb/s input pulse widths (6.25 ps) [96]. The fibers only differ in their fiber dispersion D.

The dependence of SPM spectral characteristics on fiber dispersion D for an input signal peak power $P_{0,in}$ = 1.3 W is shown in Fig. 4.3. The SPM spectra show a strong dependence on D. In particular, the SPM spectrum for D = -0.3 ps/nm-km has considerably larger amplitude variations than D = -8.3 ps/nm-km. The large amplitude variations can be explained by the effect group velocity dispersion (GVD) has on the properties of the SPM spectrum.

For example, GVD does not have a significant effect on the properties of the SPM spectrum for D = -0.3 ps/nm-km. As a result, the signal mainly experiences SPM induced nonlinear frequency chirp. When the chirp is nonlinear, the carrier has the

[2]Pulse widths are full-width at half-maximum (FWHM), unless otherwise specified.

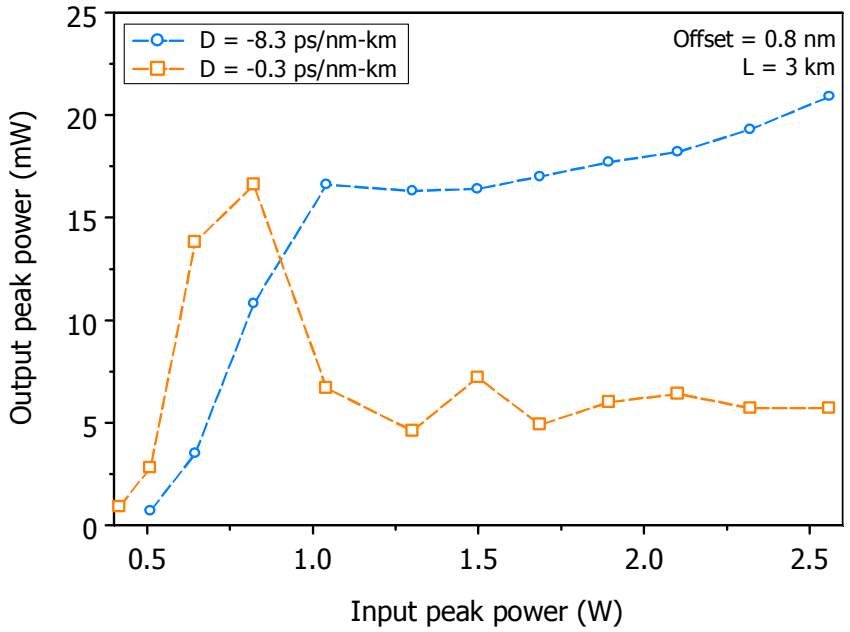

Figure 4.4: Dependence of power transfer characteristics on fiber dispersion.

same instantaneous frequency at two instances in time. This can be viewed as the interference of two waves having the same frequency, but different phase. Spectral amplitude variations occur because of the relative differences in phase for the same frequency at two instances in time [55].

In contrast, GVD does have a significant effect on the properties of the SPM spectrum for D = -8.3 ps/nm-km. As a result, the signal experiences the combined effects of GVD and SPM, which linearizes the induced frequency chirp [55]. Since the chirp is more linear, the carrier does not have the same instantaneous frequency at two instances in time. Therefore, interference of the same instantaneous frequency is reduced, thereby reducing amplitude variations in the broadened signal spectrum.

The implications of spectral amplitude variations are observed in the PTC (Fig. 4.4). For the PTC, input and output signal peak powers are measured after the spectral

slicing (bandwidth = 0.09 nm) using a DCA (electrical bandwidth = 55 GHz). For D = -0.3 ps/nm-km, spectral amplitude variations in the broadened signal spectrum translate into a large peak excursion in the PTC. As a result, amplitude variations are increased in the output signal. For example, consider the eye diagrams before and after the reshaping stage shown in Fig. 4.5. Compared to the input signal to the regenerator/retiming stage (47 ps pulse width) (Fig. 4.5a) and the input signal to the reshaping stage (30 ps pulse width) (Fig. 4.5b), the output signals from the reshaping stage show an increase in amplitude variations in the 1-level (Fig. 4.5c-f).

The performance is improved for D = -8.3 ps/nm-km. Since the broadened signal spectrum has low spectral amplitude variations, the peak excursion is significantly reduced in the PTC. In addition, the PTC exhibits a well-defined saturation region. As a result, amplitude variations (noise) can be potentially reduced in the output signal. When the input signal does not have large amplitude noise, the output signal is able to maintain high performance. For example, consider the eye diagrams before and after the reshaping stage shown in Fig. 4.6. Compared to the performance for D = -0.3 ps/nm-km (Fig. 4.5c-f), the performance for D = -8.3 ps/nm-km (Fig. 4.6c-f) shows significant improvements in the 1-level of the output signals.

Output signals from the reshaping stage also have reduced power in the 0-level. As a result, the reshaping stage can improve the output signal ER. The dependence of the output signal ER on the input signal peak power $P_{0,in}$ and fiber dispersion D is shown in Fig. 4.7. The fiber dispersion does not have a significant effect on the output signal ER. For $P_{0,in} > 1.5$ W, the output signal ER saturates around 22 dB. For example, when $P_{0,in} > 1.5$ W, the output signal ER is improved by about 8.3 dB (13.2 to 22 dB).

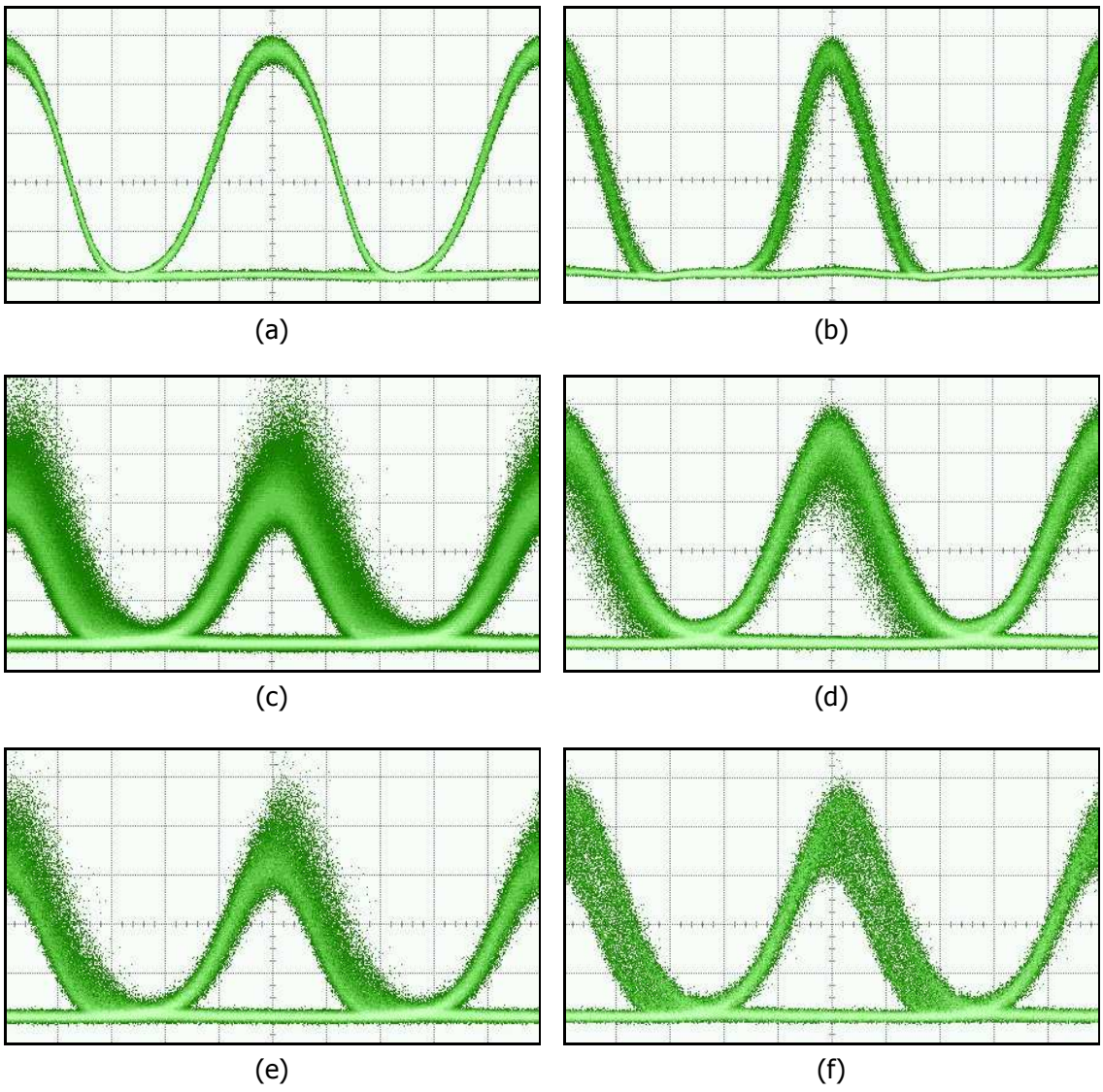

Figure 4.5: Effect of fiber dispersion: D = -0.3 ps/nm-km. Eye diagrams at (a) input of AO-3R, (b) output of retiming stage, (c-f) output of reshaping stage (output of AO-3R) for input peak power: (c) 1.3 W, (d) 1.5 W, (e) 1.7 W, (f) 1.9 W (20 ps/div).

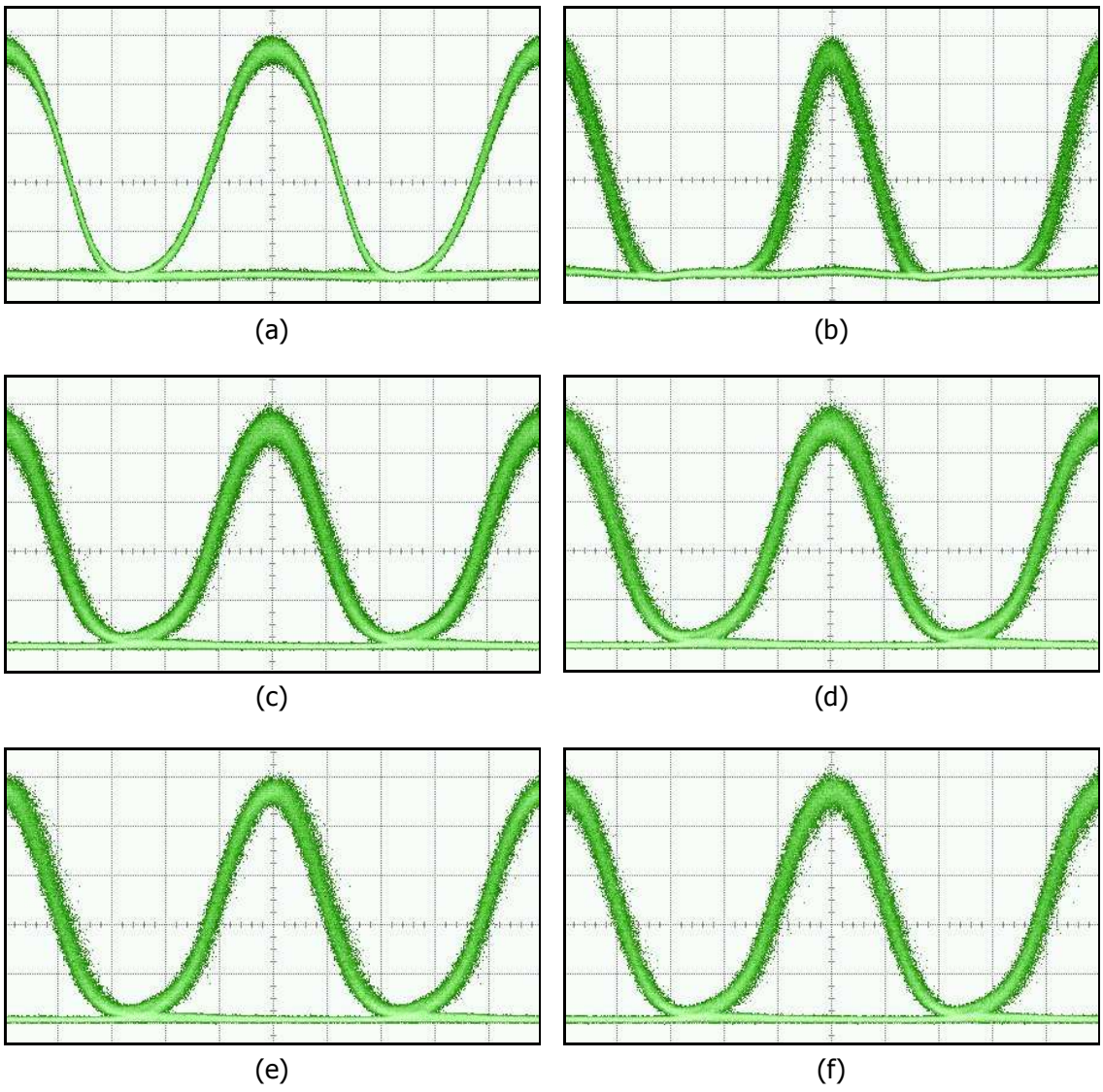

Figure 4.6: Effect of fiber dispersion: D = -8.3 ps/nm-km. Eye diagrams at (a) input of AO-3R, (b) output of retiming stage, (c-f) output of reshaping stage (output of AO-3R) for input peak power: (c) 1.3 W, (d) 1.5 W, (e) 1.7 W, (f) 1.9 W (20 ps/div).

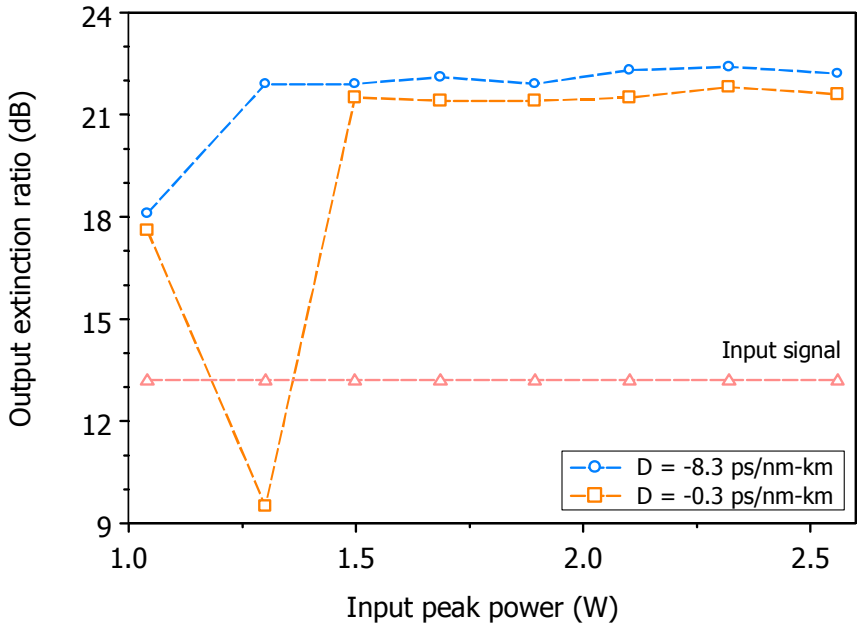

Figure 4.7: Dependence of output ER on input peak power and fiber dispersion.

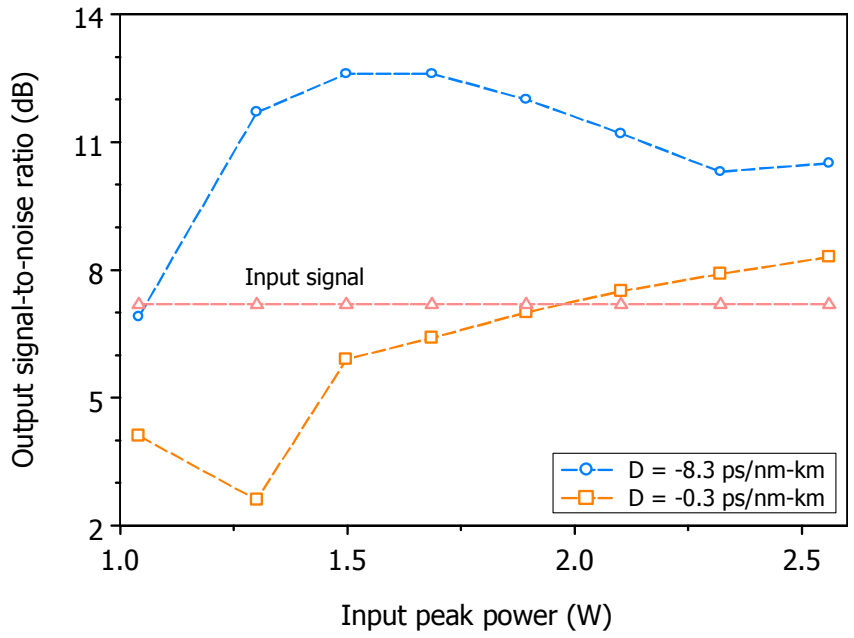

Figure 4.8: Dependence of output SNR on input peak power and fiber dispersion.

In contrast, the fiber dispersion has a significant effect on the output signal SNR. The dependence of the output signal SNR on the input signal peak power $P_{0,in}$ and fiber dispersion D is shown in Fig. 4.8. For fiber dispersion D = -0.3 ps/nm-km, large spectral amplitude variations in the broadened signal spectrum (Fig. 4.3) cause a degradation in the output signal SNR. For example, when $P_{0,in} = 1.3$ W, the output signal SNR is 4.6 dB smaller than the input signal SNR (7.2 to 2.6 dB). The output signal SNR is improved when $P_{0,in} = 2.6$ W, however, an improvement of only 1.1 dB (7.2 to 8.3 dB) is achieved.

The output signal SNR is further improved with fiber dispersion D = -8.3 ps/nm-km. The SNR improvement is provided by low spectral amplitude variations in the broadened signal spectrum (Fig. 4.3). For example, when $1.3 \leq P_{0,in} \leq 1.7$ W, the output signal SNR is improved by up to 5.4 dB (7.2 to 12.6 dB). This range of input signal peak powers coincides with the saturation region in the PTC (Fig. 4.4).

The effect of fiber dispersion D is also observed in the eye diagrams shown in Fig. 4.9. The input signal to the regenerator is degraded by ASE noise (Fig. 4.9a). The output signals from the reshaping stage are observed for D = -0.3 ps/nm-km (Fig. 4.9b) and D = -8.3 ps/nm-km (Fig. 4.9b) using the (optimal) input signal peak powers that maximize the output signal SNR (Fig. 4.8). For D = -0.3 ps/nm-km, even at the optimal input signal peak power, the output signal still shows amplitude variations (noise). However, with proper design of the fiber dispersion D, amplitude noise can be reduced in the output signal. For example, for D = -8.3 ps/nm-km, the output signal shows reduced amplitude noise in the 0- and 1-levels. Therefore, the designed operating conditions for the fiber dispersion D = -8.3 ps/nm-km provide the desired performance for 10 Gb/s input signals with practical pulse widths (i.e., 47 ps).

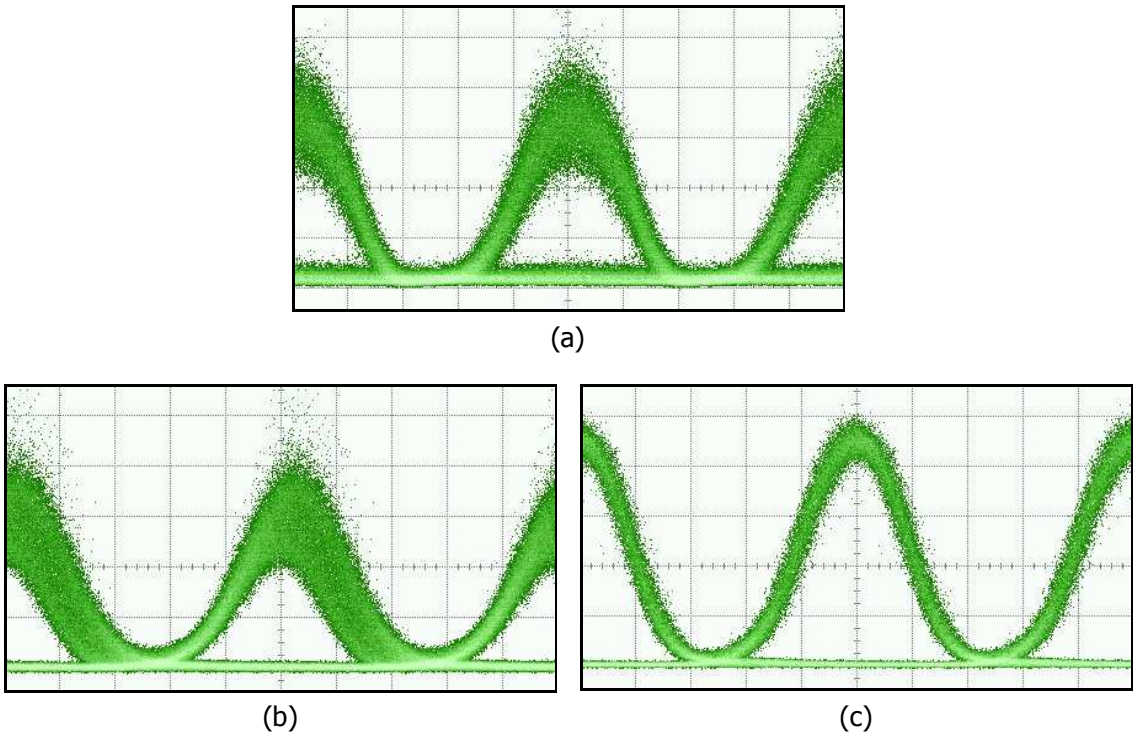

Figure 4.9: Effect of fiber dispersion: Eye diagrams at (a) input of AO-3R and (b,c) output of reshaping stage (output of AO-3R): (b) D = -0.3 ps/nm-km, $P_{0,in}$ = 2.6 W; (c) D = -8.3 ps/nm-km, $P_{0,in}$ = 1.5 W (20 ps/div).

Similar to fiber dispersion, the effect of fiber length on the performance of the reshaping stage is reported. Using the designed operating conditions for the fiber dispersion D = -8.3 ps/nm-km and fiber length L = 3 km, performance is evaluated in comparison to fibers of different lengths (L = 2 and 4 km).

The dependence of SPM spectral broadening and power transfer characteristics on fiber length are shown in Figs. 4.10 and 4.11, respectively. In Fig. 4.10, the input signal peak power $P_{0,in}$ = 1.3 W. The SPM spectral broadening increases with fiber length L since the SPM induced phase $\phi_{SPM} \propto L_{eff}$. This causes the sliced spectral power to show a dependence on fiber length. Consider the PTC for a slicing

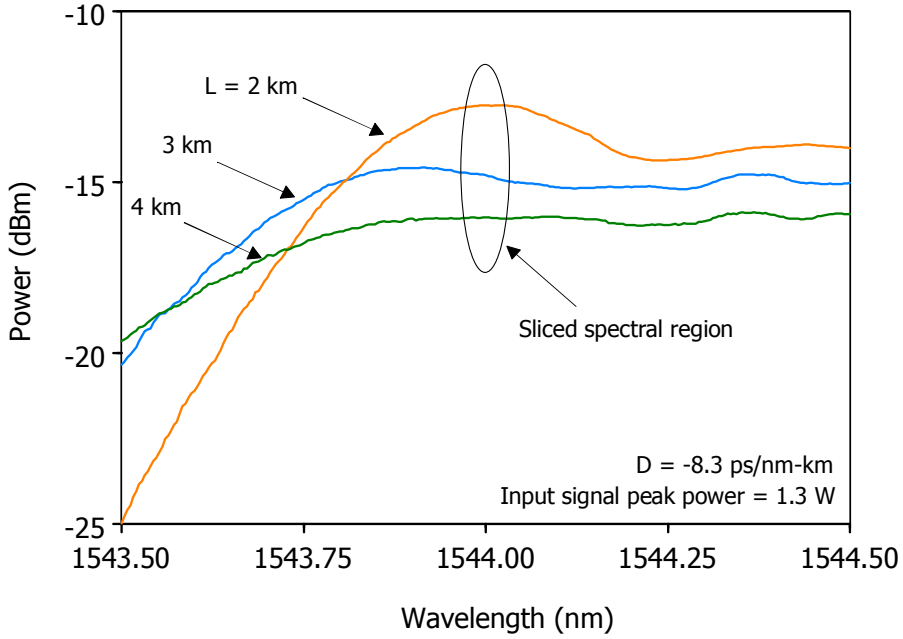

Figure 4.10: Dependence of SPM spectral broadening on fiber length.

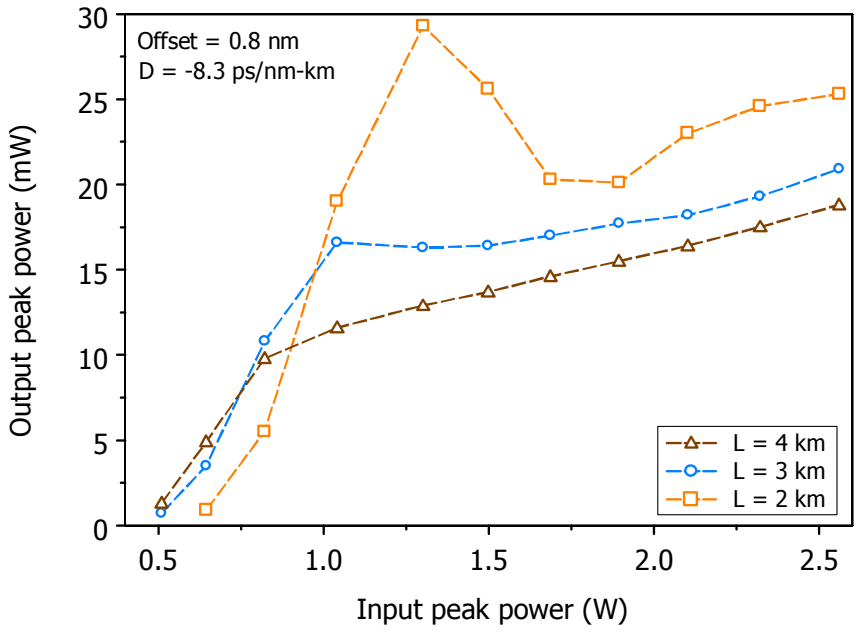

Figure 4.11: Dependence of power transfer characteristics on fiber length.

filter centered at 1539.97 nm (bandwidth = 0.09 nm) (Fig.4.11). When $L = 2$ km, the spectrum has not yet broadened flatly over the filter passband. As a result, a spectral side lobe is sliced, creating a peak excursion in the PTC. From previous results, when a peak excursion exists in the PTC, amplitude variations increase in the output signal (Fig. 4.5). In contrast, when $L = 3$ and 4 km, the spectrum broadens flatly over the filter passband, preventing a peak excursion from occurring in the PTC. Also from previous results, when a peak excursion does not occur in the PTC, amplitude variations can be decreased in the output signal (Fig. 4.6). Since the spectrum broadens flatly, $L = 3$ and 4 km exhibit similar slopes in the high power region of their respective PTC (e.g., $P_{0,in} > 1.5$ W).

Although the PTC slopes are similar, the performance differs for $L = 3$ and 4 km because of pulse broadening effects. Pulse broadening occurs because of group velocity dispersion (GVD), but is affected by the signal peak power because of SPM. As a result, pulse broadening is accelerated as the input signal peak power increases. As an example, consider eye diagrams for $L = 3$ km with increasing peak power (Fig. 4.12). The Gaussian shaped input pulses (Fig. 4.12a) are shown to evolve into a parabolic pulse shape at the output of the HNLF (before the slicing filter) (Fig. 4.12b). As the peak power increases, the pulses continue to broaden (Fig. 4.12c), eventually broadening into adjacent bit slots (Fig. 4.12d).

The pulses broaden even further as the fiber length is increased from $L = 3$ to 4 km. For $P_{0,in} = 1.9$ W, a comparison of eye diagrams before and after spectral slicing for $L = 3$ and 4 km is shown in Fig. 4.13. At the output of the HNLF (before spectral slicing), compared to $L = 3$ km (Fig. 4.13a), pulse broadening is more advanced for $L = 4$ km (Fig. 4.13c). For $L = 4$ km, pulses develop from a parabolic shape into a more

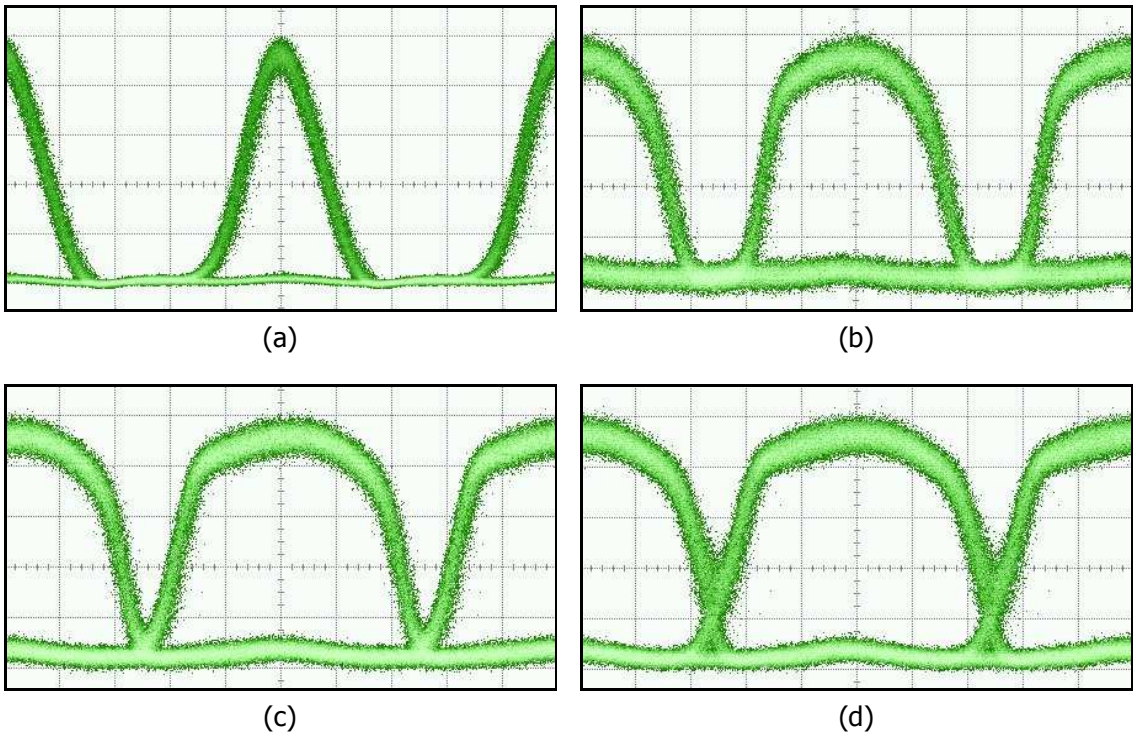

Figure 4.12: Effect of fiber length: $L = 3$ km. Eye diagrams at (a) input of HNLF; (b-d) output of HNLF: (b) $P_{0,in} = 0.8$ W, (c) $P_{0,in} = 1.5$ W, (d) $P_{0,in} = 1.9$ W (20 ps/div).

trapezoidal shape with significant overlap into adjacent bit slots (Fig. 4.13c). The pulse overlap induces intra-channel nonlinear effects, such as intra-channel four-wave mixing (iFWM), which causes amplitude variations from so-called ghost pulses [102]. As a result, for $L = 4$ km, the eye diagram after spectral slicing exhibits amplitude distortion in the form of a double-peak (Fig. 4.13d). In comparison, for $L = 3$ km, the sliced signal does not exhibit any amplitude distortion (Fig. 4.13b). For $L = 3$ km, pulses just begin to overlap with adjacent bit slots when $P_{0,in} = 1.9$ W. It is important to prevent further pulse broadening in order to avoid intra-channel nonlinear effects that can degrade the performance.

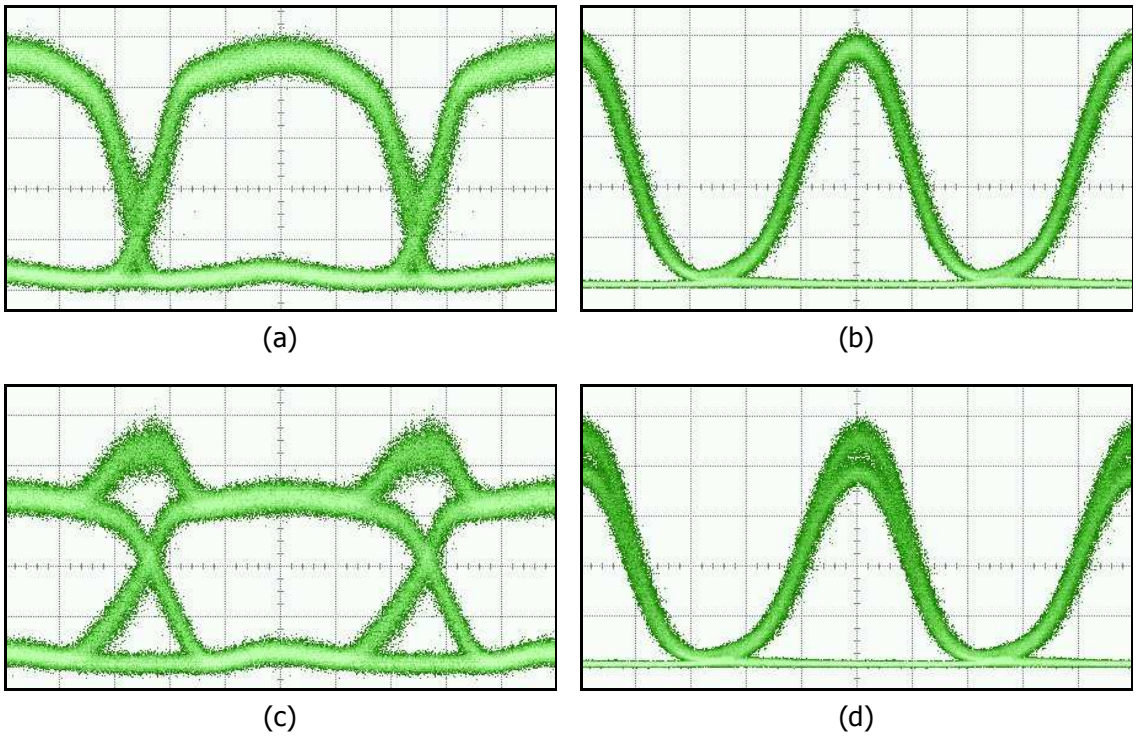

Figure 4.13: Effect of fiber length: $P_{0,in} = 1.9$ W. Eye diagrams for (a,b) $L = 3$ km: (a) output of HNLF, (b) output of slicing filter; (c,d) $L = 4$ km: (c) output of HNLF, (d) output of slicing filter (20 ps/div).

Intra-channel nonlinear effects are avoided when pulses are confined to their bit slots. An analytical expression, derived for pulse broadening of Gaussian shaped input pulses is given by [103]

$$\frac{T_{RMS,out}}{T_{RMS,in}} = \left\{1 + \sqrt{2}\phi_{max}\frac{z}{L_D} + \left(1 + \frac{4}{3\sqrt{3}}{\phi_{max}}^2\right)\left(\frac{z}{L_D}\right)^2\right\}^{1/2} \tag{4.11}$$

where $T_{RMS,in}$ is the rms half-width of the pulse at the input of the fiber ($z = 0$) and $T_{RMS,out}$ is the rms half-width of the pulse at propagation distance z. At the output of the HNLF, the propagation distance $z = L$. Since the maximum SPM induced phase ϕ_{max} coincides with the peak of the pulses, $\phi_{max} = \gamma P_{0,in} L_{eff}$. Therefore, in

terms of signal and fiber parameters, Eq. 4.11 can be expressed as

$$\frac{T_{RMS,out}}{T_{RMS,in}} = \left\{1 + \sqrt{2}\frac{\gamma P_{0,in} L_{eff} |\beta_2| L}{{T_{0,in}}^2} + \left(1 + \frac{4}{3\sqrt{3}}(\gamma P_{0,in} L_{eff})^2\right)\left(\frac{|\beta_2| L}{{T_{0,in}}^2}\right)^2\right\}^{1/2} \tag{4.12}$$

As shown in Fig. 4.12, Gaussian shaped input pulses evolve into a parabolic shape. The normalized power for a parabolic shaped pulse $P_p(t)$ can be represented as

$$P_p(t) = \begin{cases} 1 - \left(\frac{t}{T_p}\right)^2 & |t| < T_p \\ 0 & \text{otherwise} \end{cases}$$

For parabolic pulses to remain confined to their bit slots T_b, the parabolic pulse half width $T_p < T_b/2$. Therefore, at the output of the HNLF, parabolic shaped pulses should have an rms half width $T_{RMS,out} < (T_b/2)\sqrt{1 - P_{p,rms}}$, where $P_{p,rms}$ is the normalized power at $t = T_{RMS}$. At the input of the HNLF, Gaussian shaped input pulses have an rms half width $T_{RMS,in} = T_{0,in}/2$. Substituting $T_{RMS,out}$ and $T_{RMS,in}$ into Eq. 4.12 provides

$$1 - 0.135\left(\frac{T_b}{T_{0,in}}\right)^2 + \frac{\sqrt{2}\gamma L_{eff} |\beta_2| L}{{T_{0,in}}^2} P_{0,in} + \left(1 + \frac{4(\gamma L_{eff})^2}{3\sqrt{3}} {P_{0,in}}^2\right)\left(\frac{|\beta_2| L}{{T_{0,in}}^2}\right)^2 < 0 \tag{4.13}$$

Eq. 4.13 can be used to solve for the maximum input signal peak power $P_{0,in,max}$ that can be launched into the HNLF before pulses begin to overlap with adjacent bit slots. For the operating conditions designed for 10 Gb/s signals ($T_b = 100$ ps), when $L = 3$ km the maximum input signal peak power $P_{0,in,max} \approx 1.84$ W. This result is in good agreement with the experimental result provided in Fig. 4.12d, which shows the beginning of pulse overlap for $P_{0,in} = 1.9$ W. Equation 4.13, therefore, provides a useful condition as an upper bound on the input signal peak power (i.e., $P_{0,in} <$ 1.9 W).

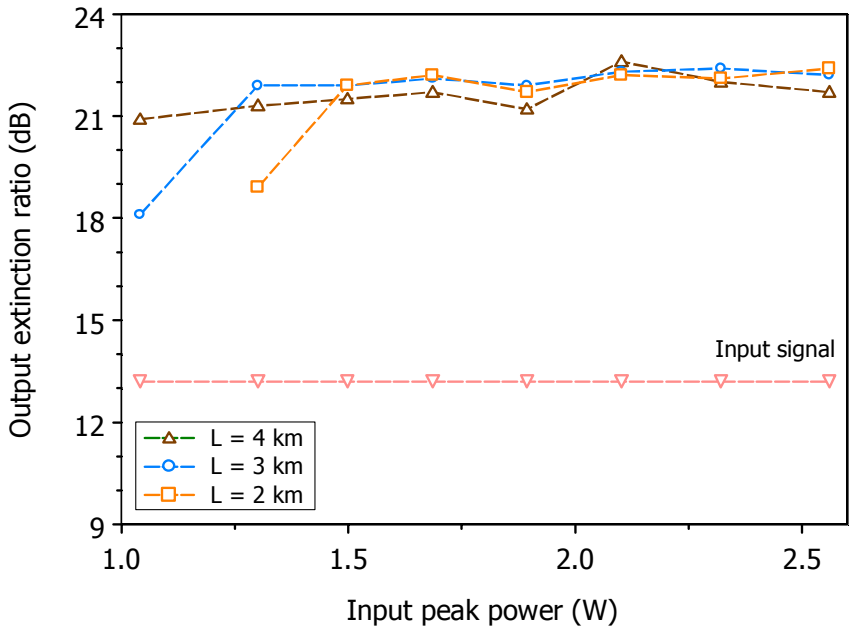

Figure 4.14: Dependence of output ER on input peak power and fiber length.

Similar to fiber dispersion D, the dependence of performance on fiber length L is described. The dependence of the output signal ER on the input signal peak power $P_{0,in}$ and fiber length L is shown in Fig. 4.14. Like fiber dispersion, the fiber length does not have a significant effect on the output signal ER, which saturates around 22 dB. The only difference between fiber lengths is the input signal peak power $P_{0,in}$ required to reach saturation. From the lowest to the highest $P_{0,in}$ required to saturate the output signal ER, the corresponding fiber lengths are 4, 3, 2 km. Since the SPM induced phase $\phi_{SPM} \propto P_{0,in} L_{eff}$, the lowest required $P_{0,in}$ occurs for the longest fiber length ($L = 4$ km). In other words, the longer the fiber, the less power is required to broaden the signal spectrum over the passband of the slicing filter, thereby saturating the output signal ER.

In contrast, the output signal SNR shows a greater dependence on fiber length.

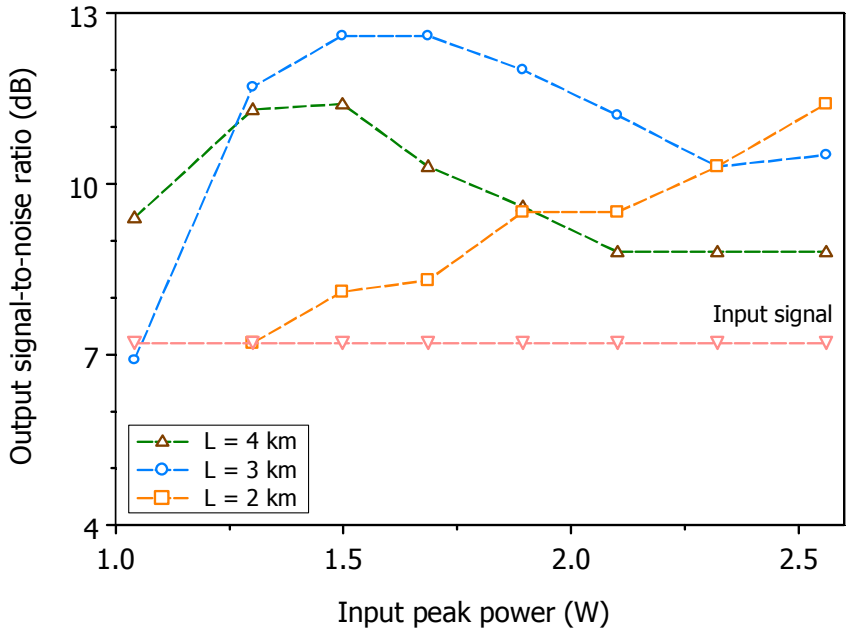

Figure 4.15: Dependence of output SNR on input peak power and fiber length.

The dependence of the output signal SNR on the input signal peak power $P_{0,in}$ and fiber length L is shown in Fig. 4.15. Optimal performance is achieved for $L = 3$ km, where an output signal SNR improvement of 5.4 dB (7.2 to 12.6 dB) is achieved for $1.5 \leq P_{0,in} \leq 1.7$ W. For shorter fibers (e.g., $L = 2$ km), higher input signal peak power $P_{0,in}$ is required to broaden the spectrum over the filter passband. As a result, higher $P_{0,in}$ is required to reduce amplitude variations in the 1-level and provide an improvement in the SNR of the output signal.

For longer fibers (e.g., $L = 4$ km), lower $P_{0,in}$ is required to broaden the signal spectrum over the filter passband. However, compared to $L = 3$ km, for $L = 4$ km the output signal SNR is reduced because of differences in the broadened signal spectra, which translate to differences in sliced signal power. As a result, the PTCs exhibit different slopes in the transition to the saturation region (Fig. 4.11). Since the PTC

for $L = 3$ km provides the lower slope (e.g., $P_{0,in} = 1.5$ W), a higher output signal SNR is achievable. Also, for $L = 4$ km, high input signal peak power (e.g., $P_{0,in} = 1.9$ W) reduces the SNR improvement since intra-channel nonlinear effects lead to amplitude distortion in the output signal (Fig. 4.13d).

In summary, the reshaping stage achieves optimal performance for the operating conditions designed for 10 Gb/s input signals with practical pulse widths (47 ps). In particular, the designed fiber dispersion D = -8.3 ps/nm-km and fiber length $L = 3$ km are shown to achieve optimal performance in terms of the output signal ER and SNR when the input signal peak power $P_{0,in}$ is within the range of $1.5 \leq P_{0,in} \leq 1.7$ W. The design of the spectral slicing filter required to provide 10 Gb/s output signals with practical pulse widths is described in the next section.

4.3 Offset Spectral Slicing

4.3.1 Design Guidelines

The properties of the reshaped output signal are dependent on the properties of the spectral slicing filter. In particular, the slicing filter offset is designed to achieve optimal performance in terms of the output signal ER and SNR. The slicing filter passband shape and bandwidth are designed to provide the output signal with the desired pulse shape and pulse width, respectively.

The spectral slicing defines the shape of the output signal spectrum. For example, if the filter passband shape is Gaussian, spectral slicing provides Gaussian shaped

output pulses $P_{out}(t)$ of the form

$$P_{out}(t) = P_{0,out} \exp\left\{-\left(\frac{t}{T_{0,out}}\right)^2\right\} \tag{4.14}$$

where the 1/e half-width of the output signal $T_{0,out}$ is related to the 1/e half-width of the slicing filter Δf_0, given by

$$\Delta f_0 = \frac{1}{2\pi T_{0,out}} \tag{4.15}$$

The FWHM output pulse width $T_{FWHM,out} = 2\sqrt{\ln(2)}T_{0,out}$ and FWHM slicing filter bandwidth $\Delta f_{FWHM} = 2\sqrt{\ln(2)}\Delta f_0$. To provide Gaussian shaped output pulses with pulse width $T_{FWHM,out}$, the slicing filter bandwidth Δf_{FWHM} is designed to be

$$\Delta f_{FWHM} = \frac{2\ln(2)}{\pi T_{FWHM,out}} \tag{4.16}$$

In terms of wavelength, the slicing filter bandwidth $\Delta\lambda_{FWHM}$ is

$$\Delta\lambda_{FWHM} = \frac{2\ln(2)\lambda^2}{\pi c T_{FWHM,out}} \tag{4.17}$$

4.3.2 Operating Conditions

The operating conditions for the slicing filter offset are determined experimentally in terms of improvements to the output signal ER and SNR. To provide Gaussian shaped output signals, the shape of the slicing filter passband is designed to be Gaussian. The filter bandwidth is designed to provide practical pulse widths for 10 Gb/s output signals. Ideally, the output signal pulse width should be comparable to the input signal pulse width. To provide output signals with pulse width $T_{FWHM,out} = 40$ ps, the slicing filter bandwidth is designed to be $\Delta\lambda_{FWHM} = 0.09$ nm (Eq. 4.17). A fiber Bragg grating (FBG), designed to provide the specified passband shape and bandwidth, is used for the spectral slicing.

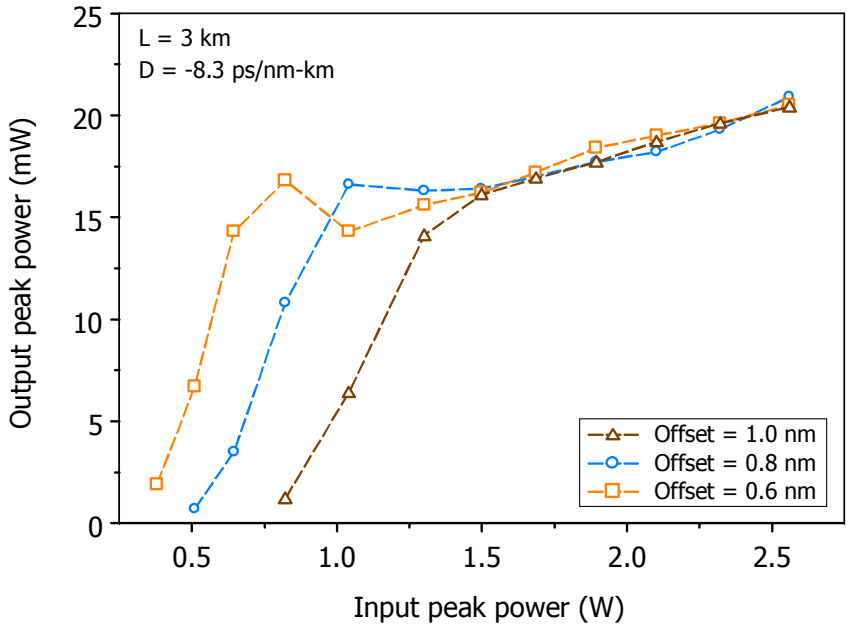

Figure 4.16: Dependence of power transfer characteristics on slicing filter offset.

4.3.3 Experimental Results

The dependence of the PTC on the input signal peak power $P_{0,in}$ and slicing filter offset $\Delta\lambda_{SPM}$ are shown in Fig. 4.16. The PTC is determined by the power in the broadened signal spectrum at the filter offset. As $P_{0,in}$ increases, the spectrum broadens over the filter offset, increasing the sliced (output) signal power. This can be observed in the rising slope region of the PTC. When the spectrum broadens beyond the filter offset, the PTC transitions from the rising slope region to the saturation region. At the transition, the PTC depends on the characteristics of the SPM spectrum at the slicing filter offset.

An important spectral characteristic is the depth of the SPM spectral side lobe. The dependence of SPM spectral side lobe suppression on input signal peak power $P_{0,in}$ is shown in Fig. 4.17. As $P_{0,in}$ increases, the SPM spectrum broadens flatly,

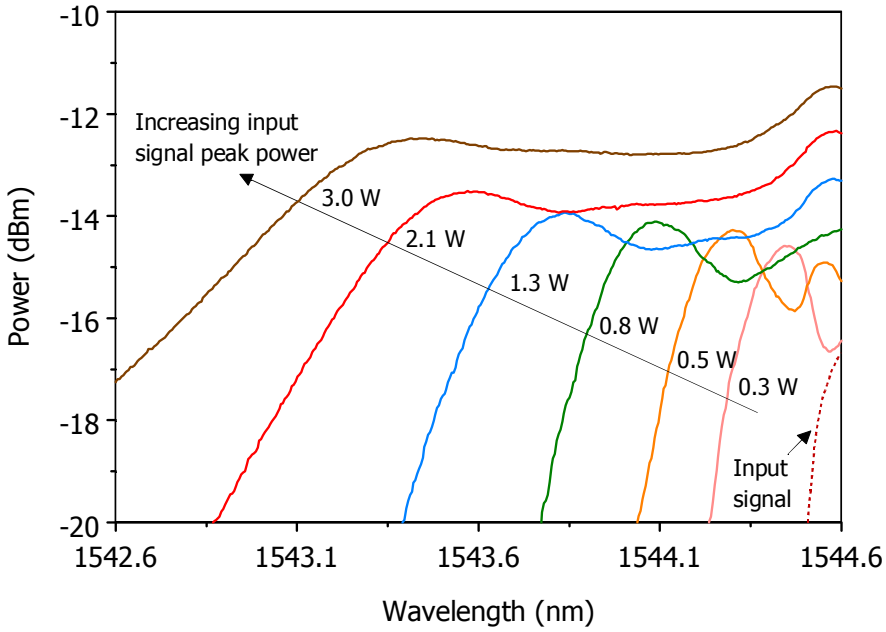

Figure 4.17: Dependence of SPM spectral side lobe suppression on input power.

reducing the depth of the side lobe. For a short filter offset (e.g., $\Delta\lambda_{SPM} = 0.6$ nm), the spectrum is sliced before the side lobe is suppressed. This translates to a peak excursion in the PTC. In contrast, for a long filter offset (e.g., $\Delta\lambda_{SPM} = 0.8$, 1.0 nm) the depth of the side lobe and the peak excursion in the PTC becomes suppressed. Once the depth of the side lobe is well suppressed, the SPM spectrum broadens flatly over the filter offsets, causing the PTCs to converge. Since the PTCs converge when $P_{0,in} = 1.5$ W, flat spectral broadening is achieved when $P_{0,in} \geq 1.5$ W.

To determine the optimal slicing filter offset, the dependence of the output signal ER and SNR on the input signal peak power $P_{0,in}$ and slicing filter offset $\Delta\lambda_{SPM}$ are measured. The results of the measurements are shown in Figs. 4.18 and 4.19. The slicing filter offset does not have a significant effect on the output signal ER, which saturates around 22 dB. Similar to the fiber length, the only difference between

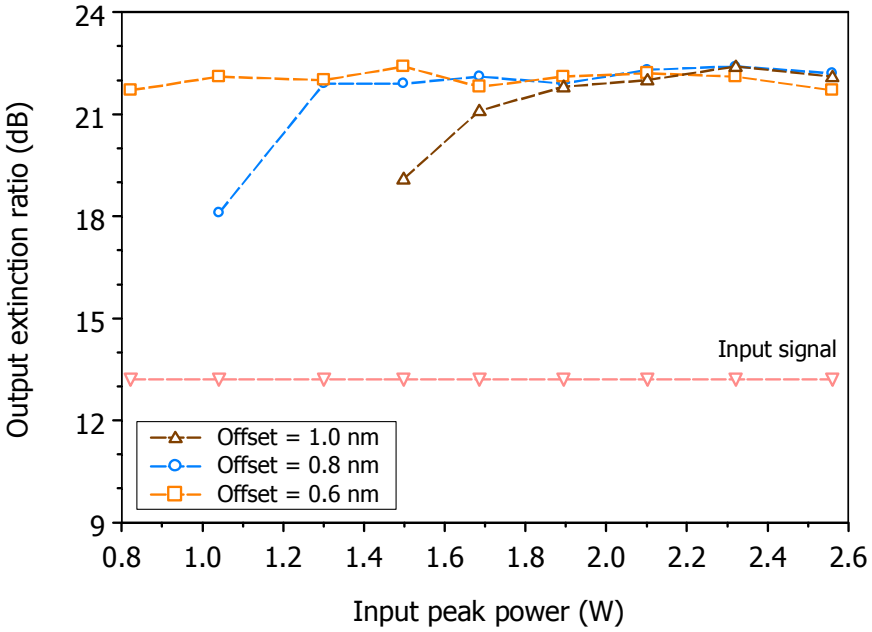

Figure 4.18: Dependence of output ER on input peak power and slicing filter offset.

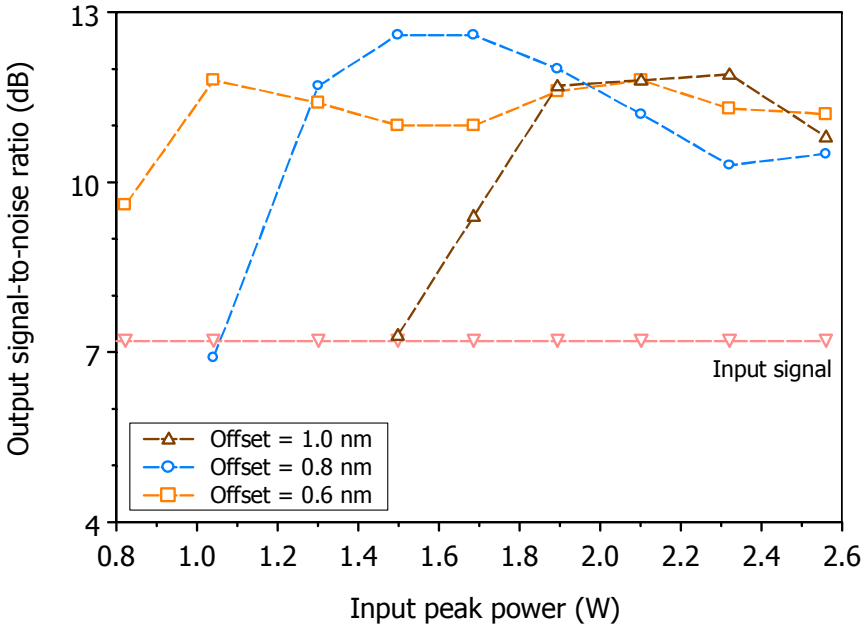

Figure 4.19: Dependence of output SNR on input peak power and slicing filter offset.

slicing filter offsets is the input signal peak power $P_{0,in}$ required to reach saturation. Higher $P_{0,in}$ is required for large slicing filter offsets (e.g., $\Delta\lambda_{SPM} = 1.0$ nm) since higher $P_{0,in}$ is required to broaden the signal spectrum beyond the filter passband. For $P_{0,in} \geq 1.9$ W, the filter offsets all achieve the maximum ER improvement of 8.8 dB (13.2 to 22 dB).

Since the filter offset does not have a significant impact on the output signal ER, the output signal SNR is used to determine the optimal filter offset. For $\Delta\lambda_{SPM} = 0.6$ nm, when $P_{0,in} = 1.0$ W the maximum SNR of 11.8 dB is obtained. In this case, $P_{0,in}$ corresponds to the dip in the transition region of the PTC (Fig. 4.16). Since input signal peak power variations swing about the dip, output signal peak power variations (noise) are reduced, thereby increasing the output signal SNR. As $\Delta\lambda_{SPM}$ increases, higher $P_{0,in}$ is required to achieve the maximum output signal SNR.

For $\Delta\lambda_{SPM} = 1.0$ nm, when $P_{0,in} = 2.3$ W the maximum output signal SNR of 11.9 dB is obtained. In this case, P_0 corresponds to the high power region of the PTC (Fig. 4.16). In this region, the spectrum is sliced when it has broadened flatly. Therefore, an increase in input signal peak power corresponds to a linear increase in output signal peak power. Because the slope is less than one, output signal peak power variations (noise) are decreased, thereby increasing the output signal SNR.

Optimal performance is achieved for slicing filter offset $\Delta\lambda_{SPM} = 0.8$ nm. For $\Delta\lambda_{SPM} = 0.8$ nm, when the input signal peak power is within $1.5 < P_{0,in} < 1.7$ W the maximum output signal SNR of 12.6 dB is obtained. In this case, $P_{0,in}$ corresponds to the region of minimum slope in the PTC (Fig. 4.16). The spectrum is sliced in a region that includes a well suppressed side lobe. The spectrally sliced (output) signal power is therefore nearly the same for the side lobe and the flatly broadened spectrum.

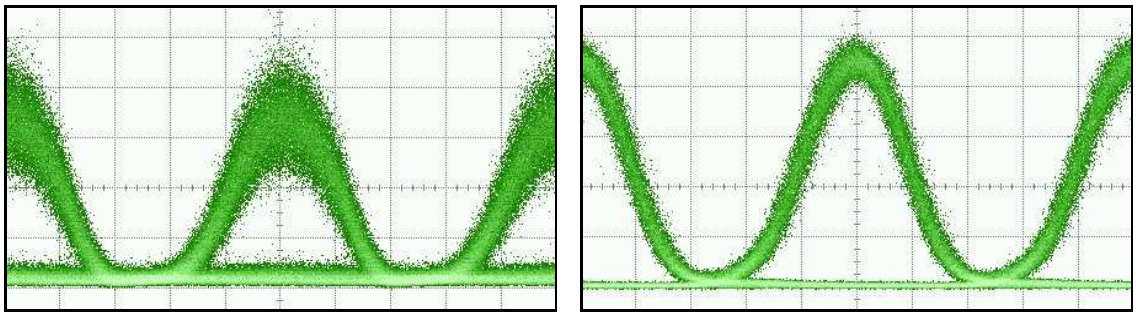

Figure 4.20: Effect of filter offset: $\Delta\lambda_{SPM} = 0.8$ nm. Eye diagrams at (a) input of AO-3R and (b) output of reshaping stage (output of AO-3R) (20 ps/div).

As a result, the sliced (output) signal power shows almost no increase as the input signal peak power increases. Therefore, variations (noise) in input signal peak power are maximally suppressed in the output signal. In other words, the maximum output signal SNR is achieved.

As an example, the eye diagrams for an input signal degraded by ASE noise and the reshaped output signal ($\Delta\lambda_{SPM} = 0.8$ nm) are shown in Fig. 4.20. With proper design of the slicing filter offset, maximum improvements are obtained in the output signal ER (8.8 dB) and SNR (5.4 dB). The output pulse width $T_{FWHM,out} = 42$ ps is in good agreement with the designed pulse width $T_{FWHM,out} = 40$ ps.

4.4 Conclusions

All-optical reshaping is achieved for 10 Gb/s signals with practical input pulse widths. The design approach uses the operating conditions for 6.25 ps input pulse widths [96] as a guideline to design the operating conditions for 47 ps input pulse widths. It was concluded that the fiber dispersion parameter D requires an increase by a factor of 16

(e.g., $D = 16 \times$ -0.7 ps/nm-km = -11.2 ps/nm-km). By increasing the fiber dispersion parameter, the combined effects of GVD and SPM provide a flatly broadened signal spectrum. The optimal fiber and signal parameters are: D = -8.3 ps/nm-km, γ = 10.5 $W^{-1}km^{-1}$, L = 3 km, and $1.5 < P_{0,in} < 1.7$ W.

The optimal slicing filter offset ($\Delta\lambda_{SPM} = 0.8$ nm) provides the greatest improvement in terms of the output signal ER and SNR. The slicing filter passband shape and bandwidth are selected to provide 10 Gb/s signals with practical output pulse widths. A slicing filter with a Gaussian shaped passband and bandwidth of 0.09 nm provides Gaussian shaped output signals with 42 ps pulse widths.

Chapter 5

Regenerator Performance

5.1 Introduction

In the two previous chapters, the performance of the retiming and reshaping stages was described. To fully assess the performance, the stages are combined to provide all-optical 3R regeneration (AO-3R). In this chapter, the system performance of AO-3R is evaluated experimentally within the context of: transmission impairments (Sect. 5.2), input signal properties (Sect. 5.3), and optical packets (Sect. 5.4). The system performance is evaluated in terms of the bit error rate (BER) at the receiver. Of particular interest in fiber-optic communication systems is the receiver sensitivity — the received optical power required to achieve a BER of 10^{-9}.

The experimental setup for AO-3R is provided in Fig. 5.1. The operating conditions for the input signal, retiming stage, and reshaping stage are listed in Tables 5.1 – 5.3. Unless otherwise stated, the operating conditions apply to all experiments described in this chapter.

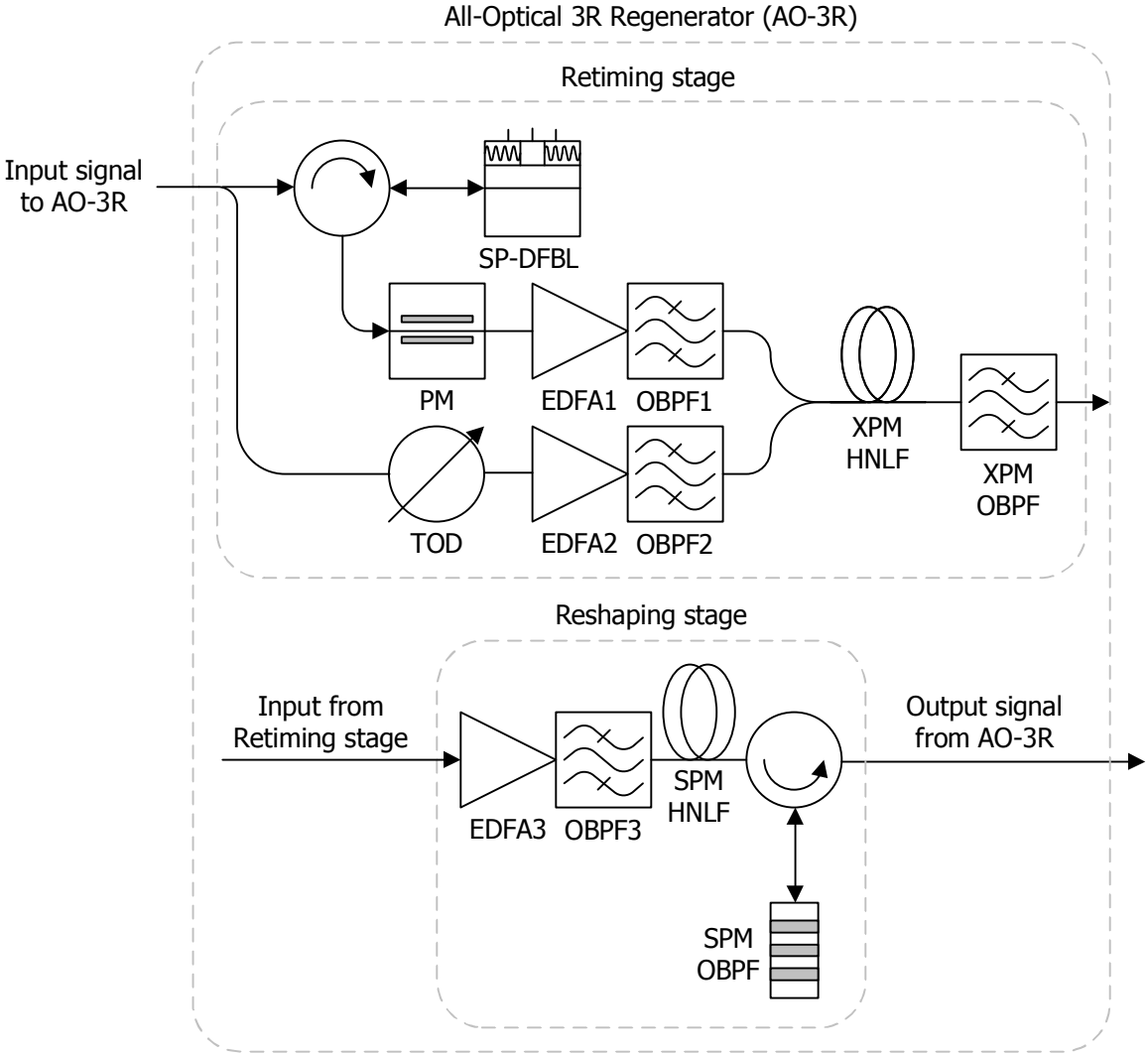

Figure 5.1: System performance: All-optical 3R regenerator (AO-3R) setup.

Parameter	Value	Units
Average input power	3.3	dBm
Pulse width	47	ps
Wavelength	1544.64	nm

Table 5.1: Operating conditions: Input signal.

Device	Parameter	Value	Units
SP-DFBL	Average input power	-1.5	dBm
	Temperature control	19.96	°C
	Current to laser section	88.23	mA
	Current to phase section	11.16	mA
	Current to reflector section	9.86	mA
PM	RF drive frequency	1	GHz
	RF drive amplitude (peak-to-peak)	9	V
EDFA1	Peak power of clock signal at input of XPM HNLF	150	mW
OBPF1	Center wavelength	1538.63	nm
	Bandwidth (-3 dB)	1.3	nm
TOD	Differential delay between clock and data signals at input of XPM HNLF	15	ps
EDFA2	Peak power of data signal at input of XPM HNLF	10	mW
OBPF2	Center wavelength	1544.64	nm
	Bandwidth (-3 dB)	0.25	nm
XPM HNLF	Length	4	km
	Attenuation	0.76	dB/km
	Nonlinearity	10.5	$W^{-1}km^{-1}$
	Dispersion	-0.3	ps/nm-km
	Dispersion slope	0.016	ps/nm^2-km
	Zero dispersion wavelength	1566	nm
XPM OBPF	Center wavelength	1544.80	nm
	Bandwidth (-3 dB)	0.25	nm

Table 5.2: Operating conditions: Retiming stage.

Device	Parameter	Value	Units
EDFA3	Peak power of data signal at input of SPM HNLF	1.5	W
OBPF3	Center wavelength	1544.80	nm
	Bandwidth (-3 dB)	0.55	nm
SPM HNLF	Length	3	km
	Attenuation	0.77	dB/km
	Nonlinearity	10.5	$W^{-1}km^{-1}$
	Dispersion	-8.3	ps/nm-km
	Dispersion slope	-0.009	ps/nm^2-km
SPM OBPF	Center wavelength	1543.97	nm
	Bandwidth (-3 dB)	0.09	nm

Table 5.3: Operating conditions: Reshaping stage.

5.2 Transmission Impairments

When optical signals are transmitted over long distances, their quality is degraded by transmission impairments. In this section the system performance of AO-3R is evaluated for the following transmission impairments: amplified spontaneous emission (ASE) noise (Sect. 5.2.1), group velocity dispersion (GVD) (Sect. 5.2.2), and polarization mode dispersion (PMD) (Sect. 5.2.3).

5.2.1 Amplified Spontaneous Emission Noise

Because of the inherent properties of optical fibers, signals are attenuated during transmission. Without compensation, the signal power is considerably reduced at the receiver. The receiver noise therefore has a greater impact and can degrade system performance. To compensate, in-line optical amplifiers (e.g., erbium-doped fiber amplifiers (EDFAs)) are used to increase the signal power during transmission.

However, optical amplifiers add noise to the signal through the process of amplified spontaneous emission (ASE). After multiple amplifications, the noise accumulates and can degrade system performance. Optical regenerators are used to prevent the noise from accumulating, thereby providing an improvement in system performance.

The experimental setup for assessing the effect of ASE noise on AO-3R performance is shown in Fig. 5.2. The section labeled *Transmission impairment (ASE)* indicates where the ASE noise is added to the signal. In this section, a variable optical attenuator (VOA1) provides the attenuation, an erbium-doped fiber amplifier (EDFA1) reamplifies the signal and adds ASE noise, and an optical bandpass filter (OBPF1) (0.55 nm bandwidth) limits the bandwidth of the noise. The attenuation provided by VOA1 controls the optical signal-to-noise ratio (OSNR), which provides a measure of the amount of ASE noise in the input signal.

To produce an input signal with a low OSNR (e.g., 20 dB), the power is reduced at the input of EDFA1 (e.g., -30 dBm). As a result, EDFA1 is unable to provide sufficient input signal power to AO-3R. To compensate, EDFA2 is used to further increase the signal power. Similar to OBPF1, OBPF2 (0.55 nm bandwidth) is used to limit the bandwidth of the noise. Since the output power of EDFA2 depends on its input power (which varies with VOA1) a second attenuator (VOA2) is used to control the power of the input signal to AO-3R. The polarization controller (PC) is used to control the state-of-polarization (SOP) of the input signal. For this experiment, both the average power and SOP of the input signal are kept constant.

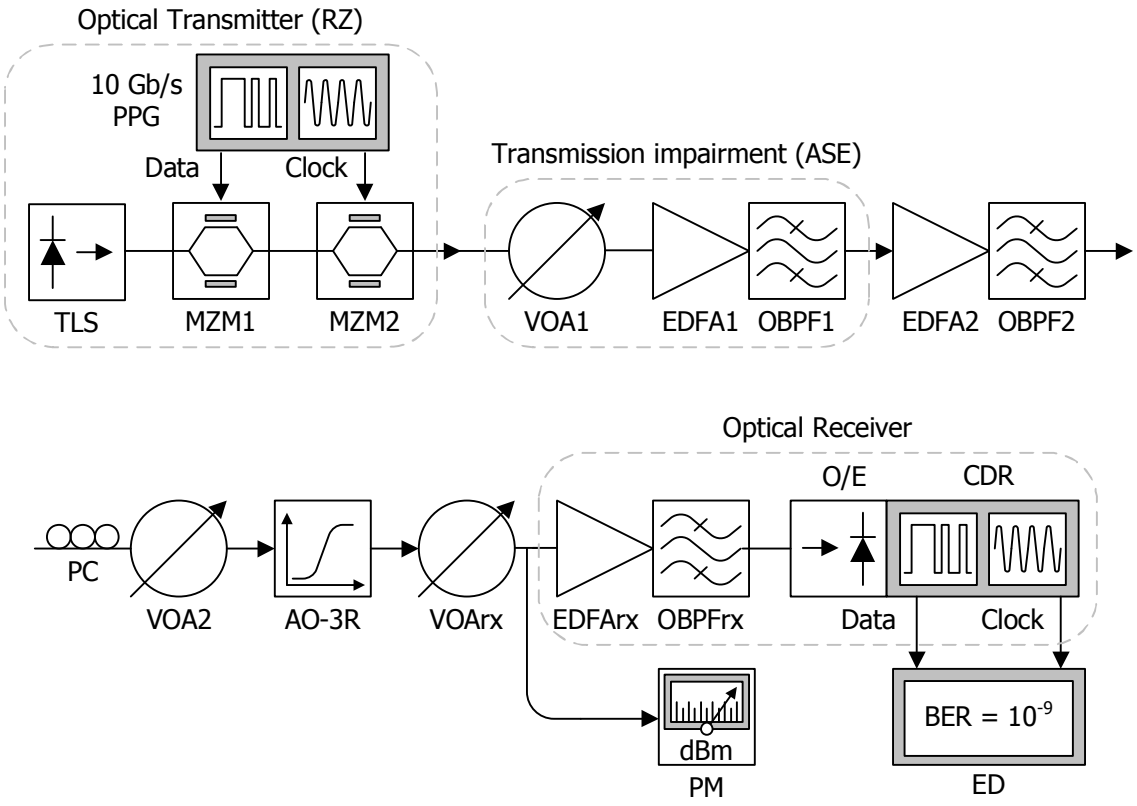

Figure 5.2: Effect of ASE noise: System setup.

The OSNR is measured at the input of AO-3R using an optical spectrum analyzer (OSA) (resolution bandwidth = 0.1 nm). In general, the OSNR at the output of AO-3R can not be accurately measured since the spectral slicing filter passband defines the output signal spectrum and suppresses out-of-band ASE noise. Instead, the (electrical) signal-to-noise ratio (SNR) is more readily obtained at the output of AO-3R. The SNR is measured using a digital communication analyzer (DCA) (electrical bandwidth = 55 GHz). The dependence of the output signal SNR on the input signal OSNR is shown in Fig. 5.3. As a reference, the input signal SNR is also indicated.

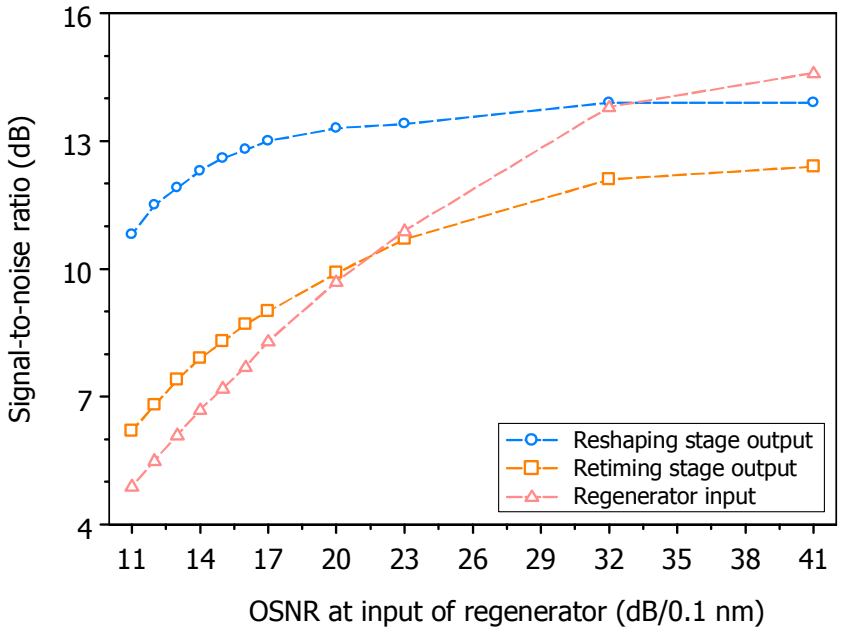

Figure 5.3: Effect of ASE noise: Dependence of output SNR on input OSNR.

The intent of the retiming stage is to reduce timing jitter in the output signal. However, the retiming stage can also reduce amplitude noise, thereby improving the output signal SNR. This is achieved by narrow-band filtering (OBPF2) of wide-band input signal ASE noise. In particular, the retiming stage output signal improves the SNR when the input signal OSNR $<$ 22 dB. However, when in-band ASE noise dominates, the retiming stage can no longer provide an improvement to the output signal SNR (e.g., input signal OSNR $>$ 22 dB). In fact, because of amplification in the retiming stage (EDFA1,2), added ASE noise degrades the retiming stage output signal SNR.

The reshaping stage compensates by reducing the impact of ASE noise, thereby improving the output signal SNR. As an example, consider eye diagrams for an input

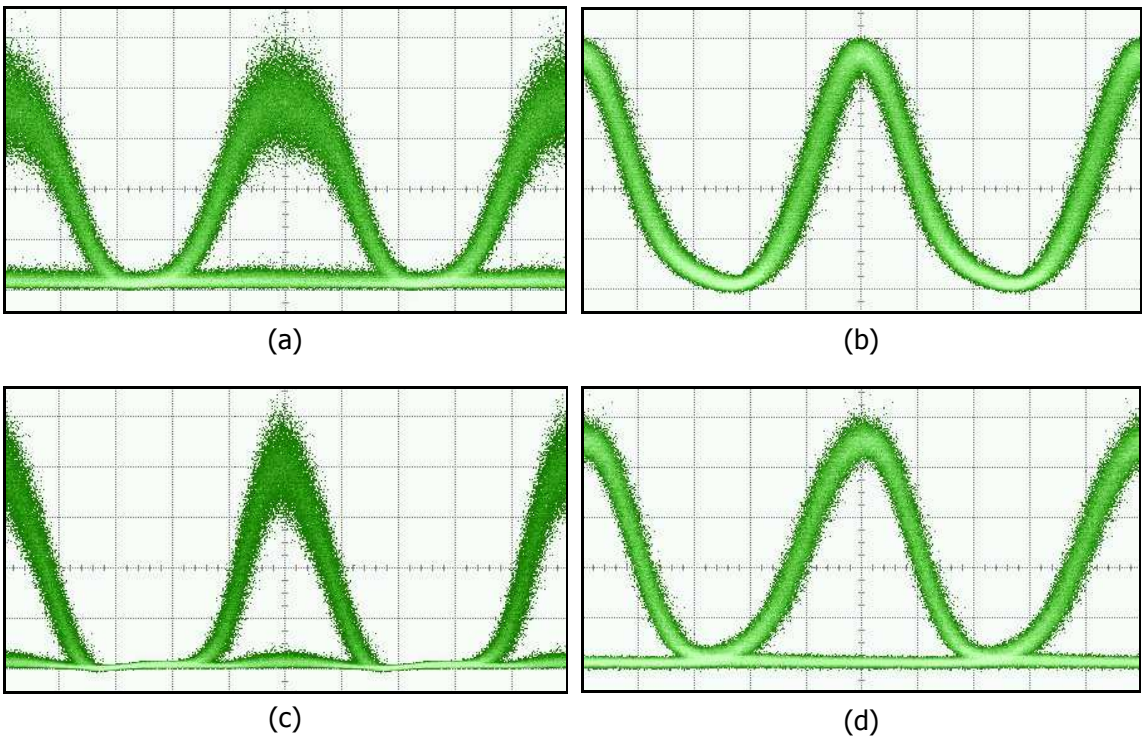

Figure 5.4: Effect of ASE noise: Eye diagrams for OSNR = 17 dB at (a) AO-3R input, (b) recovered clock signal, (c) retiming stage output, and (d) reshaping stage output (AO-3R output) (20 ps/div).

signal with OSNR = 17 dB (Fig. 5.4). The input signal exhibits amplitude variations due to ASE noise (Fig. 5.4a), which remain in the retiming stage output signal (Fig. 5.4c). The reshaping stage output signal exhibits reduced amplitude variations (Fig. 5.4d). As a result, the reshaping stage output signal provides an SNR improvement of 4.7 dB (8.3 to 13 dB). The improvement in output signal SNR is determined by the slope of the power transfer characteristic (PTC) (see Fig. 4.16). For AO-3R, the maximum output signal SNR = 13.9 dB (Fig. 5.3).

The system performance of AO-3R is measured in terms of the BER at the receiver. The transmitted (input) signal is a $2^{31}-1$ pseudorandom bit sequence (PRBS).

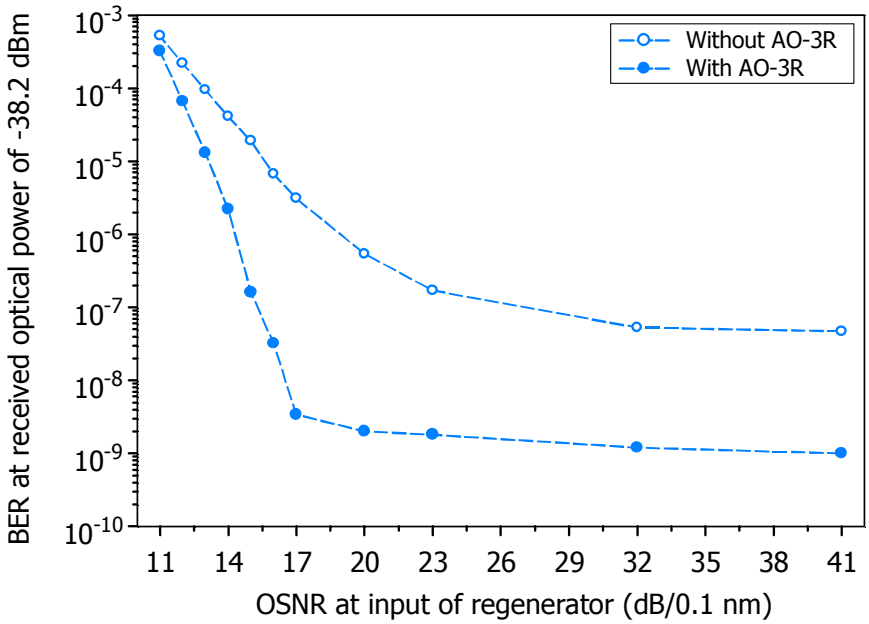

Figure 5.5: Effect of ASE noise: BER versus OSNR.

The received signal is detected using a preamplified optical receiver setup (Fig. 5.2): VOArx controls the received optical power, EDFArx amplifies the received optical signal, OBPFrx (0.25 nm bandwidth) limits the bandwidth of the optical noise, and an optical receiver provides optical-to-electrical (OE) conversion and clock/data recovery (CDR). The electrical clock and data signals are connected to an error detector (ED) for measurement of the BER. The received optical power, corresponding to a specific BER, is measured using an optical power meter (PM).

The BER versus input signal OSNR for a fixed received optical power is shown Fig. 5.5. The BER improvement provided by AO-3R depends on the input signal OSNR. When the input signal OSNR $>$ 32 dB, AO-3R provides a constant improvement in the BER. The BER is improved because AO-3R improves the output signal extinction ratio (ER). For example, when the input signal OSNR $=$ 32 dB, the output

signal ER is improved by 4.6 dB (16.9 to 21.5 dB).

When the input signal OSNR is in the range of 17 < OSNR < 32 dB, AO-3R further improves the BER. The BER is further improved because the AO-3R increases the output signal SNR. For example, when the input signal OSNR = 17 dB, the output signal SNR is improved by 4.7 dB (8.3 to 13 dB).

However, when input signal OSNR < 17 dB, the BER improvement provided by AO-3R is reduced. This can be explained by the fundamental limitation of optical regenerators. With the exception of [82], regenerators can only reduce the probability of bit errors from occurring *after* the regenerator. In other words, if a bit is in error before the regenerator, it is still in error after the regenerator. As the input signal OSNR is degraded, the probability of bit errors incurred before the AO-3R increases, thereby reducing the BER improvement that AO-3R can provide.

The BER versus received optical power is shown in Fig. 5.6. As described in the introduction, the receiver sensitivity at BER = 10^{-9} is of interest for evaluation of system performance. For an input signal OSNR range of 24 dB (17 to 41 dB), the difference in receiver sensitivity between AO-3R signals is only 0.4 dB. This indicates that AO-3R provides excellent resilience to ASE noise.

The receiver sensitivity versus input signal OSNR is shown in Fig. 5.7. AO-3R provides an improvement in receiver sensitivity of up to 4.5 dB (-33.6 to -38.1 dBm) for an input signal OSNR = 17 dB. However, when the input OSNR < 17 dB, AO-3R can not achieve BER = 10^{-9}. This is because a BER floor (i.e., BER > 10^{-9}) is observed without AO-3R. Therefore, to provide a receiver sensitivity improvement at BER = 10^{-9}, the input signal OSNR should not be less than 17 dB. For an ASE noise limited system, this criteria can be used to determine AO-3R spacing in the network.

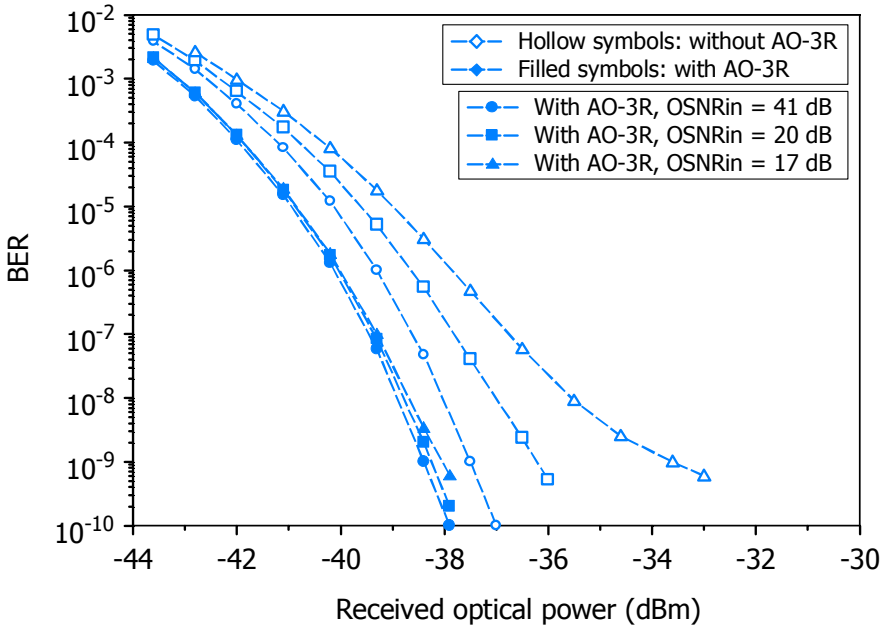

Figure 5.6: Effect of ASE noise: BER versus received optical power.

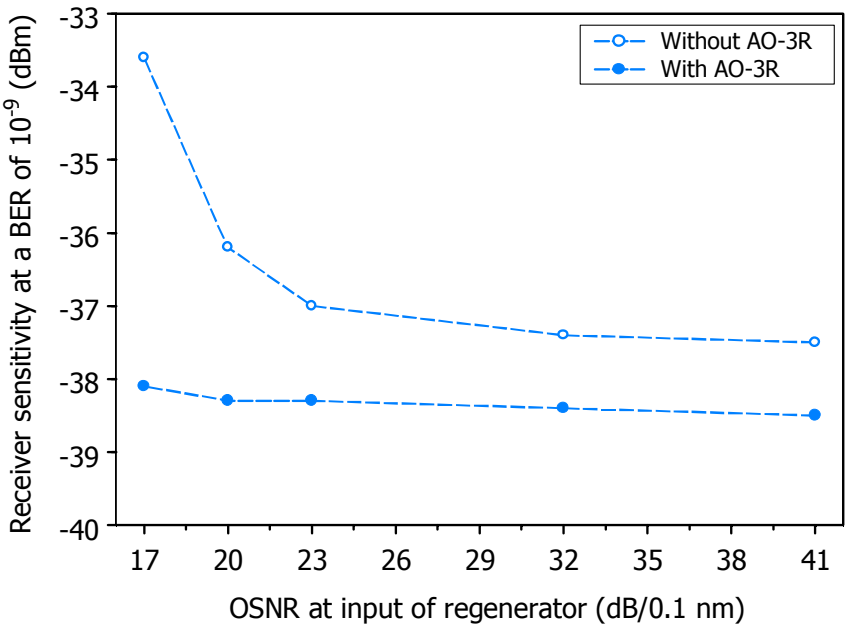

Figure 5.7: Effect of ASE noise: Receiver sensitivity versus OSNR.

5.2.2 Group Velocity Dispersion

Like ASE noise, group velocity dispersion (GVD) is a common impairment in optical transmission systems. The impairment is caused by material and waveguide properties of optical fibers and manifests as a differential delay between frequency components in the optical signal. In the time domain, GVD causes pulses that represent bits of information to spread during propagation. When pulses spread into adjacent bit slots they can induce inter-symbol interference (ISI), which can lead to a degradation in the BER at the receiver.

In optical networks, dispersion maps provide an effective means of coping with GVD. In this approach, positive and negative dispersive fiber spans are alternated, such that the net dispersion for the span is zero. For systems that use multiple carrier wavelengths (i.e., WDM), the net dispersion per span is intentionally made nonzero to reduce the impact of nonlinear effects, such as four-wave mixing (FWM) and cross-phase modulation (XPM). The residual dispersion per span (RDPS) is given by

$$RDPS = D_+L_+ + D_-L_- \tag{5.1}$$

where D is the dispersion parameter and L is the fiber length. The +/- subscripts refer to positive and negative dispersive fibers. When the RDPS is the same from span-to-span, the dispersion map is known as singly periodic. In this type of map, the net residual dispersion (RD) of the link is the RDPS times the number of spans. In general, pre- and/or post-dispersion compensation is employed such that the net RD of the link is zero for all wavelengths at the receiver. This approach is effective for dispersion compensation when the net RD is known ahead of time.

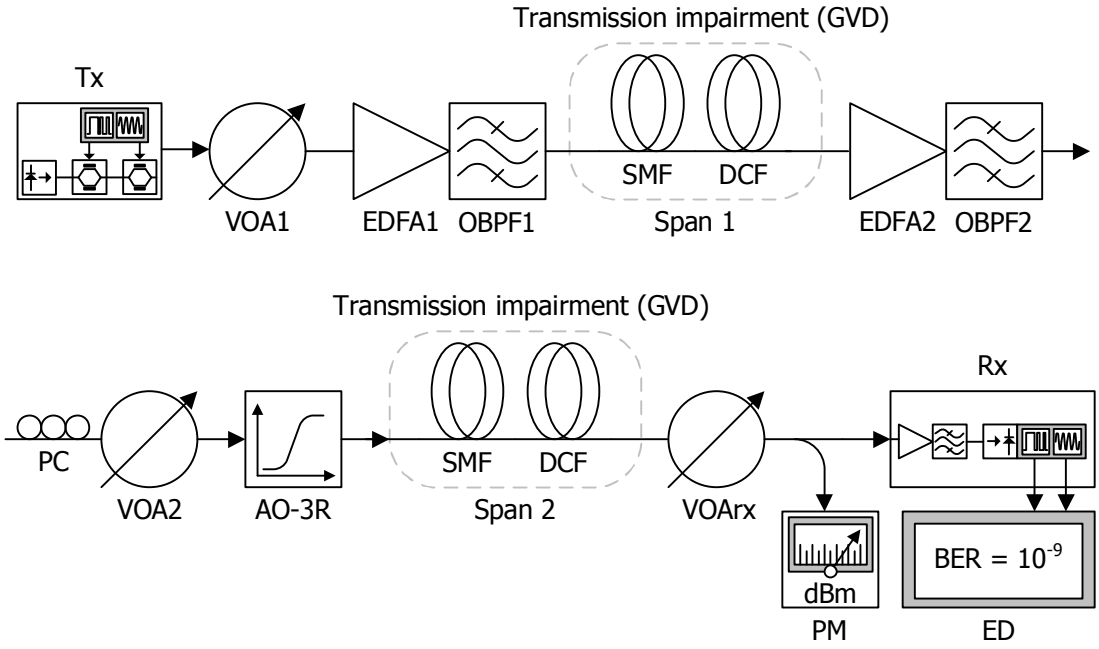

Figure 5.8: Effect of GVD: System setup.

In agile all-photonic networks (AAPNs), optical packets are dynamically routed through different transmission paths in the network. As a result, optical signals may propagate across a different number of fiber spans. The net RD may therefore not be known ahead of time, resulting in imperfect dispersion compensation at the receiver. Over multiple routing paths, the RD can accumulate and lead to significant ISI, which ultimately degrades the BER. Optical regenerators can improve system performance by preventing the effects of RD from accumulating.

The experimental setup for assessing the effect of RD on AO-3R performance is shown in Fig. 5.8. The setup is similar to the one used for the ASE noise experiments (Fig. 5.2), except that in these experiments the transmission impairment is provided by RD before (span 1) and after (span 2) the regenerator, indicated by the sections labeled *Transmission impairment (GVD)*. The RD before and after AO-3R is varied by

combining different lengths of single-mode fiber (SMF) and dispersion compensating fiber (DCF).

To limit the effect of ASE noise, VOA1 is set to 0 dB. An average power of 1 dBm is launched into span 1. The launch power is intentionally low in order to limit the stimulation of nonlinear effects in the fiber (e.g., SPM). PC and VOA2 are used, respectively, to keep the input signal SOP and average power constant. After AO-3R, an average power of 1 dBm is retransmitted into span 2. At the end of span 2, the signal is detected using the same preamplified receiver setup as in the ASE noise experiments (Fig. 5.2).

Using this setup, the BER versus received optical power is measured at the receiver for both negative and positive RD. The RDs before and after AO-3R (i.e., span 1 and span 2) are denoted by RD1 and RD2, respectively. BER results for three cases when RD1 is negative are shown in Fig. 5.9. In the first case, RD1 = -303 ps/nm and RD2 = 340 ps/nm (total link RD = 37 ps/nm). This represents the case when the link dispersion is almost completely compensated. In this case, AO-3R provides a receiver sensitivity improvement of 0.9 dB (-37.5 to -38.4 dBm). This is in good agreement with the 1 dB receiver sensitivity improvement measured for an input signal OSNR = 41 dB with RD = 0 (i.e., back-to-back) (Fig. 5.6).

In the second case, RD1 = -133 ps/nm and RD2 = -303 ps/nm (total link RD = -436 ps/nm). Because the total link RD is increased, without AO-3R there is a power penalty of 0.7 dB (-37.5 to -36.8 dBm). With AO-3R, the receiver sensitivity is improved by 0.4 dB (-36.8 to -37.2 dBm). The relatively small improvement occurs because RD1 is not large enough to cause significant ISI. When RD1 increases, the ISI increases and the improvement provided by AO-3R becomes more evident.

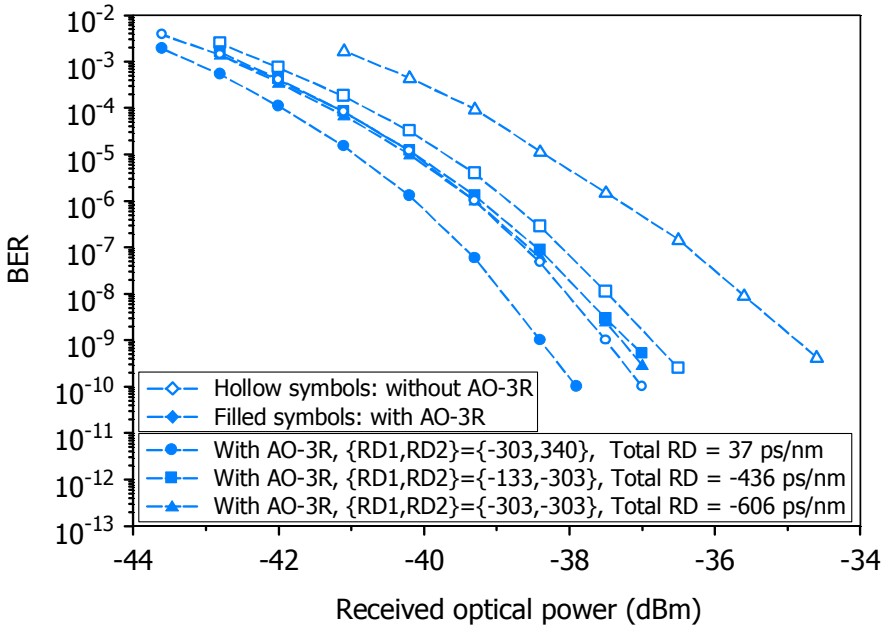

Figure 5.9: Effect of GVD: Negative RD. BER versus received optical power.

In the third case, RD1 is increased to -303 ps/nm and RD2 remains at -303 ps/nm (total link RD = -606 ps/nm). Since RD1 is increased, the power penalty without regeneration increases to 2.6 dB (-37.5 to -34.9 dBm). With regeneration, the receiver sensitivity is improved by 2.3 dB (-34.9 to -37.2 dBm). Even though the link RD increases by 130 ps/nm (-436 to -606 ps/nm), the regenerator performance is not degraded. The performance is consistent since the regenerator reshapes the waveform distortion caused by RD1. Therefore, after regeneration the signals are equally reshaped. Since RD2 (i.e., 303 ps/nm) is the same in both cases, its impact on the regenerator's system performance is the same.

To help visualize how the regenerator improves system performance for the case RD1 = RD2 = -303 ps/nm, consider the eye diagrams shown in Fig. 5.10. Because of residual dispersion (RD), the transmitted signal (Fig. 5.10a) becomes distorted after

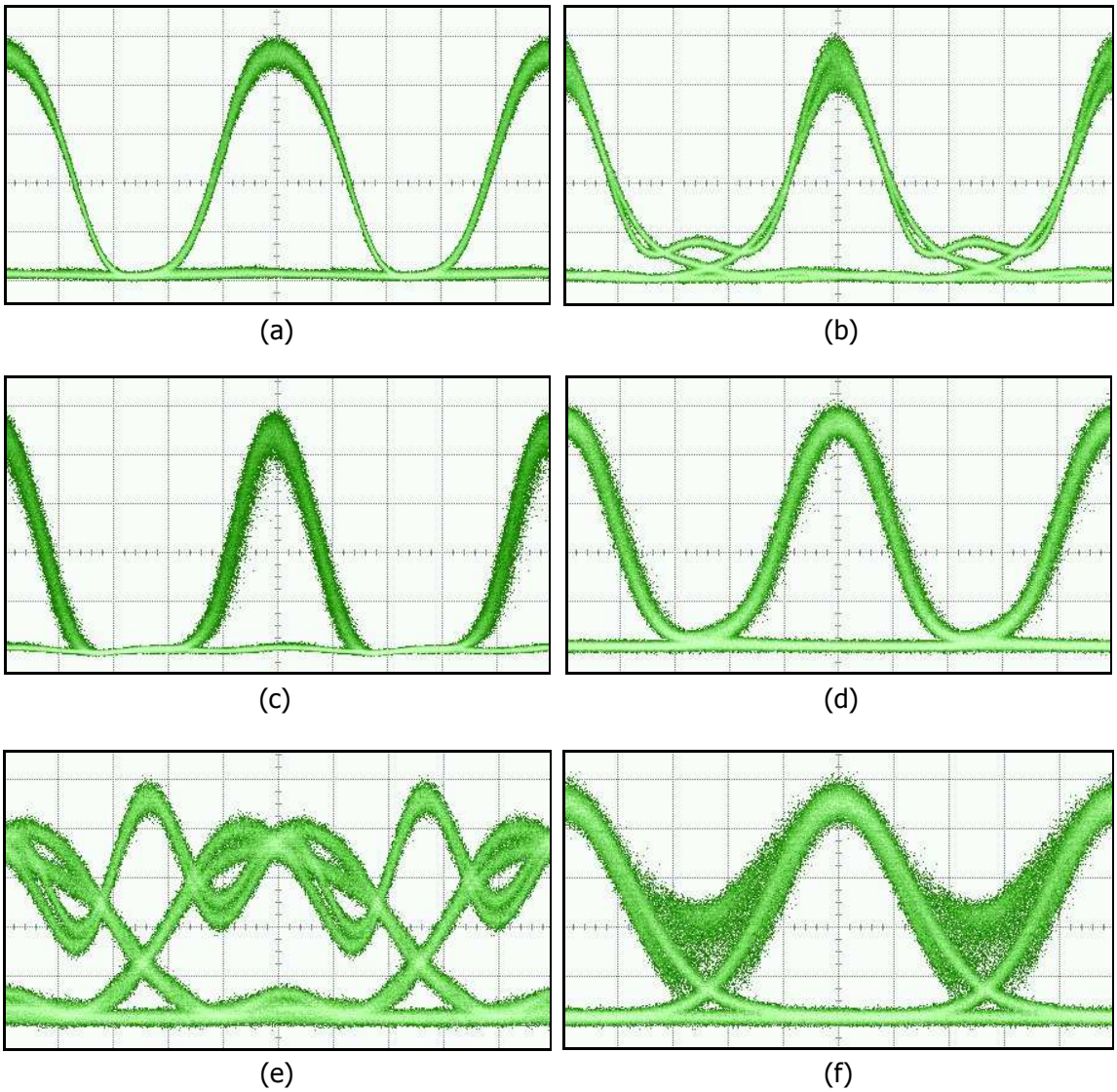

Figure 5.10: Effect of GVD: Negative RD. Eye diagrams for RD1 = -303 ps/nm, RD2 = -303 ps/nm at (a) transmitter, (b) after span 1, (c) after retiming stage, (d) after reshaping stage (AO-3R output), and (e) after span 2 without and (f) with AO-3R (20 ps/div).

span 1 (Fig. 5.10b). Without AO-3R, signal distortion accumulates, leading to ISI induced eye closure at the end of span 2 (Fig. 5.10e). With AO-3R between spans, the distortion caused by span 1 is removed by the regenerator through signal reshaping (Fig. 5.10c-d)). Since the reshaping is performed after span 1, signal distortion caused by span 2 has less of an impact on ISI induced eye closure. As a result, with AO-3R the eye is more open at the end of span 2 (Fig. 5.10f).

An interesting observation can be made by considering where the reshaping of waveform distortion takes place. In this particular case, the retiming stage provides reshaping of the distorted input waveform (Fig. 5.10c). The waveform reshaping is provided by the spectral slicing of the XPM broadened signal spectrum, where the pulse shape of the sliced signal is determined by the shape of the slicing filter passband. By reshaping the input waveform in the retiming stage, two advantages are realized.

First, since XPM is induced by intensity variations in the optical clock signal, the XPM spectral broadening is independent of intensity variations in the input signal (i.e., waveform distortion). Second, since the output of the retiming stage serves as the input to the reshaping stage, the self-phase modulation (SPM) spectral broadening is also independent of input waveform distortion. This is especially important for the reshaping stage since SPM based regenerators are typically sensitive to the input pulse shape [82]. Since the performance of the retiming and reshaping stages are independent of input waveform distortion, an argument can be made that AO-3R performance is not dependent on the input signal pulse shape. This is a highly desirable property for AO-3R since the input pulse shape may vary in practical systems due the properties of the transmitter (e.g., modulator bias voltage), network elements (e.g., bandwidth), or the fiber itself (e.g., dispersion).

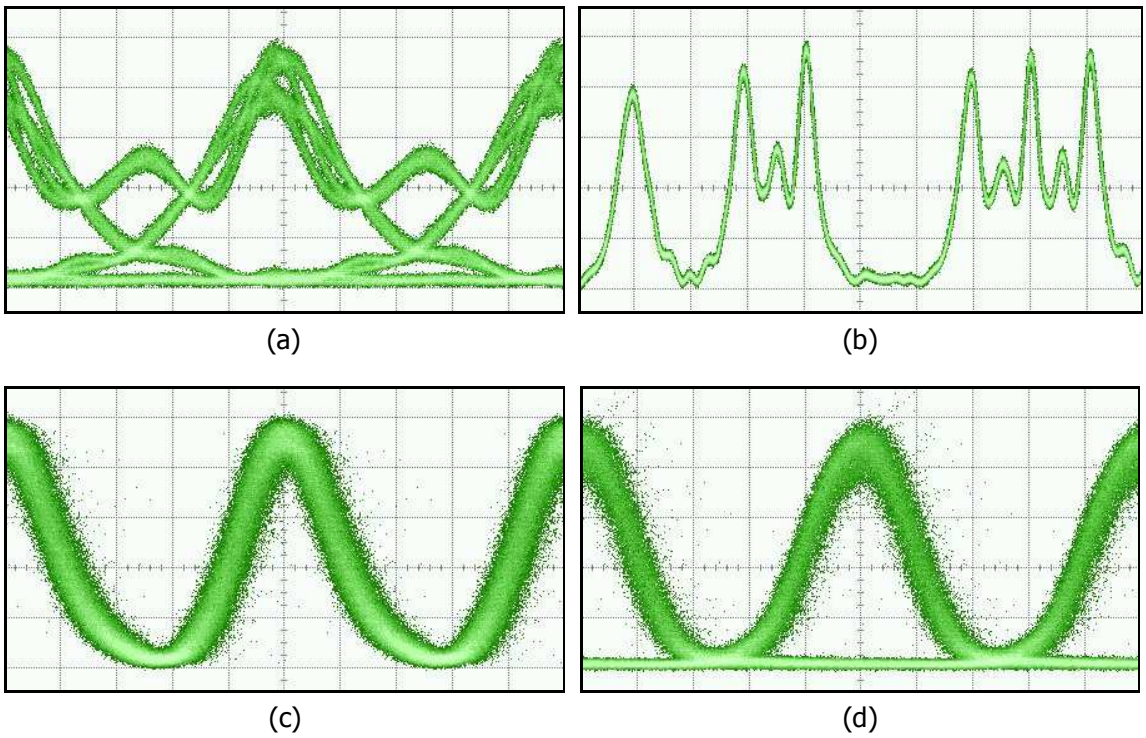

Figure 5.11: Effect of GVD: Excess RD. Eye diagrams for RD1 = 510 ps/nm at (a) input eye (20 ps/div), (b) input pattern (100 ps/div), (c) recovered clock signal (20 ps/div), and (d) AO-3R output (20 ps/div).

However, since the recovered clock signal jitter is sensitive to the input pulse width [104], AO-3R preformance is limited by clock recovery. For example, consider the eye diagrams for RD1 = 510 ps/nm shown in Fig. 5.11. When the input signal is distorted, its modulation depth is reduced (Fig. 5.11a-b). As a result, the amplitude of the clock frequency of the input signal is reduced, preventing the self-pulsating distributed feedback laser (SP-DFBL) from completely locking. This prevents the clock signal from suppressing the intrinsic timing jitter of self-pulsation (Fig. 5.11c). The clock signal jitter is translated to the output signal (Fig. 5.11d), potentially leading to significant power penalties at the receiver (e.g., BER floor).

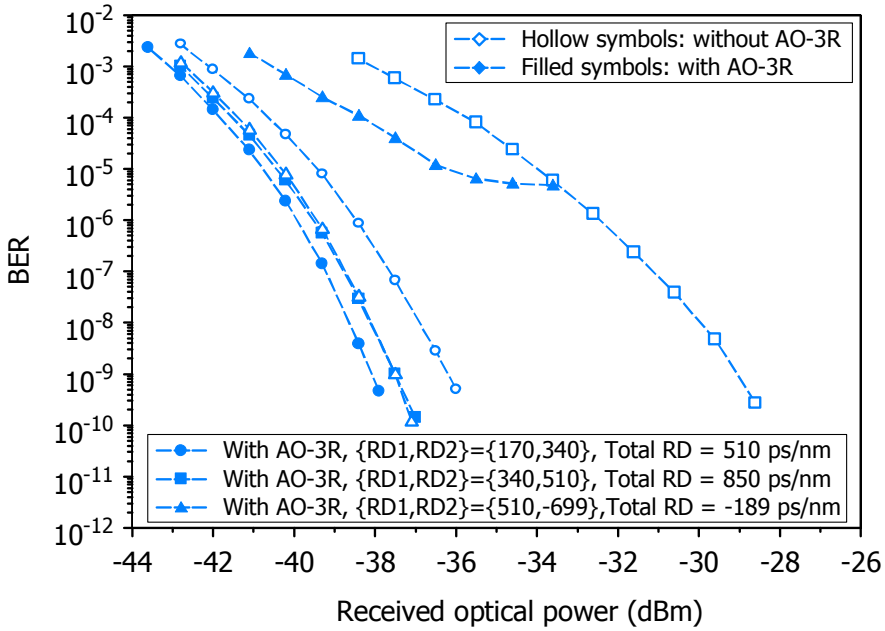

Figure 5.12: Effect of GVD: Positive RD. BER versus received optical power.

An example of a BER floor caused by an increase in clock signal jitter from input signal waveform distortion is shown in Fig. 5.12. In this example, RD1 = 510 ps/nm and RD2 = -699 ps/nm (total link RD = -189 ps/nm). Compared to near perfect dispersion compensation (e.g., Fig. 5.9), without AO-3R the power penalty is negligible. However, because of an increase in clock signal jitter, with AO-3R the system performance is degraded since the output signal jitter induces a BER floor (BER = 10^{-5}).

Provided RD1 < 510 ps/nm, AO-3R provides an improvement in system performance. In the case where RD1 = 170 ps/nm and RD2 = 340 ps/nm (total link RD = 510 ps/nm), AO-3R provides a receiver sensitivity improvement of 1.9 dB (-36.2 to -38.1 dBm). As the total link RD increases, the receiver sensitivity improvement provided by AO-3R increases. For example, in the case where RD1 = 340 ps/nm and

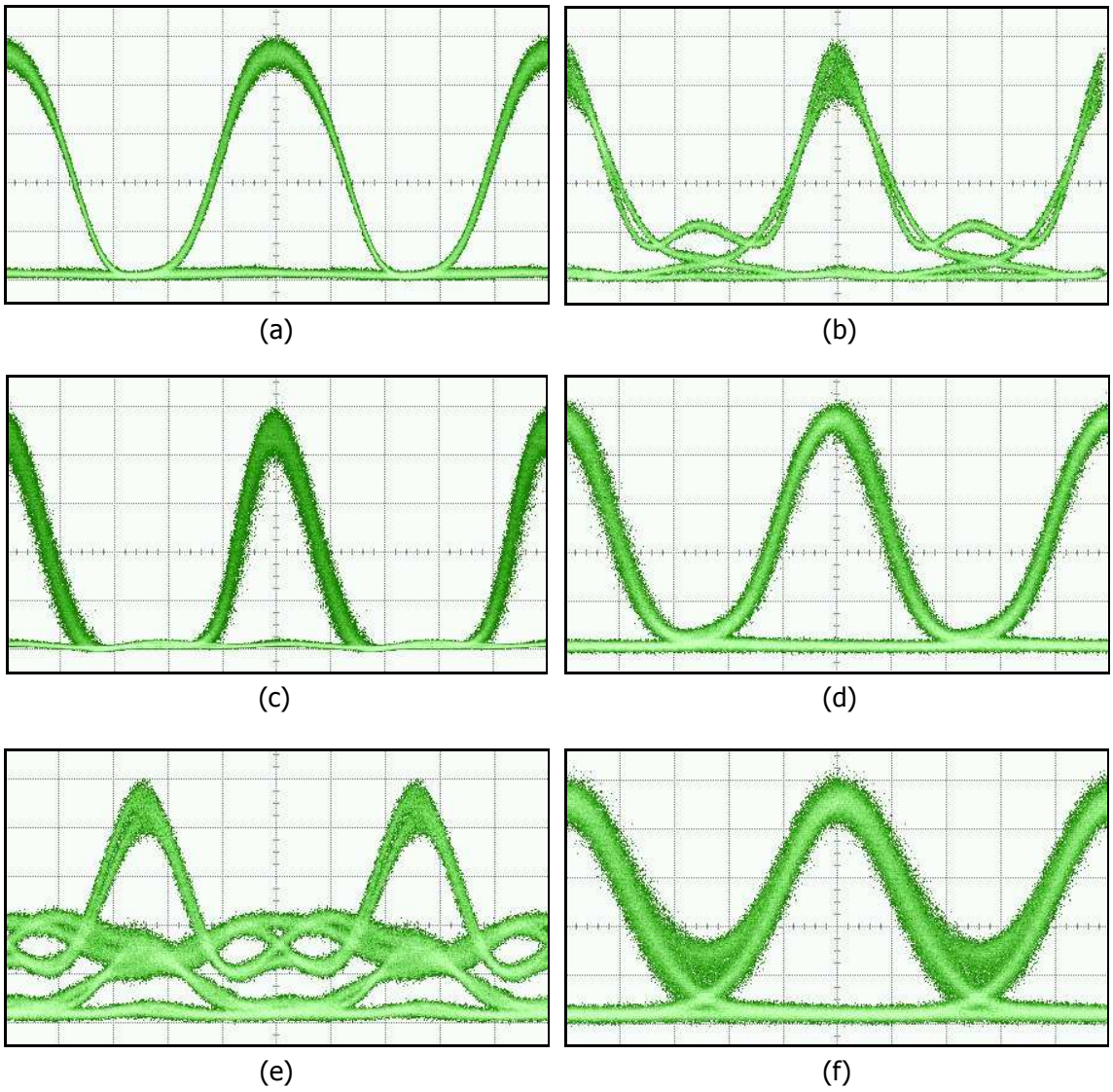

Figure 5.13: Effect of GVD: Positive RD. Eye diagrams for RD1 = 340 ps/nm, RD2 = 510 ps/nm at (a) transmitter, (b) after span 1, (c) after retiming stage, (d) after reshaping stage (AO-3R output), and (e) after span 2 without and (f) with AO-3R (20 ps/div).

RD2 = 510 ps/nm (total link RD = 850 ps/nm), AO-3R provides a receiver sensitivity improvement of 7.4 dB (-29.1 to -36.5 dBm). The eye diagrams for this case are shown in Fig. 5.13. The results are similar, but more dramatic, than the results shown in Fig. 5.10. Without AO-3R considerable waveform distortion accumulates, leading to significant eye closure at the end of span 2 (Fig. 5.13e). With AO-3R the signal is reshaped after span 1 (Fig. 5.13c-d), thereby reducing the accumulated waveform distortion after span 2. As a result, with AO-3R the eye is much more open at the end of span 2 (Fig. 5.13f), indicating an improvement in system performance.

The ability of AO-3R to improve system performance is limited by the input signal RD (i.e., RD1). When the input signal RD is within the range of -303 ps/nm $<$ RD1 $<$ 340 ps/nm, AO-3R provides an improvement in system performance. The input signal RD range is limited by the ability of clock recovery to provide a clock signal with low timing jitter (e.g., 2 ps rms). It can be speculated that the input signal RD range in which AO-3R can provide an improvement in system performance may be extended with the use of a clock recovery technique that is more robust to input signal waveform distortion.

5.2.3 Polarization Mode Dispersion

Similar to GVD, PMD is a type of dispersion common in optical transmission systems. Because of imperfect manufacturing of optical fibers and environmental stresses, the cylindrical core of fibers are not perfectly symmetric. As a result, optical fibers exhibit birefringence, causing the two polarization modes to experience a different refractive index and therefore propagate at different group velocities. This leads to a differential

group delay (DGD) between polarization modes and manifests as pulse broadening. Like GVD, PMD induced pulse broadening can lead to waveform distortion and inter-symbol interference (ISI), increasing the likelihood that bits are detected in error at the receiver.

To reduce penalties at the receiver, considerable research effort has been focused on techniques for PMD compensation [105]. The techniques often require adaptive control to compensate for PMD since temperature variations and mechanical vibrations cause PMD to vary with time. The rate at which PMD varies depends on the environmental influences, causing PMD to vary on different timescales [106]. Typically, the fastest variation occurs on a millisecond timescale for aerial fibers [107] and patchchords interconnecting equipment. Providing adaptive PMD compensation on such a short timescale presents a sizable challenge [108]. In AAPNs, the challenge is even greater since PMD may vary on a microsecond timescale from packet-to-packet. Optical regenerators that are capable of regenerating signals impaired by PMD are therefore a considerable asset to AAPNs.

The experimental setup for assessing the effect of PMD on AO-3R performance is shown in Fig. 5.14. The setup is similar to the one used for the ASE noise experiments (Fig. 5.2), except that in this case the transmission impairment is provided by a PMD emulator (PMDE) at the input of AO-3R. The PMDE controls the DGD between the two polarization modes. In practical systems, DGD is equivalent to the average PMD of the transmission link.

In the PMD experiments, the effect of ASE noise is limited by setting VOA1 to 0 dB. The PC is used to keep the input signal SOP to the PMD emulator constant at 45° so that the power is divided equally between the two polarization modes. When

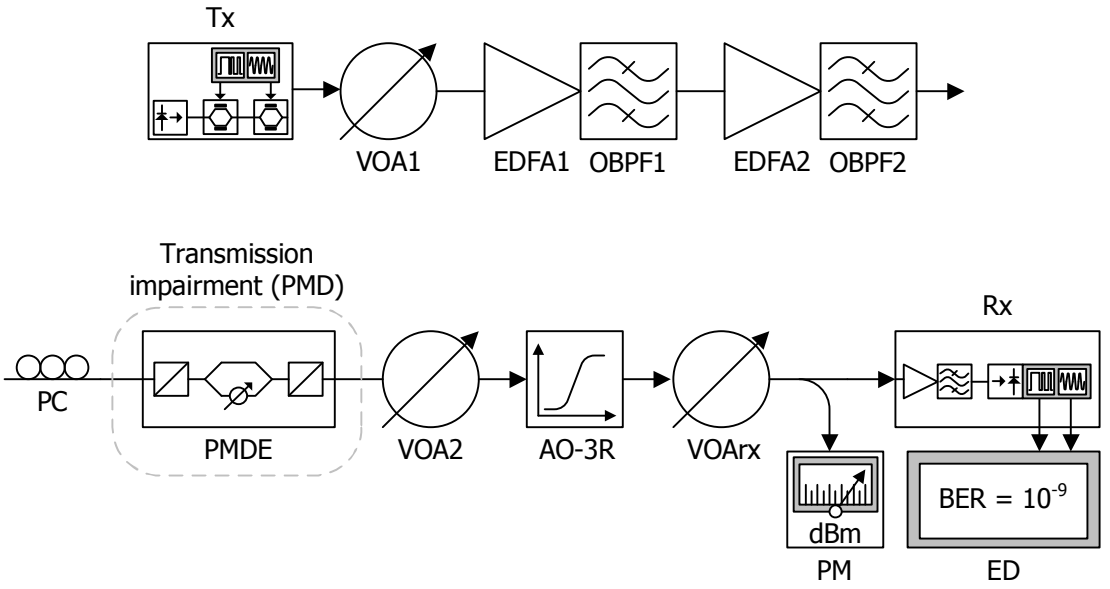

Figure 5.14: Effect of PMD: System setup.

the power in the two polarization modes are equal, PMD is in its worst case [109]. After PMD emulation, VOA2 is used to keep the average input signal power constant.

The effect of PMD is measured in terms of the receiver sensitivity for different amounts of DGD. The results for receiver sensitivity versus DGD are shown in Fig. 5.15. Without AO-3R a power penalty is observed when DGD $>$ 25 ps. For example, when DGD $=$ 35 ps a power penalty of 0.7 dB is observed. The results are in good agreement with published results on power penalty versus DGD [110]. From the published results, when the DGD $>$ 35 ps, the power penalty increases exponentially, reaching 2 dB for DGD $=$ 50 ps [110]. With AO-3R a slight improvement in receiver sensitivity is observed when the DGD $<$ 25 ps. Because the input signal does not show ISI, the receiver sensitivity improvement does not come from reshaping, but rather from an increase in the ER after AO-3R.

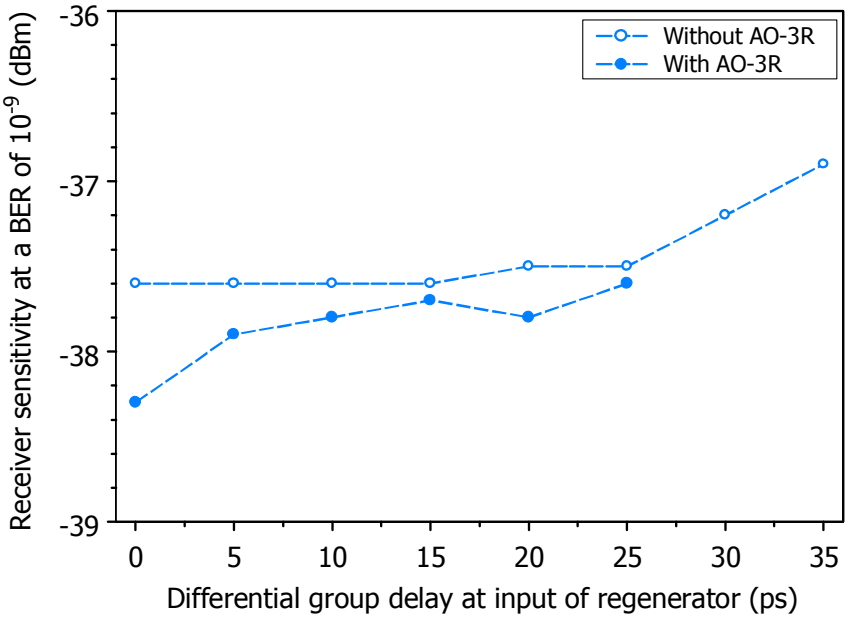

Figure 5.15: Effect of PMD: Receiver sensitivity versus DGD.

For $0 <$ DGD < 25 ps, the regenerated signals show a receiver sensitivity variation of 0.7 dB (-38.3 to -27.6 dB). The variation can be attributed to the slight polarization sensitivity of AO-3R and the sensitivity of clock recovery to the input pulse width [104]. In terms of polarization sensitivity, mechanical vibrations in the polarization mode dispersion emulator (PMDE) cause the input signal SOP to vary randomly over time. When the input signal SOP varies, AO-3R is found to have a power penalty of less than 1 dB (see Sect. 5.3.1).

The more significant contributor to the power penalty comes from the sensitivity of clock signal jitter to input signal DGD. The power penalty induced by jitter may be significant. For example, when the DGD $= 30$ ps, without AO-3R the power penalty relative to DGD $= 0$ ps is 0.4 dB. With AO-3R the jitter induces a BER floor

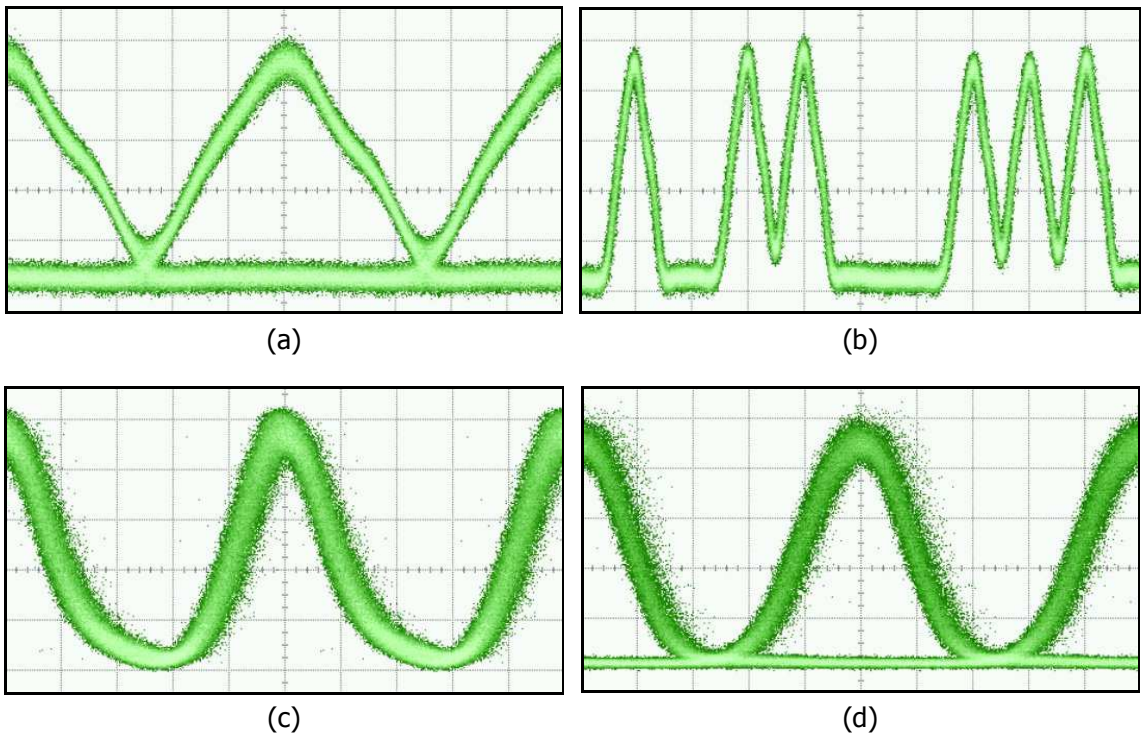

Figure 5.16: Effect of PMD: Eye diagrams DGD = 30 ps at (a) input eye (20 ps/div), (b) input pattern (100 ps/div), (c) recovered clock signal (20 ps/div), and (d) AO-3R output (20 ps/div).

(BER = 10^{-5})[1].

The increase in clock signal jitter can be attributed to pulse broadening of the input signal induced by DGD (Fig. 5.16a). Despite the fact that the input pulse width increases, compared to the case for RD, the signal waveform retains its modulation depth (Fig. 5.16b). However, the self-pulsation (SP) frequency shifts in time during the modulation of carriers in the lasing section of the SP-DFBL when the input pulse width increases. This causes the clock signal jitter to increase (Fig. 5.16c) and leads to an increase in the regenerated (output) signal jitter (Fig. 5.16d).

[1]The clock signal jitter that induces a BER floor is too large to accurately measure on the DCA.

Because of the sensitivity of clock recovery to the input pulse width, AO-3R is not able to provide an improvement in system performance when the DGD $>$ 25 ps. The implications of increased pulse width are significant, as the recovered clock signal jitter can lead to a BER floor at the receiver. Even though the clock recovery is limiting, AO-3R is still able to reshape waveform distortion caused by DGD (Fig. 5.16d). Using a similar argument to the one made for GVD, it is reasonable to speculate that a clock recovery technique that is more robust to the input pulse width can potentially enable the regeneration of signals with larger amounts of PMD.

5.3 Input Signal Properties

AO-3R provides a means of coping with transmission impairments common in transport networks. For AAPNs, AO-3R should also be able to cope with variable packet-to-packet changes in input signal properties. In this section the system performance of AO-3R is evaluated for the following input signal properties: state-of-polarization (SOP) (Sect. 5.3.1), average power (Sect. 5.3.2), and wavelength (Sect. 5.3.3).

5.3.1 Input State-of-Polarization

Because of environmental influences, the SOP of optical signals is generally unknown and varies randomly with time. Like PMD, the SOP can vary on a millisecond timescale [106]. In AAPNs, the variation may be more rapid since the SOP may vary from packet-to-packet (microsecond timescale). Optical regenerators must therefore be able to cope with rapid changes in the SOP of input signals. Since SOP tracking from packet-to-packet is not practical in the near term, it is critical that regenerators

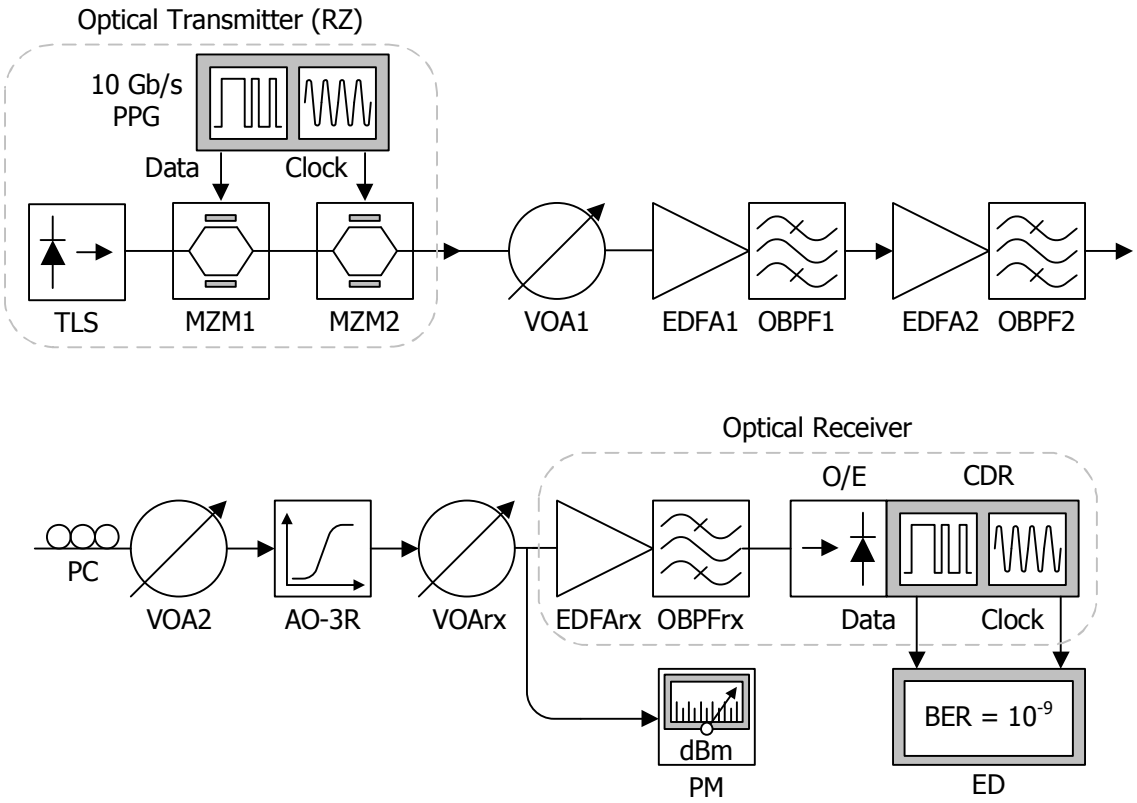

Figure 5.17: Effect of input signal properties: System setup.

not be dependent on the SOP of input signals.

The polarization sensitivity of AO-3R is governed by the sensitivity of the regeneration stages to the input signal SOP. The retiming stage relies on XPM, which is a polarization dependent effect, however, with proper selection of the design parameters the retiming can be made polarization insensitive (Sect. 3.4). The reshaping stage relies on SPM, which is a polarization independent effect, therefore, the reshaping is inherently polarization insensitive. Combined, the two stages are designed to enable polarization insensitive AO-3R.

Index	S1	S2	S3
1	0.70	-0.55	0.46
2	0.45	0.39	0.81
3	-0.60	0.80	0.01
4	-0.06	-0.61	0.79
5	0.34	-0.15	-0.91
6	0.34	0.94	-0.11
7	-1.00	0.04	-0.04
8	-0.64	-0.11	-0.76

Table 5.4: Effect of input SOP: Table of input SOPs.

The experimental setup for assessing the effect of input signal SOP on AO-3R performance is shown in Fig. 5.17. VOA1 is used to control the input signal OSNR. VOA2 is used to keep the average input signal power constant. PC is used to control the input signal SOP, which is variable in this set of experiments.

In this experiment, AO-3R properties are measured for variable input signal SOPs. To provide a representative sample, eight input signal SOPs are selected, one from each octant on the Poincaré sphere. The index used to reference the SOPs, along with the corresponding Stokes parameters (S1, S2, S3) are listed in Table 5.4.

The dependence of AO-3R properties (timing jitter, ER, and SNR) on the input signal SOPs are measured using a DCA (electrical bandwidth = 55 GHz). For the measurements, the input signal OSNR = 14 dB. The dependence of output signal timing jitter on input signal SOP is shown in Fig. 5.18. The input signal timing jitter (i.e., 3.4 ps) is reduced by the recovered clock signal. The clock signal shows low sensitivity to the input signal SOP. The retiming stage output signal has the same jitter as the clock signal. The reshaping stage output signal retains the retiming, as

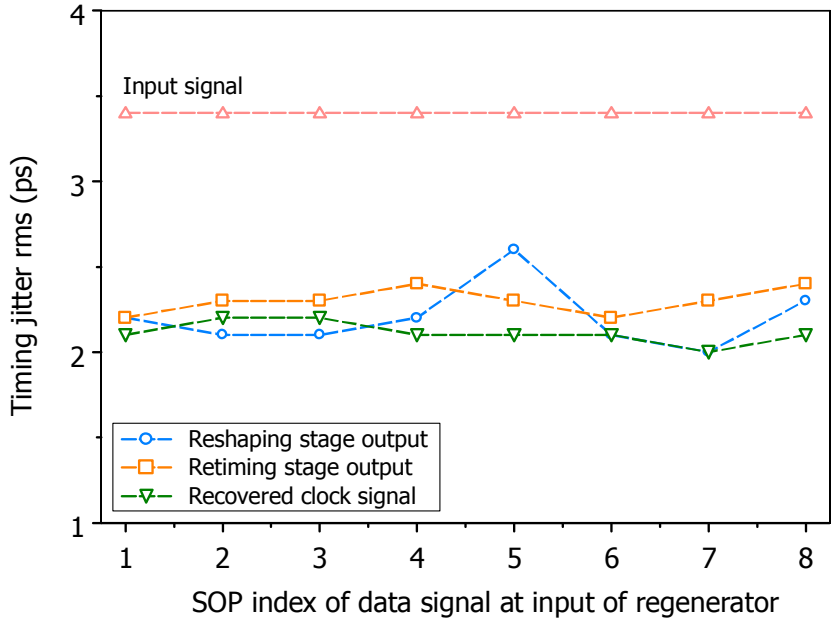

Figure 5.18: Dependence of output timing jitter on input SOP.

an increase in jitter is not observed.

The dependence of output signal ER and SNR on the input signal SOP are shown in Figs. 5.19 and 5.20, respectively. Similar to timing jitter, the ER shows low sensitivity to the input signal SOP. For example, the retiming stage output signal ER varies by less than 1 dB (21.0 to 21.7 dB) with input signal SOP (Fig. 5.19). The SNR shows a slightly higher sensitivity to the input signal SOP. When the XPM spectrum is sliced, small variations in the signal translate to variations in the SPM broadened signal spectrum. When the SPM spectrum is sliced, spectral variations translate into amplitude variations. As a result, the reshaping stage output signal SNR shows varies by 1.8 dB (9.6 to 11.4 dB) with input signal SOP.

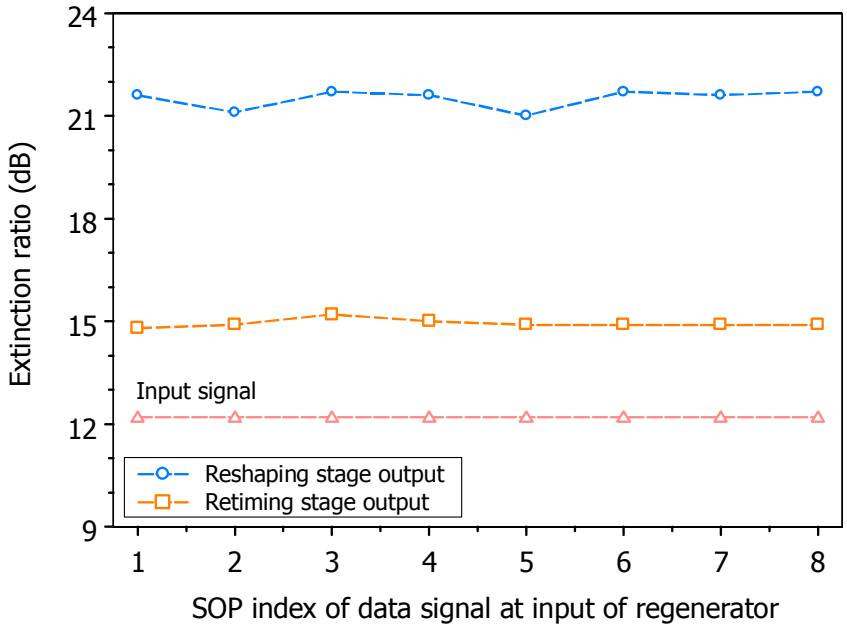

Figure 5.19: Dependence of output ER on input SOP.

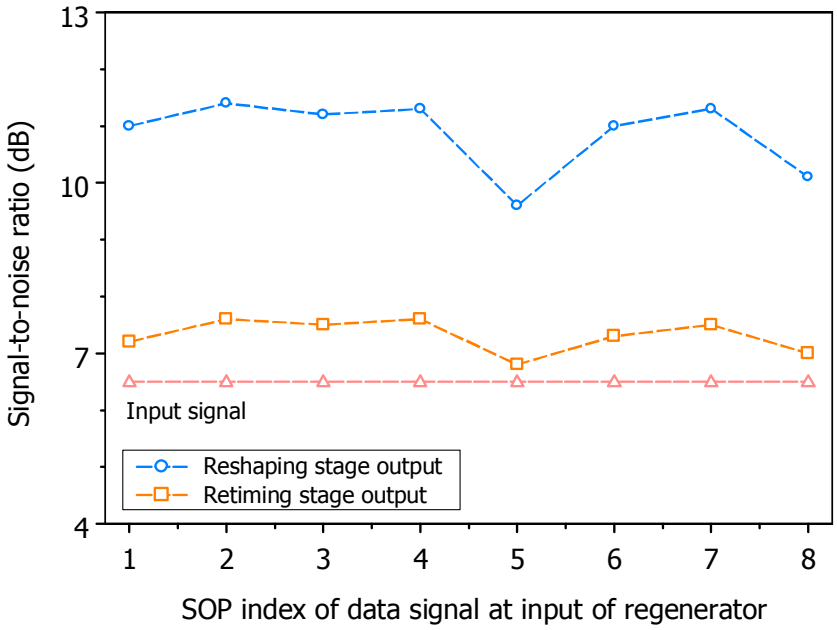

Figure 5.20: Dependence of output SNR on input SOP.

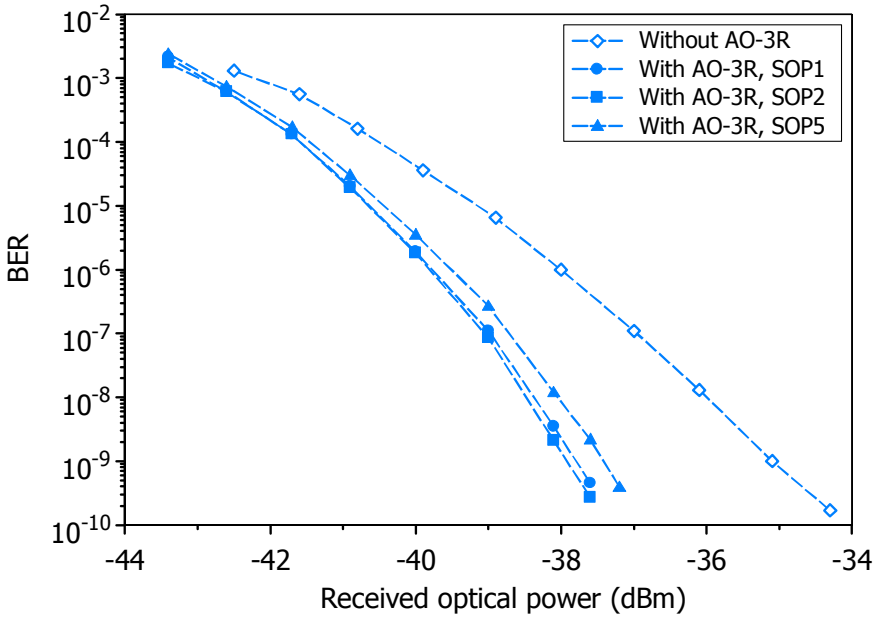

Figure 5.21: Effect of input SOP: BER versus received optical power.

The BER versus received optical power for an input signal OSNR = 19 dB is shown in Fig. 5.21. The measurement is performed for three input signal SOPs. The input signal SOPs are chosen to produce minimum (SOP5), intermediate (SOP1), and maximum (SOP2) sliced signal power from the XPM broadened signal spectrum (i.e., output of retiming stage). For the three input SOPs, the receiver sensitivity of AO-3R differs by only 0.5 dB (-37.9 to -37.5 dBm). The result is in good agreement with the other five input SOPs (Fig. 5.22). This confirms that the power penalty due to the input signal polarization is at most 0.5 dB. To achieve this level of performance, it is critical that the operating conditions of AO-3R be properly selected. In particular, for low polarization sensitivity the most important design parameter is the offset wavelength of the XPM slicing filter (Sect. 3.4).

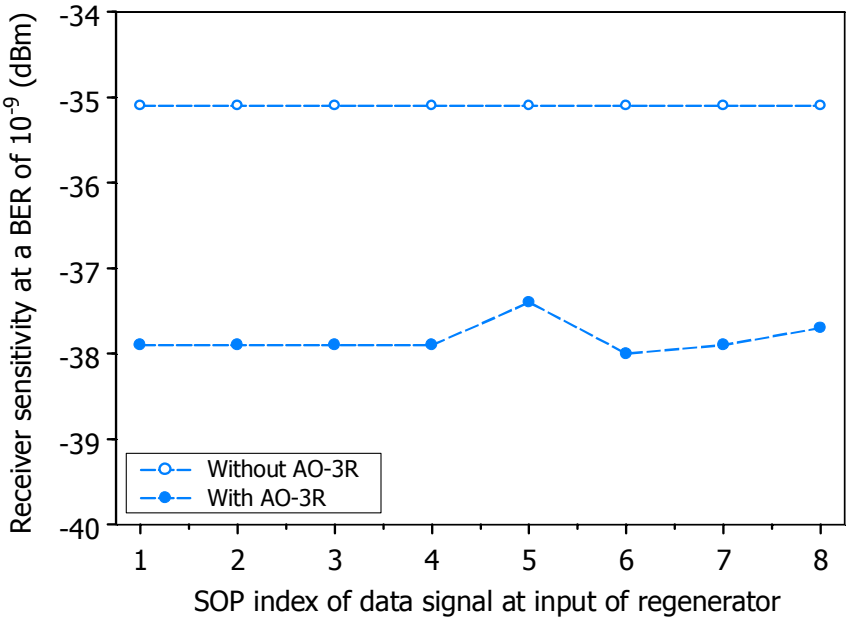

Figure 5.22: Effect of input SOP: Receiver sensitivity versus input SOP.

5.3.2 Average Input Power

In AAPNs, optical packets are routed through different transmission paths. As a result, the packets experience different amounts of attenuation. Therefore, like the SOP, the average power of signals input to regenerators may vary from packet-to-packet. Optical regenerators should therefore be able to cope with a range of input signal powers.

The experimental setup for assessing the effect of average input signal power on AO-3R performance is the same as the setup used for the effect of input signal SOP (Fig. 5.17). In this case, the input signal SOP is kept constant and the average input signal power is varied. For the measurements, the input signal OSNR = 14 dB and timing jitter = 3.8 ps. The dependence of output signal timing jitter on average input signal power is shown in Fig. 5.18. The clock shows a dependence on the input signal

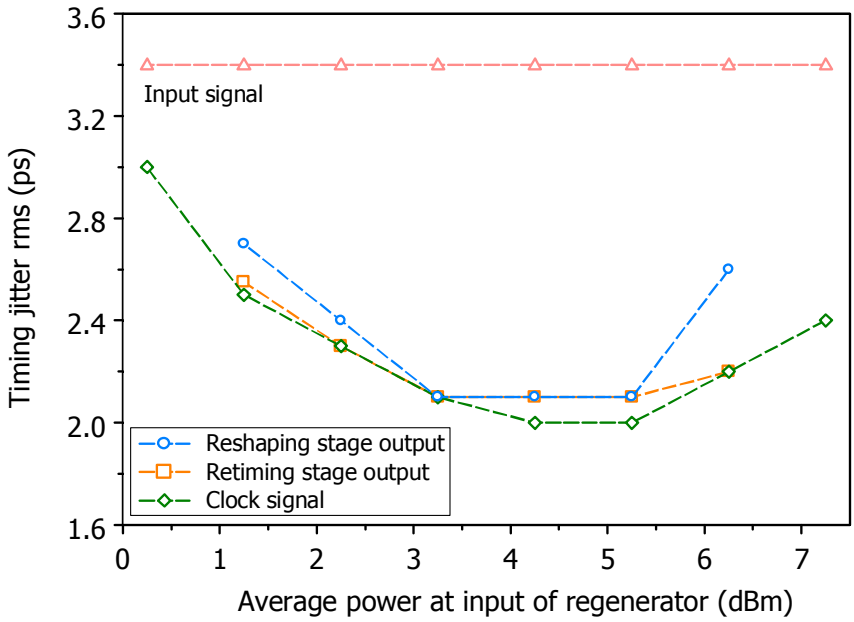

Figure 5.23: Dependence of output timing jitter on average input power.

power, where the minimum clock signal jitter (2.0 ps) is achieved for an input signal power of 4.3 dBm. The clock signal jitter increases when the input signal power is low since carriers in the lasing section of the SP-DFBL are not sufficiently modulated [104]. For high input signal power, the clock signal jitter increases because high input power disrupts the refractive index in the reflector section of the SP-DFBL [104]. The output signal jitter follows the clock signal and therefore exhibits the same dependence on the average input signal power.

The dependence of the output signal ER and SNR on the average input signal power are shown in Figs. 5.24 and 5.25, respectively. The retiming stage output signal ER and SNR are insensitive to the average input signal power since XPM is induced by the clock signal. However, since the average XPM sliced signal power varies with average input signal power, the input signal power to the reshaping stage also varies. This may

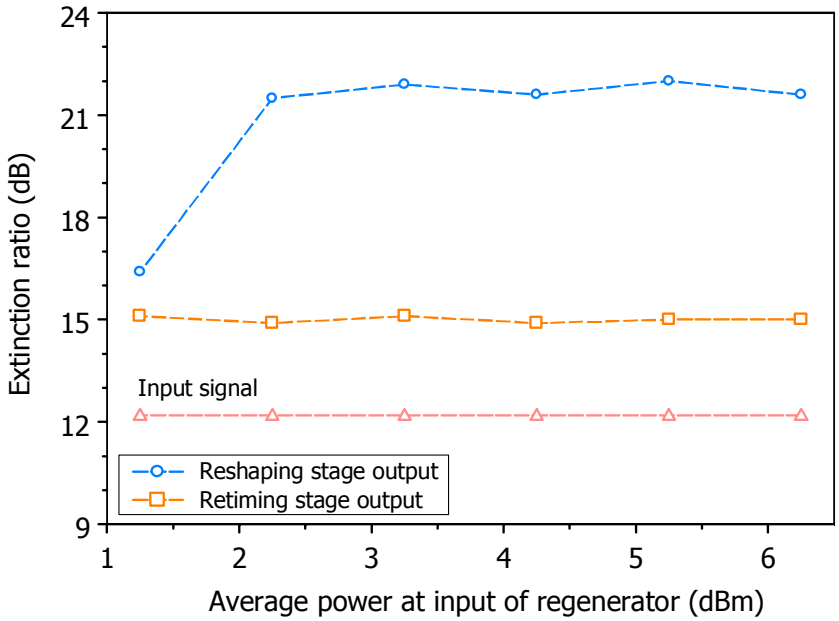

Figure 5.24: Dependence of output ER on average input power.

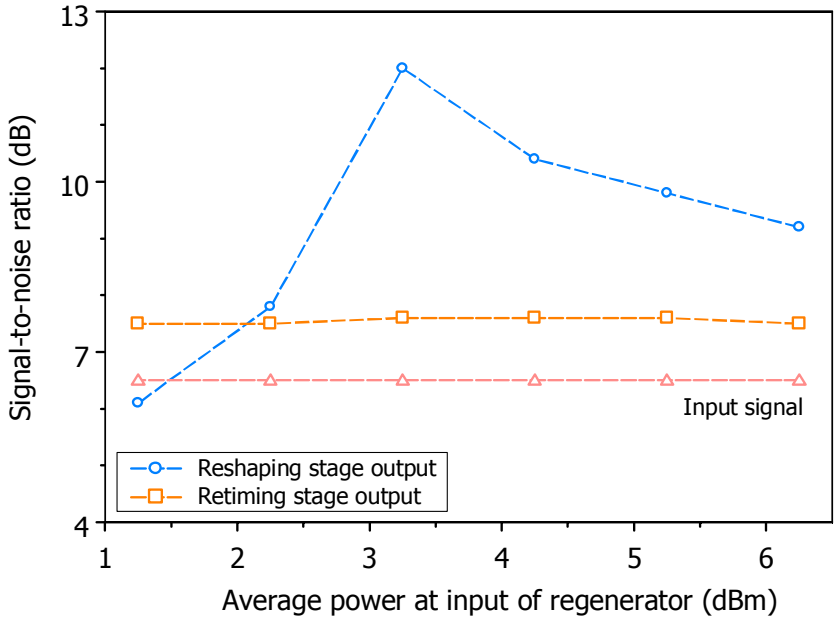

Figure 5.25: Dependence of output SNR on average input power.

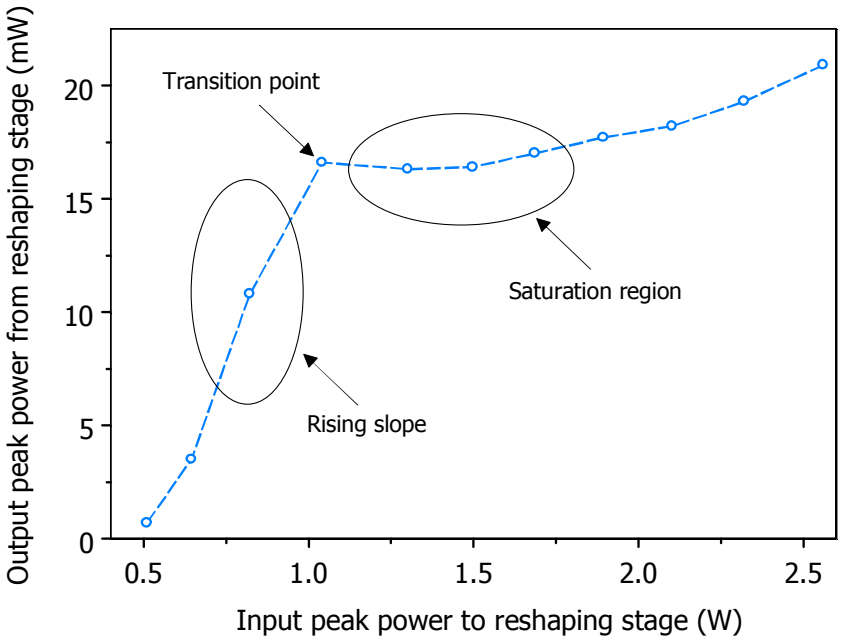

Figure 5.26: Power transfer characteristic of reshaping stage.

cause sub-optimal operating conditions in terms of the power transfer characteristics (Fig. 5.26), reducing the achievable output signal ER and SNR.

For example, when the input signal power $<$ 2.3 dBm, the reshaping stage is operating on the rising slope of the its PTC. This reduces the achievable output signal ER and SNR. The ER is reduced since because the output signal 1-level decreases when the input power resides on the rising slope compared to the saturation region. The SNR is reduced since amplitude variations (noise) in the 1-level are not suppressed on the rising slope. In general, when the slope $S_{PTC} < 1$, AO-3R reduces 1-level noise, improving the SNR. Whereas, when $S_{PTC} > 1$, AO-3R increases 1-level noise, degrading the SNR. The latter occurs when the input power resides on the rising slope. This is the case for an input signal power of 1.3 dBm since the 1-level noise is increased in the output signal (Fig. 5.27b).

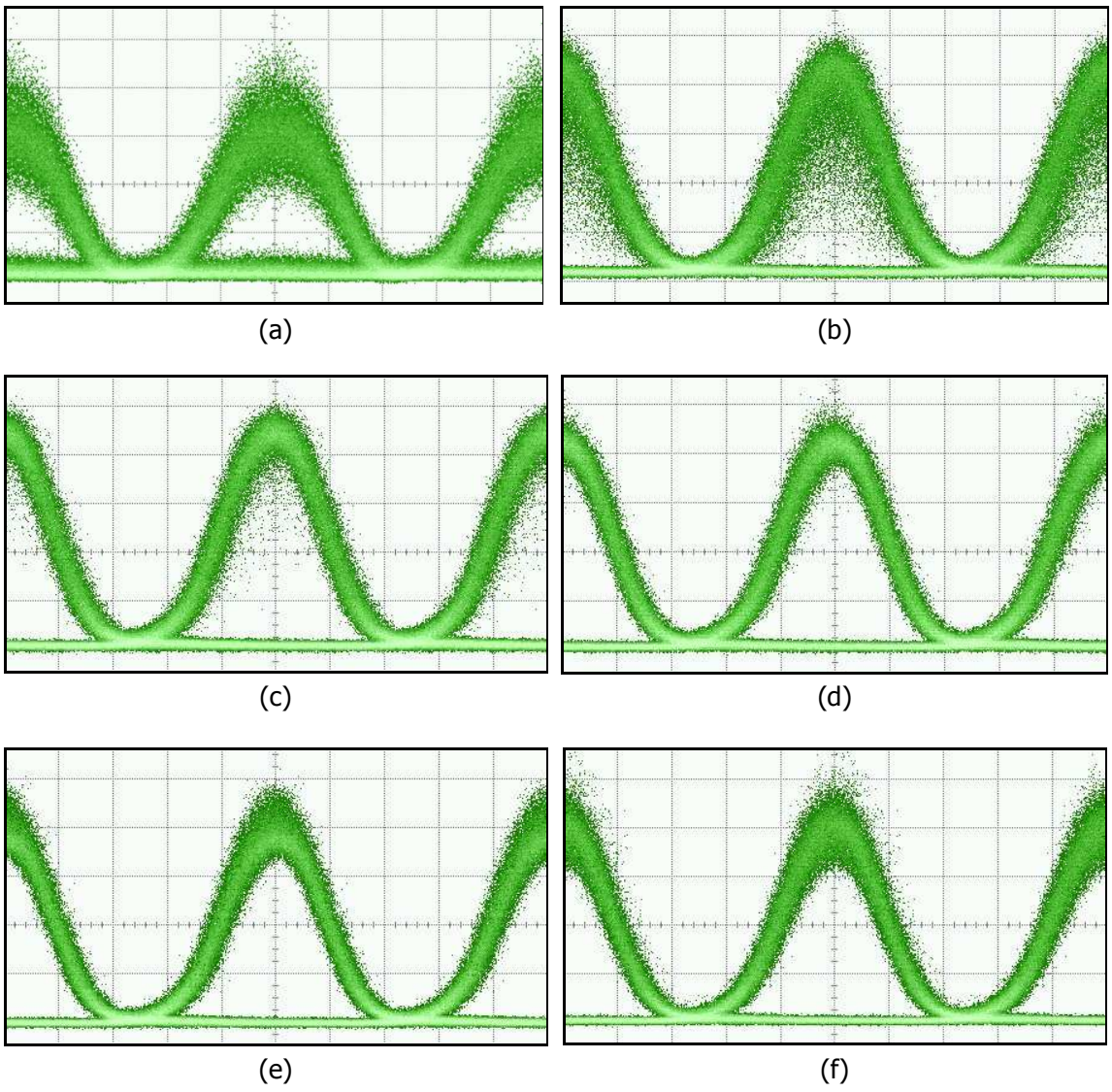

Figure 5.27: Effect of average input power: Eye diagrams at (a) input and (b-f) output of AO-3R for input power: (b) 1.3 dBm, (c) 2.3 dBm, (d) 3.3 dBm, (e) 4.3 dBm, and (f) 5.3 dBm.

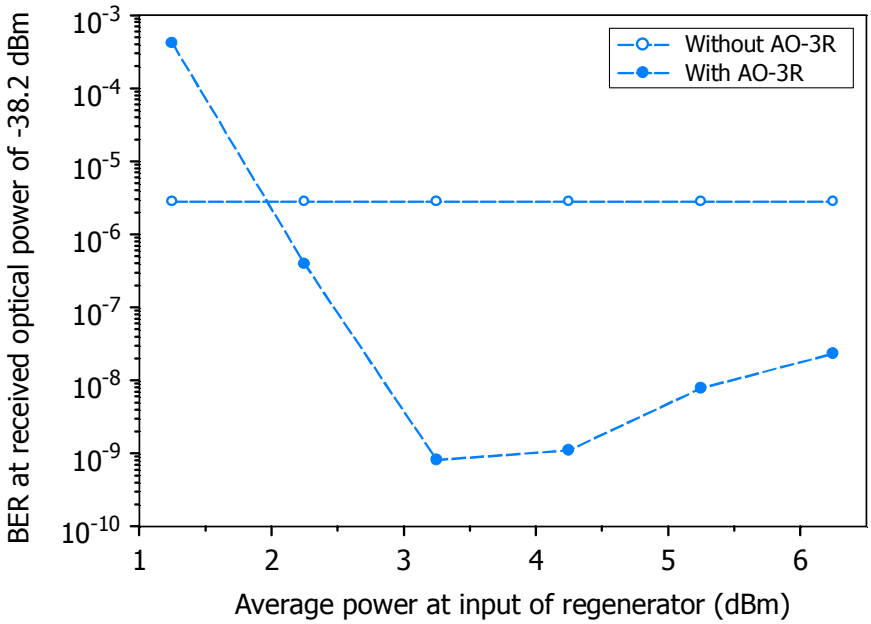

Figure 5.28: Effect of average input power: BER versus average input power.

When the input power is 3.3 dBm the reshaping stage is operating at its optimal conditions. At this input power, the reshaping stage is operating in the saturation region, where the slope is minimum ($S_{PTC} \approx 0.16$). As a result, the output signal ER and SNR are maximum. Compared to the input signal, the ER is improved by 9.5 dB (12.2 to 21.7 dB) (Fig. 5.24) and the SNR is improved by 5.6 dB (6.4 to 12 dB) (Fig. 5.25). In particular, 1-level noise is shown to be well suppressed in the eye diagram of the output signal (Fig. 5.27d).

The BER versus average input signal power for a fixed received optical power in Fig. 5.28. The BER follows a similar trend as the output signal SNR (Fig. 5.25) since the probability of bit errors is directly related to the amplitude noise. For a received optical power of -38.2 dBm, the best performance is achieved for an average input signal power of 3.3 dBm. At this input signal power, the output signal has an SNR =

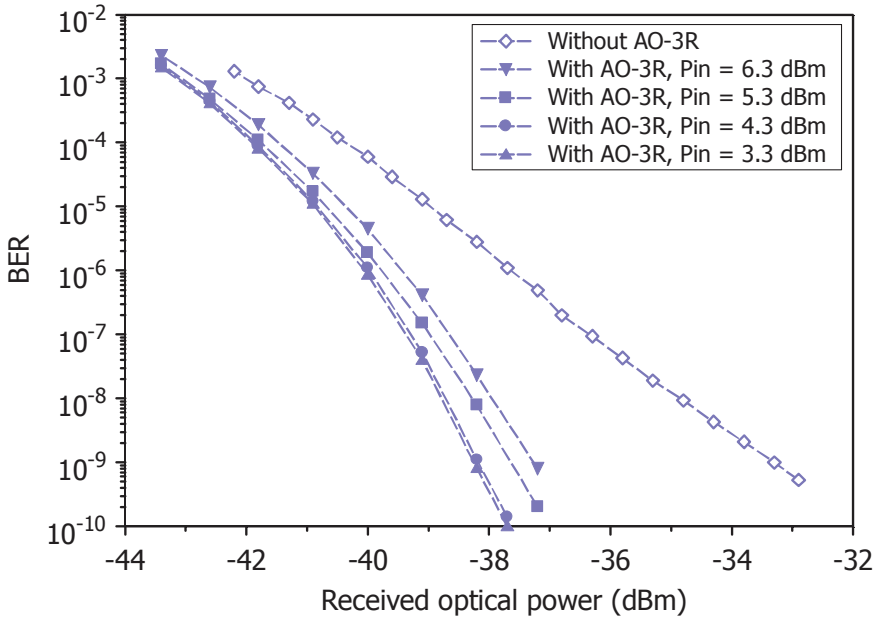

Figure 5.29: Effect of average input power: BER versus received optical power.

12 dB (maximum) and BER = 8.1×10^{-10} (minimum). AO-3R performance degrades when the average input signal power $<$ 3.3 dBm. This is observed in both the output signal SNR and BER. Similarly, AO-3R performance also degrades when the input signal power $>$ 3.3 dBm. However, like the output signal SNR, the performance is only slightly degraded by an increase in input signal power.

AO-3R still provides an improvement in system performance for average input signal powers ranging from 3.3 to 6.3 dBm. The BER versus received optical power for an input signal OSNR = 17 dB is shown in Fig. 5.29. AO-3R provides an improvement in receiver sensitivity with little difference between AO-3R signals. A receiver sensitivity improvement of up 4.9 dB (-38.2 to -33.3 dBm) is observed for an average input signal power of 3.3 dBm with a difference of only 0.9 dB (-33.3 to -32.4 dBm) between AO-3R signals (Fig. 5.30).

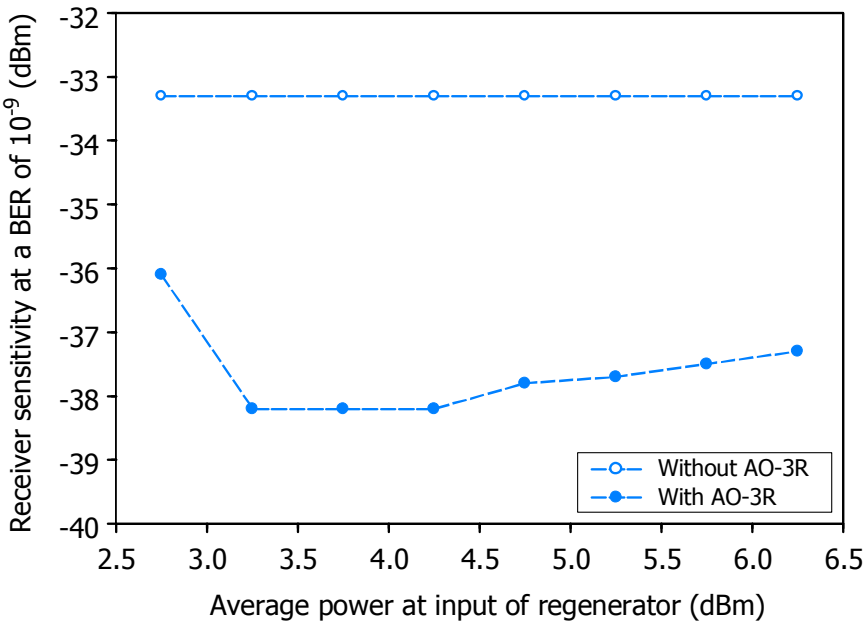

Figure 5.30: Effect of average input power: Receiver sensitivity versus average input power.

5.3.3 Input Wavelength

Like the SOP and average power, the carrier wavelength of optical signals may vary at the input of regenerators. The variation in input signal wavelength may not be as rapid, but because of wavelength division multiplexing (WDM) in the network, regenerators should be able to cope with different input signal wavelengths. Regenerators that can cope with a range of input signal wavelengths, with minimal changes required to their operating conditions, are highly desirable.

The experimental setup for assessing the effect of input signal wavelength on AO-3R performance is the same as the setup used for the effect of average input signal power/SOP (Fig. 5.17). In this case, both the input signal SOP and average input signal power are constant at the input of AO-3R. At the transmitter, the input signal

wavelength is varied over the C-band (i.e., 1535 to 1565 nm) using a tunable laser source (TLS). In the reshaping stage, the custom fiber Bragg grating (FBG) based filter used for the spectral slicing has a fixed center wavelength. To assess the effect of variable input signal wavelength, the FBG is replaced with a tunable optical bandpass filter (OBPF). Compared to the FBG, the tunable OBPF also has a Gaussian passband shape, but has a wider bandwidth (i.e., 0.22 nm). Because of its wider bandwidth, the sliced signal spectrum produces narrower output pulses (i.e., 16 ps) than the input signal (i.e., 47 ps). Since the pulse widths are not similar, a comparison of system performance (i.e., BER) with and without AO-3R is not informative. However, pulse width differences between the input and output signals do not affect the validity of the measurements since the intent is to assess the sensitivity of AO-3R to input signal wavelength, not the ability of AO-3R to improve system performance.

The sensitivity of AO-3R system performance depends on walk-off effects in the retiming stage (see Sect. 3.3.1). The impact of walk-off effects is seen in the retiming stage output signal SNR (Fig. 5.31). For input signal wavelengths ranging from 1535 to 1545 nm, pulse walk-off is minimal. As a result, the retiming stage output signal SNR shows low sensitivity to input signal wavelength. In contrast, for input signal wavelengths ranging from 1545 to 1565 nm, pulse walk-off causes the retiming stage output signal SNR to vary with input signal wavelength. The variation in SNR indicates that walk-off effects manifest as amplitude variations (noise). By design, the reshaping stage follows the retiming stage in order to provide compensation for the amplitude variations. Walk-off effects are effectively compensated by the reshaping stage, since over a 30 nm range (i.e., 1535 to 1565 nm), the reshaping stage output signal SNR shows low sensitivity to the input signal wavelength.

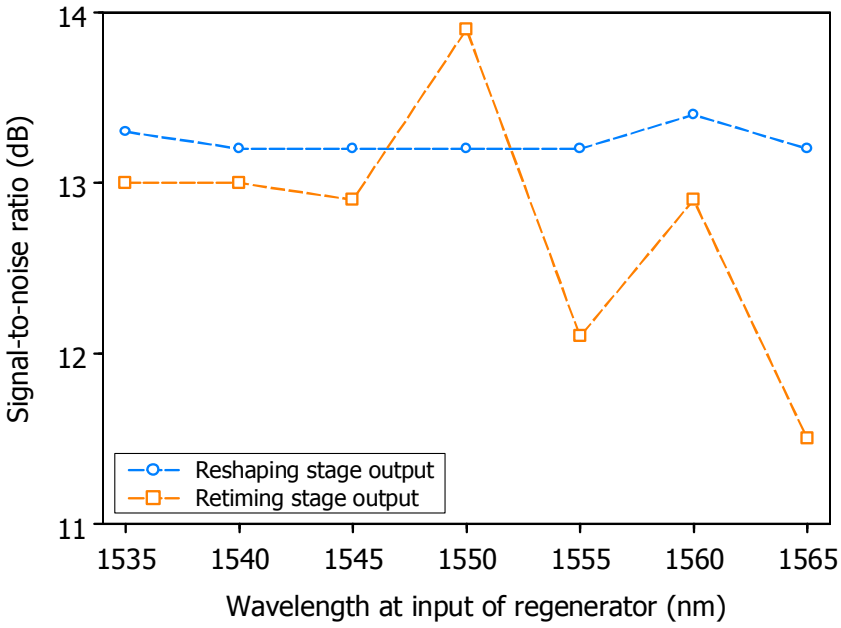

Figure 5.31: Dependence of output SNR on input wavelength.

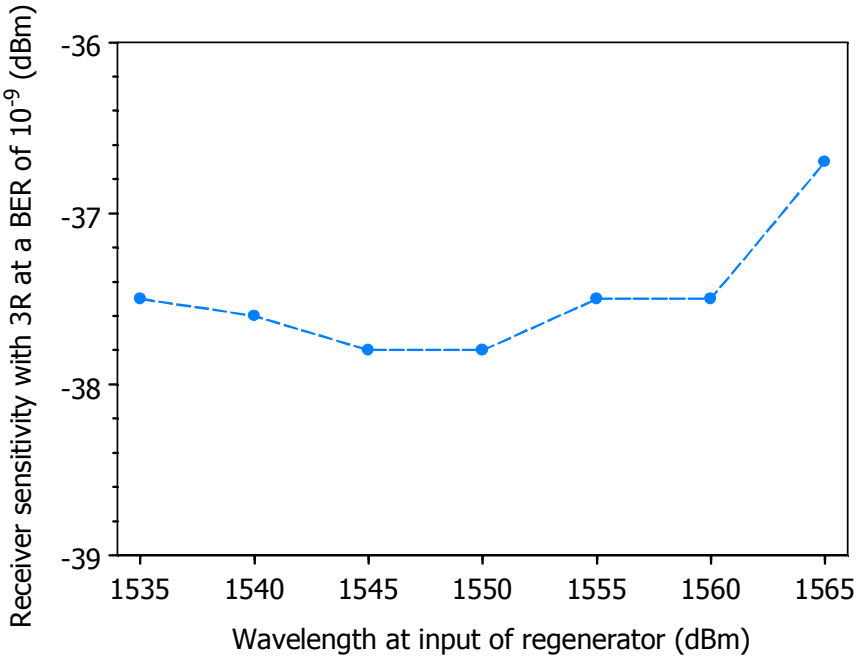

Figure 5.32: Effect of input wavelength: Receiver sensitivity versus input wavelength.

To assess AO-3R system performance, the receiver sensitivity is measured over the 30 nm range of input signal wavelengths. The receiver sensitivity versus input signal wavelength with AO-3R is shown in Fig. 5.32. Because the reshaping stage compensates for walk-off effects, for input signal wavelengths ranging from 1535 to 1560 nm, the difference between AO-3R receiver sensitivity is only 0.3 dB (i.e., -37.8 to -37.5 dBm). Including the result for an input signal wavelength at 1565 nm, the difference in receiver sensitivity increases to 1.1 dB (i.e., -37.8 to -36.7 dBm). However, the increase in receiver sensitivity does not arise from an SNR penalty (Fig. 5.31), but rather a decrease in preamplifier gain at 1565 nm.

Although walk-off effects still occur, AO-3R is achieved with low sensitivity to the input signal wavelength. Moreover, the performance is achieved with minimal change to the operating conditions. In fact, the only change required is the tuning of the slicing filter center wavelength λ_s, using the same offset for all wavelengths (i.e., $\lambda_s = \lambda_{in} + 0.8$ nm). This is the minimum control that can be expected for any regenerator.

5.4 Optical Packet Regeneration

The use of WDM provides an effective means of provisioning available bandwidth. To increase bandwidth efficiency, AAPNs may also assign multiple time slots (TDM) to traffic flows as the demand varies. As a result, the traffic is expected to be bursty since it will consist of data streams segmented into optical packets. The bursty nature of the traffic has two implications on optical regeneration.

First, optical regenerators should not exhibit "packet effects". In other words, the properties of one packet should not affect the regeneration of subsequent packets. Because AO-3R is based on the Kerr effect (XPM/SPM), which has a femtosecond response time, AO-3R does not exhibit pattern effects. This means that one bit does not affect the regeneration of subsequent bits. Since the bit duration (100 ps) is much shorter than the packet arrival time (1 μs), it follows that AO-3R does not exhibit packet effects either.

The caveat, however, is that AO-3R does not rely solely on the Kerr effect for the regeneration. Because AO-3R provides retiming, the SP-DFBL must also be free of packet effects. This means that the clock frequency associated with one packet must be released by the optical clock signal before the arrival of the next packet. In other words, the clock signal must not hold the clock frequency for a time duration longer than the inter-packet guard time. When the clock frequency is released, the clock signal jitter increases because of a return to self-pulsation. Using the jitter induced power penalty as a measure of release time, the SP-DFBL was found to release the input signal clock frequency in less than 40 bits [104]. For a bit rate of 10 Gb/s, this translates to a release time of 4 ns, which is much shorter than the packet inter-guard time of 1 μs. Therefore, the SP-DFBL is also free of packet effects.

Similar to release time, the SP-DFBL should be able to quickly lock onto the clock frequency of the input signal. The time it takes to lock onto the clock frequency of the input signal determines the time before regeneration can take place. A packet header consisting of a sequence of 1-bits is used to allow the SP-DFBL to achieve locking. To reduce overhead, the clock signal should lock within the least number of bits as possible.

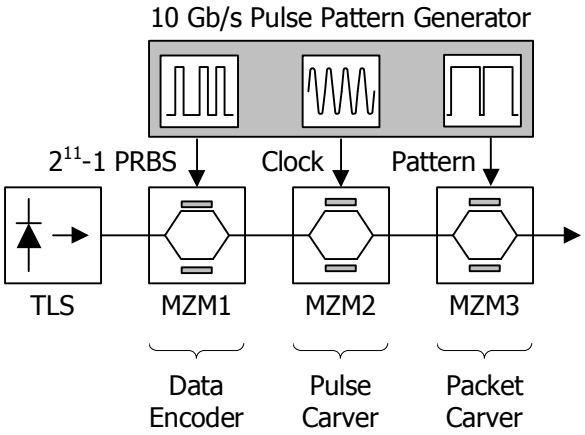

Figure 5.33: Optical packet regeneration: Transmitter setup.

To assess the locking time the transmitter is modified to generate optical packets. The optical packet transmitter is shown in Fig. 5.33. The transmitter uses a TLS and three Mach-Zehnder modulators (MZMs) to generate the optical packets. MZM1 is used to encode nonreturn-to-zero (NRZ) data onto a continuous wave (CW) signal. The signal is encoded with a 20-bit header of 1-bits, followed by a $2^{11} - 1$ PRBS that repeats 53 times per period. For a bit rate of 9.95328 Gb/s, the encoded header plus PRBS has a period of 11.1 μs. MZM2 is used to produce return-to-zero (RZ) modulation by carving pulses out of the NRZ data signal. The pulse carving is achieved using the clock signal with a frequency of 9.95328 GHz to drive MZM2. MZM3 is used to produce optical packets out of the RZ data signal. The packet carving is achieved using a repeating bit pattern, consisting of 11,025 0-bits followed by 99,533 1-bits, to drive MZM3. The bit pattern generates 10 μs optical packets with a 1.1 μs inter-packet guard time.

For input packets, the SP-DFBL locks onto the clock frequency of the input signal, generating an "optical clock packet". This means that the optical clock signal

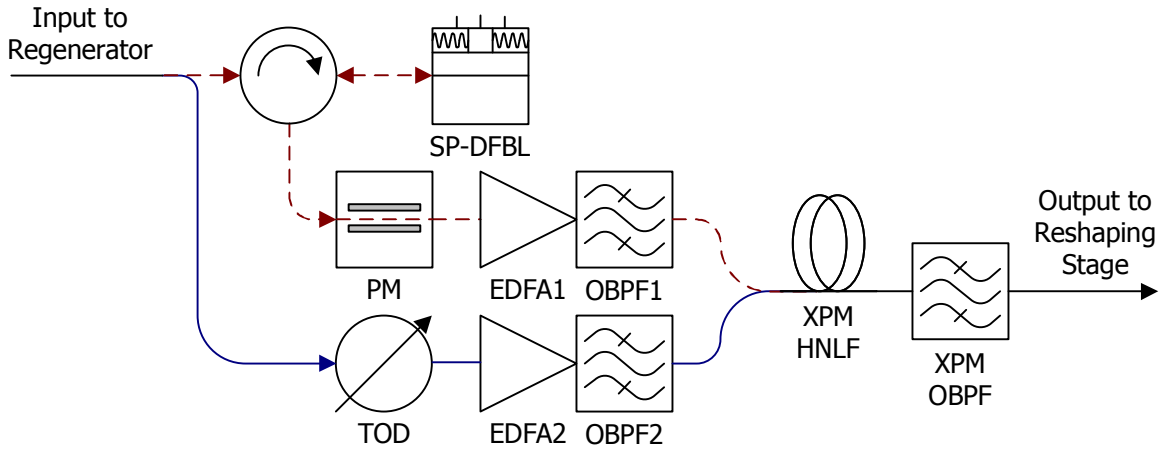

Figure 5.34: Optical packet regeneration: Retiming stage setup.

oscillates at the (low jitter) clock frequency of the input signal for the duration of the packet (10 μs) and at the (high jitter) self-pulsation frequency for the duration of the inter-packet guard time (1.1 μs). To prevent "retiming" with high jitter clock pulses, it is critical that the data and clock packets are aligned in time at the input of the XPM HNLF. To align packet arrival times, the input data and clock packets should experience the same time delay along their respective paths to the XPM HNLF. The paths for the input data and clock packets are indicated by solid and dashed lines, respectively, in Fig. 5.34. The path time delays are set using optical fibers (course tuning) and a tunable optical delay (TOD) (fine tuning)[2], which provides a tuning range of 300 ps (3 bits). To determine the appropriate delays for alignment, packet waveforms are monitored using a digital communication analyzer (DCA) at the input of the XPM HNLF. Once aligned, the locking time is measured at the output of AO-3R in terms of the number of data bits needed before the timing jitter of the data

[2]The tunable optical delay (TOD) provides tuning resolution of 0.001 ps.

signal is the same as the clock signal.

The header bits of the AO-3R output signal are shown in Fig. 5.35. For the first 5 bits, the clock signal has not yet locked onto the clock frequency of the data signal and is still oscillating at the self-pulsation frequency as evident by the considerable noise caused by the clock signal timing jitter (Fig. 5.35a). Through bits 1 – 20, the noise appears to decreases, indicating that the clock signal is locking onto the input signal clock frequency (Fig. 5.35b). Upon closer observation, the jitter is still considerable for bits 1 – 10 (Fig. 5.35c), but appears to rapidly decrease for bits 11 – 20 (Fig. 5.35d). A comparison between bit 1 (start of header) and bit 21 (start of data) shows a significant improvement in terms of the noise associated with timing jitter (Fig. 5.36). This indicates that the self-pulsation frequency locks onto the clock frequency of the data signal within the first 20 bits of the packet.

The result is verified by measuring the timing jitter versus bit number in the AO-3R output signal (Fig. 5.37). The time delay (in bits) between the clock and data packets is the number of bits, counting from the end of the packet (bit 99,533), in which the jitter begins to increase. The increase in jitter at the end of the packet occurs because the clock and data packets are no longer aligned, causing the clock frequency to slowly return to the self-pulsation frequency. Therefore, the number of bits from the end of the packet in which the jitter begins to increase is equivalent to the number of bits in which the clock packet arrives before the data packet at the input of the XPM HNLF. For a 4 bit time delay, the clock signal is locked by bit 17 since the data signal jitter is the same the clock signal (2.1 ps). Because the data signal is delayed by 4 bits relative to the clock signal, the jitter begins to increase 4 bits before the end of the packet (bit 99,529). The increase in jitter is slow, however, increasing from 2.1 to

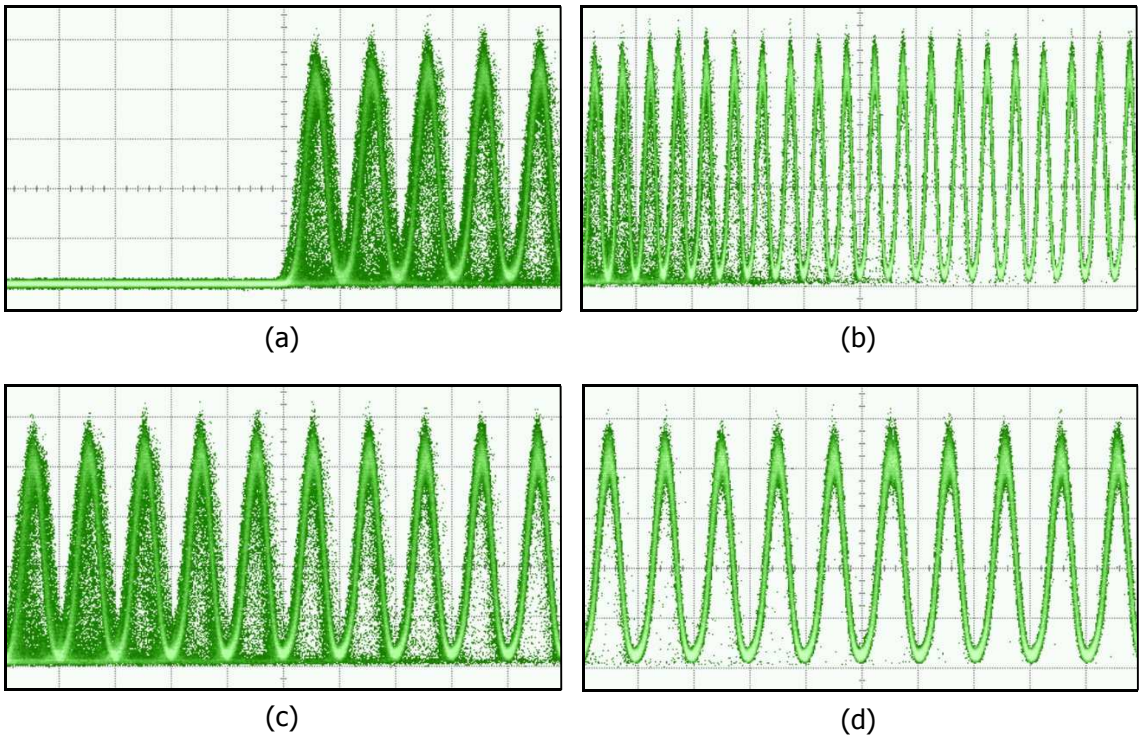

Figure 5.35: Optical packet regeneration: Bits in data packet header at output of regenerator (a) bits 1-5 (100 ps/div), (b) bits 1-20 (200 ps/div), (c) bits 1-10 (100 ps/div), and (d) bits 11-20 (100 ps/div).

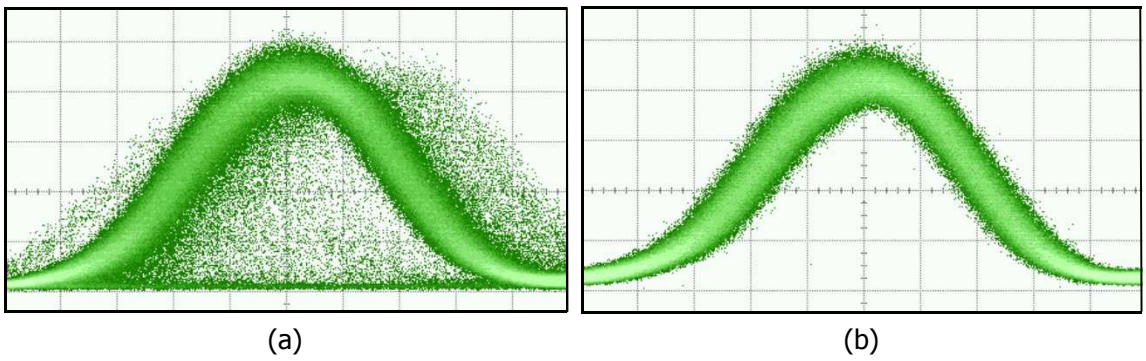

Figure 5.36: Optical packet regeneration: Bits in data packet header at output of regenerator (a) bit 1 (start of header) and (b) bit 21 (start of data) (10 ps/div).

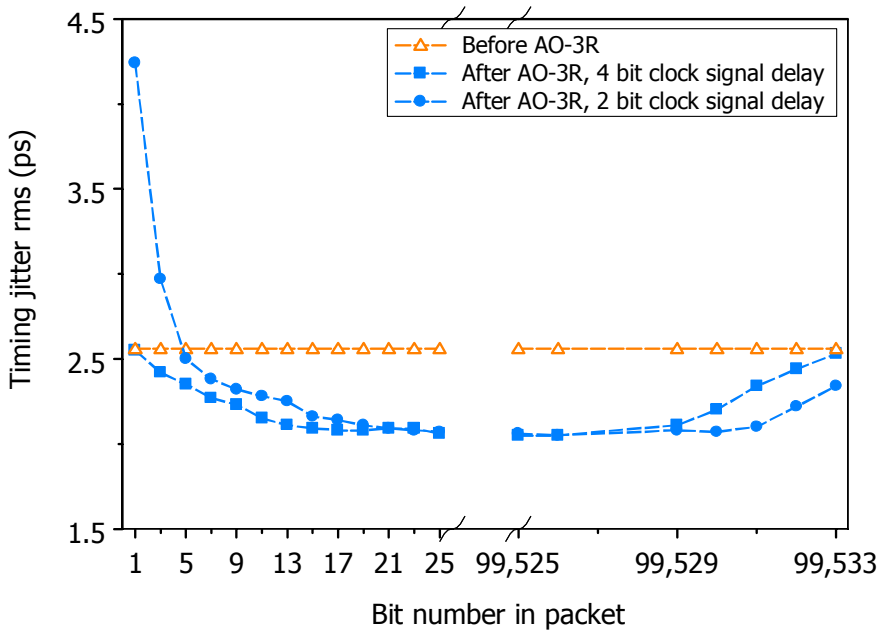

Figure 5.37: Optical packet regeneration: Timing jitter versus bit number in packet.

2.6 ps by the last bit. The behaviour is consistent with a 2 bit time delay. That is, the clock signal is locked (bit 19) and released (bit 99,531) 2 bits later. It follows that for a 0 bit time delay (packets aligned), the clock signal locks by bit 21 and releases at the last bit of the data packet (bit 99,533). AO-3R is therefore capable of providing regeneration by bit 21.

AO-3R of optical packets is demonstrated for signals degraded by ASE noise. On the packet level, the input signal shows amplitude noise in its packet envelope (Fig. 5.38a), whereas the AO-3R output signal shows a reduced level of noise in its packet envelope (Fig. 5.38b). Since the packet envelope is formed by the 1-level of the signal, reduced variations in the amplitude of the envelope indicates that AO-3R reduces noise in the 1-level. The lower power level seen in the guard band of the AO-3R output signal indicates that AO-3R also reduces low power variations, such as

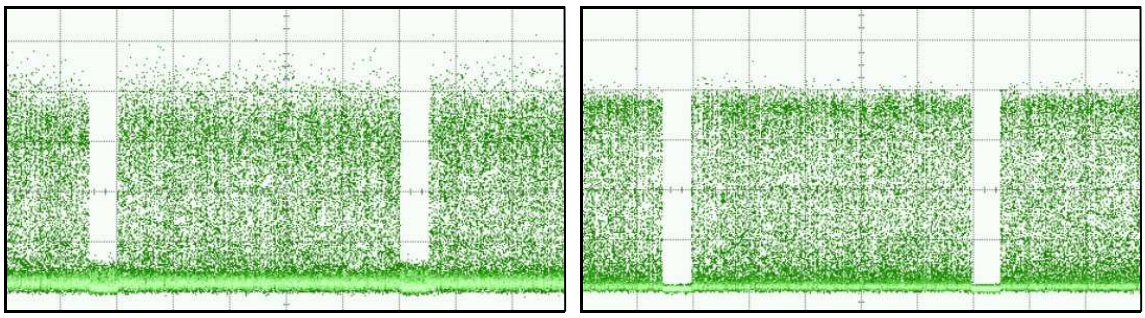

Figure 5.38: Optical packet regeneration: Waveform patterns for (a) input and (b) output signals of AO-3R (2 μs/div).

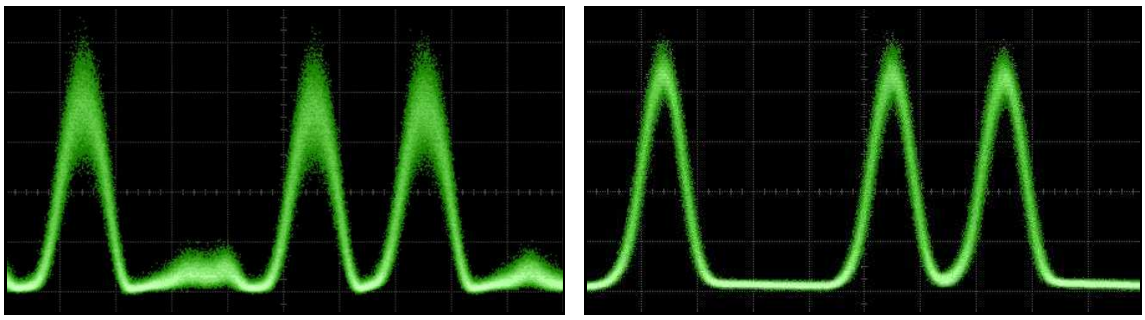

Figure 5.39: Optical packet regeneration: Waveform pattern 10110 within the packet for (a) input and (b) output signals of AO-3R (50 ps/div).

noise in the 0-level. The reduction of noise in both the 0- and 1-levels is more clearly seen by comparing bits within the packet. For a 10110 bit sequence, the noise present in the input signal (Fig. 5.39a) is reduced and the waveform reshaped in the AO-3R output signal (Fig. 5.39b).

For signals degraded by ASE noise, varying the input signal SOP is observed to not significantly affect the performance of optical packet regeneration. The input signal SOP is randomly varied (scrambled) using a polarization controller with continuously rotating $\lambda/2$ and $\lambda/4$ waveplates. With the input signal SOP scrambled, compared to

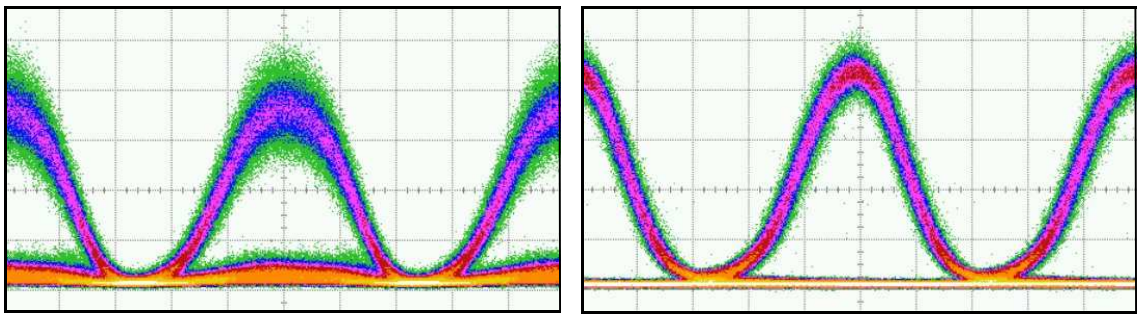

Figure 5.40: Optical packet regeneration: Eye diagrams for (a) input and (b) output signals of AO-3R with varying input SOPs (20 ps/div).

the input signal eye diagram (Fig. 5.40a), the AO-3R output signal eye diagram does not show degradation (Fig. 5.40b), indicating its insensitivity to the input signal SOP, while providing the desired signal improvements in terms of retiming and reshaping.

5.5 Conclusions

AO-3R system performance is evaluated within the context of: transmission impairments (Sect. 5.2), input signal properties (Sect. 5.3), and optical packets (Sect. 5.4). Experimental results demonstrate excellent performance. For transmission impairments, AO-3R improves (or maintains) the system performance for input signals degraded by: ASE noise, GVD (RD), and PMD (DGD). The performance is shown to be highly dependent on the ability of the clock recovery technique (SP-DFBL) to provide a clock signal with low timing jitter. In particular, the SP-DFBL shows lower sensitivity to the input signal noise (ASE) than waveform/pulse width distortion (RD/DGD).

The SP-DFBL provides low sensitivity to the input signal properties. As a result, AO-3R is achieved over a wide dynamic range of input signal properties, including:

input signal SOPs, average input powers, and input wavelengths. AO-3R of optical packets is enabled by the ability of the SP-DFBL to quickly recover a clock signal. By achieving fast clock recovery (20 bits), AO-3R of optical packets is successfully demonstrated for input signals with ASE noise and varying SOPs.

Chapter 6

Conclusions

6.1 Thesis Contributions

The original contributions in this thesis include:

1. A novel technique for 10 Gb/s all-optical 3R regeneration (AO-3R), specifically designed to meet the requirements of AAPNs (Ch. 2) [4].

   Based on a literature review, it was concluded that the requirements of AAPNs can be met using a 2-stage design. In the first stage, an optical clock signal is recovered through dispersive self-Q-switching (DSQS) in a self-pulsating distributed feedback laser (SP-DFBL). This implementation is selected because of its ability to quickly recover an optical clock signal while providing low sensitivity to the input signal properties. The clock signal is used to induce cross-phase modulation (XPM) onto the input signal in a highly nonlinear fiber (HNLF). With offset spectral slicing, the sliced signal achieves retiming and wavelength conversion. Because XPM is induced by the clock signal, retiming is achieved

with low sensitivity to the input signal properties. However, a second stage is required to perform reshaping and wavelength reconversion.

In the second stage, reshaping and wavelength conversion (back to the input signal wavelength) are achieved using self-phase modulation (SPM) in a HNLF with offset spectral slicing. While SPM provides low sensitivity to most input signal properties, it is highly sensitive to the input signal power and pulse shape. However, since the first stage (XPM) performs spectral slicing of the input signal, input signal power variations are reduced over the slicing filter passband, thereby reducing input signal power variations to the second stage (SPM). In addition, since the shape of the slicing filter passband determines the shape of the sliced signal, the same pulse shape is provided to the second stage (SPM) regardless of the input pulse shape to the first stage (XPM). Furthermore, the shape of the slicing filter passband in the second stage can be designed to provide a sliced (3R regenerated) output signal with the same pulse width as the input signal.

2. Demonstration that AO-3R can be made polarization insensitive without any additional complexity or control of the clock signal polarization (Ch. 3) [4], [5].

   A technique originally proposed for demultiplexing [78] is successfully extended to achieve polarization insensitive retiming [5] and AO-3R [4]. Polarization insensitive retiming is enabled by a remarkable property of XPM that provides a polarization insensitive wavelength in the XPM broadened signal spectrum. Therefore, by merely selecting the slicing filter offset properly, polarization insensitive retiming is achieved. An expression derived to predict the polarization insensitive offset shows good agreement with experimental results for $b = 1/3$.

3. Demonstration that AO-3R can be achieved for 10 Gb/s signals with practical input and output pulse widths (Ch. 4) [4].

   AO-3R can be achieved for 10 Gb/s signals with practical input and output pulse widths by properly designing the operating conditions of the second stage (i.e., reshaping stage). In particular, proper design of the HNLF properties (dispersion and length) enables AO-3R of signals with practical input pulse widths (47 ps). Similarly, proper design of the slicing filter passband shape and bandwidth also allows AO-3R to provide signals with practical output pulse widths (42 ps).

4. Evaluation of AO-3R system performance within the context of (Ch. 5):

   (a) Transmission impairments.

   AO-3R provides improvements in system performance for input signals degraded by transmission impairments. The receiver sensitivity at a BER of 10^{-9} is used as a measure of system performance. For input signals degraded by ASE noise, AO-3R provides an improvement in receiver sensitivity of up to 4.5 dB for an input signal with an OSNR = 17 dB. The system performance of AO-3R for input signals degraded by ASE noise is determined by the amount of amplitude noise that can be suppressed by the reshaping stage.

   In contrast, for input signals degraded by GVD (RD) and PMD (DGD), the system performance of AO-3R is determined by the ability of the SP-DFBL to recover a clock signal with low timing jitter. The SP-DFBL recovers a clock signal with low jitter (e.g., 2 ps) provided the input signal RD is within the range of -303 to 340 ps/nm and DGD $<$ 25 ps. Within the specified

limits, AO-3R is able to either improve or maintain system performance. For example, for input signals with RD = 340 ps/nm, AO-3R provides an improvement in receiver sensitivity of up to 7.4 dB when RD = 510 ps/nm between AO-3R and the receiver. For input signals with DGD = 25 ps, AO-3R is able to cope, maintaining a receiver sensitivity of -37.5 dBm.

(b) Input signal properties.

AO-3R also demonstrates the ability to cope with variability in the properties of input signals. Low sensitivity to the properties of input signals is achieved by proper design of the operating conditions in the retiming and reshaping stages. For example, in the retiming stage, proper selection of the slicing filter offset is critical for achieving low sensitivity to the input signal SOP. For the input signal properties, AO-3R exhibits sensitivities of only: 0.5 dB over eight input signal SOPs [4]; 0.9 dB over an input signal power range of 3 dB (i.e., 3.3 to 6.3 dBm) [6]; 1.1 dB over an input signal wavelength range of 30 nm range (i.e., 1535 to 1565 nm).

(c) Optical packets.

AO-3R also demonstrates the ability to regenerate optical packets [4]. The regeneration of optical packets is enabled by the use of a SP-DFBL for clock recovery, which provides a recovered clock signal within the first 20 bits of the input packet. The ability to quickly recover a clock signal is essential for reducing the packet overhead required before regeneration can occur. For example, since the clock signal is recovered by bit 20, packet overhead of only 20 (header) bits is required before regeneration can be achieved.

6.2 Future Directions

In this thesis, the regeneration of optical packets is demonstrated in terms of qualitative improvements to the regenerated signal. In future work, it will be useful to quantify the improvements to the regenerated signal through system performance measurements, such as the BER. To perform BER measurements, an optical receiver capable of measuring the BER from the first bit of the packet is required.

Furthermore, in this thesis, AO-3R system performance is measured for one pass through the regenerator. In ultra-long haul transmission systems, optical signals will pass through multiple regenerators. To fully assess AO-3R, it is important to measure the system performance for multiple passes through the regenerator. In a laboratory setting, this is typically achieved using a recirculating loop configuration. While recirculating loop measurements have yet to be conducted, measurements of the regenerated signal chirp properties provides insight into performance. In particular, the low negative chirp of the regenerated signal indicates the potential for successful retransmission over multiple links. Preliminary tests demonstrated successful retransmission of the regenerated signal over an 80 km dispersion-managed link.

Bibliography

[1] D. V. Plant, "Agile all-photonic networks," in *Proc. LEOS Annual Meeting*, vol. 1, 2003, p. 227.

[2] G. V. Bochmann, T. Hall, O. Yang, M. J. Coates, L. Mason, and R. Vickers, "The agile all-photonic network: an architectural outline," in *Proc. 22nd. Bien. Symp. on Comm., Kingston, Canada*, 2004.

[3] J. Livas, "Optical transmission evolution: From digital to analog to ? Network tradeoffs between optical transparency and reduced regeneration cost," *IEEE Journ. of Lightwave Technol.*, vol. 23, no. 1, pp. 219–224, Jan. 2005.

[4] C. Ito and J. C. Cartledge, "Polarization independent all-optical 3R regeneration of optical packets based on the Kerr effect and offset spectral slicing," in *Proc. Eur. Conf. Optical Communications (ECOC) (accepted)*, 2007.

[5] C. Ito, S. H. Chung, I. Monfils, and J. C. Cartledge, "Polarization independent all-optical retiming based on cross-phase modulation and spectral slicing," in *Proc. Optical Fiber Communication Conf. (OFC)*, 2006, p. OThB5.

[6] C. Ito and J. C. Cartledge, "Input power dynamic range of a polarization independent all-optical 3R regenerator," in *Proc. LEOS Annual Meeting (accepted)*, 2007.

[7] S. Vehovc, M. Vidmar, and A. Paoletti, "80 Gbit/s optical clock recovery with automatic lock acquisition using electrical phase-locked loop," *Electron. Lett.*, vol. 39, no. 8, pp. 673–674, Apr. 2002.

[8] S. R. Han, C. N. Chuang, and S. I. Liu, "A time-constant calibrated phase-locked loop with a fast-locked time," *IEEE Trans. Circuits Syst. II, Exp. Briefs*, vol. 54, no. 1, pp. 34–37, Jan. 2007.

[9] M. Jinno and T. Matsumoto, "Optical tank circuits used for all-optical timing recovery," *IEEE J. Quantum Electron.*, vol. 28, no. 4, pp. 895–900, Apr. 2002.

[10] K. Taira and K. Kikuchi, "All-optical clock recovery using a mode-locked laser," *Electron. Lett.*, vol. 28, no. 19, pp. 1814–1816, Sep. 1992.

[11] B. Sartorius, M. Möhrle, S. Malchow, and S. Reichenbacher, "Wavelength and polarisation independent all optical synchronisation of high frequency DFB type self-pulsations," *Electron. Lett.*, vol. 32, no. 11, pp. 1026–1028, May 1996.

[12] B. Sartorius, C. Bornholdt, O. Brox, H. J. Ehrke, D. Hoffmann, R. Ludwig, and M. Möhrle, "All-optical clock recovery module based on self-pulsating DFB laser," *Electron. Lett.*, vol. 34, no. 17, pp. 1664–1665, Aug. 1998.

[13] C. Johnson, K. Demarest, C. Allen, R. Hui, K. V. Peddanarappagari, and B. Zhu, "Multiwavelength all-optical clock recovery," *IEEE Photon. Technol. Lett.*, vol. 11, no. 7, pp. 895–897, Jul. 1999.

[14] C. Bintjas, K. Yiannopoulos, N. Pleros, G. Theophilopoulos, M. Kalyvas, H. Avramopoulos, and G. Guekos, "Clock recovery circuit for optical packets," *IEEE Photon. Technol. Lett.*, vol. 14, no. 9, pp. 1363–1365, Sep. 2002.

[15] C. Bornholdt, J. Slovak, M. Möhrle, and B. Sartorius, "Jitter analysis of all-optical clock recovery at 40 GHz," in *Proc. Optical Fiber Communication Conf. (OFC)*, 2003, pp. 120–121.

[16] N. Pleros, K. Vyrsokinos, C. Bintjas, K. Yiannopoulos, K. Vlachos, and H. Avramopoulos, "All-optical clock recovery from short asynchronous data packets at 10 Gb/s," *IEEE Photon. Technol. Lett.*, vol. 15, no. 9, pp. 1291–1293, Sep. 2003.

[17] R. Salem and T. E. Murphy, "Broad-band optical clock recovery system using two-photon absorption," *IEEE Photon. Technol. Lett.*, vol. 16, no. 9, pp. 2141–4143, Sep. 2004.

[18] E. Kehayas, L. Stampoulidis, H. Avramopoulos, Y. Liu, E. Tangdiongga, and H. Dorren, "40 Gb/s all-optical packet clock recovery with ultrafast lock-in time and low inter-packet guardbands," *Opt. Express*, vol. 13, no. 2, pp. 475–480, Jan. 2005.

[19] S. Arahira and Y. Ogawa, "Electrical clock recovery based on all-optical signal processing in a monolithic passively mode-locked laser diode," *IEEE Photon. Technol. Lett.*, vol. 18, no. 16, pp. 1765–1767, 2006.

[20] T. von Lerber, J. Tuominen, H. Ludvigsen, S. Honkanen, and F. Kueppers, "Multichannel and rate all-optical clock recovery," *IEEE Photon. Technol. Lett.*, vol. 18, no. 12, pp. 1395–1397, Jun. 2006.

[21] S. Bauer, C. Bornholdt, O. Brox, D. Hoffmann, M. Möhrle, G. Sahin, B. Sartorius, and S. Schelhase, "Ultrafast locking optical clock for IP packet switching applications," in *Proc. Optical Fiber Communication Conf. (OFC)*, 2000, pp. 78–80.

[22] X. Zhou, C. Lu, P. Shum, H. H. M. Shalaby, T. H. Cheng, and Y. Peida, "A performance analysis of an all-optical clock extraction circuit based on Fabry-Pérot filter," *IEEE Journ. of Lightwave Technol.*, vol. 19, no. 5, pp. 603–613, 2001.

[23] Z. Zhu, M. Funabashi, P. Zhong, L. Paraschis, D. L. Harris, and S. J. B. Yoo, "High-performance optical 3R regeneration for scalable fiber transmission system applications," *IEEE Journ. of Lightwave Technol.*, vol. 25, no. 2, pp. 504–511, 2007.

[24] R. J. Essiambre, B. Mikkelsen, and G. Raybon, "Self-pulsating DFB laser for all-optical clock recovery at 40 Gbit/s," *Electron. Lett.*, vol. 36, no. 4, pp. 327–328, Feb. 2000.

[25] B. Sartorius, M. Möhrle, S. Reichenbacher, H. Preier, H. J. Wünsche, and U. Bandelow, "Dispersive self-Q-switching in self-pulsating DFB lasers," *IEEE J. Quantum Electron.*, vol. 33, no. 2, pp. 211–218, Feb. 1997.

[26] O. Brox, S. Bauer, M. Radziunas, M. Wolfrum, J. Sieber, J. Kreissl, B. Sartorius, and H. J. Wünsche, "High-frequency pulsations in DFB lasers with amplified feedback," *IEEE J. Quantum Electron.*, vol. 39, no. 11, pp. 1381–1387, Nov. 2003.

[27] H. J. Wünsche, M. Radziunas, S. Bauer, O. Brox, and B. Sartorius, "Modeling of mode control and noise in self-pulsating PhaseCOMB lasers," *IEEE J. Select. Topics Quantum Electron.*, vol. 9, no. 3, pp. 857–864, May-June 2003.

[28] B. Lavigne, J. Renaudier, F. Lelarge, O. Legouezigou, H. Gariah, and G. H. Duan, "Polarization-insensitive low timing jitter and highly optical noise tolerant all-optical 40-GHz clock recovery using a bulk and a quantum-dots-based self-pulsating laser cascade," *IEEE Journ. of Lightwave Technol.*, vol. 25, no. 1, pp. 170–176, Jan. 2007.

[29] T. Otani, T. Miyazaki, and S. Yamamoto, "40-Gb/s optical 3R regenerator using electroabsorption modulators for optical networks," *IEEE Journ. of Lightwave Technol.*, vol. 20, no. 2, pp. 195–200, Feb. 2002.

[30] H. F. Chou and J. E. Bowers, "Simplified optoelectronic 3R regenerator using nonlinear electro-optical transformation in an electroabsorption modulator," *Opt. Express*, vol. 13, no. 7, pp. 2742–2746, Apr. 2005.

[31] L. Huo, Y. Yang, Y. Nan, C. Lou, and Y. Gao, "A study on the wavelength conversion and all-optical 3R regeneration using cross-absorption modulation in a bulk electroabsorption modulator," *IEEE Journ. of Lightwave Technol.*, vol. 24, no. 8, pp. 3035–3044, Aug. 2006.

[32] T. Wood, J. Pastalan, A. Burrus, B. Johnson, B. Miller, J. deMiguel, U. Koren, and M. Young, "Electric field screening by photogenerated holes in multiple quantum wells: A new mechanism for absorption saturation," *Phys. Rev. Lett.*, vol. 57, no. 11, p. 10811083, Sep. 1990.

[33] S. Høfeldt, S. Bischoff, and J. Mørk, "All-optical wavelength conversion and signal regeneration using an electroabsorption modulator," *IEEE Journ. of Lightwave Technol.*, vol. 18, no. 8, pp. 195–200, Aug. 2000.

[34] K. Nishimura, R. Inohara, M. Usami, and S. Akiba, "All-optical wavelength conversion by electroabsorption modulator," *IEEE J. Select. Topics Quantum Electron.*, vol. 11, no. 1, pp. 278–284, Jan.-Feb. 2005.

[35] L. Billes, J. C. Simon, B. Kowalski, M. Henry, G. Michaud, P. Lamouler, and F. Alard, "20 Gbit/s optical 3R regenerator using SOA based Mach-Zehnder interferometer gate," in *Proc. Eur. Conf. Optical Communications (ECOC)*, 1997, pp. 269–272.

[36] B. Lavigne, D. Chiaroni, P. Guerber, L. Hamon, and A. Jourdan, "Improvement of regeneration capabilities in semiconductor optical amplifier-based 3R regenerator," in *Proc. Optical Fiber Communication Conf. (OFC)*, 1999, pp. 128–130.

[37] A. E. Kelly, I. D. Phillips, R. J. Manning, A. D. Ellis, D. Nesset, D. G. Moodie, and R. Kashyap, "80 Gbit/s all-optical regenerative wavelength conversion using semiconductor optical amplifier based interferometer," *Electron. Lett.*, vol. 35, no. 17, pp. 1477–1478, Aug. 1999.

[38] D. Wolfson, A. Kloch, T. Fjelde, C. Janz, B. Dagens, and M. Renaud, "40-Gb/s all-optical wavelength conversion, regeneration, and demultiplexing in an SOA-based all-active Mach-Zehnder interferometer," *IEEE Photon. Technol. Lett.*, vol. 12, no. 3, pp. 332–334, Mar. 2000.

[39] J. Leuthold, B. Mikkelsen, R. E. Behringer, G. Raybon, C. H. Joyner, and P. A. Besse, "Novel 3R regenerator based on semiconductor optical amplifier delayed-interference configuration," *IEEE Photon. Technol. Lett.*, vol. 13, no. 8, pp. 860–862, Aug. 2001.

[40] Y. Ueno, S. Nakamura, and K. Tajima, "Penalty-free error-free all-optical data pulse regeneration at 84 Gb/s by using a symmetric-Mach-Zehnder-type semiconductor regenerator," *IEEE Photon. Technol. Lett.*, vol. 13, no. 5, pp. 469–471, May 2001.

[41] R. J. Essiambre, B. Mikkelsen, and G. Raybon, "Semiconductor-based all-optical 3R regenerator demonstrated at 40 Gbit/s," *Electron. Lett.*, vol. 40, no. 3, pp. 192–194, Feb. 2004.

[42] Y. A. Leem, D. C. Kim, E. Sim, S. B. Kim, H. Ko, K. H. Park, D. S. Yee, J. O. Oh, S. H. Lee, and M. Y. Jeon, "The characterization of all-optical

3R regeneration based on InP-related semiconductor optical devices," *IEEE J. Select. Topics Quantum Electron.*, vol. 12, no. 4, pp. 726–735, July-Aug. 2006.

[43] J. L. Pleumeekers, M. Kauer, K. Dreyer, C. Burrus, A. G. Dentai, S. Shunk, J. Leuthold, and C. H. Joyner, "Analysis and optimization of SPM-based 2R signal regeneration at 40 Gb/s," *IEEE Photon. Technol. Lett.*, vol. 14, no. 1, pp. 12–14, 2002.

[44] T. Durhuus, B. Mikkelsen, C. Joergensen, S. L. Danielsen, and K. E. Stubkjaer, "All-optical wavelength conversion by semiconductor optical amplifiers," *IEEE Journ. of Lightwave Technol.*, vol. 14, pp. 942 – 954, Jun. 1996.

[45] P. S. Cho, D. Mahgerefteh, J. Goldhar, L. G. Joneckis, and G. L. Burdge, "High performance non-interferometric semiconductor-optical-amplifier/fibre-bragg-grating wavelength converter," *Electron. Lett.*, vol. 34, no. 4, pp. 371–373, Feb. 1998.

[46] H. Lee, H. Yoon, Y. Kim, and J. Jeong, "Theoretical study of frequency chirping and extinction ratio of wavelength-converted optical signals by XGM and XPM using SOAs," *IEEE J. Quantum Electron.*, vol. 35, no. 8, pp. 1213–1219, Aug. 1999.

[47] K. Obermann, S. Kindt, D. Breuer, K. Petermann, C. Schmidt, S. Diez, and H. G. Weber, "Noise characteristics of semiconductor-optical amplifiers used for wavelength conversion via cross-gain and cross-phase modulation," *IEEE Photon. Technol. Lett.*, vol. 9, no. 3, pp. 312–314, Mar. 1997.

[48] G. P. Agrawal, *Fiber-optic communication systems*, 3rd ed. New York: John Wiley & Sons, Inc., 2002.

[49] S. Fischer, M. Dulk, E. Gamper, W. Vogt, E. Gini, H. Melchior, W. Hunziker, D. Nesset, and A. D. Ellis, "Optical 3R regenerator for 40 Gbit/s networks," *Electron. Lett.*, vol. 35, no. 23, pp. 2047–2049, Nov. 1999.

[50] J. Wiesenfeld, "Wavelength conversion techniques in optical networks," in *Proc. LEOS Annual Meeting*, 1997, p. ThB4.

[51] T. Ito, N. Yoshimoto, K. Magari, and H. Sugiura, "Wide-band polarization-independent tensile-strained InGaAs MQW-SOA gate," *IEEE Photon. Technol. Lett.*, vol. 10, no. 5, pp. 657–659, May 1998.

[52] A. Bogris and D. Syvridis, "Regenerative properties of a pump-modulated four-wave mixing scheme in dispersion-shifted fibers," *IEEE Journ. of Lightwave Technol.*, vol. 21, no. 9, pp. 1892–1902, Sep. 2003.

[53] C. Ito, I. Monfils, and J. C. Cartledge, "All-optical 3R regeneration using higher-order four-wave mixing with a clock-modulated optical pump signal," in *Proc. LEOS Annual Meeting*, 2006, pp. 223–224.

[54] C. Yu, T. Luo, B. Zhang, Z. Pan, M. Adler, Y. Wang, J. E. McGeehan, and A. E. Willner, "Wavelength-shift-free 3R regenerator for 40-Gb/s RZ system by optical parametric amplification in fiber," *IEEE Photon. Technol. Lett.*, vol. 18, no. 24, pp. 2569–2571, Dec. 2006.

[55] G. P. Agrawal, *Nonlinear fiber optics*, 3rd ed. San Diego: Academic Press, Inc., 2001.

[56] K. Inoue, "Optical nonlinearity in optical fibers and semiconductor optical amplifiers," in *Proc. Conf. Lasers and Electro-Optics (CLEO)*, 1999, pp. 1089–1090.

[57] A. Reale, P. Lugli, and S. Betti, "Format conversion of optical data using four-wave mixing in semiconductor optical amplifiers," *IEEE J. Select. Topics Quantum Electron.*, vol. 7, no. 4, pp. 703–709, July-Sept. 2001.

[58] C. Politi, D. Klonidis, and M. J. O'Mahony, "Waveband converters based on four-wave mixing in SOAs," *IEEE Journ. of Lightwave Technol.*, vol. 21, no. 3, pp. 1203–1217, Mar. 2006.

[59] E. Ciaramella and S. Trillo, "All-optical signal reshaping via four-wave mixing in optical fibers," *IEEE Photon. Technol. Lett.*, vol. 12, no. 7, pp. 849–851, Jul. 2000.

[60] K. Inoue, "Suppression of level fluctuation without extinction ratio degradation based on output saturation in higher order optical parametric interaction in fiber," *IEEE Photon. Technol. Lett.*, vol. 13, no. 4, pp. 338–340, Apr. 2001.

[61] Y. Chen and A. W. Snyder, "Four-photon parametric mixing in optical fibers: effect of pump depletion," *Opt. Lett.*, vol. 14, no. 1, pp. 87–89, Jan. 1989.

[62] T. Torounidis, M. Karlsson, and P. A. Andrekson, "Fiber optical parametric amplifier pulse source: theory and experiments," *IEEE Journ. of Lightwave Technol.*, vol. 23, no. 12, pp. 4067–4073, Dec. 2005.

[63] D. Dahan, E. Shumakher, and G. Eisenstein;, "A multiwavelength short pulse source based on saturated optical fiber parametric amplification," *IEEE Photon. Technol. Lett.*, vol. 18, no. 4, pp. 592–594, Feb. 2006.

[64] T. Yamamoto and M. Nakazawa, "Active optical pulse compression with a gain of 29.0 dB by using four-wave mixing in an optical fiber," *IEEE Photon. Technol. Lett.*, vol. 9, no. 12, pp. 1595–1597, Dec. 1997.

[65] K. Inoue and H. Toba, "Wavelength conversion experiment using fiber four-wave mixing," *IEEE Photon. Technol. Lett.*, vol. 4, no. 1, pp. 69–72, Jan. 1992.

[66] K. Inoue and T. Mukai, "Signal wavelength dependence of gain saturation in a fiber optical parametric amplifier," *Opt. Lett.*, vol. 26, no. 1, pp. 10–12, Jan. 2001.

[67] K. K. Chow, C. Shu, C. Lin, and A. Bjarklev, "Polarization-insensitive widely tunable wavelength converter based on four-wave mixing in a dispersion-flattened nonlinear photonic crystal fiber," *IEEE Photon. Technol. Lett.*, vol. 17, no. 3, pp. 624–626, Mar. 2005.

[68] S. Song, C. T. Allen, K. R. Demarest, and R. Hui, "Intensity-dependent phase-matching effects on four-wave mixing in optical fibers," *IEEE Journ. of Lightwave Technol.*, vol. 17, no. 11, pp. 2285–2290, Nov. 1999.

[69] C. Schubert, R. Ludwig, S. Watanabe, E. Futami, C. Schmidt, J. Berger, C. Boerner, S. Ferber, and H. G. Weber, "160 Gbit/s wavelength converter with 3R-regenerating capability," *Electron. Lett.*, vol. 38, no. 16, pp. 903–904, Aug. 2002.

[70] S. Watanabe, F. Futami, R. Okabe, Y. Takita, S. Ferber, R. Ludwig, C. Schubert, C. Schmidt, and H. G. Weber, "160 Gbit/s optical 3R-Regenerator in a fiber transmission experiment," in *Proc. Optical Fiber Communication Conf. (OFC)*, 2002, pp. PD16–1 – PD16–3.

[71] S. Arahira and Y. Ogawa, "160-Gb/s OTDM signal source with 3R function utilizing ultrafast mode-locked laser diodes and modified NOLM," *IEEE Photon. Technol. Lett.*, vol. 17, no. 5, pp. 992–994, 2005.

[72] A. Bogoni, P. Ghelfi, M. Scaffardi, and L. Potì, "All-optical regeneration and demultiplexing for 160-Gb/s transmission systems using a NOLM-based three-stage scheme," *IEEE J. Select. Topics Quantum Electron.*, vol. 10, no. 1, pp. 92–96, Jan.-Feb. 2004.

[73] J. Li, B. E. Olsson, M. Karlsson, and P. A. Andrekson, "OTDM demultiplexer based on XPM-induced wavelength shifting in highly nonlinear fiber," *IEEE Photon. Technol. Lett.*, vol. 15, no. 12, pp. 1770–1772, Dec. 2003.

[74] J. Suzuki, T. Tanemura, K. Taira, Y. Ozeki, and K. Kikuchi, "All-optical regenerator using wavelength shift induced by cross-phase modulation in highly nonlinear dispersion-shifted fiber," *IEEE Photon. Technol. Lett.*, vol. 17, no. 2, pp. 423–425, Feb. 2005.

[75] K. Uchiyama, H. Takara, S. Kawanishi, T. Morioka, and M. Saruwatari, "Ultrafast polarization-independent all-optical switching using a polarization diversity scheme in the nonlinear optical loop mirror," *Electron. Lett.*, vol. 28, no. 20, pp. 1864–1866, Sep. 1992.

[76] B. E. Olsson and P. A. Andrekson, "Polarization independent demultiplexing in a polarization diversity nonlinear optical loop mirror," *IEEE Photon. Technol. Lett.*, vol. 9, no. 6, pp. 764–766, Jun. 1997.

[77] C. H. Kwok and C. Lin, "Polarization-insensitive all-optical NRZ-to-RZ format conversion by spectral filtering of a cross phase modulation broadened signal spectrum," *IEEE J. Select. Topics Quantum Electron.*, vol. 12, no. 3, pp. 451–458, May-Jun. 2006.

[78] R. Salem, A. S. Lenihan, G. M. Carter, and T. E. Murphy, "160-Gb/s polarization-independent optical demultiplexing in 2-m nonlinear fiber," *IEEE Photon. Technol. Lett.*, vol. 18, no. 21, pp. 2245–2247, Nov. 2006.

[79] B. E. Olsson, P. Ohlen, L. Rau, and D. J. Blumenthal, "A simple and robust 40-Gb/s wavelength converter using fiber cross-phase modulation and optical filtering," *IEEE Photon. Technol. Lett.*, vol. 12, no. 7, pp. 846–848, Jul. 2000.

[80] T. Yang, C. Shu, and C. Lin, "Depolarization technique for wavelength conversion using four-wave mixing in a dispersion-flattened photonic crystal fiber," *Opt. Express*, vol. 13, pp. 5409–5415, Jul. 2005.

[81] P. V. Mamyshev, "All-optical data regeneration based on self-phase modulation effect," in *Proc. Eur. Conf. Optical Communications (ECOC)*, vol. 1, 1998, pp. 475–476.

[82] M. Rochette, F. Libin, V. Ta'eed, D. J. Moss, and B. J. Eggleton, "2R optical regeneration: an all-optical solution for BER improvement," *IEEE J. Select. Topics Quantum Electron.*, vol. 12, no. 4, pp. 736–744, Jul.-Aug. 2006.

[83] S. K. Korotky, P. B. Hansen, L. Eskildsen, and J. J. Veselka, "Efficient phase modulation scheme for suppressing stimulated Brillouin scattering," in *Proc. IOOC*, 1995, pp. 110–111.

[84] T. Tanemura, J. Suzuki, K. Katoh, and K. Kikuchi, "Polarization-insensitive all-optical wavelength conversion using cross-phase modulation in twisted fiber and optical filtering," *IEEE Photon. Technol. Lett.*, vol. 17, no. 5, pp. 1052–1054, May 2005.

[85] A. S. Lenihan, R. Salem, T. E. Murphy, and G. M. Carter, "All-optical 80-Gb/s time-division demultiplexing using polarization-insensitive cross-phase modulation in photonic crystal fiber," *IEEE Photon. Technol. Lett.*, vol. 18, no. 12, pp. 1329–1331, Jun. 2006.

[86] L. B. Fu, M. Rochette, V. G. Taeed, D. J. Moss, and B. J. Eggleton, "Investigation of self-phase modulation based optical regeneration in single mode As_2Se_3 chalcogenide glass fiber," *Opt. Express*, vol. 13, pp. 7637–7644, Sep. 2005.

[87] N. Sugimoto, T. Nagashima, T. Hasegawa, and S. Ohara, "Bismuth-based optical fiber with nonlinear coefficient of 1360 $W^{-1}km^{-1}$," in *Proc. Optical Fiber Communication Conf. (OFC)*, vol. 2, 2004, p. PDP26.

[88] J. H. Lee, T. Nagashima, T. Hasegawa, S. Ohara, N. Sugimoto, and K. Kikuchi, "Bismuth-oxide-based nonlinear fiber with a high SBS threshold and its application to four-wave-mixing wavelength conversion using a pure continuous-wave

pump," *IEEE Journ. of Lightwave Technol.*, vol. 24, no. 1, pp. 22–28, Jan. 2006.

[89] J. H. Lee, T. Tanemura, and K. Kikuchi, "Experimental comparison of a Kerr nonlinearity figure of merit including the stimulated Brillouin scattering threshold for state-of-the-art nonlinear optical fibers," *Opt. Lett.*, vol. 30, no. 13, pp. 1698–1700, Jul. 2005.

[90] K. Tai, A. Hasegawa, and A. Tomita, "Observation of modulational instability in optical fibers," *Phys. Rev. Lett.*, vol. 56, no. 2, pp. 135–138, Aug. 1986.

[91] D. A. Fishman and J. A. Nagel, "Degradations due to stimulated Brillouin scattering in multigigabit intensity-modulated fiber-optic systems," *IEEE Journ. of Lightwave Technol.*, vol. 11, pp. 1721–1728, Nov. 1993.

[92] M. Horowitz, A. R. Chraplyvy, and J. L. Zyskind, "Broad-band transmitted intensity noise induced by stokes and anti-stokes brillouin scattering in single-mode fibers," *IEEE Photon. Technol. Lett.*, vol. 9, no. 1, pp. 124–126, Jan. 1997.

[93] A. Aoki, K. Tajima, and I. Mito, "Input power limits of single-mode optical fibers due to stimulated Brillouin scattering in optical communication systems," *IEEE Journ. of Lightwave Technol.*, vol. 6, no. 5, pp. 710–719, May 1988.

[94] T. Her, G. Raybon, and C. Headley, "Experimental demonstration of a fiber-based optical 2R regenerator in front of an 80 Gbit/s receiver," in *Proc. Optical Fiber Communication Conf. (OFC)*, 2003, pp. 194–195.

[95] M. Matsumoto, "Performance analysis and comparison of optical 3R regenerators utilizing self-phase modulation in fibers," *IEEE Journ. of Lightwave Technol.*, vol. 23, no. 6, pp. 1472–1482, Jun. 2004.

[96] T. Her, G. Raybon, and C. Headley, "Optimization of pulse regeneration at 40 Gb/s based on spectral filtering of self-phase modulation in fiber," *IEEE Photon. Technol. Lett.*, vol. 16, no. 1, pp. 200–202, Jan. 2004.

[97] P. Johannisson and M. Karlsson, "Characterization of a self-phase-modulation-based all-optical regeneration system," *IEEE Photon. Technol. Lett.*, vol. 17, no. 12, pp. 2667 – 2669, Dec. 2005.

[98] A. Striegler and B. Schmauss, "Analysis and optimization of SPM-based 2R signal regeneration at 40 Gb/s," *IEEE Journ. of Lightwave Technol.*, vol. 24, no. 7, pp. 2835–2843, Jul. 2006.

[99] T. Miyazaki and F. Kubota, "All-optical reshaping in a 160-Gb/s OTDM receiver using an XAM gate followed by an SPM discriminator," *IEEE Photon. Technol. Lett.*, vol. 16, no. 8, pp. 1909–1911, Aug. 2004.

[100] S. Taccheo and L. Boivin, "Investigation and design rules of supercontinuum sources for WDM applications," in *Proc. Optical Fiber Communication Conf. (OFC)*, vol. 3, 2000, pp. 2–4.

[101] C. G. Joergensen, T. Veng, L. Grüner-Nielsen, and M. Yan, "Dispersion flattened highly non-linear fiber," in *Proc. Eur. Conf. Optical Communications (ECOC)*.

[102] R. J. Essiambre, B. Mikkelsen, and G. Raybon, "Intra-channel cross-phase modulation and four-wave mixing in high-speed TDM systems," *Electron. Lett.*, vol. 35, no. 18, pp. 1576–1578, Sep. 1999.

[103] M. J. Potasek, G. P. Agrawal, and S. C. Pinault, "Analytic and numerical study of pulse broadening in nonlinear dispersive optical fibers," *J. Opt. Soc. Am. B.*, vol. 3, no. 2, pp. 205–211, Feb. 1984.

[104] I. Monfils, "All-optical clock recovery in a Q-switching self-pulsating DFB laser," Ph.D. dissertation, Queen's University, Kingston, Canada, 2007.

[105] F. Buchali and H. Bülow, "Adaptive PMD compensation by electrical and optical techniques," *IEEE Journ. of Lightwave Technol.*, vol. 22, no. 4, pp. 1116–1126, Apr. 2004.

[106] O. Karlsson, J. Brentel, and P. A. Andrekson, "Long-term measurement of pmd and polarization drift in installed fibers," *IEEE Journ. of Lightwave Technol.*, vol. 18, no. 7, pp. 941–951, Jul. 2000.

[107] D. L. Peterson, P. J. Leo, and K. B. Rochford, "Field measurements of state of polarization and pmd from a tier-1 carrier," in *Proc. Optical Fiber Communication Conf. (OFC)*, vol. 2, 2004, p. 4.

[108] C. Xie, D. Werner, and H. F. Haunstein, "Dynamic performance and speed requirement of polarization mode dispersion compensators," *IEEE Journ. of Lightwave Technol.*, vol. 24, no. 11, pp. 3968–3975, Nov. 2006.

[109] J. Zhou and M. J. O'Mahony, "Optical transmission system penalties due to fiber polarization mode dispersion," *IEEE Photon. Technol. Lett.*, vol. 6, no. 10, pp. 1265–1267, Oct. 1994.

[110] R. M. Jopson, L. E. Nelson, G. J. Pendock, and A. H. Gnauck, "Polarization-mode dispersion impairment in return-to-zero and nonreturn-to-zero systems," in *Proc. Optical Fiber Communication Conf. (OFC)*, 1999, pp. 80–82.

Appendix A

List of Acronyms

AAPN agile all-photonic network

AO-3R all-optical 3R regeneration

AR anti-reflection

ASE amplified spontaneous emission

BER bit error rate

CDR clock/data recovery

CW continuous wave

DCA digital communication analyzer

DCF dispersion compensating fiber

DFB distributed feedback

DGD differential group delay

DI delayed interferometer

DSQS dispersive self-Q-switching

EAM electroabsorption modulator

ED error detector

EDFA erbium-doped fiber amplifier

EO electrical-to-optical

ER extinction ratio

FBG fiber Bragg grating

FOM figure of merit

FSR free spectral range

FPF Fabry-Pérot filter

FWHM full-width at half-maximum

FWM four-wave mixing

GVD group velocity dispersion

HF holey fiber

HNLF highly nonlinear fiber

HO-FWM higher-order four-wave mixing

iFWM intra-channel four-wave mixing

ISI inter-symbol interference

IXPM intra-channel cross-phase modulation

JTC jitter transfer characteristic

MI modulation instability

MZI Mach-Zehnder interferometer

MZM Mach-Zehnder modulator

NOLM nonlinear optical loop mirror

NRZ nonreturn-to-zero

OBPF optical bandpass filter

OE optical-to-electrical

OEO optical-to-electrical-to-optical

OO optical-to-optical

OPA optical parametric amplification

OPLL optical phase locked loop

OSA optical spectrum analyzer

OSNR optical signal-to-noise ratio

PC polarization controller

PCF photonic crystal fiber

PLL phase locked loop

PM phase modulator

PMD polarization mode dispersion

PMDE polarization mode dispersion emulator

PRBS pseudorandom bit sequence

PTC power transfer characteristic

RBW resolution bandwidth

RD residual dispersion

RDPS residual dispersion per span

RIN relative intensity noise

RZ return-to-zero

SBS stimulated Brillouin scattering

SC supercontinuum

SMF single-mode fiber

SNR signal-to-noise ratio

SOA semiconductor optical amplifier

SOA-DI SOA-delayed interferometer

SOA-MZI SOA-Mach-Zehnder interferometer

SOP state-of-polarization

SP self-pulsation

SP-DFBL self-pulsating distributed feedback laser

SPM self-phase modulation

SRS stimulated Raman scattering

TDM time division multiplexing

TLS tunable laser source

TOD tunable optical delay

TWM three-wave mixing

UNI ultrafast nonlinear interferometer

VOA variable optical attenuator

WC wavelength conversion

WDM wavelength division multiplexing

XAM cross-absorption modulation

XGM cross-gain modulation

XPM cross-phase modulation

Appendix B

List of Symbols

B.1 Fiber Parameters

$\chi^{(3)}$	third-order nonlinear susceptibility
n	refractive index
n_{eff}	effective refractive index
Δn	change in refractive index
n_0	linear refractive index
n_2	nonlinear refractive index coefficient
γ	nonlinear parameter
α	attenuation coefficient
L	fiber length

L_{eff}	effective fiber length
L_W	walk-off length
L_{NL}	nonlinear length
L_D	dispersion length
N	soliton order
$\Delta\tau_g$	group delay
v_g	group velocity
d	group velocity mismatch parameter
β_2	second-order dispersion parameter
D	dispersion parameter
λ_0	zero dispersion wavelength
S	dispersion slope
S_0	dispersion slope at the zero dispersion wavelength

B.2 Signal Parameters

B	bit rate
ω	carrier radian frequency

ω_0	free-space carrier radian frequency
λ_0	free-space carrier wavelength
k_0	free-space wave number
λ	carrier wavelength
T_{RMS}	pulse half-width (root-mean square)
T_0	pulse half-width at 1/e of the peak power
T_{FWHM}	pulse full-width at half-maximum
Δf_{FWHM}	frequency spectral full-width at half-maximum
$\Delta\lambda_{FWHM}$	wavelength spectral full-width at half-maximum
I	intensity
P	signal power
P_0	signal peak power
E	electric field
ϕ_{SPM}	SPM induced phase
ϕ_{XPM}	XPM induced phase
ϕ_{max}	maximum nonlinear phase
A_{eff}	effective core area

B.3 Regenerator Parameters

λ_c	clock signal carrier wavelength
λ_d	data signal carrier wavelength
λ_{in}	input signal carrier wavelength
λ_{out}	output signal carrier wavelength
f_d	data signal frequency
f_c	clock signal frequency
f_{sp}	self-pulsation signal frequency
$\Delta\tau_{cd}$	time delay between clock and data signals
$P_{0,c}$	clock signal peak power
$P_{0,d}$	data signal peak power
$P_{0,in}$	input signal peak power
$P_{0,out}$	output signal peak power
$T_{FWHM,c}$	clock signal pulse full-width at half-maximum
$T_{FWHM,d}$	data signal pulse full-width at half-maximum
$T_{FWHM,in}$	input pulse full-width at half-maximum
$T_{FWHM,out}$	output pulse full-width at half-maximum

$T_{0,c}$	clock pulse half-width at 1/e of the peak power
$T_{0,d}$	data pulse half-width at 1/e of the peak power
$T_{0,in}$	input pulse half-width at 1/e of the peak power
$T_{0,out}$	output pulse half-width at 1/e of the peak power
$T_{RMS,in}$	input pulse half-width (root-mean square)
$T_{RMS,out}$	output pulse half-width (root-mean square)
ξ	propagation length (normalized to the dispersion length)
M	spectral broadening factor
$\Delta\lambda_{out}$	SPM output spectral width
$\Delta\lambda_{in}$	SPM input spectral width
$\Delta\lambda_{XPM}$	XPM slicing filter offset
$\Delta\lambda_{SPM}$	SPM slicing filter offset
a_M	spectral broadening coefficient
a_ξ	propagation length coefficient
S_{PTC}	slope of power transfer characteristic